Switching Device Fault Analysis for Low Voltage Inverters Used in Microgrid

Thesis Submitted

by

Sankha Subhra Ghosh

Doctor of Philosophy (Engineering)

Department of Electrical Engineering
Faculty Council of Engineering &Technology
Jadavpur University
Kolkata, India

2025

INDEX NO.: 198/22/E

1. Title of the thesis	**Switching Device Fault Analysis for Low Voltage Inverters Used in Microgrid**
2. Name, Designation & Institution of Supervisor/s	**Dr. Arabinda Das** Professor Department of Electrical Engineering, Jadavpur University, Kolkata, West Bengal, India, Pin-700032 **Dr. Surajit Chattopadhyay** Associate Professor Department of Electrical Engineering, Ghani Khan Choudhury Institute of Engineering & Technology, Narayanpur, Malda, West Bengal, India, Pin-732141

3. List of Publication

Journal Publications:

[1] **S. S. Ghosh**, S. Chattopadhyay and A. Das, "Identification of an Incipient Snubber Failure in Inverter Employed in Solid Oxide Fuel Cell (SOFC) Fed Microgrid," in ***IEEE Transactions on Instrumentation and Measurement***, vol. 74, pp. 1-10, 2025, Art no. 3511510, doi: 10.1109/TIM.2025.3544391. **(SCI/Scopus Indexed)**

[2] **S. S. Ghosh**, S. Chattopadhyay, S. Banerjee, and A. Das, "Study of Budding Snubber Quality Deterioration in Solid Oxide Fuel Cell-Fed Inverter Used in Microgrid Energy Conversion," ***Energy Technology (Wiley)***, Jul. 2024, doi: 10.1002/ente.202400568. **(SCI/Scopus Indexed)**

[3] **S. S. Ghosh**, S. Chattopadhyay, S. Das, A. Das, G. R. K. Prasad, and A. Das, "Identification of GTO Switch Fault in Voltage Source Inverter in PV Integrated Microgrid," ***Journal of Nano- and Electronic Physics***, vol. 16, no. 3, pp. 03022-1-03022–5, 2024, doi: 10.21272/jnep.16(3).03022. **(Scopus Indexed)**

[4] **S. S. Ghosh**, S. Chattopadhyay, R. V. V. Krishna, R. K. Mahapatra, A. Das, and S. Das, "Measurement of Very Small Variation of Effective Resistance of MOSFET Deputed in Active Microgrid Inverter Operation," ***Journal of Nano- and Electronic Physics***, vol. 16, no. 3, pp. 03029-1-03029–5, 2024, doi: 10.21272/jnep.16(3).03029. **(Scopus Indexed)**

[5] **S. S. Ghosh,** S. Chattopadhyay, S. H. Arigela, V. V. Kamesh, A. Das, S. Das, "Expeditious identification of IGBT switch fault in bidirectional microgrid inverter linked to distributed energy resources," ***Journal of Nano- and Electronic Physics***, vol. 16, no. 1, pp. 01019–5, Jan. 2024, doi: 10.21272/jnep.16(1).01019. **(Scopus Indexed)**

[6] **S. S. Ghosh,** S. Chattopadhyay, A. Das, N. R. Medikondu, A. H. M. Almawgani, A. R.H. Alhawari, S. Das, "Wavelet-based rapid identification of IGBT switch breakdown in voltage source converter," ***Microelectronics Reliability (Elsevier)***, vol. 152, p. 115283, Jan. 2024, doi: 10.1016/j.microrel.2023.115283. **(SCI/Scopus Indexed)**

[7] **S. S. Ghosh**, S. Mukherjee, S. Chattopadhyay, and A. Das, "Premature Breakdown Identification in Photovoltaic Array Fed IGBT-based Voltage Source Converter," ***Journal of Nano- and Electronic Physics***, vol. 15, no. 3, pp. 03016-1-03016–5, 2023, doi: 10.21272/jnep.15(3).03016. **(Scopus Indexed)**

[8] **S. S. Ghosh**, S. Chattopadhyay, and A. Das, "Fast Fourier transform and wavelet-based statistical computation during fault in snubber circuit connected with robotic brushless direct current motor," ***Cognitive Computation and Systems (IET-Wiley)***, vol. 4, no. 1, pp. 31–44, Mar. 2022, doi: 10.1049/ccs2.12041. **(SCI/Scopus Indexed)**

Conference Publication:

[1] **S. S. Ghosh**, S. Chattopadhyay, A. Das, "Harmonics Monitoring for Winding Fault Diagnosis of Brushless DC motor," ***Michael Faraday IET International Summit: MFIIS-2020***, October 03 – 04, 2020, Kolkata, India, pp. 164-169, ISBN of Proceedings: 978-1- 83953-272-6. doi: 10.1049/icp.2021.1137. **(Scopus Indexed)**

Book Chapter:

[1] **S. S. Ghosh**, S. Chattopadhyay, and A. Das, "Fault Detection Approaches for AC Microgrid Power Converters Employed in Distributed Energy Sources: A Review," "**Computer Aided Power System Condition Monitoring**", The book will be published under the Wiley-Scrivener imprint and will be indexed by Scopus and offered to Web of Science. **(Accepted)**

4. List of Patents: Nil

5. List of Presentations in National/International/Conferences/Workshops:

[1] **S. S. Ghosh**, S. Chattopadhyay, S. Das, A. Das, G. R. K. Prasad, and A. Das, "Identification of GTO Switch Fault in Voltage Source Inverter in PV Integrated Microgrid," ***4th International conference on Innovative Research in Renewable Energy Technologies (IRRET-2024)***, April 07-08, 2024, Malda, West Bengal, India.

[2] **S. S. Ghosh**, S. Chattopadhyay, S. Banerjee, and A. Das, "Investigation of Budding Snubber Quality Deterioration in Solid Oxide Fuel Cell (SOFC) Used in Microgrid Energy Conversion," ***International Conference on Global Conference for Decarbonization of Energy and Materials (GC-DEM 2023)***, December 27-31, 2023, at NTU Alumni, Singapore.

[3] **S. S. Ghosh**, S. Mukherjee, S. Chattopadhyay, and A. Das, "Premature Breakdown Identification in Photovoltaic Array Fed IGBT-based Voltage Source Converter," ***3rd International conference on Innovative Research in Renewable Energy Technologies (IRRET-2023)***, April 09-10, 2023, Malda, West Bengal, India.

[4] **S. S. Ghosh**, S. Chattopadhyay, A. Das, "Harmonics Monitoring for Winding Fault Diagnosis of Brushless DC motor," ***Michael Faraday IET International Summit: MFIIS-2020***, October 03 – 04, 2020, Kolkata, India.

"Statement of Originality"

I, **Sankha Subhra Ghosh** registered on **20th June 2022** do hereby declare that this thesis entitled **"Switching Device Fault Analysis for Low Voltage Inverters Used in Microgrid"** contains literature survey and original research work done by the undersigned candidate as part of Doctoral studies.

All information in this thesis have been obtained and presented in accordance with existing academic rules and ethical conduct. I declare that, as required by these rules and conduct, I have fully cited and referred all materials and results that are not original to this work.

I also declare that I have checked this thesis as per the "Policy on Anti Plagiarism, Jadavpur University, 2019", and the level of similarity as checked by iThenticate software is 05 %.

Signature of Candidate: Sankha Subhra Ghosh

Date: 23/09/2025

Certified by Supervisor(s):
(Signature with date, seal)

1. Analinda Das
23/09/2025
Professor
Electrical Engineering Department
Jadavpur University

2. Surajit Chattopadhyay
23/09/25

GKCIET

CERTIFICATE FROM THE SUPERVISORS

This is to certify that the thesis entitled **"Switching Device Fault Analysis for Low Voltage Inverters Used in Microgrid"** submitted by **Shri Sankha Subhra Ghosh**, who got his name registered on **20th June 2022** for the award of Ph. D. (Engg.) degree of Jadavpur University is absolutely based upon his own work under the supervision of **Dr. Arabinda Das** and **Dr. Surajit Chattopadhyay** and that neither his thesis nor any part of the thesis has been submitted for any degree/diploma or any other academic award anywhere before.

1. Arabinda Das. 23/09/2025
Signature of the Supervisor
and date with Office Seal

Professor
Electrical Engineering Department
Jadavpur University

2. Surajit Chattopadhyay 23/09/25
Signature of the Supervisor
and date with Office Seal

Ghani Khan Choudhury Institute of Engg & Tech ★ (A CFTI Under the Ministry of Education, Govt. of India)
GKCIET
Narayanpur
Dist. Malda
732141 (W.B.)

Acknowledgement

First and foremost, I bow with deepest reverence to Lord Shri Krishna, whose divine blessings and guidance have been my constant source of strength, inspiration, and perseverance throughout this journey.

I would like to record my profound gratitude to my esteemed supervisors, Dr. Arabinda Das, Professor, Department of Electrical Engineering, Jadavpur University, and Dr. Surajit Chattopadhyay, Associate Professor, Department of Electrical Engineering, Ghani Khan Choudhury Institute of Engineering & Technology. Their vision, patience, and immense knowledge have guided me at every stage of this work. Their relentless motivation and scholarly mentorship have not only shaped my research but have also been invaluable in completing this thesis. I remain especially indebted to them for their empathy, encouragement during difficult times, and above all, the faith with which they entrusted me with this research. It has been both a privilege and an honor to conduct my work under their esteemed supervision.

I sincerely thank the Head of the Department of Electrical Engineering, Jadavpur University, for the opportunity and facilities to carry out this research, and also the respected members of my thesis committee for their valuable comments and constructive feedback, which have significantly enriched this work.

My heartfelt gratitude goes to my parents, whose sacrifices, blessings, and unconditional love have laid the foundation of my academic journey.

I am profoundly thankful to my wife for her great understanding, patience, prayers, admiration, and continuous support. Her constant encouragement and inspiration throughout my research have been truly instrumental in completing this thesis. I am also grateful to my little son and daughter for their affection and thoughtful support, which have been a source of joy and strength during this journey. My sincere thanks also go to my family members, friends, and colleagues for their encouragement and inspiration at different stages of this work.

Finally, I gratefully acknowledge all who supported me in various ways toward the completion of this thesis.

Date: 23/09/2025

Place: Kolkata

Sankha Subhra Ghosh

(Sankha Subhra Ghosh)

Dedicated to Lord Shri Krishna

and

to my beloved parents, wife, son, and daughter.

Preface

The changing features of contemporary power systems, propelled by the rising integration of renewable and distributed energy sources, have profoundly transformed conventional energy generation and distribution models. Microgrids (MGs) have become a crucial component of resilient, sustainable, and locally based energy solutions in this regard. Increased energy independence, less transmission losses, and greater grid dependability are all benefits of these decentralized systems. The power electronic converter (PEC), especially the low-voltage inverter, is essential to the smooth functioning of microgrids because it makes it easier to integrate, monitor, and regulate a variety of energy sources. These inverters' essential switching components are Gate Turn-Off Thyristors (GTOs), Metal-Oxide-Semiconductor Field-Effect Transistors (MOSFETs), and Insulated Gate Bipolar Transistors (IGBTs). Despite being essential for energy conversion and control, these parts are prone to malfunctions that might jeopardize the stability, security, and effectiveness of microgrids.

This thesis thoroughly examines the failure processes, detection techniques, and diagnostic approaches for switching devices used in microgrid low-voltage inverters. For the PECs in MGs to operate safely, continuously, and effectively, it develops and evaluates sophisticated, quick, and trustworthy fault detection methods. The work is organized in many chapters, each of which focuses on an entirely distinct type of problem, inverter configuration, or application situation. The basis is laid by the literature review, which looks at a variety of AC MG converter defect modes. It explores current failure detection methods, pointing out shortcomings in existing diagnostic techniques and the requirement for precise, continual monitoring systems designed for the dynamic microgrid environment. The main hypothesis of the thesis is supported by this survey: different statistical indicators in conjunction with signal processing techniques like fast Fourier transform (FFT) and discrete wavelet transform (DWT) provide effective tools for the early identification of defects in inverters switching components.

The succeeding chapters present focused approaches for identifying faults in numerous types of inverter applications and configurations. The identification of inverters snubber circuits resistance defects in BLDC motor applications demonstrates how FFT and wavelet-based analysis of stator currents may help to uncover minute irregularities by examining harmonic and statistical features. In a similar vein, the thesis investigates early IGBT failure in the 3-Phase voltage source converter (VSC) connected to a photovoltaic (PV) microgrid, identifying fault characteristics by an FFT-based analysis of the output phase voltage. An attempt is made to investigate accelerated IGBT switch failures in bidirectional inverters connected to dispersed resources like solar panels and battery storage.

Additionally, the thesis broadens its focus to include changes in MOSFET effective resistance (MER) in MG H-bridge inverters. MOSFETs' aging or thermal stress is indicated by very slight MER changes, which are detected by the inverter output current's FFT spectrum analysis. Additionally, the thesis focuses on GTO switch failure (GSF) in a PV-incorporated MG's 3-phase voltage source inverter (VSI). The recommended FFT-based technique enables efficient identification of current distortion brought on by GSFs.

Thesis also includes a technique for determining the DWT-based IGBT switches breakdown failures in 3-phase VSCs connected to the PV system. The identification of early and emerging defects in snubber circuits coupled to SOFC-fed inverters is a noteworthy contribution. Both FFT and DWT procedures are used to examine inverter output current data for these kinds of degradations, which are sometimes hard to identify using conventional techniques. In order to provide increased system durability, algorithms were developed to identify flaws early on, well before they cause a catastrophic failure.

This work's innovative feature is the development of fault detection algorithms customized for certain inverter topologies and device kinds. Numerous circumstances and configurations are used to validate the approaches. Simulation tests, laboratory evaluations, and comparison with current methods are used to validate the algorithms' efficacy. This thesis provides a strong and cohesive framework for identifying a variety of switching device issues in low voltage microgrid inverters.

Contents

List of Abbreviations

1phHBI	Single-Phase H-Bridge Inverter
3Ph	Three-Phase
3PhHBI	Three-Phase H-Bridge Inverter
3PhI	3-Phase Inverter
AI	Artificial Intelligence
ANN	Artificial Neural Network
AR	Accuracy Rate
BC	Boost Converter
BDAI	Bidirectional DC/AC Inverter
BDI	Bidirectional Inverter
BLDC	Brushless DC
BLDCMD	Brushless DC Motor Drive
BN	Bayesian Network
BSS	Battery Storage System
C	Capacitor
CC	Ceramic Capacitor
CHBMLI	Cascaded H-Bridge Multi-Level Inverter
CHMLI	Cascaded H-Bridge Multilevel Inverter
CM	Clustering Method
CMN	Condition Monitoring
CNN	Convolutional Neural Network
CNPC	Cascaded Neutral-Point-Clamped
CSI	Current-Source Inverter
CWT	Continuous Wavelet Transform
DCC	DC Component
DCMLI	Diode-Clamped Multi-Level Inverter
DD	Detection Duration
DER	Distributed Energy Resource
DES	Distributed Energy Source
DG	Distributed Generation
DT	Decision Tree

DWT	Discrete Wavelet Transform
EC	Electrolytic Capacitor
ECM	Electrochemical Migration
ECS	Energy Conversion System
EM	Electromigration
ERM	Effective Resistance of MOSFET
ESR	Equivalent Series Resistance
ESS	Energy Storage System
FC	Film Capacitor
FCC	Fundamental Current Component
FCV	Fundamental Component of Voltage
FDM	Failure Detection Method
FFT	Fast Fourier Transform
FIL	Fault Identification and Localization
FT	Fourier Transform
GA	Genetic Algorithm
GSC	Grid-Side Converter
GSF	GTO Switch Fault
%GSF	Percent of GSF
GTO	Gate Turn-Off Thyristor
HBI	H-Bridge Inverter
HS	Hall Sensor
IBDF	IGBT Switches Breakdown Failure
%IBDF	Percentages of IBDF
IFMD	Inverter-Fed Motor Drive
IGBT	Insulated Gate Bipolar Transistor
ISCF	Initial Snubber Circuitry Failure
%ISCF	Percentages of ISCF
ISF	IGBT Switch Fault
%ISF	ISF Percentage Level
ISSCRF	Inverter Switch's Snubber Circuit Resistance Failure
%ISSCRF	ISSCRF Percentage
KNN	K-Nearest Neighbor

LV	Low Voltage
LVI	Low-Voltage Inverter
M	Mean
MCD	Matrix Converter Drive
MG	Microgrid
MGI	Microgrid Inverter
ML	Machine Learning
MLHBI	Multilevel H-Bridge Inverter
MLI	Multilevel Inverter
MMC	Modular Multilevel Converter
MOSFET	Metal-Oxide-Semiconductor Field-Effect Transistor
MPC	Microgrid Power Converter
MPPT	Maximum Power Point Tracking
MRA	Multi-Resolution Analysis
MRAS	Model Reference Adaptive System
MSD	Mean and Standard Deviation
MSF	MOSFET Switch Fault
%MSF	MSF Percentage
NPC	Neutral-Point-Clamped
NSF	Nascent Snubber-Resistance Fault
%NSF	Percentage of NSF
OC	Open-Circuit
OCD	Open Circuit Defect
OCF	Open Circuit Failure
OSF	Overstressed Fault
OSI	Over-Stressed Issue
PCA	Principal Component Analysis
PD	Performance Drift
PEC	Power Electronic Converter
PES	Power Electronic Switch
PIBDF	Prematurely IGBT Breakdown Failure
%PIBDF	Percentage Values of the PIBDF
PNN	Probabilistic Neural Network

PV	Photovoltaic
PWM	Pulse-Width Modulation
RC	Resistance-Capacitance
RES	Renewable Energy Source
RF	Random Forest
RMG	Residential Microgrid
RMS	Root Mean Square
RUL	Remaining Usable Life
SC	Short-Circuit
SCC	Sub-Harmonic Current
SCD	Short Circuit Defects
SCF	Short Circuit Failure
SCV	Sub-Harmonic Components of Voltage
SD	Standard Deviation
SDMV	Standard Deviation and Mean Value
SDV	Standard Deviation Value
SHC	Subharmonic
SL	Supervised Learning
SMGI	Small Microgrid Inverter
SOFC	Solid-Oxide Fuel Cell
SPHBI	Single-Phase H-Bridge Inverter
SVM	Support Vector Machine
TF	Thermal Fatigue
THD	Total Harmonic Distortion
THDC	Total Harmonic Distortion of Current
THDF	Total Harmonic Distortion Factor
TPHBI	3-phase H-bridge Inverter
TPVSI	Three-Phase Voltage Source Inverter
TS	Thermal Stress
VSC	Voltage Source Converter
VSI	Voltage Source Inverter
WOF	Wear-Out Faults
WOI	Wear-Out Issue

WPC	Wind Power Converter
ZFC	Zero-Frequency Component

***Abbreviations not listed above and symbols are defined in their respective contexts within the thesis.**

List of Figures

List of Tables

Chapter 1

Introduction

1.1 Background

The growing worldwide focus on sustainable energy, environmental stewardship, and distributed generation has markedly expedited the implementation of microgrids (MGs). Distributed energy resources (DERs), including photovoltaic solar power, wind turbines, fuel cells, and energy storage devices, are all integrated into these localized energy systems. Microgrids, which may function in both grid-connected and islanded forms, provide enhanced efficiency, resilience, and dependability, particularly in distant or high-demand locations.

Power electronic converters (PECs), especially low-voltage inverters (LVIs), are crucial parts of microgrids since they serve as a conduit between the AC grid and DERs. LVIs employ different switching elements like insulated gate bipolar transistors (IGBTs), metal-oxide-semiconductor field-effect transistors (MOSFETs), etc., to accomplish effective energy conversions. It is anticipated that these inverters would operate with great performance and dependability.

The inverters' longer functioning and greater complexity, however, have also made them more susceptible to numerous failures, particularly those involving their switching elements. If left undiagnosed or neglected, these issues may jeopardize the microgrid's complete safety and stability in addition to the inverter's functionality. In light of this, switching devices' fault detections in LVIs have emerged as a crucial research topic in contemporary power systems.

1.2 Motivation

The inverter's switching elements are essential to its functioning since they manage fast switching at elevated frequencies, ensuring efficient power conversion. Switching devices are still vulnerable to failures from overvoltage, overcurrent, heat stress, and deterioration over extended periods, even with improvements in device manufacture and thermal handling.

Even one switching device malfunction might result in distorted output, decreased efficiency, or, in the worst situations, a fire danger or total system failure. Such malfunctions in microgrids might have a domino effect, impacting several DERs or vital loads. System resilience may be improved, maintenance expenses can be decreased, and downtime can be avoided with early defect detection and investigation.

There has been research on identifying faults in typical electrical systems, but given the particular operating circumstances, control schemes, and load interactions of microgrids, more targeted, thorough research is required on switching device faults in the LVI field. The necessity to provide a reliable, precise, and efficient computational diagnostic approach based on the fast Fourier transform (FFT) and discrete wavelet transform (DWT) oriented feature extraction and statistical analysis that is validated by real-world inverter case studies pertinent to microgrid applications is what spurred this research.

1.3 Need

A microgrid is mostly powered by renewable energy sources. The converter unit and the control unit are the two primary components of an energy conversion system (ECS). The use of DERs, the integration of various grid types, and the general functioning of the grid are all significantly impacted by energy conversion units.

Given this momentous scenario, further research is required, especially in the subsequent areas:

- Early identification of numerous kinds of ECSs switching device defects.
- Minimizing the many kinds of defects in real-time applications.
- Microgrid protection and fault monitoring.

1.4 Research Objectives

Investigating and creating efficient diagnostic methods for locating switching device issues in LVIs used in microgrids is the primary objective of this study. The following is an outline of the precise goals:

- To study numerous kinds of errors that might arise in LVI switching components.
- To investigate and demonstrate how different switching device malfunctions affect the inverter's output.

- To devise and assess diagnostic methods for the early identification of malfunctions in switching devices.
- To verify the suggested diagnostic methods using simulated studies and real-world experimental setups under various fault conditions, if feasible.
- To evaluate the suggested methodology's computational effectiveness, sensitivity, and dependability for real-world implementation in microgrid systems.

1.5 Flow of Work

This thesis is primarily focused on diagnosing switching device faults in LVIs used in microgrid systems. The flow of work includes:

- Literature survey
- Analysis of various DERs for MG applications
- Investigation of several ECS types
- Identifying different issues with the ECS switching elements
- Modelling various ECS types
- Approach for identifying various issues and distinct utilization metrics
- Results and comparisons
- General conclusion

1.6 Application Modes

The following application modes have been employed to develop and validate the suggested fault identification methodologies:

- **Simulation:** To assess the diagnostic methods under controlled circumstances with the use of MATLAB/Simulink.
- **Real-time:** The diagnostic approach is put into practice on the inverter configuration at the laboratory. The algorithms are tested in real-time signal gathering and processing to verify their dependability in identifying real switching faults and to test them under realistic operational settings.

1.7 Mathematical Tools and Advanced Technology Used

The following modern mathematical techniques and technologies are included in this research:

- FFT: To analyze the signals in the frequency domain.

- DWT: To analyze the signals in both the frequency and time domains.
- Signal Processing Techniques: For filtering, decomposition, and feature extraction.
- Statistical Analysis: To assess and categorize signal characteristics.

1.8 Faults under Consideration

The AC microgrid power converter's (MPC's) switching device faults under consideration are shown in Fig. 1.1.

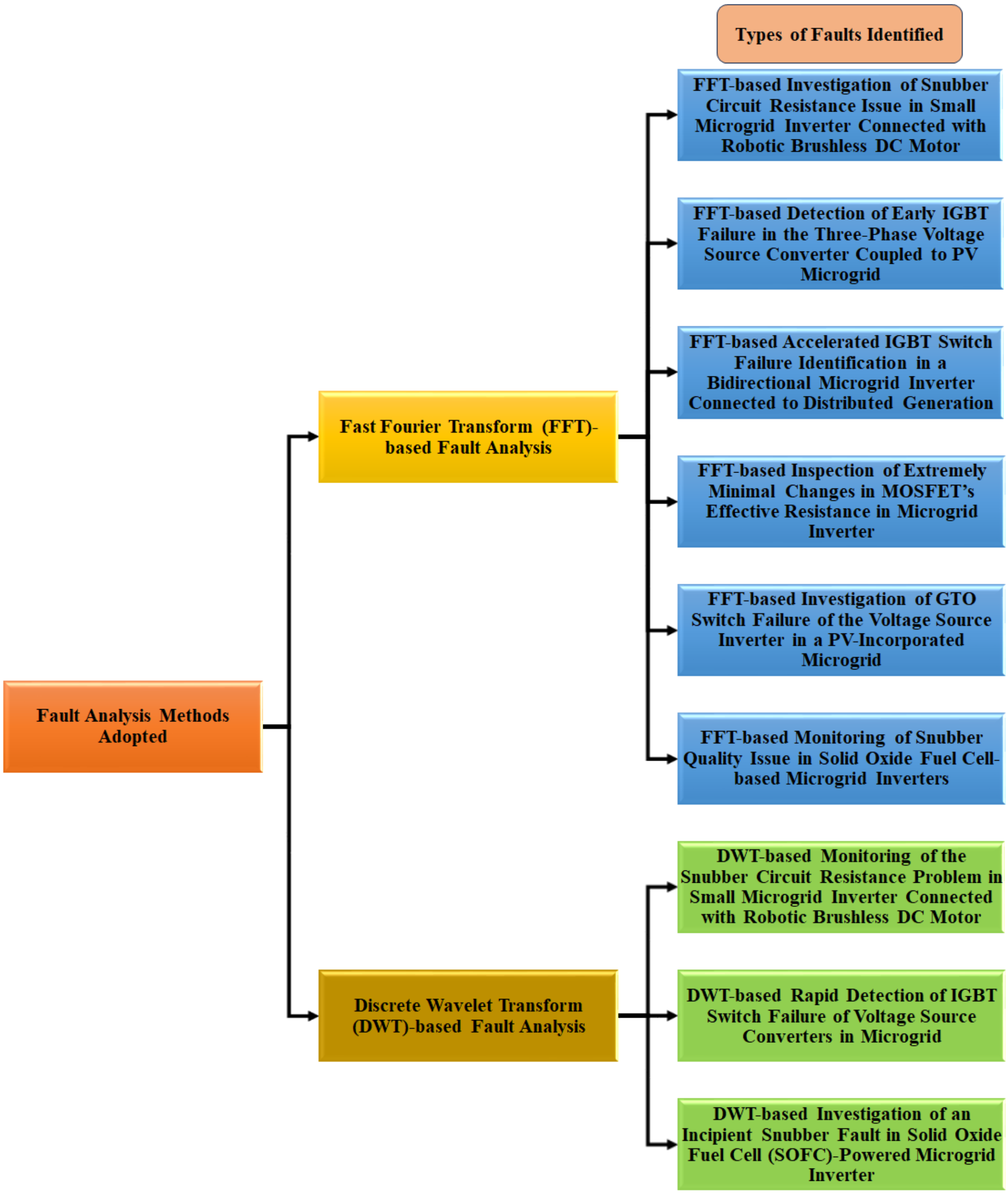

Fig. 1.1. MPC's switching device faults under consideration

1.9 Chapter at a Glance

This thesis is structured as follows for the remainder:

Chapter 2 provides a comprehensive review of the literature on different inverter failure diagnostic methods, focusing on approaches for signal processing and switching component failures.

Chapter 3 discusses an FFT-based effort to identify the inverter switch's snubber circuit resistance failure in a small microgrid inverter connected with robotic brushless DC (BLDC) motors.

Chapter 4 describes an FFT-based methodology for identifying prematurely IGBT breakdown failure in the three-phase voltage source converter that is coupled to a photovoltaic grid.

Chapter 5 demonstrates an FFT-based technique for detecting a quick IGBT switch fault in the MG's bidirectional inverter connected to a photovoltaic and battery storage system.

Chapter 6 introduces an FFT-based technique for identifying a quick MOSFET switch fault in a single-phase H-bridge inverter connected to a photovoltaic system.

Chapter 7 illustrates an FFT-based method for figuring out the GTO switch fault for a photovoltaic-based three-phase voltage source inverter in the MG.

Chapter 8 presents an innovative strategy based on FFT for detecting nascent snubber-resistance faults in MG's 3-phase inverters that is coupled to the solid-oxide fuel cell.

Chapter 9 discusses an effort to recognize the inverter switch's snubber circuit resistance failure in robotic brushless BLDC motors through a DWT-based approach.

Chapter 10 presents a DWT-based technique for determining the IGBT switches' breakdown failures in three-phase voltage source converters connected to the photovoltaic system.

Chapter 11 presents a DWT-based innovative strategy for detecting initial snubber circuitry failure detection method in MG's IGBT-based 3-phase inverters that is linked to the solid-oxide fuel cell.

Chapter 12 emphasizes the research's contributions, summarizes the main conclusions, and suggests possible paths of research for further study.

Chapter 2

Literature Survey

Abstract- The seamless integration, management, and control of distributed energy resources (DERs) inside AC microgrid (MG) systems is made possible by microgrid power converters (MPCs), which enhance grid efficiency, resilience, and dependability. The implications of MPC faults might vary according to the kind of fault and the microgrid system's configuration. In this literature review, numerous ways in which the MPC module might malfunction are thoroughly discussed.

Keywords: *Distributed energy resource (DER), fault detection, microgrid power converter (MPC)*

2.1 Introduction

This chapter provides an in-depth overview of the several ways that the AC MPC modules might malfunction. Technical review covers a range of failure detection methods (FDMs), the majority of which are model-free and model-based. The fundamental layout and arrangement of the AC microgrid have been described. The functional variety of AC MG is also demonstrated in this chapter. It outlines the types, origins, and consequences of MPC malfunctions. The prevailing approaches for defect diagnostics of the multiple MPC switching elements are reviewed.

2.2 AC Microgrid's General Framework

An AC MG with a variety of DERs attached to the main grid is illustrated in Fig. 2.1. This kind of MG is simpler to link to a conventional AC grid, allowing it greater flexibility and adaptability than other types. Microgrid inverters (MGIs) are utilized for converting DERs' dc power into ac energy. AC MGs are frequently divided into three distinct categories according to their voltage levels: low, medium, and high.

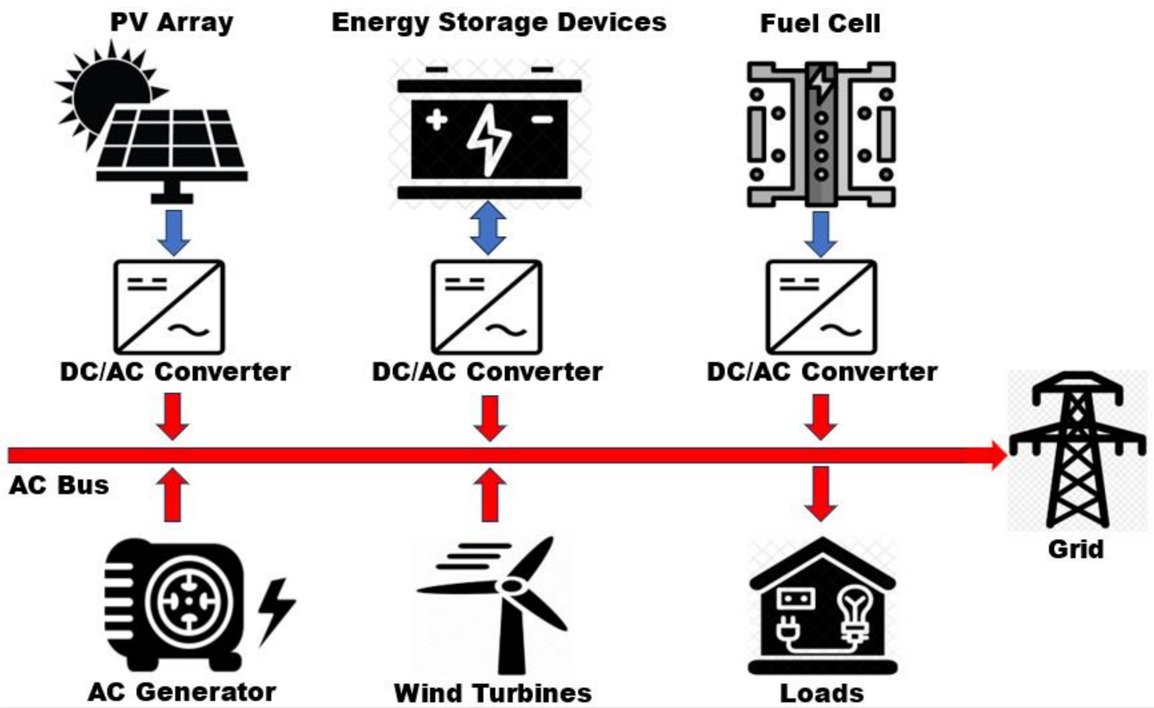

Fig. 2.1. General layout illustration of an AC MG

2.2.1 Different Components of an AC MG

AC MGs are comprised of MPCs, DERs, loads, energy storage systems (ESSs), and various other components. A brief description of each component of an MG is discussed here.

2.2.1.1 MPCs

MPCs use technology that is based on power electronics. They act as a link within the AC MG and each component of it. Based on their functions, the AC MPCs are classified as either grid-feeding, grid-forming, or grid-supporting systems.

2.2.1.2 DERs

According to the kind of power they produce, DERs are frequently separated into two types: DC and AC sources. Based upon their dispatchability, DERs are additionally separated into two groups: non-dispatchable and dispatchable.

2.2.1.3 Loads

Many characteristics, including power type, load handling techniques, location, linearity, and operating conditions, are all used to classify loads, including ac and dc loads, non-linear loads, linear loads, etc.

2.2.1.4 ESSs

ESSs are used to improve MGs' overall stability and performance. ESSs are used to store surplus energy generated by different DERs and serve as a backup power source.

2.3 AC MG's Functional Diversity

AC MGs can operate in a variety of modes, each of them is designed to control power distribution and offer stability in certain situations. MGs can operate in two different modes: (1) grid-dependent and (2) islanded.

When an MG is connected to the primary grid, it operates in a grid-linked state. "Island mode," as used by MG, refers to the operating state where the MG operates independently from the main power grid.

2.4 Modes, Origin, and Consequences of MPC Components' Faults

Discussion of the many forms, causes, and negative effects of problems with MPCs' power electronic switches (PESs) and capacitors is the main focus of this section.

2.4.1 PES

Typical PESs found in AC MPCs include gate turn-off thyristor (GTO), metal-oxide-semiconductor field-effect transistor (MOSFET), and insulated gate bipolar transistor (IGBT). One of the IGBTs' and GTOs' typical features is their high current and voltage ratings [1]. Fig. 2.2 shows the various percent breakdown rates of PCBs, PESs, and capacitors [2], [3], [4], [5].

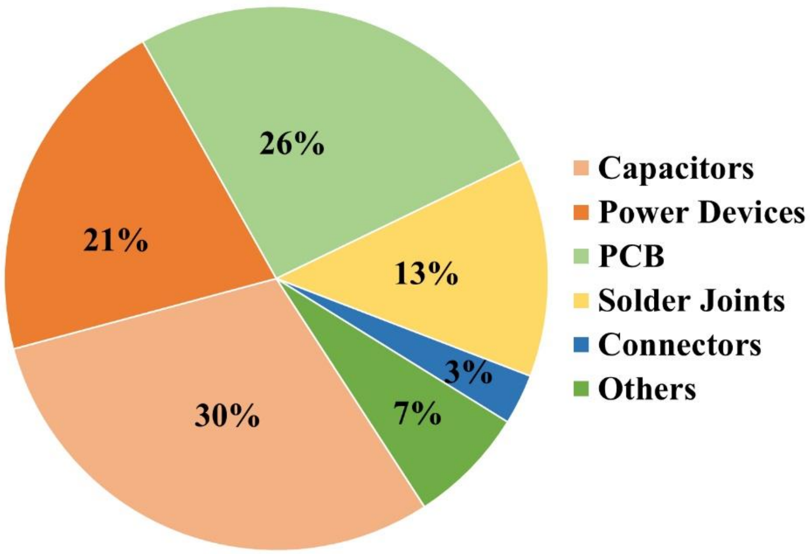

Fig. 2.2. Failing rates of the primary elements of the MPC

PESs like MOSFETs and IGBTs are accounted for around 21% of inverter faults [5], [6]. The complete system may shut down if the PESs in MPCs malfunction. The effectiveness of PESs can be impacted by fault events like open circuit defects (OCDs), short circuit defects (SCDs), etc. As Fig. 2.3 illustrates, PESs are especially prone to malfunction for a variety of reasons. Temperature is the most prevalent source of stress on electronic elements, accounting for 55% of all stress variance.

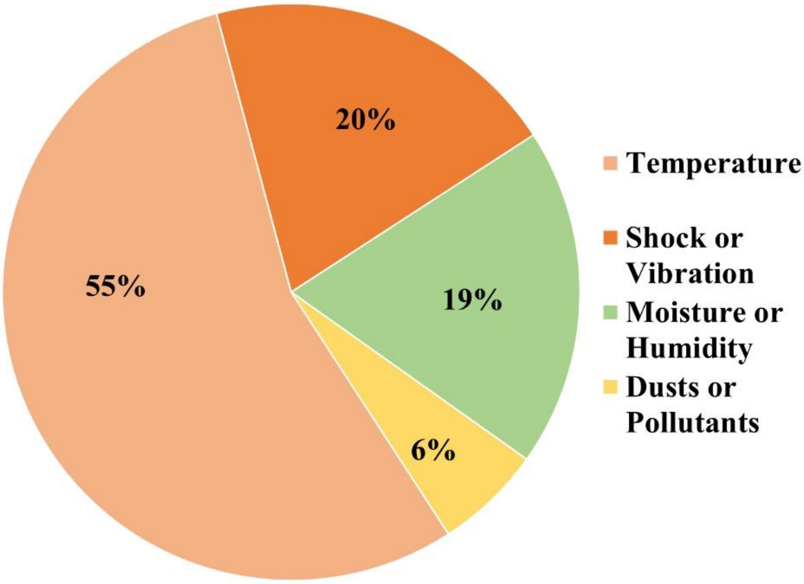

Fig. 2.3. Factors that contribute to PES faults

An abnormally high surge in current that causes the temperature to rise and damages the IGBT might cause failure [5]. Furthermore, insulation failure might result from a voltage surge. The IGBT module might malfunction for a variety of reasons. The failure modes for power switches can happen at the chip or package level. Wear-out issues (WOIs) and over-stressed issues (OSIs) are two subtypes of faults that fall under these two primary categories. Table 2.1 illustrated many forms, causes, and negative effects of IGBT faults [5], [7]. The failure forms, causes, and negative effects of MPC PESs, such as MOSFETs and GTOs, are nearly comparable to those listed in Table 2.1, except for a few slight variations.

Table 2.1. Diverse forms, causes, and effects of IGBT malfunctions

Failure Scenarios		Causes	Various Impacts on the System
Chip associated issues	WOI	Time-sensitive dielectric failures	• Issues with the gate driver and switch • Leakage current increase • Decline in the chip's efficacy to block voltage
		Injection of hot carriers	
		Electrochemical migration (ECM)	
	OSI	Overcurrent	• Open circuit (OC) • Short circuit (SC) • Lift-off of wire-bonds • Secondary malfunction
		The excessive voltage in the Gate	
		Elevated collector-emitter voltage	
		Cosmic radiation fatigue	
Package associated issues	WOI	Thermal stress and fatigue	• Diminished rigidity of different packaging layer • Bond-wire breakage and solder defects • Leakage current • Bond-wire erosion and hot spots • Decline in the chip's efficacy to block voltage
		ECM and Electromigration (EM)	
		Insulation decay	
	OSI	Flashover	• Wear-out issues • Burnouts • OC or SC • Disruption of voltage • Package link melting
		Mechanical stresses and strains	
		Thermal runaway	
		Thermal shock	

2.4.2 Capacitors

In MPCs, capacitors are crucial parts. They function in MGIs as a dc-link. Capacitors in MPCs have the most significant rates of damage, estimated to be 30%, as seen in Fig. 2.2. Typically, dc-link applications use three distinct kinds of capacitors: film, electrolytic, and ceramic [3], [8]. OCD, SCD, and performance drifts (PDs) are the three primary types of capacitor failure. Table 2.2, Table 2.3, Table 2.4 illustrated many forms [2], [9], [10], causes [2], [11], and negative effects [2], [9], [12], [13] of various capacitor faults.

Table 2.2. Diverse forms, causes, and effects of film capacitor (FC) malfunctions

Capacitor Type	Failure Scenarios	Causes	Various Consequences
Film capacitors (FCs)	OCD	Environmental temperature, voltage strain	• Dielectric failure • Instability of connection • Electrode area reduction
		Ripple current strain	
		Humidity	
	SCD	Voltage strain	• Dielectric film failure • Overcurrent • Retention of humidity on film
		Ripple current strain	
		Environmental temperature	
		Humidity	
	PD	Environmental temperature, voltage strain	• Loss of dielectric
		Ripple current strain	
		Humidity	

Table 2.3. Diverse forms, causes, and effects of ceramic capacitor (CC) malfunctions

Capacitor Type	Failure Scenarios	Causes	Various Consequences
Ceramic capacitors (CCs)	OCD	Environmental temperature	• Extreme rupture • Dielectric failure
		Ripple current strain	
		Vibration	
		Voltage strain	
	SCD	Vibration	• Rupturing of capacitor • Damages on the capacitor body
	PD	Voltage strain	• Oxygen vacancy diffusion • Dielectric piercing • Degrading of insulation • Tiny fracture in the ceramic
		Environmental temperature	
		Ripple current strain	
		Vibration	

Table 2.4. Diverse forms, causes, and effects of electrolytic capacitor (EC) malfunctions

Capacitor Type	Failure Scenarios	Causes	Various Consequences
Electrolytic capacitors (ECs)	OCD	Voltage strain	• Dielectric failure • Disconnected terminals
		Environmental temperature	
		Ripple current strain	
		Vibration	
	SCD	Voltage strain	• Oxide layer's dielectric failure
		Environmental temperature	
		Ripple current strain	
	PD	Environmental temperature	• Electrolyte vaporizing • Depletion of the oxide layer and/or a reduction in capacitance of anode foil
		Ripple current strain	
		Voltage strain	

2.5 Methods of Fault Diagnosis Employed

To provide improved dependability, MGs employ several fault identification and localization (FIL) procedures. The two strategies for execution are model-free and model-based [11].

2.5.1 Model-free Methods

These FDMs have evolved into an efficient diagnostic tool. The main reasons for this are the low cost and adaptability of comprehending the system's dynamics and behaviour.

In [14], an artificial neural network (ANN)-based FDM for a multilevel H-bridge inverter (MLHBI) was presented. To identify the flaw, the inverter terminal's voltage was carefully examined. It extracted a number of attributes using the discrete wavelet transform (DWT). Three-phase voltage source inverter (TPVSI) switch OCD diagnosis using ANN via stator current assessment was proposed [15]. For the cascaded H-bridge multi-level inverters (CHBMLIs), the fast Fourier transform (FFT) and ANN-based FDM are proposed in [16]. Multilevel inverters (MLIs) OCD and SCD detection using an ANN-oriented FDM is illustrated in [17]. Through supervised learnings (SLs), researchers have developed probabilistic neural networks (PNNs) based FDM for the diode-clamped multi-level inverter (DCMLI) [18]. ANN-based FDM [19] through DWT is recommended for single-phase H-bridge inverters (SPHBIs). A K-nearest neighbor (KNN)-oriented fault evaluation technique using DWT-based features extraction [20] is suggested, addressing grid-sided flaws.

Amongst some of the most popular SL-oriented methods include decision trees (DTs) [11]. A DT-based FDM was developed by the authors to classify different inverter malfunctions [21]. Random forest (RF), yet another SL-based method, makes use of a set of DTs [11]. To generate accurate estimations, various independent DTs are aggregated to create the forest-like framework. For neutral-point-clamped (NPC) inverters, L. Kou et al. proposed a technique for detecting OCD issues [22]. For the switch OCDs of 3-phase H-bridge inverters (TPHBIs), K. Dhibi et al. suggested several FDMs [23], [24].

In complex systems like MPCs, Bayesian Networks (BNs) are helpful tools for problem analysis since they may handle uncertainties and define probabilistic relationships amongst parameters. The BN-based defect-detection technique for TPHBI [25] was presented by B. Cai et al. For various failure kinds, this FDM monitors line-to-line voltage outputs. To get the signal features, FFT is utilized. Principal component analysis (PCA) has been used to reduce the dimensions of every sample, and BNs are subsequently employed to identify the defects.

Amongst some of the most popular SL-oriented methods also include support vector machine (SVM) [11]. It is used for classification issues and regression. Using extracted attributes, SVM can effectively classify an inverter's functioning states, enabling the swift detection of the inverter flaws. In [11], [26], for TPHBI, an SVM-based FDM is proposed. Following output current normalization, multi-resolution analysis (MRA) with DWT is employed to extract features. Switch OCD is diagnosed by feeding the obtained characteristics into the SVM classifier. To find OCD in an inverter-fed motor drive (IFMD), an FDM based on SVM is proposed [27]. For IFMD inceptive faults, the authors suggested an FDM based on SVM [28]. An FDM based on PCA-SVM is utilized for CHBMLI [29]. Using SVM, W. Yuan et al. suggested FDM for TPVSI problems [30]. Clustering methods (CMs) are a kind of unsupervised learning technique that groups data points according to their comparative degree of likeness. Addressing switch OCD in TPHBI, a CM-based FDM is suggested [31]. In [32] CMs are used to diagnose defects in NPC Converters.

Convolutional neural networks (CNNs), one type of deep learning model, excel at comprehending and evaluating spatial information. W. Gong et al. conveyed a CNN-based FDM for TPHBI switch OCD [33]. Here, an inverter's output voltage diagnosis was made. Q. Sun et al. proposed another CNN-based FDM [34] for TPHBI's switch OCD. Model-free FDMs are summarized in Table 2.5.

2.5.2 Model-based Methods

Model-based approaches that use threshold-based procedures generate sets of critical system parameters during both ideal and inadequate conditions by simulating complex models of MPC components [35]. It is crucial to create thresholds that reflect the inherent properties of the system. Every time certain thresholds are exceeded, an event is triggered, and an issue is recognized [35]. The implementation of these methods is easy.

The authors of [36] devised a switch OCD detection strategy for TPHBI. Several circumstances of switch flaws have been modelled for the converter in this FDM. Additionally, the converter's state space representation was acquired for every likely error mode. To find flaws in this FDM, the TPBHI's current signal was carefully tracked. In [37], A. Mashreghi et al. presented an additional switch OCD identification method for TPHBI. The inverter model formulae for sensors and switches in this FDM are computed during healthy and OCD situations. Here, a link between the defective events and their flawed signature is found using the residual generator. Using experimental results and residual computations, this FDM can detect switch and sensor defects. A switch OCD diagnostic approach for TPVSI was proposed by Q. An et al. in 2011 [38]. This FDM tracks the collector-emitter voltages of the IGBTs. The authors of [39] introduced the OCD and SCD detecting method for inductor motors' voltage source inverter (VSI) switches. To identify OCD for switching components in PV systems' NPC converters, the authors developed a technique in [40]. OCD problems in one or more devices could be diagnosed using this FDM. An OCD identification technique [41] for cascaded neutral-point-clamped (CNPC) inverters in parallel has been presented by X. Wei et al. This FDM analyzes the fluctuation in output currents and capacitor voltages to determine the OCD in either of the switches. Model-based FDMs are summarized in Table 2.6.

Table 2.5. Model-free FDMs

Ref.	Failure Type	Converter Type	Approach used in FDM
[14]	Switch OCD	Cascaded H-Bridge Multi-Level Inverter (CHBMLI)	ANN
[15]		Three-Phase Voltage Source Inverter (TPVSI)	ANN
[16]		CHBMLI	ANN
[21]		TPVSI	DT
[22]		Neutral-Point-Clamped (NPC) Inverter	RF
[23]		3-phase H-bridge Inverter (TPHBI)	RF
[24]		TPHBI	RF
[26]		TPHBI	SVM
[27]		TPHBI	SVM
[29]		CHBMLI	SVM
[31]		TPHBI	CM
[32]		NPC Converter	CM
[33]		TPHBI	CNN
[34]		TPHBI	CNN
[17]	Switch OCD, and SCD	CHBMLI	ANN
[18]		Diode-Clamped Multi-Level Inverter (DCMLI)	ANN
[20]	Additional faults such as 3-phase failure, diode failure, multiple switch defects, degradation failures	TPHBI	KNN
[25]		TPHBI	BN
[19]		Single-Phase H-Bridge Inverter (SPHBI)	ANN
[28]		TPHBI	SVM
[30]		TPVSI	SVM

Table 2.6. Model-based FDMs

Ref.	Failure Type	Inverter Type
[36]	Switch OCD	3-phase H-bridge Inverter (TPHBI)
[37]	Switch OCD	TPHBI
[38]	Switch OCD	Three-Phase Voltage Source Inverter (TPVSI)
[39]	Switch OCD, and SCD	TPVSI
[40]	OCD in single and multiple switches	Neutral-Point-Clamped (NPC) Inverter
[41]	OCD in single and multiple switches	Cascaded Neutral-Point-Clamped (CNPC) Inverter

2.5.3 FDMs for Capacitors Issues

Condition monitoring (CMN)-focused techniques are commonly used for capacitors to increase system reliability [11], [42]. A technique [43] is proposed to estimate and replace an LCL filter's capacitance (C). Capacitor degradation has been shown to have detrimental effects on the system's overall power factor and to move the resonant frequency near the switching frequency. H. Li et al. suggested a technique [44] for tracking the DC-link capacitance for VSI by using the circuit's LC resonance properties. Here, the resonance current serves as the diagnostic component to assess the capacitor's physical state. An alternative CMN technique [45] that makes use of predicting parameter values has been presented for the boost converters (BCs) capacitor. The condition elements under discussion include the output voltage and input current of the BC related to capacitance. A FDM for electrolytic capacitors using the equivalent series resistances (ESRs) estimate was presented by M. Hao et al. [46]. For the purpose of identifying switch issues and monitoring capacitor lifespans in DC-DC converters, H. Givi et al. proposed FDM [47]. A genetic algorithm (GA) [48] was developed by A. Braham et al. to estimate capacitors' ESRs while determining the residual duration till failure. This method considers the negative effects of the skin effect, which causes an increase in ESR at high frequencies. A capacitance estimation technique [49] utilizing an ANN is proposed for DCL capacitors. In [50], a film capacitance estimate-based online CMN for propulsion systems is proposed. A different approach to real-time CMN of ECs is proposed in [51]. FDMs for capacitors are summarized in Table 2.7.

Table 2.7. FDMs for capacitors

Ref.	Capacitor type investigated	Values (ESR or C)	Approach Online/Offline
[43]	Film Capacitor	C	Online
[44]	Film Capacitor	C	Quasi online
[45]	Film Capacitors and Electrolytic Capacitors	ESR and C	Online
[46]	Electrolytic Capacitor	ESR	Online
[47]	Electrolytic Capacitor	ESR	Online
[48]	Electrolytic Capacitor	ESR	Offline
[49]	Electrolytic Capacitor	C	Online
[50]	Film Capacitor	C	Online
[51]	Electrolytic Capacitor	C and ESR	Online

2.6 Conclusion

The FDMs covered here provide illustrations of the several methods for diagnosing MPC faults that are available in the literature. The PESs and capacitor issues with MPCs are reviewed in this chapter. Discussions of the many forms, causes, and negative effects of problems with MPCs' PESs and capacitors are also covered here. The results demonstrated that every method available provides trustworthy fault diagnosis and subsequent converter protection. However, due to their relatively short response time, several of the methods are unable to prevent the system from collapsing shortly after the issue occurs. This developing area of MPC fault diagnostics keeps looking for quicker and more intelligent techniques. Researchers can create defect detection systems that are more sophisticated, intelligent, and responsive by examining existing methods and comprehending their shortcomings. This study can be utilized to improve the MPCs' diagnostic capabilities by identifying the best diagnosis strategy for the system and accounting for various system configurations.

References

[1] H. O. A. Ahmed, Y. Yu, Q. Wang, M. Darwish, and A. K. Nandi, "Intelligent Fault Diagnosis Framework for Modular Multilevel Converters in HVDC Transmission," *Sensors*, vol. 22, no. 1, p. 362, Jan. 2022, doi: 10.3390/s22010362.

[2] S. Rahimpour, H. Tarzamni, N. V. Kurdkandi, O. Husev, D. Vinnikov, and F. Tahami, "An Overview of Lifetime Management of Power Electronic Converters," *IEEE Access*, vol. 10, pp. 109688–109711, 2022, doi: 10.1109/ACCESS.2022.3214320.

[3] S. Yang, D. Xiang, A. Bryant, P. Mawby, L. Ran, and P. Tavner, "Condition Monitoring for Device Reliability in Power Electronic Converters: A Review," *IEEE Trans Power Electron*, vol. 25, no. 11, pp. 2734–2752, Nov. 2010, doi: 10.1109/TPEL.2010.2049377.

[4] H. Renaudineau, P. Paradell-Solà, L. Trilla, A. Filba-Martinez, D. Cardoner, and J. L. Domínguez-García, "Reliability Assessment of a Fault-Tolerant PV Multistring Inverter," *Energies (Basel)*, vol. 13, no. 24, p. 6525, Dec. 2020, doi: 10.3390/en13246525.

[5] S. S. Ghosh *et al.*, "Wavelet-based rapid identification of IGBT switch breakdown in voltage source converter," *Microelectronics Reliability*, vol. 152, p. 115283, Jan. 2024, doi: 10.1016/j.microrel.2023.115283.

[6] S. S. Ghosh, S. Chattopadhyay, and A. Das, "Identification of an Incipient Snubber Failure in Inverter Employed in Solid Oxide Fuel Cell (SOFC) Fed Microgrid," *IEEE Trans Instrum Meas*, vol. 74, pp. 1–10, 2025, doi: 10.1109/TIM.2025.3544391.

[7] A. Abuelnaga, M. Narimani, and A. S. Bahman, "A Review on IGBT Module Failure Modes and Lifetime Testing," *IEEE Access*, vol. 9, pp. 9643–9663, 2021, doi: 10.1109/ACCESS.2021.3049738.

[8] Z. Zhao, P. Davari, W. Lu, H. Wang, and F. Blaabjerg, "An Overview of Condition Monitoring Techniques for Capacitors in DC-Link Applications," *IEEE Trans Power Electron*, vol. 36, no. 4, pp. 3692–3716, Apr. 2021, doi: 10.1109/TPEL.2020.3023469.

[9] S. Peyghami, Z. Wang, and F. Blaabjerg, "Reliability Modeling of Power Electronic Converters: A General Approach," in *2019 20th Workshop on Control and Modeling for Power Electronics (COMPEL)*, IEEE, Jun. 2019, pp. 1–7. doi: 10.1109/COMPEL.2019.8769685.

[10] C. Bhargava *et al.*, "Review of Health Prognostics and Condition Monitoring of Electronic Components," *IEEE Access*, vol. 8, pp. 75163–75183, 2020, doi: 10.1109/ACCESS.2020.2989410.

[11] A. Malik, A. Haque, V. S. B. Kurukuru, M. A. Khan, and F. Blaabjerg, "Overview of fault detection approaches for grid connected photovoltaic inverters," *e-Prime - Advances in Electrical Engineering, Electronics and Energy*, vol. 2, p. 100035, 2022, doi: 10.1016/j.prime.2022.100035.

[12] H. Wang and F. Blaabjerg, "Reliability of Capacitors for DC-Link Applications in Power Electronic Converters—An Overview," *IEEE Trans Ind Appl*, vol. 50, no. 5, pp. 3569–3578, Sep. 2014, doi: 10.1109/TIA.2014.2308357.

[13] H. Wang *et al.*, "Transitioning to Physics-of-Failure as a Reliability Driver in Power Electronics," *IEEE J Emerg Sel Top Power Electron*, vol. 2, no. 1, pp. 97–114, Mar. 2014, doi: 10.1109/JESTPE.2013.2290282.

[14] D. Chowdhury, M. Bhattacharya, D. Khan, S. Saha, and A. Dasgupta, "Wavelet decomposition based fault detection in cascaded H-bridge multilevel inverter using artificial neural network," in *2017 2nd IEEE International Conference on Recent Trends in Electronics, Information & Communication Technology (RTEICT)*, IEEE, May 2017, pp. 1931–1935. doi: 10.1109/RTEICT.2017.8256934.

[15] R. B. Dhumale and S. D. Lokhande, "Neural Network Fault Diagnosis of Voltage Source Inverter under variable load conditions at different frequencies," *Measurement*, vol. 91, pp. 565–575, Sep. 2016, doi: 10.1016/j.measurement.2016.04.051.

[16] G. Kiran Kumar, E. Parimalasundar, D. Elangovan, P. Sanjeevikumar, F. Lannuzzo, and J. B. Holm-Nielsen, "Fault Investigation in Cascaded H-Bridge Multilevel Inverter through Fast Fourier Transform and Artificial Neural Network Approach," *Energies (Basel)*, vol. 13, no. 6, p. 1299, Mar. 2020, doi: 10.3390/en13061299.

[17] S. Khomfoi and L. M. Tolbert, "Fault Diagnostic System for a Multilevel Inverter Using a Neural Network," *IEEE Trans Power Electron*, vol. 22, no. 3, pp. 1062–1069, May 2007, doi: 10.1109/TPEL.2007.897128.

[18] M. Bhattacharya, S. Saha, D. Khan, and T. Nag, "Wavelet based component fault detection in diode clamped multilevel inverter using probabilistic neural network," in *2017 2nd International Conference for Convergence in Technology (I2CT)*, IEEE, Apr. 2017, pp. 1163–1168. doi: 10.1109/I2CT.2017.8226310.

[19] V. S. Bharath Kurukuru, A. Haque, R. Kumar, M. A. Khan, and A. K. Tripathy, "Machine Learning based Fault Classification Approach for Power electronic converters," in *2020 IEEE International Conference on Power Electronics, Drives and Energy Systems (PEDES)*, IEEE, Dec. 2020, pp. 1–6. doi: 10.1109/PEDES49360.2020.9379365.

[20] M. Manohar, E. Koley, Y. Kumar, and S. Ghosh, "Discrete Wavelet Transform and kNN-Based Fault Detector and Classifier for PV Integrated Microgrid," 2018, pp. 19–28. doi: 10.1007/978-981-10-8360-0_2.

[21] N.-T. Nguyen and H.-P. Nguyen, "Fault Diagnosis of Voltage Source Inverter for Induction Motor Drives Using Decision Tree," 2017, pp. 819–826. doi: 10.1007/978-981-10-1721-6_88.

[22] L. Kou, C. Liu, G. Cai, J. Zhou, Q. Yuan, and S. Pang, "Fault diagnosis for open-circuit faults in NPC inverter based on knowledge-driven and data-driven approaches," *IET Power Electronics*, vol. 13, no. 6, pp. 1236–1245, May 2020, doi: 10.1049/iet-pel.2019.0835.

[23] K. Dhibi *et al.*, "A Hybrid Fault Detection and Diagnosis of Grid-Tied PV Systems: Enhanced Random Forest Classifier Using Data Reduction and Interval-Valued Representation," *IEEE Access*, vol. 9, pp. 64267–64277, 2021, doi: 10.1109/ACCESS.2021.3074784.

[24] K. Dhibi *et al.*, "Reduced Kernel Random Forest Technique for Fault Detection and Classification in Grid-Tied PV Systems," *IEEE J Photovolt*, vol. 10, no. 6, pp. 1864–1871, Nov. 2020, doi: 10.1109/JPHOTOV.2020.3011068.

[25] B. Cai, Y. Zhao, H. Liu, and M. Xie, "A Data-Driven Fault Diagnosis Methodology in Three-Phase Inverters for PMSM Drive Systems," *IEEE Trans Power Electron*, vol. 32, no. 7, pp. 5590–5600, Jul. 2017, doi: 10.1109/TPEL.2016.2608842.

[26] Dong-Eok Kim and Dong-Choon Lee, "Fault diagnosis of three-phase PWM inverters using wavelet and SVM," in *2008 IEEE International Symposium on Industrial Electronics*, IEEE, Jun. 2008, pp. 329–334. doi: 10.1109/ISIE.2008.4676998.

[27] C. Bowen and T. Wei, "Switch open-circuit faults diagnosis of inverter based on wavelet and support vector machine," in *2019 14th IEEE International Conference on Electronic Measurement & Instruments (ICEMI)*, IEEE, Nov. 2019, pp. 1178–1184. doi: 10.1109/ICEMI46757.2019.9101567.

[28] I. Bandyopadhyay, P. Purkait, and C. Koley, "Performance of a Classifier Based on Time-Domain Features for Incipient Fault Detection in Inverter Drives," *IEEE Trans Industr Inform*, vol. 15, no. 1, pp. 3–14, Jan. 2019, doi: 10.1109/TII.2018.2854885.

[29] W. Yuan, T. Wang, and D. Diallo, "A Secondary Classification Fault Diagnosis Strategy Based on PCA-SVM for Cascaded Photovoltaic Grid-connected Inverter," in *IECON 2019 - 45th Annual Conference of the IEEE Industrial Electronics Society*, IEEE, Oct. 2019, pp. 5986–5991. doi: 10.1109/IECON.2019.8927090.

[30] Z. Hu, W. Gui, C. Yang, P. Deng, and S. X. Ding, "Fault classification method for inverter based on hybrid support vector machines and wavelet analysis," *Int J Control Autom Syst*, vol. 9, no. 4, pp. 797–804, Aug. 2011, doi: 10.1007/s12555-011-0423-9.

[31] T. H. Pham, S. Lefteriu, E. Duviella, and S. Lecoeuche, "Auto-adaptive and Dynamical Clustering for Double Open-Circuit Fault Diagnosis of Power Inverters," in *2019 4th Conference on Control and Fault Tolerant Systems (SysTol)*, IEEE, Sep. 2019, pp. 306–311. doi: 10.1109/SYSTOL.2019.8864777.

[32] N. Torabi, F. Naghavi, and H. A. Toliyat, "Real-time fault isolation in multiphase multilevel NPC converters using active semi-supervised fuzzy clustering algorithm with pairwise constraints," in *2017 IEEE International Electric Machines and Drives Conference (IEMDC)*, IEEE, May 2017, pp. 1–7. doi: 10.1109/IEMDC.2017.8002409.

[33] W. Gong, H. Chen, Z. Zhang, M. Zhang, and H. Gao, "A Data-Driven-Based Fault Diagnosis Approach for Electrical Power DC-DC Inverter by Using Modified Convolutional Neural Network With Global Average Pooling and 2-D Feature Image," *IEEE Access*, vol. 8, pp. 73677–73697, 2020, doi: 10.1109/ACCESS.2020.2988323.

[34] Q. Sun, X. Yu, and H. Li, "Open-circuit Fault Diagnosis Based on 1D-CNN for Three-phase Full-bridge Inverter," in *2020 11th International Conference on Prognostics and System Health Management (PHM-2020 Jinan)*, IEEE, Oct. 2020, pp. 322–327. doi: 10.1109/PHM-Jinan48558.2020.00064.

[35] J. Hare, X. Shi, S. Gupta, and A. Bazzi, "Fault diagnostics in smart micro-grids: A survey," *Renewable and Sustainable Energy Reviews*, vol. 60, pp. 1114–1124, Jul. 2016, doi: 10.1016/j.rser.2016.01.122.

[36] J. Poon, P. Jain, I. C. Konstantakopoulos, C. Spanos, S. K. Panda, and S. R. Sanders, "Model-Based Fault Detection and Identification for Switching Power Converters," *IEEE Trans Power Electron*, vol. 32, no. 2, pp. 1419–1430, Feb. 2017, doi: 10.1109/TPEL.2016.2541342.

[37] A. Mashreghi and M. Namvar, "A Geometric Approach to Fault Detection and Isolation in a Grid-Connected Inverter," *IEEE Transactions on Control Systems Technology*, vol. 29, no. 6, pp. 2622–2629, Nov. 2021, doi: 10.1109/TCST.2020.3034717.

[38] Q.-T. An, L.-Z. Sun, K. Zhao, and L. Sun, "Switching Function Model-Based Fast-Diagnostic Method of Open-Switch Faults in Inverters Without Sensors," *IEEE Trans Power Electron*, vol. 26, no. 1, pp. 119–126, Jan. 2011, doi: 10.1109/TPEL.2010.2052472.

[39] D. R. Espinoza-Trejo, D. U. Campos-Delgado, E. Bárcenas, and F. J. Martínez-López, “Robust fault diagnosis scheme for open-circuit faults in voltage source inverters feeding induction motors by using non-linear proportional-integral observers,” *IET Power Electronics*, vol. 5, no. 7, pp. 1204–1216, Aug. 2012, doi: 10.1049/iet-pel.2011.0309.

[40] J. A. Pecina Sánchez, D. U. Campos-Delgado, D. R. Espinoza-Trejo, A. A. Valdez-Fernández, and C. H. De Angelo, “Fault diagnosis in grid-connected PV NPC inverters by a model-based and data processing combined approach,” *IET Power Electronics*, vol. 12, no. 12, pp. 3254–3264, Oct. 2019, doi: 10.1049/iet-pel.2018.5237.

[41] X. Wei *et al.*, “Parallel Open-Circuit Fault Diagnosis Method of a Cascaded Full-Bridge NPC Inverter With Model Predictive Control,” *IEEE Transactions on Industrial Electronics*, vol. 68, no. 10, pp. 10180–10192, Oct. 2021, doi: 10.1109/TIE.2020.3028801.

[42] S. Peyghami, H. Wang, P. Davari, and F. Blaabjerg, “Mission-Profile-Based System-Level Reliability Analysis in DC Microgrids,” *IEEE Trans Ind Appl*, vol. 55, no. 5, pp. 5055–5067, Sep. 2019, doi: 10.1109/TIA.2019.2920470.

[43] H.-J. Heo, W.-S. Im, J.-S. Kim, and J.-M. Kim, “A Capacitance Estimation of Film Capacitors in an LCL-Filter of Grid-Connected PWM Converters,” *Journal of Power Electronics*, vol. 13, no. 1, pp. 94–103, Jan. 2013, doi: 10.6113/JPE.2013.13.1.94.

[44] H. Li, D. Xiang, X. Han, X. Zhong, and X. Yang, “High-Accuracy Capacitance Monitoring of DC-Link Capacitor in VSI Systems by *LC* Resonance,” *IEEE Trans Power Electron*, vol. 34, no. 12, pp. 12200–12211, Dec. 2019, doi: 10.1109/TPEL.2019.2904551.

[45] G. M. Buiatti, J. A. Martín-Ramos, C. H. R. García, A. M. R. Amaral, and A. J. M. Cardoso, “An Online and Noninvasive Technique for the Condition Monitoring of Capacitors in Boost Converters,” *IEEE Trans Instrum Meas*, vol. 59, no. 8, pp. 2134–2143, Aug. 2010, doi: 10.1109/TIM.2009.2032960.

[46] Hao Ma and Linguo Wang, “Fault diagnosis and failure prediction of aluminum electrolytic capacitors in power electronic converters,” in *31st Annual Conference of IEEE Industrial Electronics Society, 2005. IECON 2005.*, IEEE, 2005, p. 6 pp. doi: 10.1109/IECON.2005.1569014.

[47] H. Givi, E. Farjah, and T. Ghanbari, “Switch fault diagnosis and capacitor lifetime monitoring technique for DC–DC converters using a single sensor,” *IET Science,*

Measurement & Technology, vol. 10, no. 5, pp. 513–527, Aug. 2016, doi: 10.1049/iet-smt.2015.0256.

[48] A. Braham, A. Lahyani, P. Venet, and N. Rejeb, "Recent Developments in Fault Detection and Power Loss Estimation of Electrolytic Capacitors," *IEEE Trans Power Electron*, vol. 25, no. 1, pp. 33–43, Jan. 2010, doi: 10.1109/TPEL.2009.2026749.

[49] H. Soliman, P. Davari, H. Wang, and F. Blaabjerg, "Capacitance estimation algorithm based on DC-link voltage harmonics using artificial neural network in three-phase motor drive systems," in *2017 IEEE Energy Conversion Congress and Exposition (ECCE)*, IEEE, Oct. 2017, pp. 5795–5802. doi: 10.1109/ECCE.2017.8096961.

[50] A. Wechsler, B. C. Mecrow, D. J. Atkinson, J. W. Bennett, and M. Benarous, "Condition Monitoring of DC-Link Capacitors in Aerospace Drives," *IEEE Trans Ind Appl*, vol. 48, no. 6, pp. 1866–1874, Nov. 2012, doi: 10.1109/TIA.2012.2222333.

[51] K. Abdennadher, P. Venet, G. Rojat, J.-M. Retif, and C. Rosset, "A Real-Time Predictive-Maintenance System of Aluminum Electrolytic Capacitors Used in Uninterrupted Power Supplies," *IEEE Trans Ind Appl*, vol. 46, no. 4, pp. 1644–1652, Jul. 2010, doi: 10.1109/TIA.2010.2049972.

Chapter 3

FFT-based Investigation of Snubber Circuit Resistance Issue in Small Microgrid Inverter Connected with Robotic Brushless DC Motor

Abstract- In electronic motor drives, the snubber circuit is significant. This chapter discusses an effort to identify the inverter switch's snubber circuit resistance failure (ISSCRF) in a small microgrid (MG) inverter connected with robotic brushless DC (BLDC) motors. The investigation examines how various ISSCRF percentages (%ISSCRFs) affect the DC component (DCC), the fundamental component of current (FCC), and the total harmonic distortion (THD) of the BLDC motor's stator current.

Keywords: Brushless DC (BLDC) motor, fast Fourier transform (FFT), fault recognition, microgrid inverter

3.1 Introduction

Electronically commutated BLDC motors offer strong dynamic response, great mechanical dependability, low vibration and noise, extended lifespan, simple controllability, and high efficiency [1]. These days, a lot of industrial and domestic applications employ these motors [1], [2]. A 3-phase BLDC motor is driven by three full-bridge inverters [3], [4].

Additionally, sensorless BLDC motors have become the most popular in recent years. A BLDC motor drive's voltage source inverter (VSI), as well as rotor, stator, and position sensors, can all experience various kinds of issues [5]. Therefore, these flaws might result in serious machinery breakdowns if they are not addressed.

About 38% of all motor malfunctions are inverter-related failures, which mostly happen in power switches [3], [6]. Over the past several decades, a number of methods have been investigated and put forth for the identification of inverter switch issues within BLDC motors. A method for detecting open-circuit (OC) and short-circuit (SC) in VSIs has been presented by Mehdi Salehifar et al. [7]. In addition, the authors suggested a method for identifying malfunctioning switches in a 5-phase VSI motor drive [8]. A diagnostic method [9] for detecting OC problems in current-source inverter (CSI)-based BLDC motor drive systems was proposed by Mohamed A. Awadallah et al. in 2006. Moseler et al. suggested a fault-identifying method [10] for online and end-of-line issue identification. Liu et al. suggested a permanent-magnet dc motor's failure diagnostic and detection technique [11].

Snubbers are important components of power electronics. The power supply module incorporates snubbers. Snubbers effectively reduce the impact of circuit reactance. In addition to increasing the switching circuit's efficiency, snubbers also boost its efficiency and dependability, which raises the switching frequency [3]. Fault identification is an essential feature that needs to be considered for drives to operate dependably. Numerous studies and investigations are being conducted in these fields [12], [13], [14] to diagnose converters and motor drives problems. Numerous sophisticated modelling, research, and snubber uses have been noted in [15], [16], [17], [18], [19]. The authors [15] discovered shortcomings within the converter that was attached to the snubber. However, very few attempts are made to identify the ISSCRF of the small MG inverter connected to the BLDC motor. Motivated by this, the identification of the ISSCRF has been addressed. To identify ISSCRF, the BLDC motor's stator current was monitored under normal conditions and at various %ISSCRF (up to 50%).

3.2 BLDC Motor Mathematical Model

BLDC motor's equivalent circuitry is depicted in Fig. 3.1. The BLDC motor is powered by a 3-phase voltage source and features star-connected stator windings.

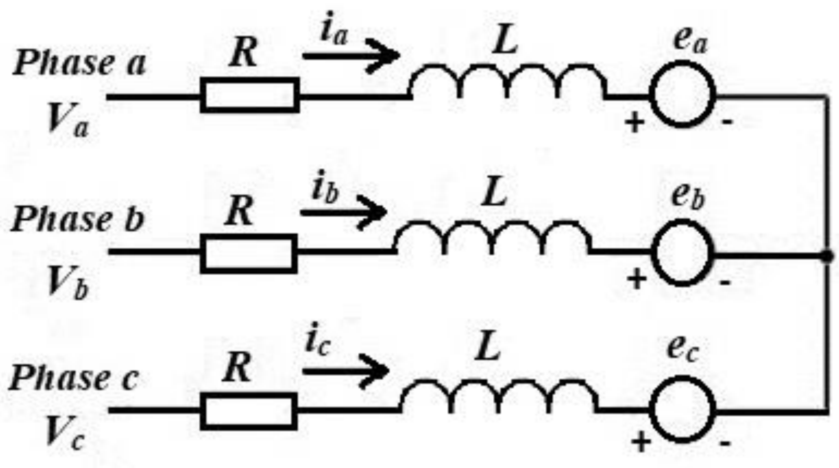

Fig. 3.1. BLDC motor's equivalent circuitry

The followings are expressions [3] for BLDC motor's armature winding's modelling:

$$V_a = Ri_a + L\frac{di_a}{dt} + e_a \tag{3.1}$$

$$V_b = Ri_b + L\frac{di_b}{dt} + e_b \tag{3.2}$$

$$V_c = Ri_c + L\frac{di_c}{dt} + e_c \tag{3.3}$$

where, V_a, V_b, V_c = stator phase voltages (V),

i_a, i_b, i_c = stator phase currents (A),

e_a, e_b, e_c = motor's back EMFs (V) of three phases

The BLDC motor's modelling can be represented in matrix form [3] underneath:

$$\begin{bmatrix} V_a \\ V_b \\ V_c \end{bmatrix} = R\begin{bmatrix} 1 & 0 & 0 \\ 0 & 1 & 0 \\ 0 & 0 & 1 \end{bmatrix}\begin{bmatrix} i_a \\ i_b \\ i_c \end{bmatrix} + L\begin{bmatrix} 1 & 0 & 0 \\ 0 & 1 & 0 \\ 0 & 0 & 1 \end{bmatrix}\frac{d}{dt}\begin{bmatrix} i_a \\ i_b \\ i_c \end{bmatrix} + \begin{bmatrix} e_a \\ e_b \\ e_c \end{bmatrix} \tag{3.4}$$

where,

$R = R_a = R_b = R_c$ = per-phase stator resistances (ohm),

$L = L_a = L_b = L_c$ = per-phase stator windings inductances (H)

To power the motor, a 3-phase, 500 V, 50 Hertz power equipment featuring a MOSFET/Diode-based inverter was employed. Followings referred in Table 3.1 are the specifications of the BLDC motor:

Table 3.1. BLDC motor specifications

Parameters	**Specifications**
Number of phases	3
Number of poles	8
Rated speed	3000 RPM
Stator's phase resistance	2.8750 ohm
Stator's phase inductance	0.0085 H
Rotor inertia	0.008 kgm^2
Friction	0.001 N-m-s

BLDC motor's stator current was monitored under normal conditions and at various ISSCRF percentages (up to 50%).

3.3 Fault in Snubber Resistance

This chapter addresses fault diagnosis of resistance-capacitance (RC) snubber circuits. A small resistor and capacitor in series are frequently employed as RC snubber circuits for inductive loads. Snubbers restrict the rate of voltage increase (dV/dt), also limit di/dt, ripples, when employed with devices such as thyristors, IGBTs, MOSFETs, and other switching components.

The snubber resistance defect, referred to here as ISSCRF, can be caused by aging, temperature, and other factors. ISSCRF arises when the snubber resistor's effective resistance's value gradually drops. In severe circumstances, it drops to zero, short-circuiting the snubber path. Here, an effort was made to identify a little and steady drop in the snubber resistance's value. Here, the degree of fault is defined as the value of the snubber resistors that exceeds the 5% tolerance level.

Simple snubber circuits consist of a resistor linked in series with a capacitor attached in parallel to the semiconductor switches. In Fig. 3.2, the RC snubber circuitry utilized in the BLDC motor's inverter circuit is displayed.

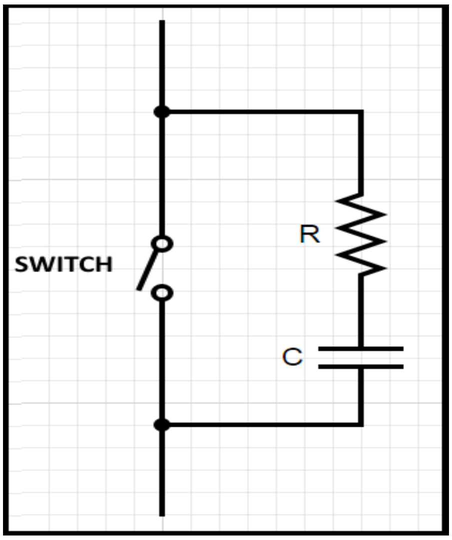

Fig. 3.2. RC snubber circuit

These formulae [3] outlined below can be used to calculate the values of the snubber resistance and snubber capacitance:

$$R_{snub} = 2.\delta\sqrt{\frac{L}{C}} \tag{3.5}$$

$$C_{snub} = L\left(\frac{I_r}{K.V_S}\right)^2 \tag{3.6}$$

where, R_{snub}, C_{snub}= snubber's resistance and capacitance value,

δ= optimal damping factor,

K= optimal current factor,

I_r= semiconductor switch's recovery current,

V_s= source voltage,

L= circuit's inductance

3.4 FFT-Oriented ISSCRF Analysis

Fourier transform [FT] is an effective technique to investigate periodic waveforms. Either FT or FFT can be employed to transform a signal between the frequency and time domains. Nevertheless, FFT is incredibly quick since it needs fewer calculations than FT. For real-time signal assessment and processing, the FFT is suitable considering its efficiency optimizations and significant acceleration compared to the standard FT [3]. The FFT-based study employed a sample rate of 100000 Samples/s.

In this study, the BLDC motor's stator current is examined in both standard and different %ISSCRF situations. A 5% to 50% reduction in snubber resistance was investigated in the fault investigation. To identify the ISSCRF, a number of variables related to the stator current, including DCC, FCC, and THD, have been assessed by FFT.

3.4.1 DCC Analysis

The DCC for various %ISSCRF levels was obtained by FFT-based computation of the recorded current signal, as depicted in Fig. 3.3. However, no distinct association between the DCC of the stator's current and various ISSCRF percentages could be identified in Fig. 3.3.

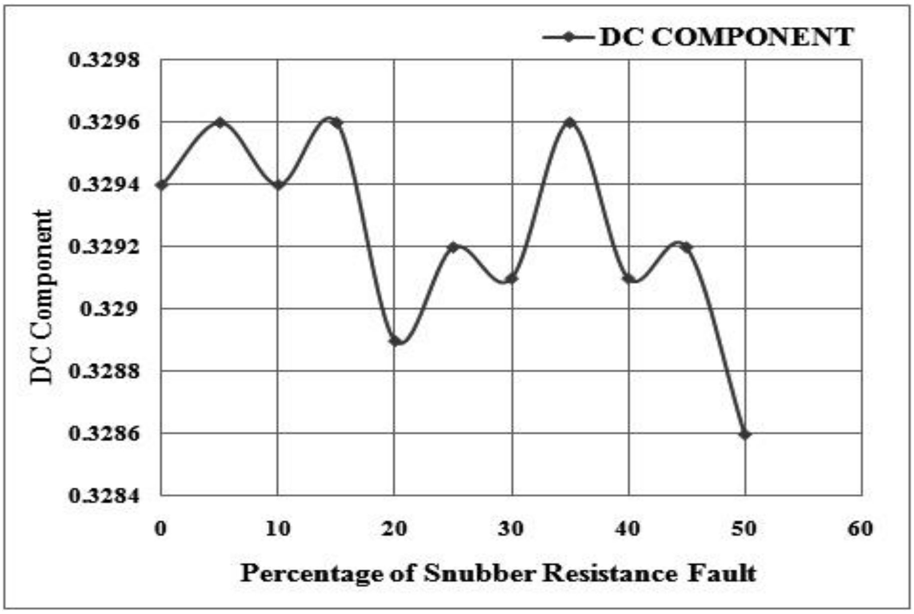

Fig. 3.3. DCC vs. %ISSCRF

3.4.2 FCC Analysis

The fundamental frequency computation is imperative when assessing the stator current's frequency patterns. In Fig. 3.4, the FCC values that were computed for different %ISSCRF values are depicted.

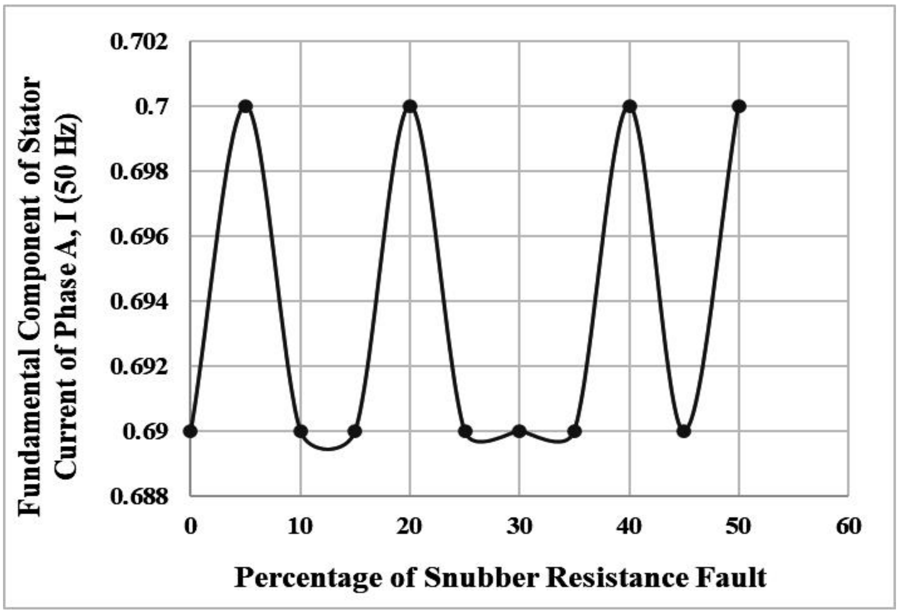

Fig. 3.4. FCC vs. %ISSCRF

It is apparent that the FCC fluctuates as the %ISSCRF alters. However, it fails to provide an insightful pattern of correlation between the FCC and the %ISSCRF readings.

3.4.3 THD Analysis

THD quantifies a signal's harmonic content. The current signal's THD may be represented as follows:

$$THD = \frac{\sqrt{\sum_{n=2}^{\infty} I_{n\_rms}^{2}}}{I_{fund\_rms}} \tag{3.7}$$

where,

I_{fund_rms}= root-mean-square (RMS) value for the fundamental frequency

I_{n_rms}= harmonic n's RMS value

Here, Fig. 3.5 illustrates the obtained THD values at different %ISSCRF levels. As can be observed in Fig. 3.5, changes in the %ISSCRF are accompanied by fluctuations in the THD values. Nevertheless, there was no evident connection between changes in the THD and changes in the %ISSCRF.

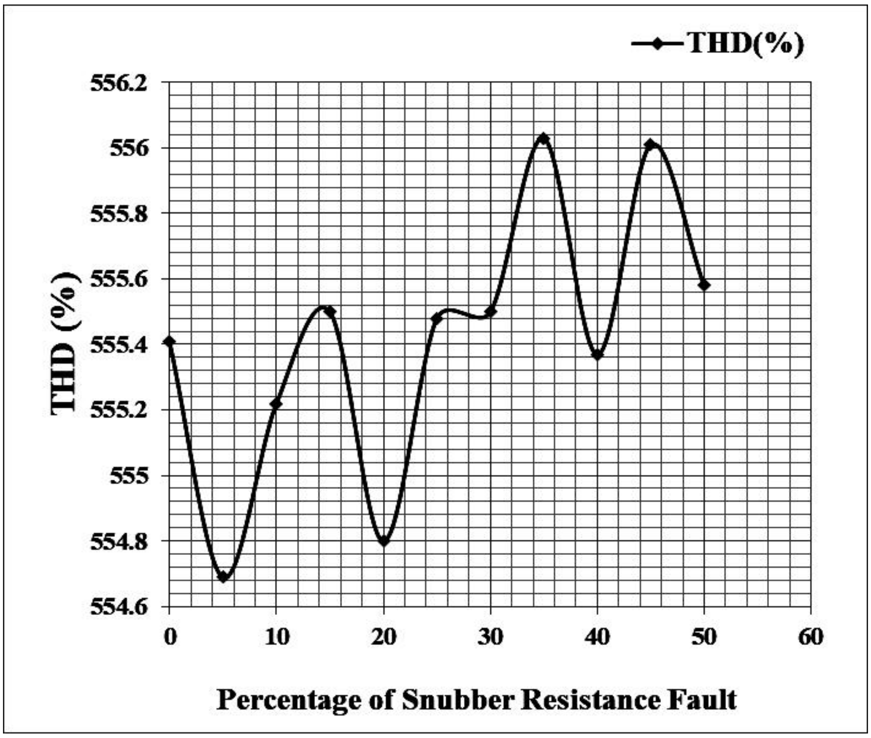

Fig. 3.5. THD vs. %ISSCRF

3.5 Limitation

The BLDC motor's stator current was diagnosed using FFT, and this chapter presents the results of studies on the DCC, THD, and FCC of the motor's stator current under normal conditions and at various %ISSCRF.

It was eventually discovered that the FFT-based diagnosis utilized here for identifying ISSCRF has not produced any insightful findings that can be applied to ISSCRF evaluation. Consequently, FFT is not suitable in situations where the signal's characteristics change over time, since temporal data is lost when a signal is converted to the frequency domain from the time domain. It is a significant drawback of this approach [3], [12]. FFT-based fault detection has been found to be an unsuitable technique for detecting ISSCRF in a BLDC motor since stator current is transitory in character. Additionally, [3], [12] state that whenever the motor current is not stationary, the FFT fails to yield an appropriate result.

Wavelet transform-based fault assessment will be explored in Chapter 9 in an effort to get beyond the drawbacks of this FFT-based diagnosis.

References

[1] A. Shabanian, A. A. P. Tousiwas, M. Pourmandi, A. Khormali, and A. Ataei, "Optimization of brushless direct current motor design using an intelligent technique," *ISA Trans*, vol. 57, pp. 311–321, Jul. 2015, doi: 10.1016/j.isatra.2015.03.005.

[2] M. Shirvani Boroujeni, G. R. A. Markadeh, and J. Soltani, "Torque ripple reduction of brushless DC motor based on adaptive input-output feedback linearization," *ISA Trans*, vol. 70, pp. 502–511, Sep. 2017, doi: 10.1016/j.isatra.2017.05.006.

[3] S. S. Ghosh, S. Chattopadhyay, and A. Das, "Fast Fourier transform and wavelet-based statistical computation during fault in snubber circuit connected with robotic brushless direct current motor," *Cognitive Computation and Systems*, vol. 4, no. 1, pp. 31–44, Mar. 2022, doi: 10.1049/ccs2.12041.

[4] H. Li, X. Ning, and W. Li, "Implementation of a MFAC based position sensorless drive for high speed BLDC motors with nonideal back EMF," *ISA Trans*, vol. 67, pp. 348–355, Mar. 2017, doi: 10.1016/j.isatra.2016.11.014.

[5] A. Tashakori and M. Ektesabi, “Fault diagnosis of in-wheel BLDC motor drive for electric vehicle application,” in *2013 IEEE Intelligent Vehicles Symposium (IV)*, IEEE, Jun. 2013, pp. 925–930. doi: 10.1109/IVS.2013.6629585.

[6] S.-M. Jung, J.-S. Park, H.-W. Kim, K.-Y. Cho, and M.-J. Youn, “An MRAS-Based Diagnosis of Open-Circuit Fault in PWM Voltage-Source Inverters for PM Synchronous Motor Drive Systems,” *IEEE Trans Power Electron*, vol. 28, no. 5, pp. 2514–2526, May 2013, doi: 10.1109/TPEL.2012.2212916.

[7] M. Salehifar, M. Moreno-Eguilaz, G. Putrus, and P. Barras, “Simplified fault tolerant finite control set model predictive control of a five-phase inverter supplying BLDC motor in electric vehicle drive,” *Electric Power Systems Research*, vol. 132, pp. 56–66, Mar. 2016, doi: 10.1016/j.epsr.2015.10.030.

[8] M. Salehifar and M. Moreno-Equilaz, “Fault diagnosis and fault-tolerant finite control set-model predictive control of a multiphase voltage-source inverter supplying BLDC motor,” *ISA Trans*, vol. 60, pp. 143–155, Jan. 2016, doi: 10.1016/j.isatra.2015.10.007.

[9] M. A. Awadallah and M. M. Morcos, “Automatic Diagnosis and Location of Open-Switch Fault in Brushless DC Motor Drives Using Wavelets and Neuro-Fuzzy Systems,” *IEEE Transactions on Energy Conversion*, vol. 21, no. 1, pp. 104–111, Mar. 2006, doi: 10.1109/TEC.2004.841502.

[10] O. Moseler and R. Isermann, “Application of model-based fault detection to a brushless DC motor,” *IEEE Transactions on Industrial Electronics*, vol. 47, no. 5, pp. 1015–1020, 2000, doi: 10.1109/41.873209.

[11] Xiang-Qun Liu, Hong-Yue Zhang, Jun Liu, and Jing Yang, “Fault detection and diagnosis of permanent-magnet DC motor based on parameter estimation and neural network,” *IEEE Transactions on Industrial Electronics*, vol. 47, no. 5, pp. 1021–1030, 2000, doi: 10.1109/41.873210.

[12] S. Karmakar, S. Chattopadhyay, M. Mitra, and S. Sengupta, *Induction Motor Fault Diagnosis*. Singapore: Springer Singapore, 2016. doi: 10.1007/978-981-10-0624-1.

[13] D. Kar Ray, T. Roy, and S. Chattopadhyay, “Single and diagonal double thrust failure assessment of quad-copter at starting,” *Measurement*, vol. 156, p. 107591, May 2020, doi: 10.1016/j.measurement.2020.107591.

[14] S. Chattopadhyay, A. Chattopadhyaya, and S. Sengupta, “Measurement of harmonic distortion and Skewness of stator current of induction motor at crawling in Clarke

plane," *IET Science, Measurement & Technology*, vol. 8, no. 6, pp. 528–536, Nov. 2014, doi: 10.1049/iet-smt.2013.0082.

[15] R. B. Dhumale and S. D. Lokhande, "Neural Network Fault Diagnosis of Voltage Source Inverter under variable load conditions at different frequencies," *Measurement*, vol. 91, pp. 565–575, Sep. 2016, doi: 10.1016/j.measurement.2016.04.051.

[16] Q. Yi *et al.*, "An Investigation of Snubber and Protection Circuits Connections for Power-Electronic Switch in Hybrid DC Circuit Breaker," in *2019 IEEE 10th International Symposium on Power Electronics for Distributed Generation Systems (PEDG)*, IEEE, Jun. 2019, pp. 43–46. doi: 10.1109/PEDG.2019.8807706.

[17] A. Iyer, R. Moghe, R. Kandula, A. Prasai, and D. Divan, "Experimental validation of active snubber circuit for direct AC/AC converters," in *2012 IEEE Energy Conversion Congress and Exposition (ECCE)*, IEEE, Sep. 2012, pp. 3856–3861. doi: 10.1109/ECCE.2012.6342283.

[18] M. Zarghani, S. Mohsenzade, and S. Kaboli, "A Series Stacked IGBT Switch Based on a Concentrated Clamp Mode Snubber for Pulsed Power Applications," *IEEE Trans Power Electron*, vol. 34, no. 10, pp. 9573–9584, Oct. 2019, doi: 10.1109/TPEL.2019.2894994.

[19] S. Dong, Q. Zhang, C. Zhou, and S. Cheng, "Analysis and design of snubber circuit for Z-source inverter," in *2014 16th European Conference on Power Electronics and Applications*, IEEE, Aug. 2014, pp. 1–10. doi: 10.1109/EPE.2014.6910870.

Chapter 4

FFT-based Detection of Early IGBT Failure in the Three-Phase Voltage Source Converter Coupled to PV Microgrid

Abstract- The insulated gate bipolar transistor (IGBT) serves as a fundamental component in modern power electronics converters. The capacity of the IGBT transistor, employed in power converter circuits, to withstand high voltages stands out as one of its most essential characteristics. Massive production of solar energy is integrated into the AC grid through the use of voltage source converters (VSCs). Moreover, VSCs are used in numerous additional applications. All VSC-based systems are affected when IGBT-based VSCs malfunction. Therefore, IGBT's fault-proof functioning is very important. This chapter describes a methodology for identifying prematurely IGBT breakdown failure (PIBDF) in the three-phase (3Ph) VSC that is coupled to a photovoltaic (PV) grid. This fault is referred to as PIBDF in this chapter. The investigation was conducted utilizing the fast Fourier transform (FFT) approach performed to the VSC's output phase voltage. The impacts on the DC and fundamental components, as well as harmonic distortions, have then been examined for varying faulty percentage amounts. Certain subharmonic component characteristics have been examined in both the IGBT's normal and malfunctioning states. Further investigation reveals that a few traits are useful for identifying PIBDF.

Keywords: Fast Fourier transform (FFT), fault diagnosis, IGBT, photovoltaic (PV), voltage source converter (VSC).

4.1 Introduction

PV systems are a readily available, sustainable technology that can be effectively used to generate electricity, and the popularity of these systems is steadily rising [1]. The power produced by the solar cell can be used by a variety of power equipment for both small and large-scale applications. It is the most abundant and ecologically benign renewable energy source (RES) on Earth [1]. In order to improve the efficient use of energy and power controllability, VSCs are being utilized in an increasing number of applications of power systems [2], [3]. IGBT is an integral part of contemporary power electronics. VSCs are now an essential part of modern power electronics following the advancements in power semiconductor technology in recent years [4]. Recently, VSCs have been used in an abundance of HVDC systems [5]. Problems with the system lead to a quick drop in voltage and a rapid increase in current. Determining the fault of a VSC-based supply system in a timely and precise manner is crucial. This assures the electrical system's safety and dependability. Different defect detection methods for VSC-based systems were proposed by the authors in [6], [7], [8], [9]. However, very little efforts were made to identify the early IGBT failure, or PIBDF, in VSCs.

This inevitably led to identifying VSCs with PIBDF. In this chapter, the PIBDF has been detected utilizing FFT. Electrical signal analysis employs the FFT mathematical technique to transform a signal from the time domain into the frequency domain. Compared to time-domain analysis, frequency-domain analysis offers greater accuracy in differentiating among transitory types. This study analyses the VSC's output phase voltage during the VSC's PIBDF. The loads have a significant impact on the current signal. Consequently, the voltage signal was acquired in this study for the aim of defect identification. Several statistical aspects of the VSC's recorded output voltage have been studied utilizing the FFT in order to identify the issue.

4.2 IGBT-Based VSC Powered by PV Array

The grid-tied PV array-powered VSC is depicted schematically in Fig. 4.1. In this work, a 100-kW PV array connected to a 25-kV grid has been taken into consideration for modelling. To link the PV array to the grid, a 3Ph VSC incorporating a boost converter (BC) was utilized. Maximum power point tracking (MPPT) [10] gets utilized by the BC. Using an MPPT system, the duty cycle can automatically be adjusted to produce the voltage needed to extract the most power. Here, the capacitor bank filters the VSC-induced harmonics. Together, the 66 parallel strands of five series-connected modules that make up the PV array produce 100.7 kW of electricity. One PV panel contains 96 cells in all, linked in series. The PV panel's short-circuit (SC) current is 5.96 A and its open-circuit (OC) voltage is 64.2 V. At its peak power output, the panel can generate 54.7 V of voltage and 5.58 A of current. The VSC's phase voltage has been tracked under both normal and varying failure percentage values of the PIBDF (%PIBDF).

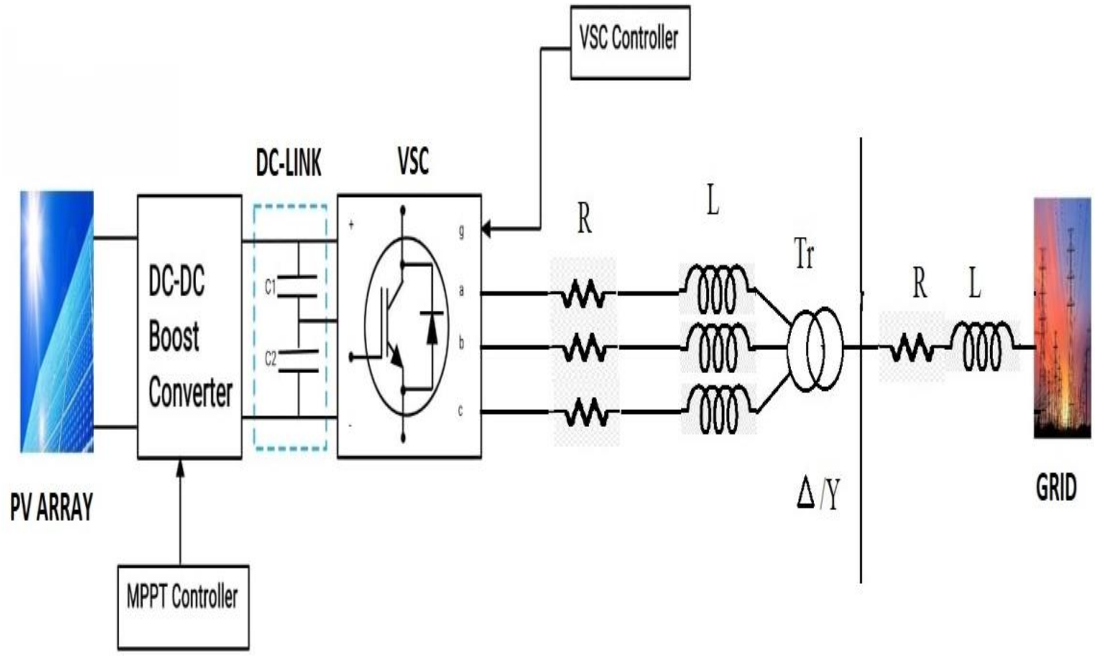

Fig. 4.1. Schematic of the PV array-powered VSC connected to the grid.

4.3 Defining the Problem

The IGBT-based VSC in this study is tied to the electric grid while powered by a PV array. The IGBT failure in VSC is taken into consideration during the PIBDF assessment. The path becomes open following the fault, which is referred to as PIBDF. It could happen because of an overabundance of current, which would raise the temperature and cause the IGBT to burn out. It could also happen following a rise in voltage that causes the insulation to wear out. When there is a problem at the DC end of multi-terminal DC linkages, the DC current rises to an extremely high value. Consequently, the equipment that is linked across it may sustain harm, and the VSC systems that are connected to it at a similar DC terminal, their performance is also impacted. When the VSC HVDC system experiences a DC-sided issue, the IGBT lacks control, and the free-wheeling diodes act as a bridge rectifier, feeding the fault. IGBT protection is extremely challenging and complicated. As a consequence, when a defect occurs, the heat accumulation during the desaturation phase will destroy them, in addition to the growing fault in the early phases of an IGBT malfunction, and the current rate is essentially infinite. Hence, prompt and efficient PIBDF detection is crucial.

Therefore, an effort has been made in this study to investigate the progressive rise of the IGBT failure of VSC. It should be mentioned that the designer's choice will influence both the system specs and the degree of fault. The early detection of PIBDF is vital for preventing harm to the system.

4.4 FFT-Based Failure Detection

Periodic waveforms can be effectively analyzed using the FFT [11]. By lowering the computational complexities, it accelerates the signal analysis significantly. It facilitates the analysis of periodic signals' frequency content by converting time-domain signals into their frequency-domain representations [11]. Its ability to efficiently resolve a signal's fundamental frequency and harmonics is essential for periodic waveform evaluation. FFT makes it possible to precisely identify and measure the harmonics because of disruptions in the system, which is crucial for evaluating power quality. This study examines the output phase voltage of the VSC during PIBDF with the objective of identifying any anomalies. The FFT technique was utilized to analyze a number of statistical features of the VSC's measured output voltage so as to identify the problem.

4.4.1 Generation of Patterns Using FFT

FFT assessment has been conducted on the recorded signal of VSC phase voltage for standard conditions and at various percentage levels of PIBDF within VSC. The collected signal of VSC output voltage, as well as the associated FFT window, which are utilized for the analysis to identify the PIBDF in VSC, are displayed in Fig. 4.2 and Fig. 4.3, accordingly. The signal spectrum that was tracked and examined for the purpose of detecting PIBDF in VSC is illustrated in Fig. 4.4.

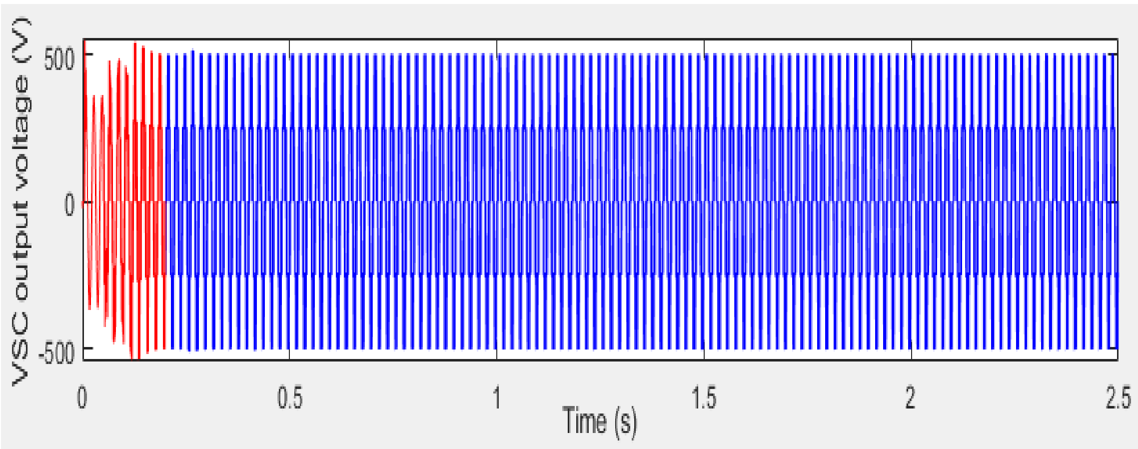

Fig. 4.2. Recorded VSC output voltage

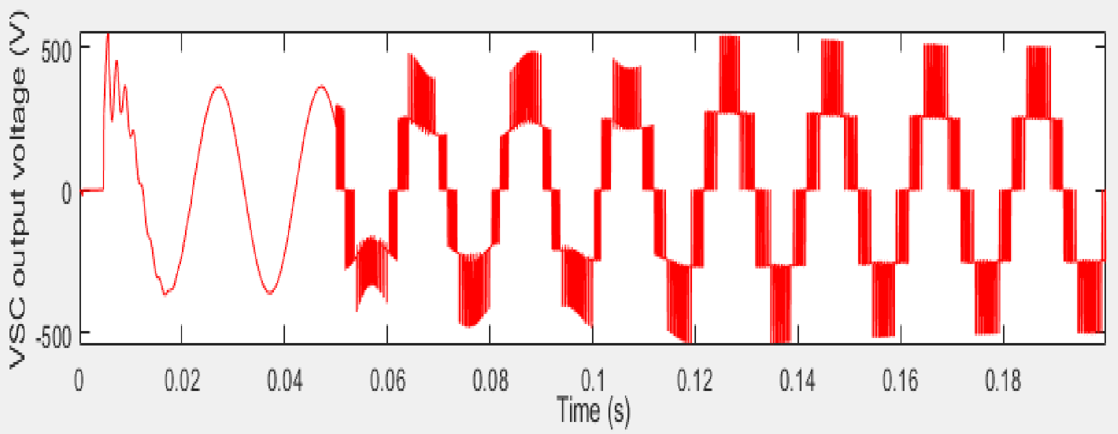

Fig. 4.3. The VSC output voltage FFT window

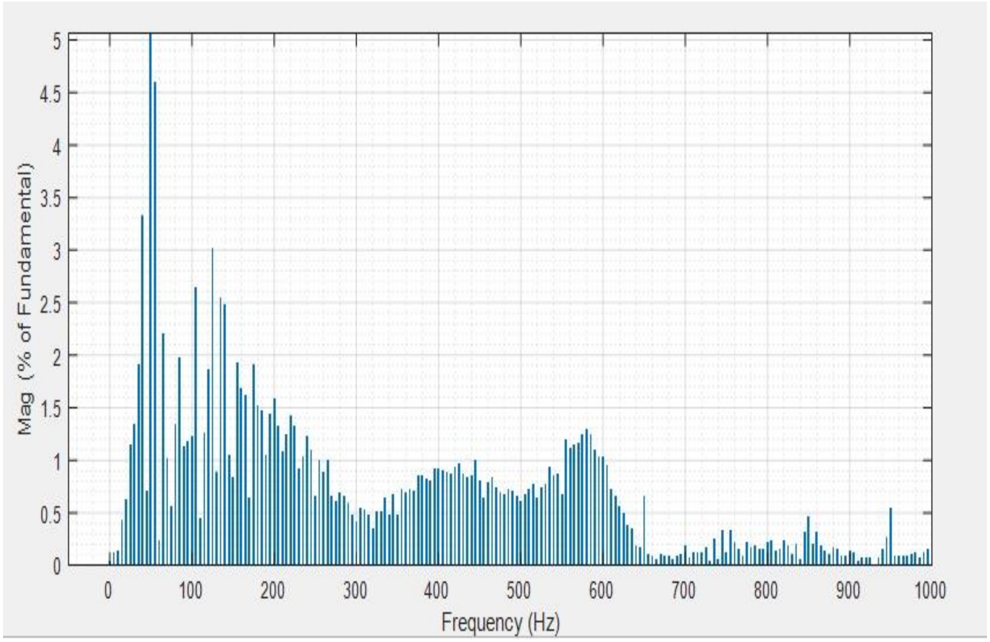

Fig. 4.4. Signal spectrum

4.4.2 Extracting Low-Frequency Features

4.4.2.1 DC Component (DCC) Evaluation

FFT has been performed on the recorded VSC's output voltage to extract the DCC for various %PIBDF values in VSC. The graphical examination of Fig. 4.5 indicates that there is no direct relationship between the DCCs and PIBDF.

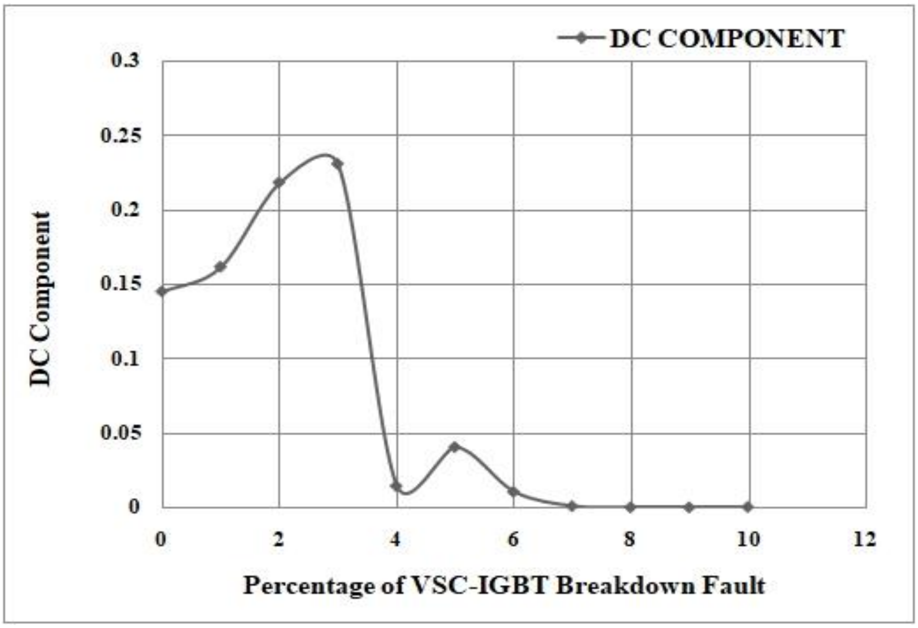

Fig. 4.5. DCC vs. %PIBDF

4.4.2.2 Fundamental Component of Voltage (FCV) Evaluation

This analysis of the VSC output voltage's frequency distribution involves fundamental frequency computation. Fig. 4.6 displays the FCV that was derived from the recorded voltage for various %PIBDF values. Observations show that it does not provide a suitable pattern of association between the various values of %PIBDF and the fundamental frequency of the VSC output voltage.

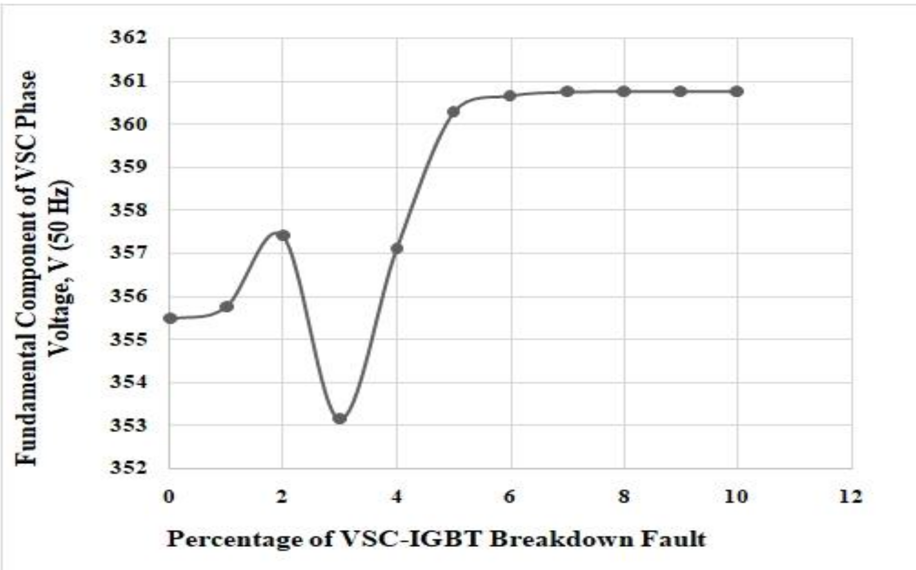

Fig. 4.6. FCV vs. %PIBDF

4.4.2.3 Total Harmonic Distortion (THD) Evaluation

The THD of the recorded signal indicates the degree of distortion caused by the signal's harmonics. The following is an expression for THD [11]:

$$THD = \frac{\sqrt{\sum_{n=2}^{\infty} I_{n\_rms}^2}}{I_{fund\_rms}} \qquad (4.1)$$

where,

I_{n_rms}= harmonic n's root-mean-square (RMS) value;

I_{fund_rms}= fundamental frequency's RMS value

Here, the THD values for the PIBDF analysis have been recovered for normal and varying %PIBDF in VSC, as shown in Fig. 4.7. It illustrates how the THD values fluctuate along with changes in the %PIBDF values. An additional finding from Fig. 4.7 shows that the THD value rises in accordance with the %PIBDF in VSC up to 3%, but then progressively falls after 3% of PIBDF.

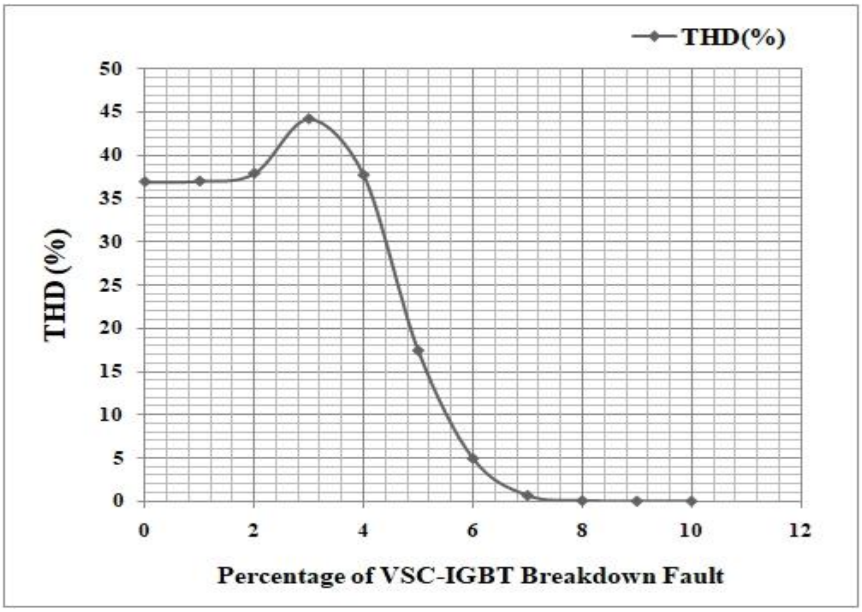

Fig. 4.7. THD vs. %PIBDF

4.4.2.4 Sub-harmonic Components of Voltage (SCV) Evaluation

Sub-harmonic elements have also been recovered from the recorded voltage signal in this investigation. Every sub-harmonic component of the recorded signal has been carefully examined for both typical and various anomalous %PIBDF values. Fig. 4.8 illustrates that all of the values of the SCV alter when the proportion of PIBDF rises.

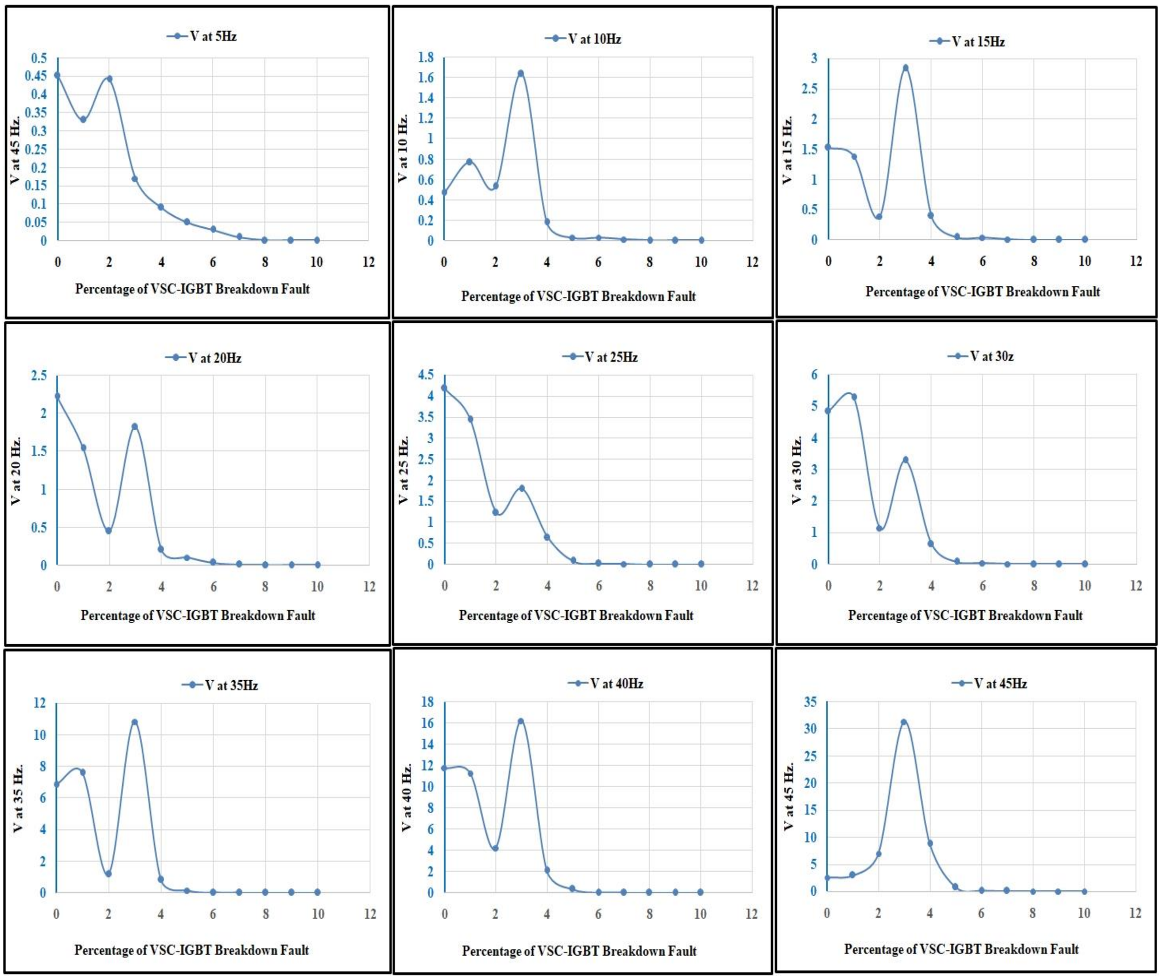

Fig. 4.8. SCV vs. %PIBDF

4.5 Precise Outcome and Discussions

This work's initial portion included FFT-based analysis for a variety of parameters, including the captured VSC voltage's DCC, FCV, THD, and SCV, although there is no discernible result that can be implemented for the identification of VSC's PIBDF.

The standard deviation and mean values (SDMVs) for the alteration in the value of all the SCV for various %PIBDF have been calculated and are shown in Fig. 4.9 for the PIBDF study. These metrics have been found to change differently under defective and normal situations. Therefore, VSC's PIBDF detection up to 5% may be accomplished using this method. Subsequent analysis shows that the suggested work additionally facilitates us to ascertain the VSC's %PIBDF.

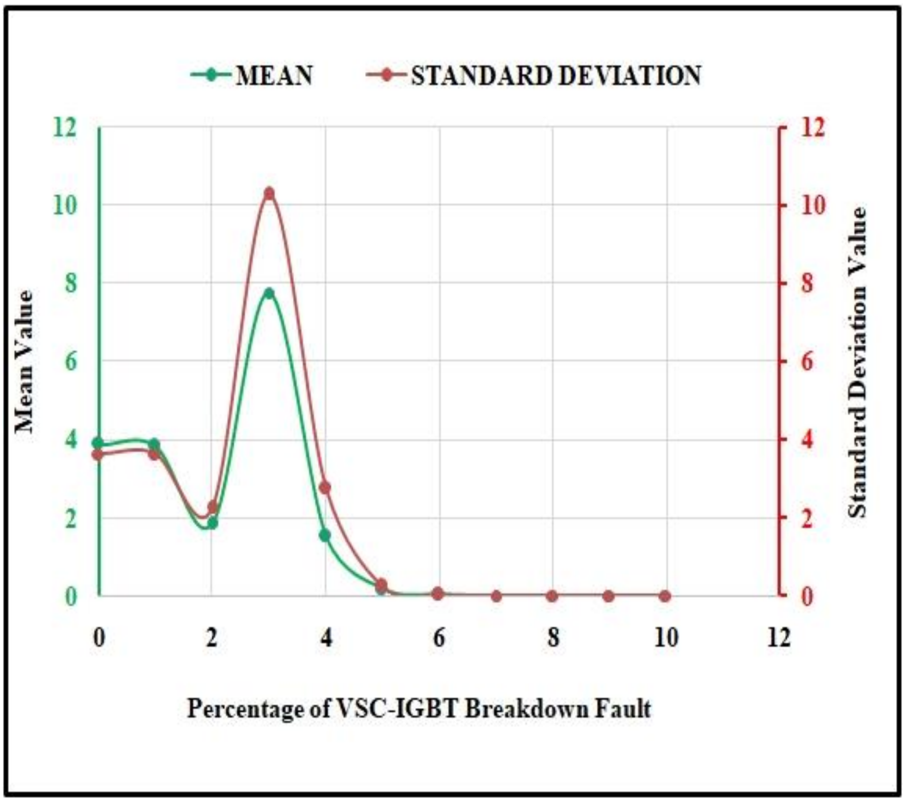

Fig. 4.9. SDMV vs. %PIBDF

4.6 Algorithm for PIBDF Detection

A PIBDF detection technique, as illustrated in Fig. 4.10 has been devised that resembles as follows:

(a) Record the voltage output from the VSC.

(b) Utilizing a sampling method, digitize the recorded voltage.

(c) Utilize FFT on the digital data to evaluate SDMVs for every SCV.

(d) Look for the PIBDF.

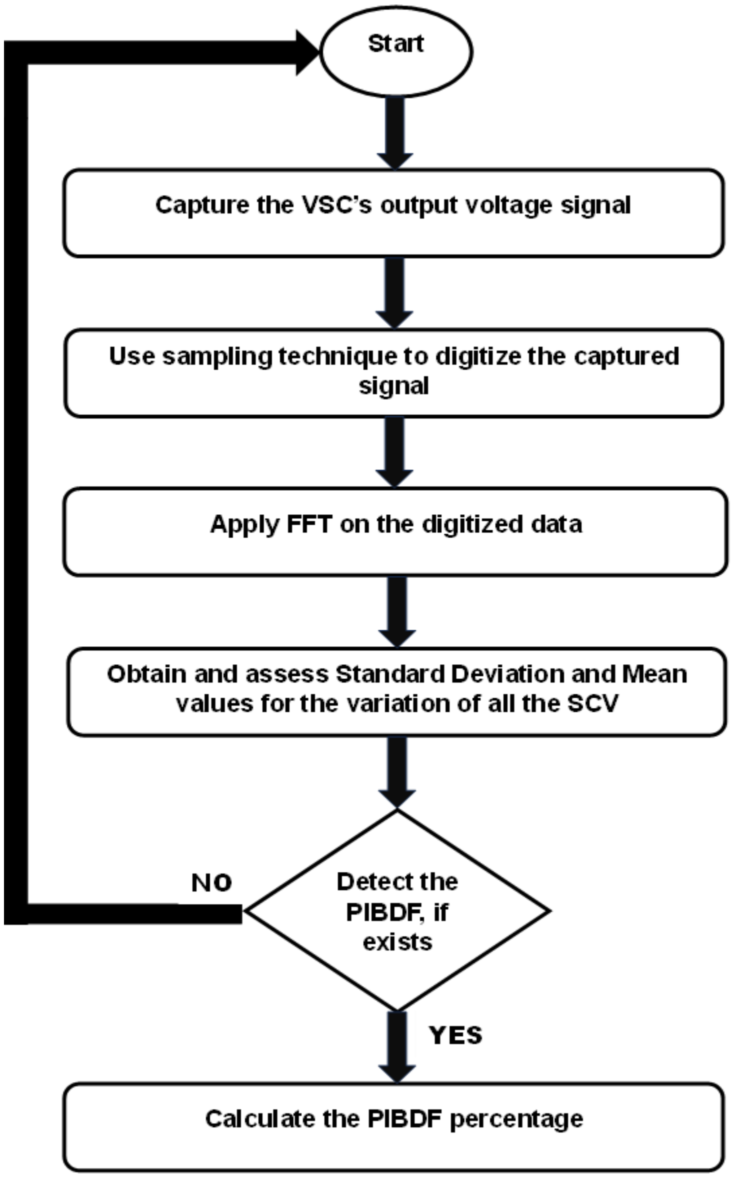

Fig. 4.10. Strategy for identifying PIBDF

4.7 Conclusion

In this chapter, the output voltage of the VSC has been statistically evaluated with FFT to detect the PIBDF. It was also noted that in both preferable and defective situations, the parameter values varied. As the %PIBDF rises, all of the parameters' values also shift.

Furthermore, it has been demonstrated that this FFT-based defect detection approach effectively detects the early presence of PIBDF in VSC. Hence, it is feasible to recognize PIBDF in VSC early through constantly tracking recorded values. Thus, the suggested method may be used to estimate the percentage of PIBDF in VSC while preventing the system from pricey losses.

References

[1] T. Shiyani and T. Bagchi, “Hybrid nanostructures for solar-energy-conversion applications,” *Nanomaterials and Energy*, vol. 9, no. 1, pp. 39–46, Jun. 2020, doi: 10.1680/jnaen.19.00029.

[2] D. Lu, X. Wang, and F. Blaabjerg, “Impedance-Based Analysis of DC-Link Voltage Dynamics in Voltage-Source Converters,” *IEEE Trans Power Electron*, vol. 34, no. 4, pp. 3973–3985, Apr. 2019, doi: 10.1109/TPEL.2018.2856745.

[3] J. Rocabert, A. Luna, F. Blaabjerg, and P. Rodríguez, “Control of Power Converters in AC Microgrids,” *IEEE Trans Power Electron*, vol. 27, no. 11, pp. 4734–4749, Nov. 2012, doi: 10.1109/TPEL.2012.2199334.

[4] O. Alavi, L. Van Cappellen, W. De Ceuninck, and M. Daenen, “Practical Challenges of High-Power IGBT’s I-V Curve Measurement and Its Importance in Reliability Analysis,” *Electronics (Basel)*, vol. 10, no. 17, p. 2095, Aug. 2021, doi: 10.3390/electronics10172095.

[5] C. Xu, B. Zhao, Z. Chen, J. Liu, Q. Song, and Z. Yu, “A Novel Converter-Breaker Integrated Voltage Source Converter Based on High-Surge IGCT and Fault Self-Clearing Strategy for DC Grid,” *IEEE Trans Power Electron*, vol. 35, no. 12, pp. 12668–12672, Dec. 2020, doi: 10.1109/TPEL.2020.2996504.

[6] X. Sun, X. Gao, and S. Ji, “Serious fault identification for VSC-HVDC converters,” in *2020 4th International Conference on HVDC (HVDC)*, IEEE, Nov. 2020, pp. 762–767. doi: 10.1109/HVDC50696.2020.9292759.

[7] D. Kar Ray, S. Chattopadhyay, and S. Sengupta, “Multi-Resolution-Analysis-based Line-to-Ground Fault Detection in a VSC-Based HVDC System,” *IETE J Res*, vol. 66, no. 4, pp. 491–504, Jul. 2020, doi: 10.1080/03772063.2018.1502626.

[8] D. Li, A. Ukil, K. Satpathi, and Y. M. Yeap, “Improved S Transform-Based Fault Detection Method in Voltage Source Converter Interfaced DC System,” *IEEE Transactions on Industrial Electronics*, vol. 68, no. 6, pp. 5024–5035, Jun. 2021, doi: 10.1109/TIE.2020.2988193.

[9] C. Sui, Y. He, Z. Li, and M. Chen, “The Post-Fault Current Model of Voltage Source Converter and Its Application in Fault Diagnosis,” *IEEE Trans Power Electron*, vol. 36, no. 2, pp. 1209–1214, Feb. 2021, doi: 10.1109/TPEL.2020.3007586.

[10] S. Chattopadhyay, *Nanogrids and Picogrids and their Integration with Electric Vehicles*. Institution of Engineering and Technology, 2022. doi: 10.1049/PBPO208E.

[11] S. S. Ghosh, S. Chattopadhyay, and A. Das, “Fast Fourier transform and wavelet-based statistical computation during fault in snubber circuit connected with robotic brushless direct current motor,” *Cognitive Computation and Systems*, vol. 4, no. 1, pp. 31–44, Mar. 2022, doi: 10.1049/ccs2.12041.

Chapter 5

FFT-based Accelerated IGBT Switch Failure Identification in a Bidirectional Microgrid Inverter Connected to Distributed Generation

Abstract- Since insulated gate bipolar transistors (IGBTs) are effective, dependable, and adaptable for managing high-power applications, they are vital elements of today's power electronics converters. In microgrid inverters (MGIs), IGBTs are key parts that provide the switching power needed to convert DC energy from renewable sources into high-quality AC power for microgrid (MG) applications. To facilitate the effortless incorporation of distributed energy resources (DERs) and enable both grid-tied and islanded functioning, the microgrid needs to incorporate bidirectional inverters (BDIs). In BDIs, IGBTs are crucial for effective energy transformation and controlling the bilateral power flow. BDI's IGBT malfunctions can have a range of adverse impacts on a microgrid, from minor issues with power quality to significant disruptions in system operation and reliability. Consequently, the IGBT ought to function flawlessly. A rapid technique for detecting the IGBT switch fault (ISF) in MG's BDI connected to a photovoltaic (PV) and battery storage system (BSS) is demonstrated in this chapter. The BDI's output current has been analysed using the fast Fourier transform (FFT) to identify ISF. At different ISF values, the effects on the captured BDI's output current quality characteristics have since been examined. Using the most favourable characteristics, an attempt has been performed to effectively identify the ISF. Additionally, a process enabling ISF detection is suggested.

Keywords: Bidirectional inverter (BDI), distributed generation (DG), fast Fourier transform (FFT), fault detection, IGBT, microgrid (MG)

5.1 Introduction

On a global scale, microgrids are being embraced more and more as part of initiatives to update energy infrastructure and increase sustainability and energy security. Microgrids depend substantially on DGs [1]. Unlike a centralized model where power is produced at a large, often distant facility and transmitted over extensive distances to consumers, DGs denote a decentralized approach to energy generation and supply. Integrating PV systems with BSS) is a prevalent and effective technique for generating a flexible and reliable power solution [2], [3]. The development of semiconductor devices, their low volume, and their reasonable costs have led to an increase in the usage of electrical power converters [4]. Numerous applications in MGs use BDIs, which can transmit power into or out of the AC mains, to increase power controllability and the effectiveness of energy usage [5]. IGBTs significantly aid in the creation of reliable and energy-effective electronic devices due to their great power-handling potential, efficacy, and versatility across a wide variety of applications [6]. Most applications in MGs make use of voltage source inverters (VSIs) [7], [8].

K. Nguyen-Duy et al. in [9] illustrated open circuit failures (OCFs) detection in the matrix converter drive's (MCD's) bidirectional switch. In [10], K. M. Reddy et al. suggested an efficient method to check for OCF within an inverter. In 2020, J. Zhang et al. in [11] introduced a unique technique for detecting OCF in grid-side converters' (GSC) IGBT module. The current-source inverter's (CSI's) OCF was proposed by the authors in [12]. In 2019, S.S. Moosavi et al. suggested approaches for detecting OCF inside an IGBT-based inverter [13]. Authors in [14] proposed a method for detecting short circuit failures (SCFs) in islanded inverters. In 2024, S. S. Ghosh et al. in [15] demonstrated the IGBT switch failure detection technique in an inverter.

Nevertheless, no significant deliberate attempts were ever made to detect early ISF in an MG's BDI. An innovative technique for identifying ISF in BDIs is presented in this chapter. The frequency-domain assessment feature of FFT [16], [17] has been employed here to assess the ISF, since the fact that frequency-domain assessment distinguishes between distinct transient forms with greater precision than time-domain assessment.

This article identifies ISF by measuring the output current of the BDI. Across a range of ISF levels, the effects of ISF on fundamental, harmonic, and subharmonic distortion have been studied.

5.2 Grid-Tied PV-Powered BDI

A schematic illustration of the grid-linked PV-powered BDI is exhibited in Fig. 4.1. With a rating of 100.7 kW, the PV system is connected with the 66 kV grid. Utilizing a DC/DC converter, the PV system is attached to an HVDC bus. Here, the power extraction from the PV system is optimized by using a DC/DC converter in combination with a maximum power point tracking (MPPT) controller. Here, a centralized controller that combines a power conditioning system and a battery management system is also used. Both normal and defective conditions of the IGBT switch have been meticulously observed. Under normal conditions and at different ISF percentage levels (%ISF), the extracted current has been evaluated to enable for identification of ISF in the BDI.

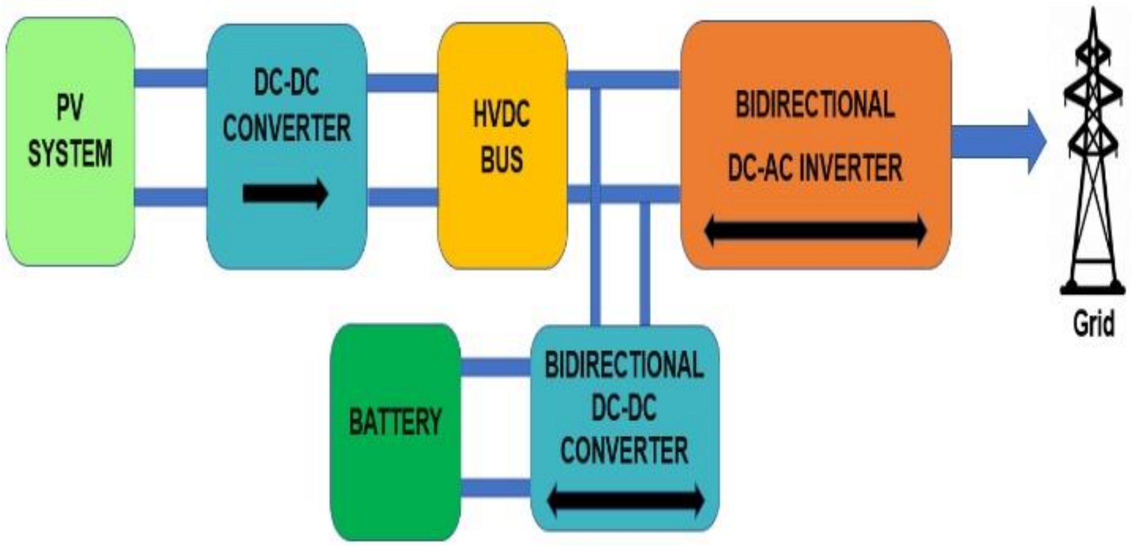

Fig. 5.1. Schematic of the grid-tied PV-powered BDI

5.3 Problem Description

In this investigation, the PV-powered BDI is coupled to the power grid. For fault inspection, the IGBT switch fault of the BDI has been put under consideration. The failure of the IGBT switch is a serious issue. The issue is described as a scenario that breaks the pathway open beyond the malfunction. IGBT switch burning could occur from an elevated current spike that builds up the temperature. Additionally, a voltage surge causing harm to insulation might cause it.

Safeguarding IGBT switches is extremely difficult and complex. Thermal buildup within the desaturation stage has the potential to destroy the switch. Therefore, it matters greatly to identify ISF quickly and successfully. Thus, an effort was undertaken in this investigation to identify the gradual rise in ISF. Design choices influence both defect rates and system parameters. ISF detection is a key factor in ensuring system reliability and preventing damage.

5.4 Using FFT to Diagnose ISF

Strong mathematical techniques for identifying a signal's frequency components are the Fourier transform (FT) and FFT [17]. However, they differ significantly in terms of efficiency and computation. FFT is rather quick. With its digital computing optimization, FFT allows real-time signal processing, facilitating the identification of particular elements, trends, or irregularities in the signal.

This investigation captured and thoroughly examined the BDI's output current to discover ISF. To discover the ISF issue, a range of metrics relating to the acquired current have been observed using the FFT.

5.4.1 Development of Patterns Using FFT Integration

FFT analysis has been performed on the captured current signal over multiple ISF percentage levels (%ISF) as well as under typical operational circumstances. Fig. 5.2 and Fig. 5.3 display the gathered signal and the FFT window for the acquired current signal, accordingly. The signal spectra of tracked BDI's output current have been demonstrated in Fig. 5.4.

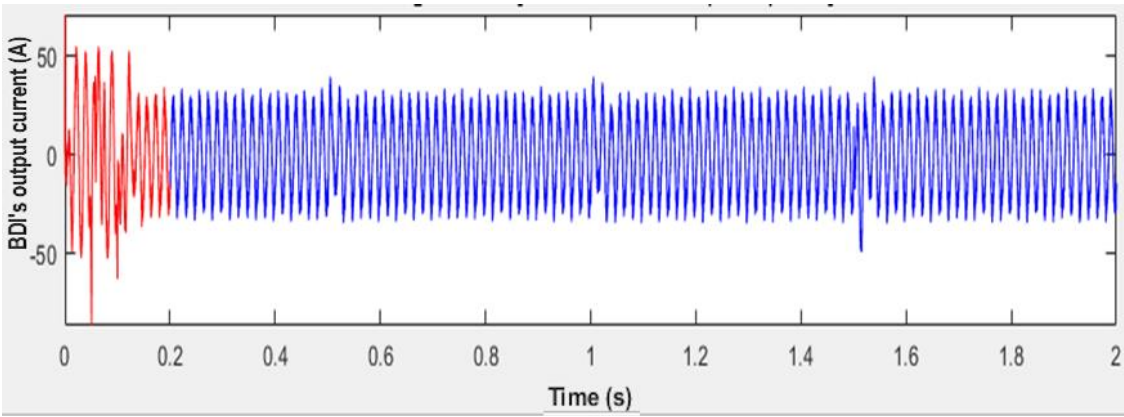

Fig. 5.2. Collected BDI's output current

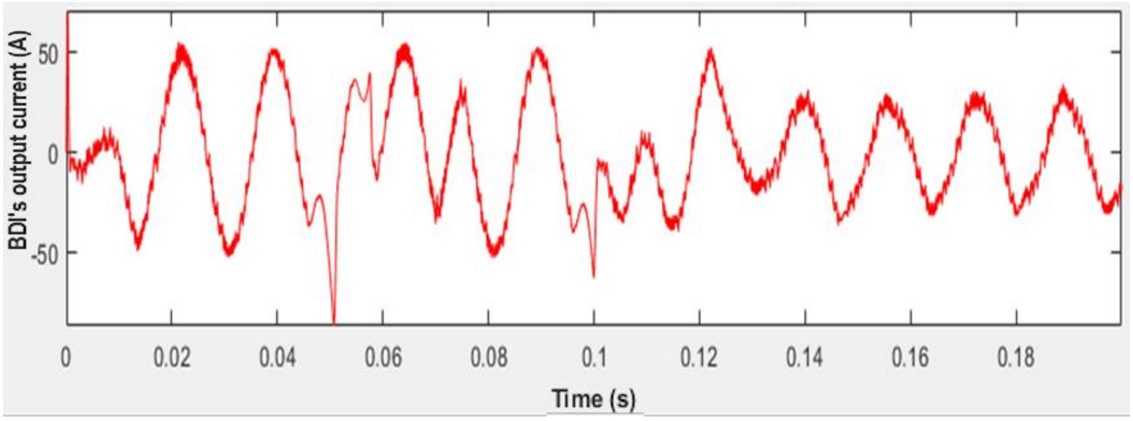

Fig. 5.3. BDI's output current FFT window

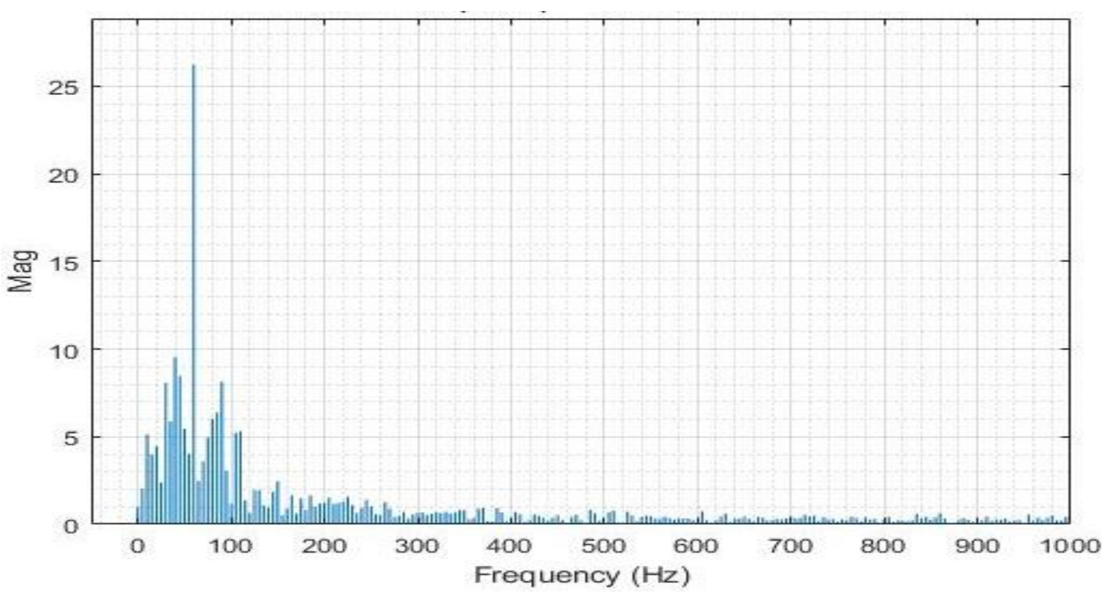

Fig. 5.4. Signal spectrum of current

5.4.2 Feature Extraction for Low-Frequency

5.4.2.1 Assessing the Fundamental Current Component (FCC)

In FFT, FCC assessment refers to the process of extracting an electrical signal's components at the fundamental frequency. In this section, the FFT outcomes are utilized to obtain the amplitude and phase data of the FCC.

Fig. 5.5 represents the FCC, which has been estimated using the acquired current for different %ISF. It is evident from the graphic analysis of Fig. 5.5 that there is an inconsistent correlation between the FCC and varying levels of %ISF.

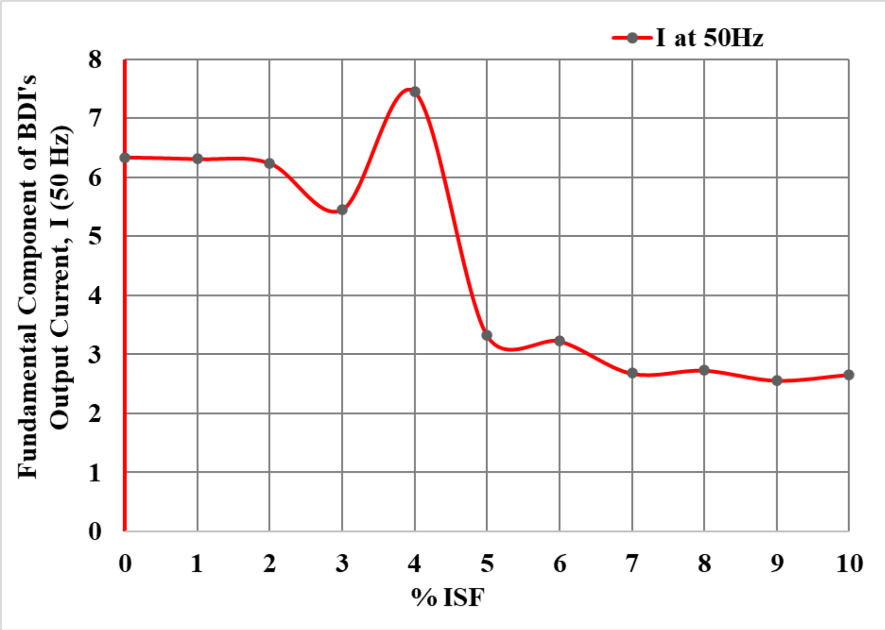

Fig. 5.5. FCC vs. %ISF

5.4.2.2 Assessing the Total Harmonic Distortion (THD)

The signal's harmonic content can be evaluated by THD [3], [17]. THD can be represented as follows:

$$THD = \frac{\sqrt{I_2^2 + I_3^2 + \cdots\cdots + I_n^2}}{I_1} \qquad (5.1)$$

where,

I_1= fundamental frequency's RMS value;

$I_2, I_3, \cdots\cdots, I_n$= harmonic n's root-mean-square (RMS) value

Fig. 5.6 depicts the THD values during the ISF analysis that have been estimated for different %ISF in BDI. It reveals that the THD value remained the same up to 2% of ISF. Figure 6 further shows that the amount of THD increases marginally up to 3% as the percentage of ISF increases. Nevertheless, following 3% of ISF, the THD level declines gradually till 4% of ISF. The THD value increases once again after 4% of ISF, while the ISF value hits 9%. Furthermore, there is no adequate proof in Fig. 5.6's graphical examination that supports a finding of ISF.

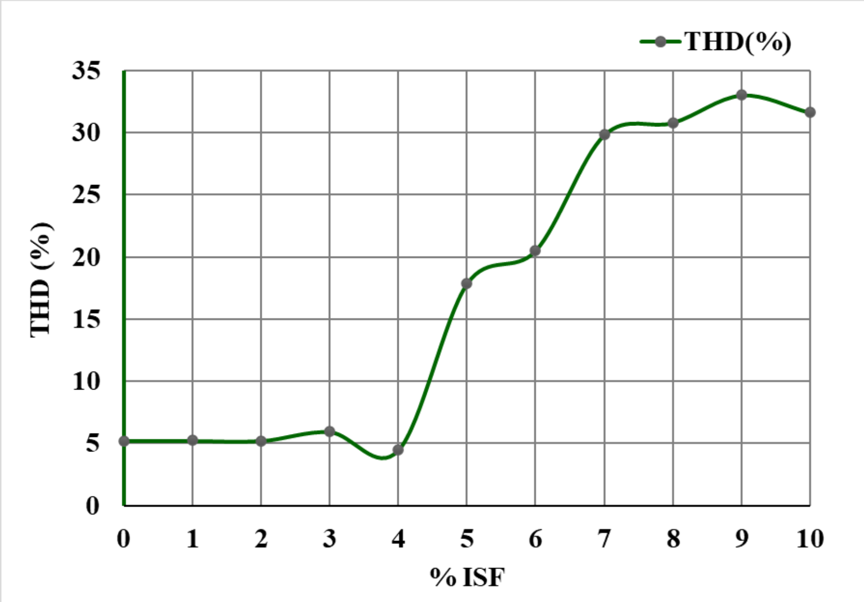

Fig. 5.6. THD vs. %ISF

5.4.2.3 Analysis of Subharmonic Current

Subharmonics (SHCs) have been similarly extracted from the collected current. Each subharmonic element has been extensively investigated for a variety of %ISF in this study. As the fraction of ISF escalates, Fig. 5.7 indicates that the SHC elements change concurrently.

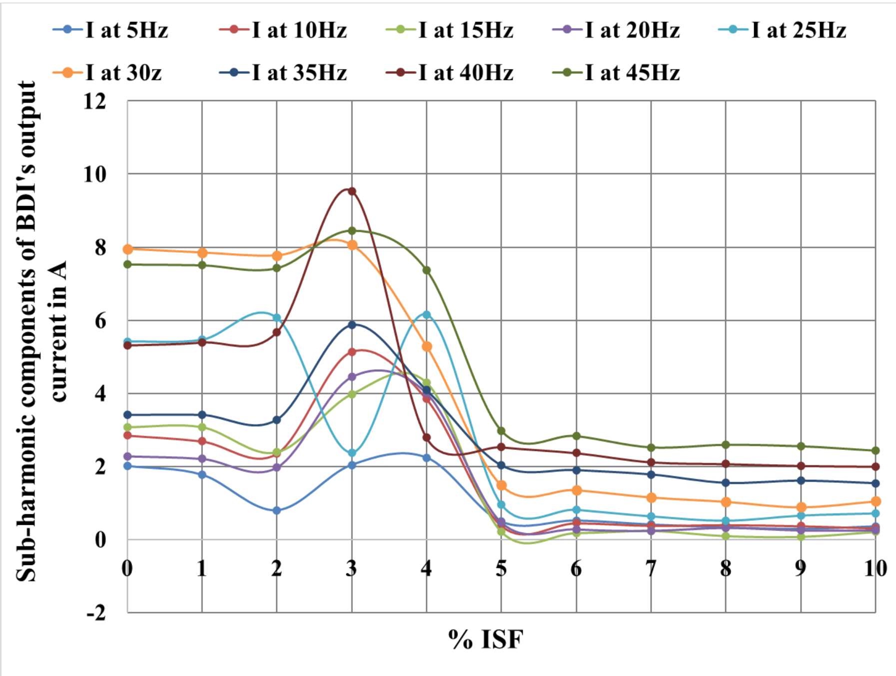

Fig. 5.7. SHCs vs. %ISF

5.5 Particular Findings and Discussion

This study's initial phase included FFT-based signal tracking for a variety of parameters. Yet, these tests are unable to yield any insightful results that might be exploited to identify ISF in BDI.

Furthermore, the standard deviation and mean values (SDMVs) for the variance in all SHC values for different %ISF have been measured. These have been displayed in Fig. 5.8 for ISF investigation.

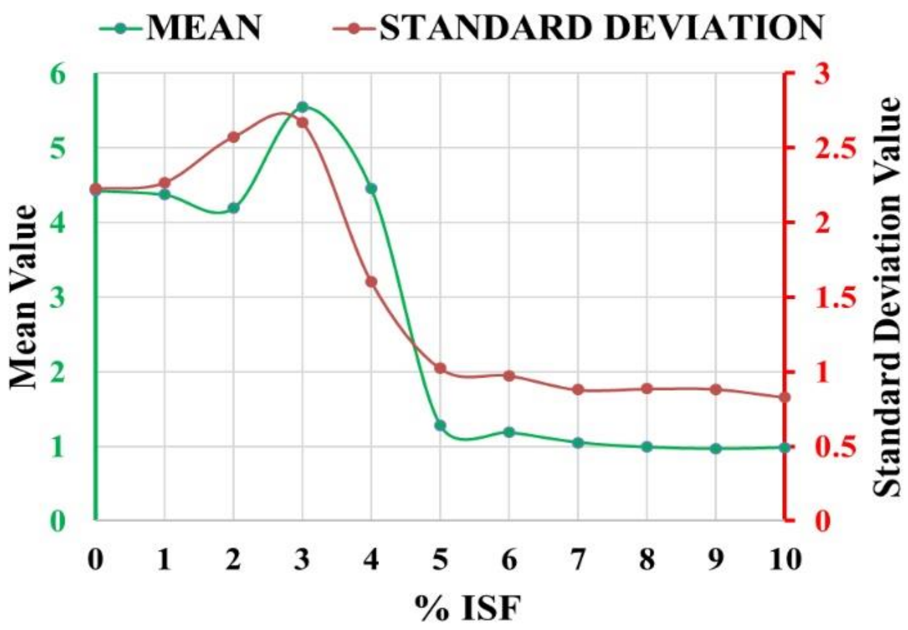

Fig. 5.8. SDMV of the SHCs vs. %ISF

Fig. 5.8's graphical monitoring indicates that the SHCs' standard deviation value (SDV) keeps rising till 3% of ISF. Later, it drops as long as the ISF rises to 10%. Therefore, it can be learned that the most effective way to detect ISF quickly (as much as ISF of 3%) in BDI is to consistently observe the SDV of the SHCs. Subsequent assessment illustrates that the proposed work additionally facilitates us to ascertain the BDI's %ISF.

5.6 Algorithm for ISF Detection

An ISF detection technique, as illustrated in Fig. 5.9 has been devised that resembles as following:

(a) Record the current at the output of the BDI.

(b) Utilizing a sampling method, digitize the acquired current.

(c) Employing FFT on the digital data, assess each SHC's SDVs.

(d) Check for the ISF.

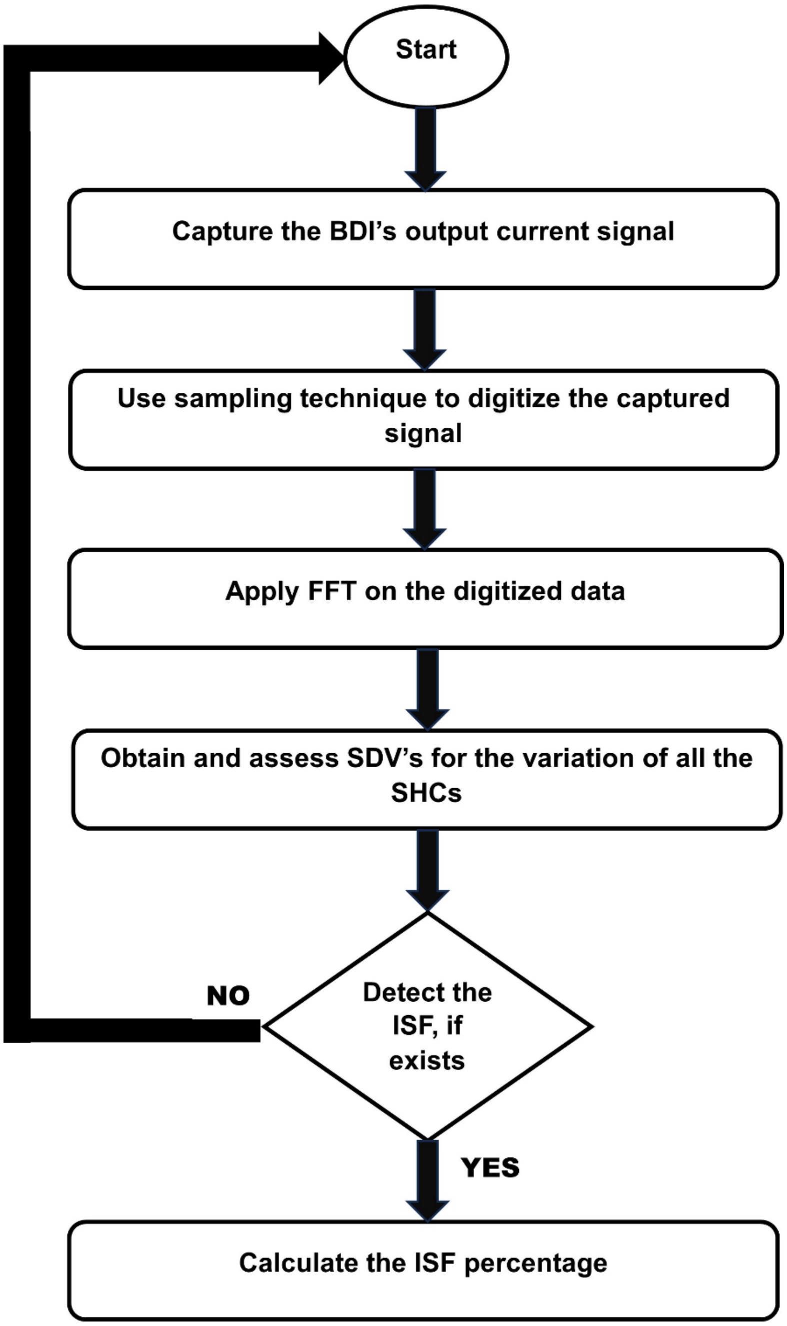

Fig. 5.9. Strategy for ISF detection

5.7 Comparative Analysis

A comparison study comparing the approach suggested and several different inverter failure diagnostic methods has been provided in Table 5.1.

Table 5.1. Comparison Analysis

Ref.	Detecting Faults	Capacity at Identifying Faults (%)
[9], [10]	MCD's and nonsensical inverter's OCF	No
[11]	GSC IGBT modules' OCF	No
[12], [13]	CSI's and IGBT inverter's OCF	No
[14]	Islanded inverter's SCF	No
Proposed method	ISF in BDI	Yes

5.8 Conclusion

In this study, in order to determine ISF, a statistical analysis using FFT on the BDI's output current has been carried out. In both optimal and suboptimal conditions, it was observed that the parameter readings fluctuate. The FFT-based defect detection strategy has been demonstrated to be an efficient means to identify ISF beforehand in BDI.

It was additionally determined through comparison assessment that the technique proposed makes it feasible for calculating the %ISF of the BDI. Thus, constant tracking of the SDV of the SHCs facilitates earlier ISF detection in BDI. Therefore, by employing the recommended strategy, the entire system could be appropriately shielded against expensive damages.

References

[1] L. Zhang, N. Gari, and L. V. Hmurcik, "Energy management in a microgrid with distributed energy resources," *Energy Convers Manag*, vol. 78, pp. 297–305, Feb. 2014, doi: 10.1016/j.enconman.2013.10.065.

[2] S. Sitompul, Y. Hanawa, V. Bupphaves, and G. Fujita, "State of Charge Control Integrated with Load Frequency Control for BESS in Islanded Microgrid," *Energies (Basel)*, vol. 13, no. 18, p. 4657, Sep. 2020, doi: 10.3390/en13184657.

[3] S. S. Ghosh, S. Chattopadhyay, S. H. Arigela, V. V. Kamesh, A. Das, and S. Das, "Expeditious Identification of IGBT Switch Fault in Bidirectional Microgrid Inverter Linked to Distributed Energy Resources," *Journal of Nano- and Electronic Physics*, vol. 16, no. 1, pp. 01019-1-01019–5, 2024, doi: 10.21272/jnep.16(1).01019.

[4] M. Hosseinpour, A. Seifi, and M. M. Rahimian, "A bidirectional diode containing multilevel inverter topology with reduced switch count and driver," *International Journal of Circuit Theory and Applications*, vol. 48, no. 10, pp. 1766–1785, Oct. 2020, doi: 10.1002/cta.2810.

[5] Yaow-Ming Chen, Kuan-Yu Liu, Shih-Kai Chiang, and Yung-Ruei Chang, "Bi-directional grid-tied inverter with predictive current control," in *2009 IEEE Energy Conversion Congress and Exposition*, IEEE, Sep. 2009, pp. 916–919. doi: 10.1109/ECCE.2009.5316072.

[6] S. S. Ghosh, S. Mukherjee, S. Chattopadhyay, and A. Das, "Premature Breakdown Identification in Photovoltaic Array Fed IGBT-based Voltage Source Converter," *Journal of Nano- and Electronic Physics*, vol. 15, no. 3, pp. 03016-1-03016–5, 2023, doi: 10.21272/jnep.15(3).03016.

[7] S. H. Latifi Majareh, F. Sedaghati, M. Hosseinpour, and S. R. Mousavi-Aghdam, "Design, analysis and implementation of a generalised topology for multilevel inverters with reduced circuit devices," *IET Power Electronics*, vol. 12, no. 14, pp. 3724–3731, Nov. 2019, doi: 10.1049/iet-pel.2019.0405.

[8] C. Xu, B. Zhao, Z. Chen, J. Liu, Q. Song, and Z. Yu, "A Novel Converter-Breaker Integrated Voltage Source Converter Based on High-Surge IGCT and Fault Self-Clearing Strategy for DC Grid," *IEEE Trans Power Electron*, vol. 35, no. 12, pp. 12668–12672, Dec. 2020, doi: 10.1109/TPEL.2020.2996504.

[9] K. Nguyen-Duy, T.-H. Liu, D.-F. Chen, and J. Y. Hung, "Improvement of Matrix Converter Drive Reliability by Online Fault Detection and a Fault-Tolerant Switching Strategy," *IEEE Transactions on Industrial Electronics*, vol. 59, no. 1, pp. 244–256, Jan. 2012, doi: 10.1109/TIE.2011.2151818.

[10] K. M. Reddy and B. Singh, "Multi-Objective Control Algorithm for Small Hydro and SPV Generation-Based Dual Mode Reconfigurable System," *IEEE Trans Smart Grid*, vol. 9, no. 5, pp. 4942–4952, Sep. 2018, doi: 10.1109/TSG.2017.2676013.

[11] J. Zhang, H. Sun, Z. Sun, Y. Dong, and W. Dong, "Open-Circuit Fault Diagnosis of Wind Power Converter Using Variational Mode Decomposition, Trend Feature Analysis and Deep Belief Network," *Applied Sciences*, vol. 10, no. 6, p. 2146, Mar. 2020, doi: 10.3390/app10062146.

[12] M. T. Fard, J. He, and Z. Wang, "Fault Diagnosis and Fault-tolerant Operation of Current Source Inverter for Safety-Critical Applications," in *2020 IEEE*

Transportation Electrification Conference & Expo (ITEC), IEEE, Jun. 2020, pp. 925–929. doi: 10.1109/ITEC48692.2020.9161725.

[13] S. S. Moosavi, A. Kazemi, and H. Akbari, "A comparison of various open-circuit fault detection methods in the IGBT-based DC/AC inverter used in electric vehicle," *Eng Fail Anal*, vol. 96, pp. 223–235, Feb. 2019, doi: 10.1016/j.engfailanal.2018.09.020.

[14] S. F. Zarei, H. Mokhtari, and F. Blaabjerg, "Fault Detection and Protection Strategy for Islanded Inverter-Based Microgrids," *IEEE J Emerg Sel Top Power Electron*, vol. 9, no. 1, pp. 472–484, Feb. 2021, doi: 10.1109/JESTPE.2019.2962245.

[15] S. S. Ghosh *et al.*, "Wavelet-based rapid identification of IGBT switch breakdown in voltage source converter," *Microelectronics Reliability*, vol. 152, p. 115283, Jan. 2024, doi: 10.1016/j.microrel.2023.115283.

[16] S. Subhra Ghosh, S. Chattopadhyay, and A. Das, "Harmonics Monitoring for Winding Fault Diagnosis of Brushless DC motor," *IET Conference Proceedings*, vol. 2020, no. 8, pp. 164–169, Jun. 2021, doi: 10.1049/icp.2021.1137.

[17] S. S. Ghosh, S. Chattopadhyay, and A. Das, "Fast Fourier transform and wavelet-based statistical computation during fault in snubber circuit connected with robotic brushless direct current motor," *Cognitive Computation and Systems*, vol. 4, no. 1, pp. 31–44, Mar. 2022, doi: 10.1049/ccs2.12041.

Chapter 6

FFT-based Inspection of Extremely Minimal Changes in MOSFET's Effective Resistance in Microgrid Inverter

Abstract- Microgrid (MG) inverter technologies incorporate metal-oxide-semiconductor field-effect transistors (MOSFETs) as the key elements in traditional electric power converters due to their effectiveness, fast switching, and small dimensions. For a distributed energy source (DES), a microgrid inverter (MGI) is essential, given its ability to transform DC power from renewable energy sources to AC. Bidirectional energy transfer is made practicable by the H-bridge inverters (HBIs) in MG operations, allowing for both grid-tied and standalone operations. The effective resistance of MOSFET (ERM) may alter as a result of the MOSFET malfunction in single-phase H-bridge inverters (1phHBIs). Failures of MOSFETs in an HBI can have adverse impacts on the MG system's performance, safety, and reliability. This chapter introduces a technique for identifying a quick MOSFET switch fault (MSF) in a 1phHBI connected to a photovoltaic (PV) system. The output current from the 1phHBI was evaluated by implementing the fast Fourier transform (FFT) to detect MSF. The effects of MSF on the fundamental component of current (FCC), DC component (DCC), total harmonic distortion of current (THDC), and subharmonics (SHCs) have been investigated at different fault levels. A successful recognition of the MSF has been accomplished relying on the best-fit features. Additionally, the technique makes ERM computation possible during MSF. In addition, an MSF identifying technique has been recommended.

Keywords: Distributed energy source (DES), fast Fourier transform (FFT), fault recognition, single-phase H-Bridge inverter (1phHBI), MOSFET, microgrid (MG).

6.1 Introduction

MG features distributed energy sources (DESs) that include sophisticated control systems and may also incorporate batteries to store energy [1], [2]. By incorporating PV systems, MGs may reduce their dependence on centralized generation facilities and traditional fossil fuels, improving energy safety and dependability [3]. As technology advances and support for DESs grows, residential microgrids (RMGs) [4], [5] are gradually becoming more widely available. RMG allows them to control, store, and produce their own electricity while still being integrated with the primary electrical grid.

The adaptability and control which HBIs provide in MG systems enable the incorporation of clean energy resources and the seamless transition between standalone and grid-tied operations. Typically, inverters employ power semiconductor switches, such as MOSFETs, to perform pulse-width modulation (PWM) in order to get their output in AC [6]. In addition to improving power conversion efficacy, this high frequency of switching assists in reducing the size and overall weight of the inverter's components. Power MOSFETs endure a greater failure probability relative to the inverter's other components [7]. MOSFETs and IGBTs contribute to 21% of converters' faults [8], [9], [10]

In [11], [12], the authors proposed effective detection methods for short circuit failure (SCF) inside the current-source inverter (CSI), and in the islanded inverter, respectively. Different open-circuit fault (OCF) detection methods have been introduced by K. Nguyen-Duy et al. in [13], M. T. Fard et al. et al. in [14], and by J. Zhang et al. in [15] for the matrix converter drive (MCD), CSI, wind power converter (WPC). The failure diagnosis procedures for the IGBT switch within the voltage source converters (VSCs) [9], [16] were illustrated by S. S. Ghosh et al.

Nevertheless, limited efforts have been undertaken to identify MSF in a 1phHBI. This study proposes a novel approach for diagnosing MSF in 1phHBI. MSF has been identified by evaluating the recorded 1phHBI's output current using FFT. In order to identify the MSF, a number of attributes were investigated, such as the DCC, FCC, THDC, and SHCs of the recorded current.

6.2 MOSFET-based Grid-linked Inverter

Fig. 6.1 schematically depicts the grid-linked DMG system. A PV system, a boost converter (DC-DC) operated by maximum power point tracking (MPPT), DC-link, a bidirectional boost converter, a battery storage, a 10 kW domestic load, and a 1phHBI are its constituent parts. The PV system with a 3.5 kW rating is attached with the 66 kV grid. The boost converter uses the MPPT controller to extract as much electrical energy as feasible out of the PV system.

The 1phHBI's output current has been precisely tracked at various MSF percentages (%MSFs) and during normal conditions in order to ascertain whether MSF exists in it.

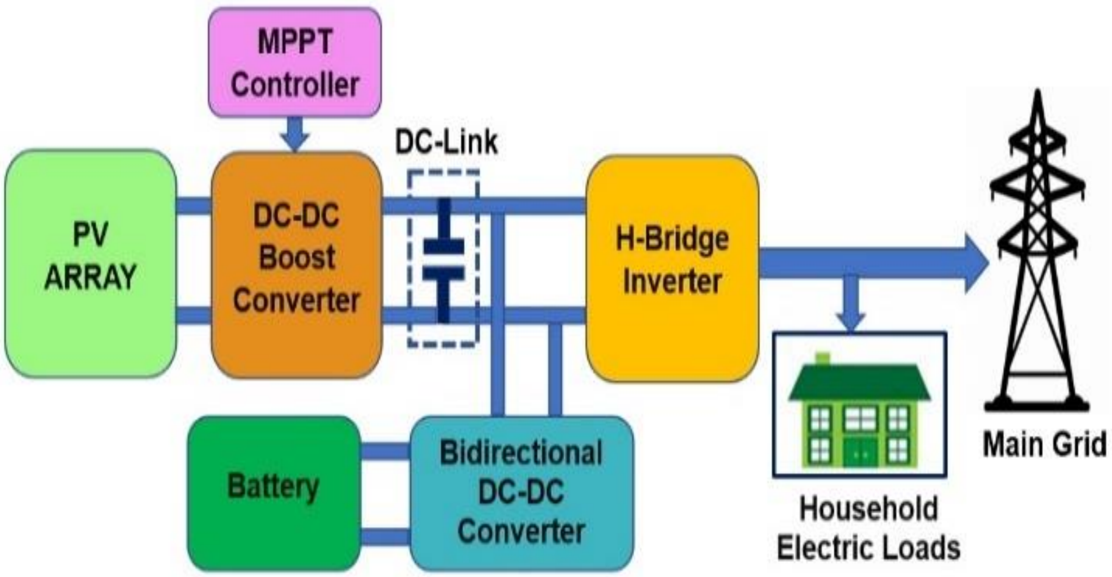

Fig. 6.1. Schematic of MOSFET-based grid-linked inverter

6.3 Problem Description

The utility grid and PV system are interconnected through MOSFET-based 1phHBI in this study. In the fault investigation, the MSF in the 1phHBI has been taken under consideration. An unanticipated problem is 1phHBI's MSF. Variations in the ERM and several issues affecting the device's operation can result from a 1phHBI's MSF. An issue has been defined as a scenario that opens the circuit's passage after a specific %MSF. Undervoltage, overheating, overvoltage spikes, overcurrent, and voltage transients can all cause the MOSFETs to become so strained that they breakdown. Over time, MOSFET aging and wear can lead to a decrease in efficiency and an increased risk of failure.

MSF has the potential to impair the system's overall operation, particularly the inverter. MOSFET-based inverters ought to include rapid and precise fault identification capabilities to reduce the adverse effects of MSF.

In order to discover MSF in 1phHBI, an attempt has been performed in this work, and also to ascertain how the ERM values in the 1phHBI evolved continuously throughout the MSF.

6.4 FFT-Oriented Detection of Faults

In electrical signal evaluation, the Fourier transform (FT) and FFT [10], [17], [18] have applications in methods, particularly for diagnosing and identifying issues. Compared to the FT, the FFT offers an even faster rate [10]. FFT transforms the time-domain signals into their frequency-domain representations, enabling an examination of a signal's frequency elements. Therefore, FFT could be adopted to continually examine electrical data in real-time systems of monitoring.

In this study, MSF is found by attentively examining the 1phHBI's output current. The FFT has been used to measure a number of parameters related to the current captured in an attempt to detect the MSF.

6.4.1 Synthesis of FFT-Oriented Patterns

The obtained current signal has been subjected to FFT analysis underneath both standard operational circumstances and at various %MSFs.

Fig. 6.2 presents the acquired 1phHBI's output current. 1phHBI's output current's FFT window is depicted in Fig. 6.3. Whereas, the signal spectrum of the captured current is presented in Fig. 6.4.

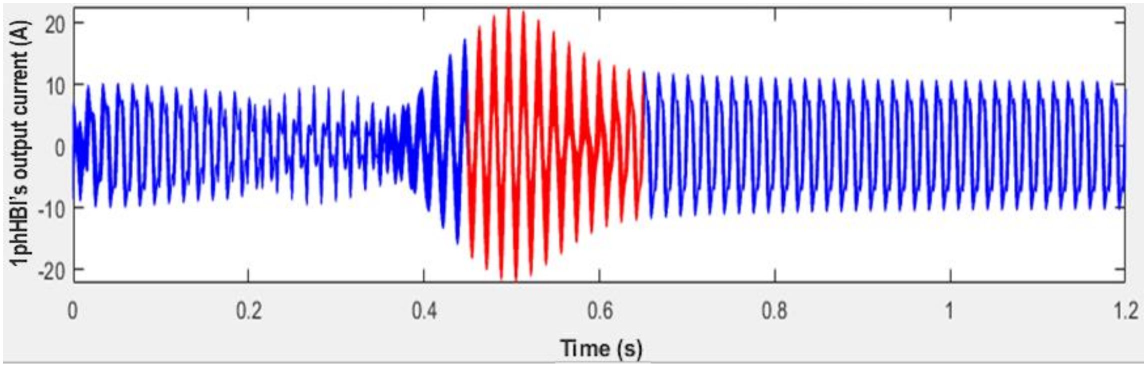

Fig. 6.2. Collected 1phHBI's output current

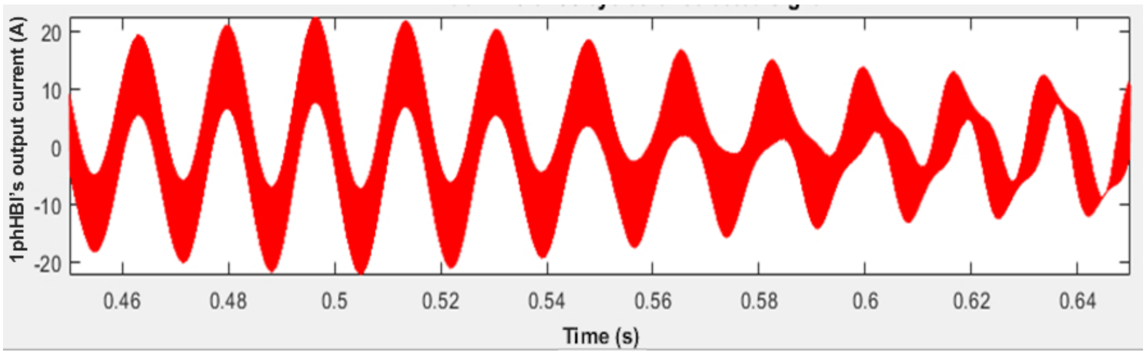

Fig. 6.3. 1phHBI's output current's FFT window

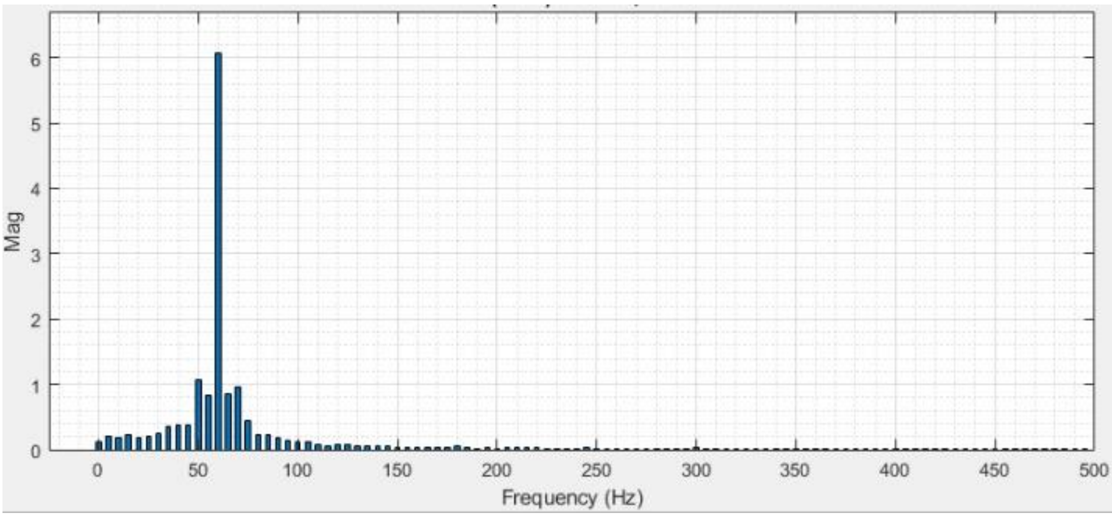

Fig. 6.4. Signal spectrum of captured current

6.4.2 Feature Extraction for Low-Frequency

6.4.2.1 Assessing the DCC

The Fig. 6.5 depicts the DCC of the captured current that was retrieved through FFT-based assessment for different %MSF. A graphical analysis of Fig. 6.5 makes it clear that the different %MSF values next to the DCC are not properly related. Therefore, it would be impossible to use this property to identify MSF in the 1phHBI.

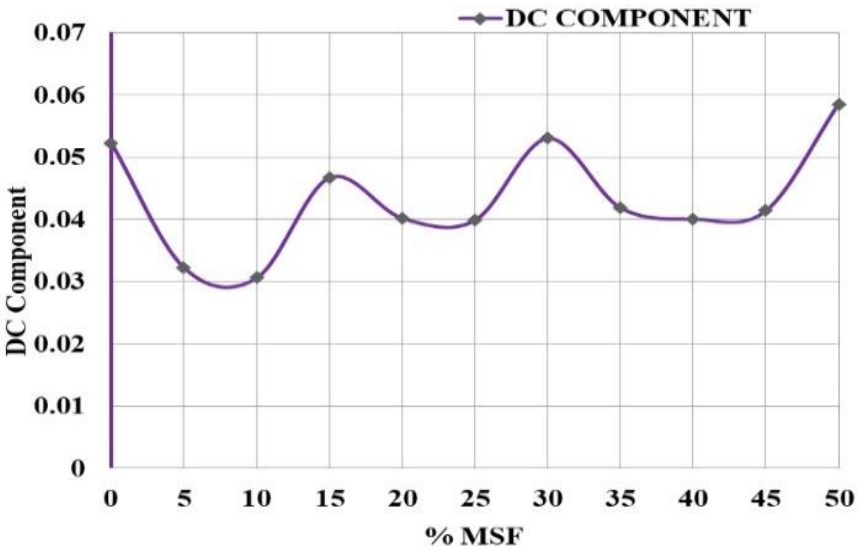

Fig. 6.5. DCC vs. %MSF

6.4.2.2 Assessing the FCC

To assess the FCC of the recorded current signal, FFT has been applied. The FCC values are displayed in Fig. 6.6 and were computed using the 1phHBI's output current for various %MSF levels. It is clear from a visual examination of Fig. 6.6 that the various %MSF values alongside the FCC are not appropriately associated. Hence, adopting this feature to identify MSF in the 1phHBI would not be conceivable.

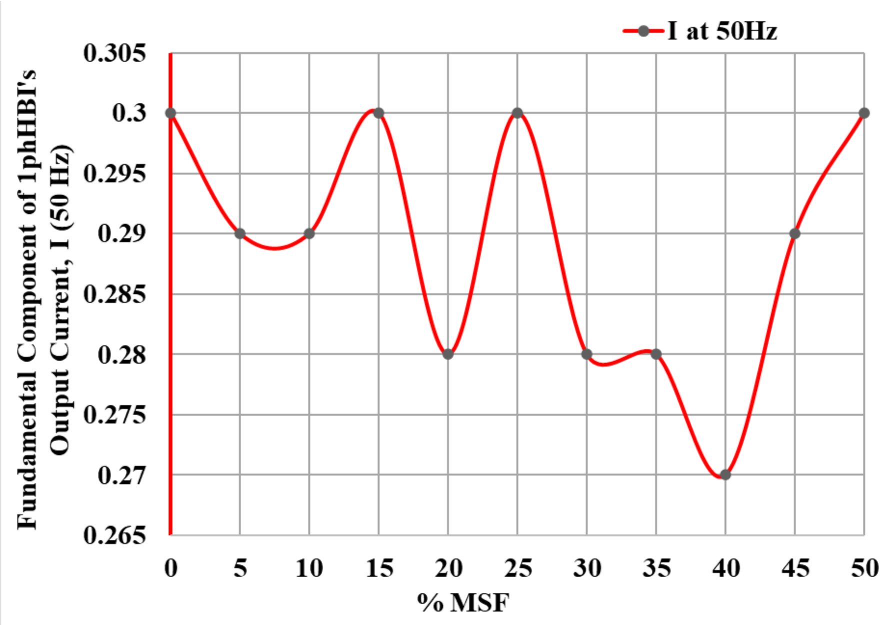

Fig. 6.6. FCC vs. %MSF

6.4.2.3 Analysis of THDC

Total harmonic distortions (THDs) are implemented to quantify the harmonic content of the signals [10]. The term total harmonic distortion of current (THDC) refers to the THD of a current signal.

THDC(%) can be represented as follows:

$$THDC(\%) = \frac{\sqrt{I_2^2+I_3^2+\cdots\cdots+I_n^2}}{I_1}\times 100 \qquad (6.1)$$

where,

I_1= root-mean-square (RMS) value for the fundamental frequency

$I_2, I_3, \cdots\cdots, I_n$= harmonic n's RMS value

The Fig. 6.7 depicts the THDC measurements at various %MSF in 1phHBI. When the 1phHBI's %MSF reaches 10%, it indicates that the THDC(%) is rising as well. However, thereafter, while the %MSF advances to 15%, the THDC(%) progressively falls. After the MSF reaches 15%, the THDC(%) rises and keeps rising unless the %MSF reaches 20%. The graphical examination of Fig. 6.7 fails to reveal compelling proof to support the MSF detection.

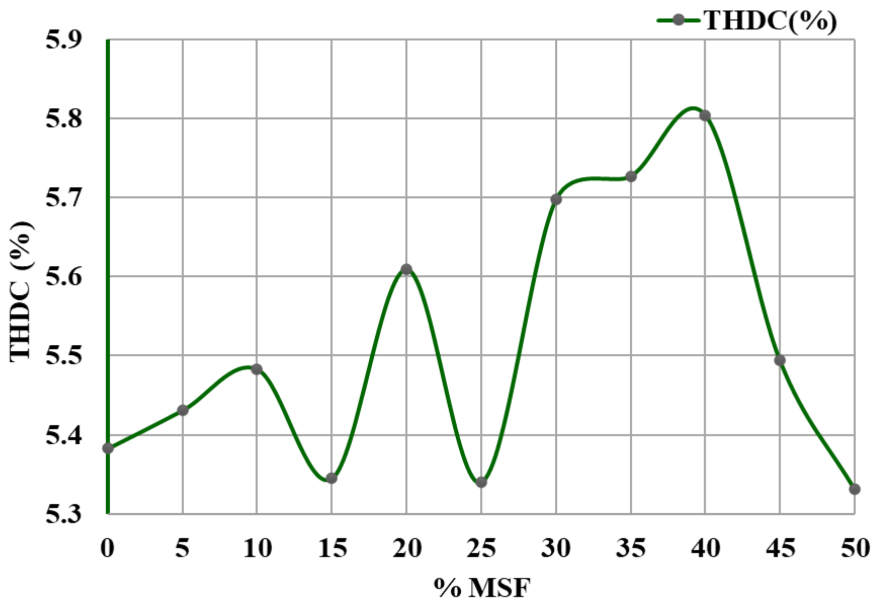

Fig. 6.7. THDC(%) vs. %MSF

6.4.2.4 Analysis of Subharmonic Current

The current that comes out of the 1phHBI has been analysed to extract SHCs. The collected signal's SHCs have all been meticulously assessed for varying %MSF levels. Fig. 6.8 showcases the way every SHC changes concurrently when the %MSF gets higher.

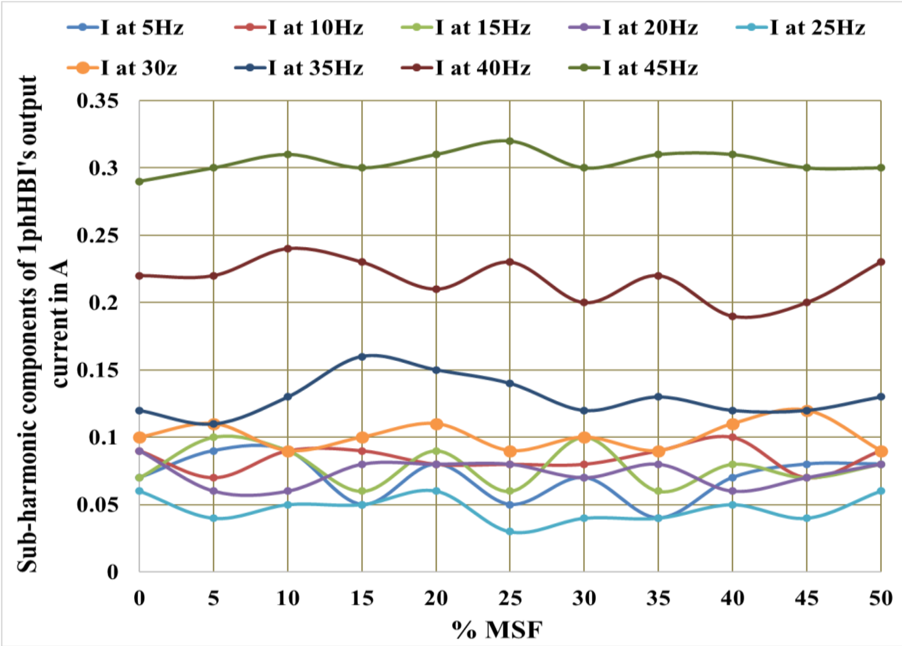

Fig. 6.8. SHCs vs. %MSF

6.5 Specific Findings and Discussion

In this work's initial phase, FFT-based computation of signals was implemented for tracking a variety of metrics, such as the obtained current's DCC, FCC, THDC, and SHCs. However, these assessments have failed to yield any crucial details that might be applicable towards the identification of MSF in 1phHBI.

Additionally, for each SHC value associated with various %MSFs, the standard deviation and mean values (SDMVs) were assessed, as depicted in Fig. 6.9.

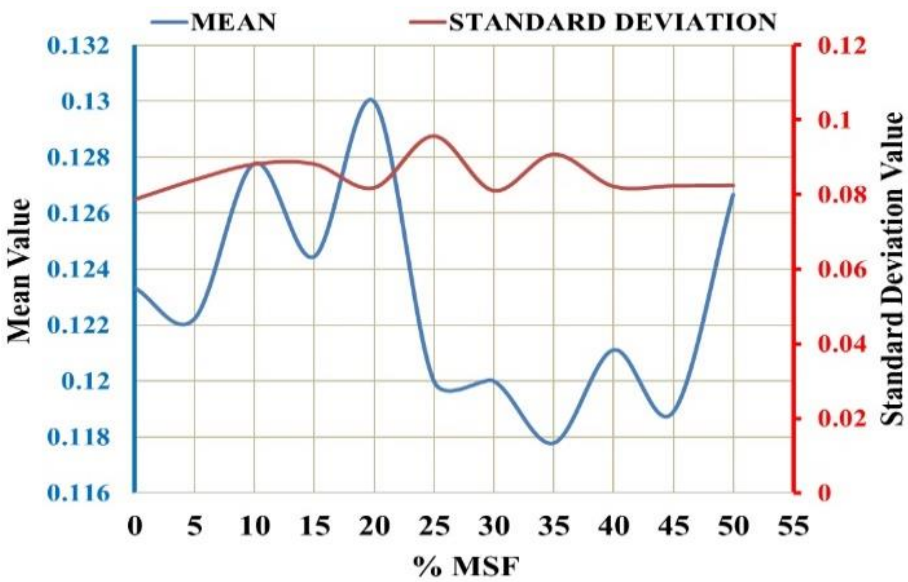

Fig. 6.9. SDMVs of the SHCs vs. %MSF

As MSF rises to 15%, merely the standard deviation values (SDVs) for the SHCs grow gradually, as can be found from the graphical assessment of Fig. 6.9. Thus, it becomes apparent that the detection of MSF (up to 15%) in 1phHBI may be achieved simply by constantly inspecting the SDVs of the SHCs.

6.6 Algorithm for MSF Detection

An MSF detection technique, as illustrated in Fig. 6.10 has been devised that resembles as following:

(a) Record the current at the output of the 1phHBI.

(b) Utilizing a sampling method, digitize the acquired current.

(c) Employing FFT on the digital data, assess each SHC's SDVs.

(d) Check for the MSF.

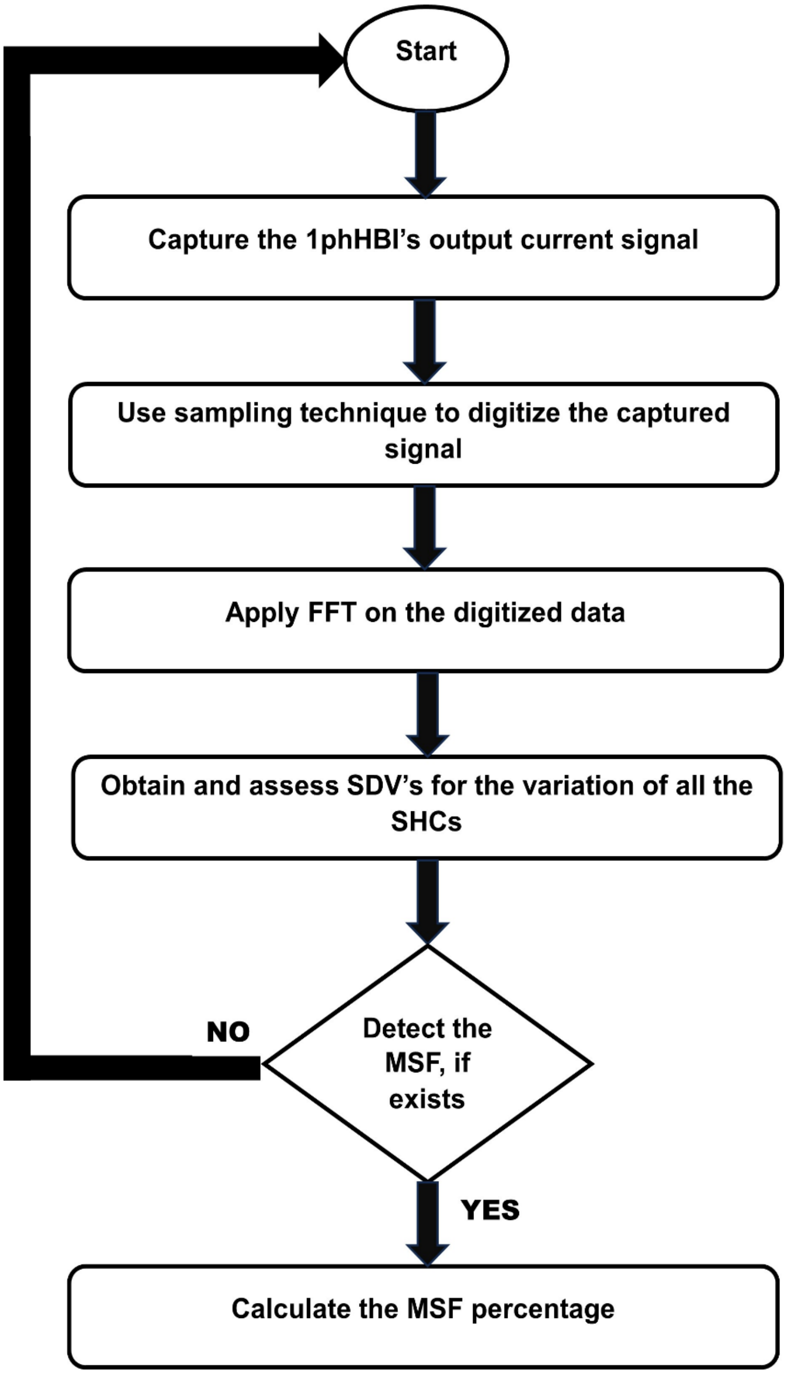

Fig. 6.10. Strategy for GSF detection

6.7 Comparative Analysis

Table 5.1 displays comparisons of the suggested methodology with other kinds of inverter fault identification systems.

Table 6.1. Comparison Analysis

Ref.	Detecting Faults	Capacity at Identifying Faults (%)
[13], [14], [15]	OCFs in MCDs, CSIs, and WPCs	No
[11], [12]	SCFs in CSIs and islanded inverters	No
[9], [16]	IGBT switch's breakdown in VSCs	No
Proposed method	MSF in 1phHBI	Yes

6.8 Conclusion

In this chapter, a statistical evaluation adopting FFT on the tracked current was conducted under both ideal and faulty environments to identify MSF in 1phHBI. Throughout the investigation, it could be observed that the values of the multiple parameters altered.

The particular results additionally demonstrate that the suggested method enables the determination of both the ERM value and the %MSF. This FFT-based failure detection process has been found to effectively detect MSF (up to 15%) in 1phHBI by continually tracking the SDVs of the SHCs. Therefore, by employing the recommended strategy, the entire system could be appropriately shielded against expensive damages.

References

[1] L. Zhang, N. Gari, and L. V. Hmurcik, "Energy management in a microgrid with distributed energy resources," *Energy Convers Manag*, vol. 78, pp. 297–305, Feb. 2014, doi: 10.1016/j.enconman.2013.10.065.

[2] S. Sitompul, Y. Hanawa, V. Bupphaves, and G. Fujita, "State of Charge Control Integrated with Load Frequency Control for BESS in Islanded Microgrid," *Energies (Basel)*, vol. 13, no. 18, p. 4657, Sep. 2020, doi: 10.3390/en13184657.

[3] T. Shiyani and T. Bagchi, "Hybrid nanostructures for solar-energy-conversion applications," *Nanomaterials and Energy*, vol. 9, no. 1, pp. 39–46, Jun. 2020, doi: 10.1680/jnaen.19.00029.

[4] I. Garip *et al.*, "Design of a Small-Scale Domestic Microgrid," *Electric Power Components and Systems*, vol. 51, no. 18, pp. 2220–2231, Nov. 2023, doi: 10.1080/15325008.2023.2246486.

[5] F. Pacaud, P. Carpentier, J.-P. Chancelier, and M. De Lara, "Optimization of a domestic microgrid equipped with solar panel and battery: Model Predictive Control and Stochastic Dual Dynamic Programming approaches," *Energy Systems*, vol. 15, no. 1, pp. 115–139, Feb. 2024, doi: 10.1007/s12667-022-00522-7.

[6] S. Hossain, N. K. Das, I. Chowdhury, and T. Ahmed, "MOSFET-based Three-Phase Inverter using Arduino - Applicable in Microgrid Systems," in *2021 6th International Conference for Convergence in Technology (I2CT)*, IEEE, Apr. 2021, pp. 1–5. doi: 10.1109/I2CT51068.2021.9417898.

[7] M. Omaña, M. Grossi, and C. Metra, "Early detection of photovoltaic system inverter faults," *Microelectronics Reliability*, vol. 135, p. 114594, Aug. 2022, doi: 10.1016/j.microrel.2022.114594.

[8] S. Rahimpour, H. Tarzamni, N. V. Kurdkandi, O. Husev, D. Vinnikov, and F. Tahami, "An Overview of Lifetime Management of Power Electronic Converters," *IEEE Access*, vol. 10, pp. 109688–109711, 2022, doi: 10.1109/ACCESS.2022.3214320.

[9] S. S. Ghosh *et al.*, "Wavelet-based rapid identification of IGBT switch breakdown in voltage source converter," *Microelectronics Reliability*, vol. 152, p. 115283, Jan. 2024, doi: 10.1016/j.microrel.2023.115283.

[10] S. S. Ghosh, S. Chattopadhyay, R. V. V. Krishna, R. K. Mahapatra, A. Das, and S. Das, "Measurement of Very Small Variation of Effective Resistance of MOSFET Deputed in Active Microgrid Inverter Operation," *Journal of Nano- and Electronic Physics*, vol. 16, no. 3, pp. 03029-1-03029–5, 2024, doi: 10.21272/jnep.16(3).03029.

[11] X. Guo, S. Sui, B. Wang, and W. Zhang, "A Current-Based Approach for Short-Circuit Fault Diagnosis in Closed-Loop Current Source Inverter," *IEEE Transactions on Industrial Electronics*, vol. 67, no. 9, pp. 7941–7950, Sep. 2020, doi: 10.1109/TIE.2019.2941143.

[12] S. F. Zarei, H. Mokhtari, and F. Blaabjerg, "Fault Detection and Protection Strategy for Islanded Inverter-Based Microgrids," *IEEE J Emerg Sel Top Power Electron*, vol. 9, no. 1, pp. 472–484, Feb. 2021, doi: 10.1109/JESTPE.2019.2962245.

[13] K. Nguyen-Duy, T.-H. Liu, D.-F. Chen, and J. Y. Hung, "Improvement of Matrix Converter Drive Reliability by Online Fault Detection and a Fault-Tolerant Switching Strategy," *IEEE Transactions on Industrial Electronics*, vol. 59, no. 1, pp. 244–256, Jan. 2012, doi: 10.1109/TIE.2011.2151818.

[14] M. T. Fard, J. He, and Z. Wang, "Fault Diagnosis and Fault-tolerant Operation of Current Source Inverter for Safety-Critical Applications," in *2020 IEEE Transportation Electrification Conference & Expo (ITEC)*, IEEE, Jun. 2020, pp. 925–929. doi: 10.1109/ITEC48692.2020.9161725.

[15] J. Zhang, H. Sun, Z. Sun, Y. Dong, and W. Dong, "Open-Circuit Fault Diagnosis of Wind Power Converter Using Variational Mode Decomposition, Trend Feature Analysis and Deep Belief Network," *Applied Sciences*, vol. 10, no. 6, p. 2146, Mar. 2020, doi: 10.3390/app10062146.

[16] S. S. Ghosh, S. Mukherjee, S. Chattopadhyay, and A. Das, "Premature Breakdown Identification in Photovoltaic Array Fed IGBT-based Voltage Source Converter," *Journal of Nano- and Electronic Physics*, vol. 15, no. 3, pp. 03016-1-03016–5, 2023, doi: 10.21272/jnep.15(3).03016.

[17] S. S. Ghosh, S. Chattopadhyay, and A. Das, "Fast Fourier transform and wavelet-based statistical computation during fault in snubber circuit connected with robotic brushless direct current motor," *Cognitive Computation and Systems*, vol. 4, no. 1, pp. 31–44, Mar. 2022, doi: 10.1049/ccs2.12041.

[18] S. Subhra Ghosh, S. Chattopadhyay, and A. Das, "Harmonics Monitoring for Winding Fault Diagnosis of Brushless DC motor," *IET Conference Proceedings*, vol. 2020, no. 8, pp. 164–169, Jun. 2021, doi: 10.1049/icp.2021.1137.

Chapter 7

FFT-based Investigation of GTO Switch Failure of the Voltage Source Inverter in a PV-Incorporated Microgrid

Abstract- On-grid and remote-grid microgrids (MGs) both use inverters incorporating gate turn-off thyristors (GTOs). GTOs' capacity to handle high currents and voltages is essential for energy conversion devices that need an elevated power level. Voltage source inverters (VSIs) employ GTOs to transform DC current to AC from energy storage devices and renewable energy. This chapter illustrates a method for figuring out the GTO switch fault (GSF) for a photovoltaic (PV) based three-phase (3Ph) VSI in an MG. In 3Ph VSI, an MG's GSF can lead to a number of problems, including reduced power output, safety concerns, fluctuating voltage and frequency, losing grid connectivity, overvoltage or overcurrent scenarios, and operational outages. An investigation on the 3Ph VSI's current at the output terminal using the fast Fourier transform (FFT) was carried out in order to identify GSF. The effects of GSF on the fundamental component of current (FCC), DC component (DCC), total harmonic distortion of current (THDC), and subharmonics (SHCs) have been investigated at different GSF levels. A successful detection of the GSF utilizing the most appropriate attribute has been attempted here. In addition, a GSF identifying technique has been recommended.

Keywords: Fast Fourier transform (FFT), fault recognition, GTO switch fault (GSF), microgrid (MG), voltage source inverter (VSI)

7.1 Introduction

MGs have emerged as a major development in modern power networks with the integration of renewable energy [1], [2]. In MGs, the PV system [3] is an essential component. They provide a clean, dependable, and sustainable source of electricity. MGs employ VSI [1] to increase their stability, efficiency, and ability to integrate renewable energy. MGs employ VSI [1] to increase their stability, efficiency, and ability to integrate renewable energy. In a wide range of applications, VSIs are utilized [4]. A VSI transforms the DC energy of renewable energies into more stable AC power. Microgrid inverters (MGIs) with GTO functionality are employed in both on-grid and remote-grid scenarios. In applications requiring considerable power, GTOs are suitable owing to their high voltage and current specifications [5].

I. Jlassi et al. suggested the failure detection of VSI's current sensors and IGBTs in [6]. The methods for detecting IGBT switch malfunctions in voltage source converters (VSCs) [3], [7] and in bidirectional MGI [8] were illustrated by S.S. Ghosh et al. An efficient defect diagnostic technique for current-source inverter's (CSI's) short circuit failures (SCFs) was introduced in [9] by X. Guo et al. The CSI's open circuit failure (OCF) detectable technique was illustrated by M. T. Fard et al. [10]. A novel method for detecting OCF within wind power converter's (WPC's) IGBT modules [11] was suggested by J. Zhang et al. Authors in [12] presented a SCF detecting technique within the islanded inverter.

However, very little emphasis was placed on identifying 3Ph VSI's GSF. This investigation recommends a distinctive technique for detecting GSF in MG's 3Ph VSI. Here, the GSF has been successfully recognized using the FFT. The GSF has been detected by utilizing the FFT on the recorded current at the output of the VSI to track a number of parameters, including the DCC, FCC, THDC, and SHCs.

7.2 Grid-Linked GTO-Based VSI

The Fig. 7.1 depicts a schematic of a grid-tied PV system, a maximum power point tracking (MPPT) controlled boost converter, a DC-link, and a VSI. For modelling objectives, a 100 kW PV system and a 25 kV utility grid are considered. The grid and PV system are interconnected by a VSI in conjunction with a boost converter. MPPT [3] enhances power production by continually modifying the operating point to harvest the most possible power from the PV system under fluctuating environmental circumstances. To provide customers with a reliable power source, the VSI controller keeps track of frequency and voltage [2], [13].

With a view to confirm GSF is present at VSI, its output current has been monitored thoroughly at normal and under varying percent of GSF (%GSF) scenarios.

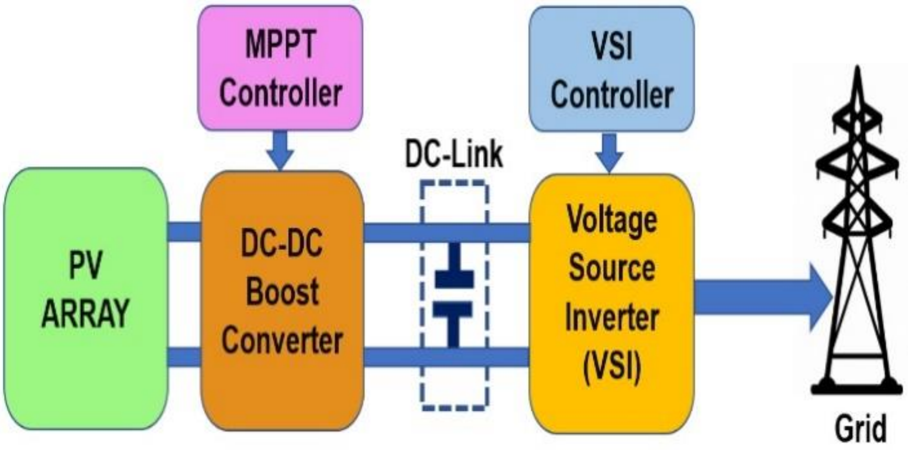

Fig. 7.1. Schematic of GTO-based grid-tied VSI

7.3 Problem Description

The GTO-based 3Ph VSI couples the grid and PV system in this investigation. The GSF of the VSI is considered in the fault assessment. The fault condition associated to GTO switches within the VSI circuits is termed GSF. In the course of the GSF, the effective resistance of the GTO-based switch varies considerably. The GSF is an occurrence that causes the circuit to open, adhering to a failure after a specific %GSF. A number of factors, including the overcurrent, overvoltage, aging, and overheating, can cause the GTO switch malfunctioning.

In the MG's VSI, a GTO switch defect may result in distortion of the output voltage, elevated harmonic content, instability of the system, or total inverter failure. Preventive steps, such as fault identification techniques, can be incorporated into VSI systems to mitigate the effects of GSF and safeguard the system's secure and reliable operation. Hence, an attempt was put forward in this work to identify the GSF of the VSI. Importantly, the system designer may decide the system's features and the severity of flaws.

7.4 FFT-Oriented Fault Detection

Electrical system breakdowns are frequently indicated by unexpected fluctuations in current, voltage, or frequency. Fourier transform (FT) or FFT may be used to detect these variances and uncover the system's fundamental issues [3], [8], [14], [15]. The FFT is suitable for processing and analyzing signals in real time, as it is efficiency-optimized and significantly faster than the standard FT [5].

To determine GSF in VSI, this study closely looks at the output current of the VSI. To identify the GSF problem, a number of variables related to the VSI's output current, including DCC, FCC, THDC, and SHCs, have been tracked using the FFT.

7.4.1 FFT-Oriented Pattern Synthesis

The obtained current was evaluated through FFT analysis at various %GSF and under normal operating circumstances. Fig. 7.2 displays the extracted output current. Fig. 7.3 exhibits the obtained output current's FFT window. Additionally, Fig. 7.4 illustrates the collected current's signal spectrum.

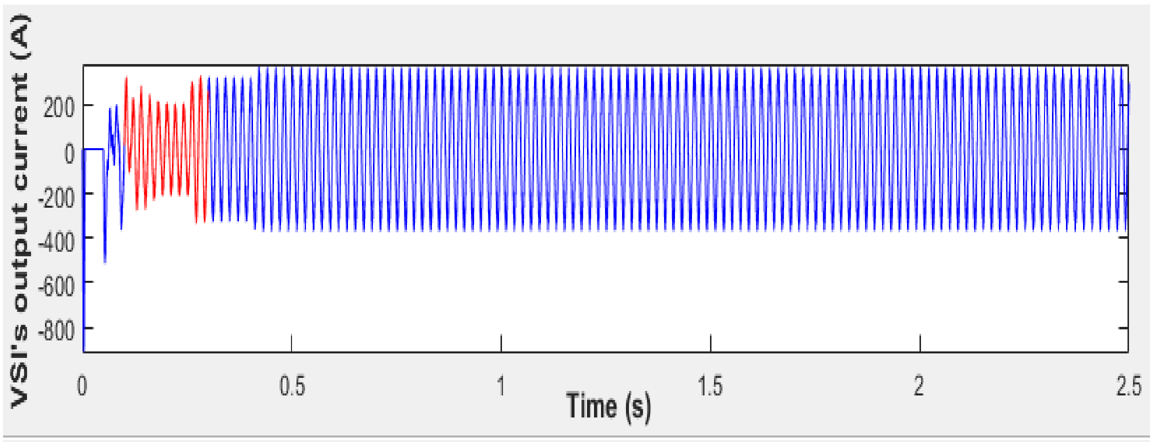

Fig. 7.2. Captured output current from VSI

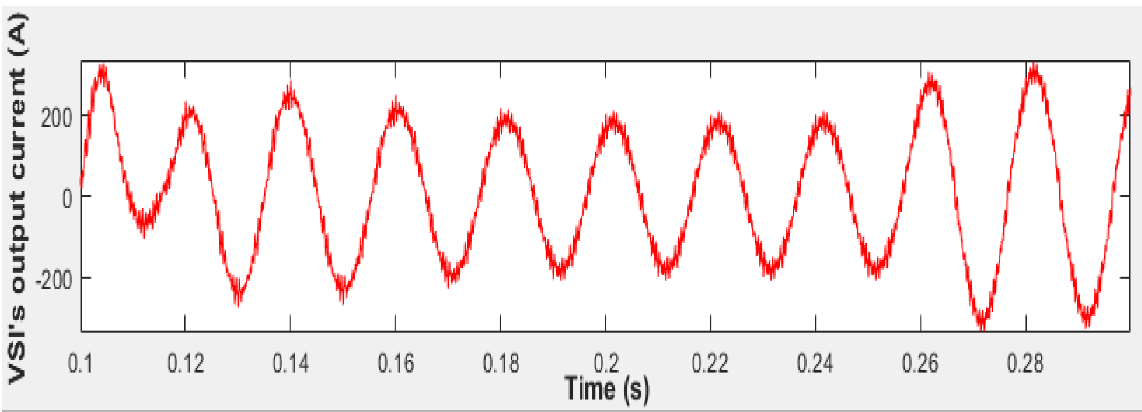

Fig. 7.3. VSI's output current's FFT window

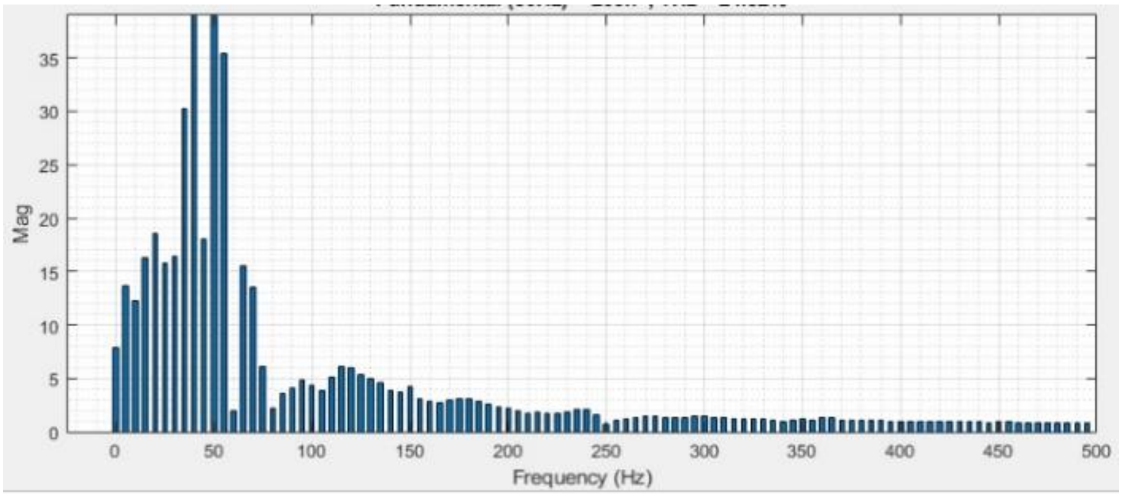

Fig. 7.4. Collected current's signal spectrum

7.4.2 Retrieval of Low-frequency Features

7.4.2.1 DCC Analysis

The DCC of VSI output currents over a range of %GSF has been retrieved using the FFT-based investigation. But according to Fig. 7.5, there is no statistically significant correlation between the DCC and %GSF. Consequently, GSF within the VSI could not be detected with this attribute.

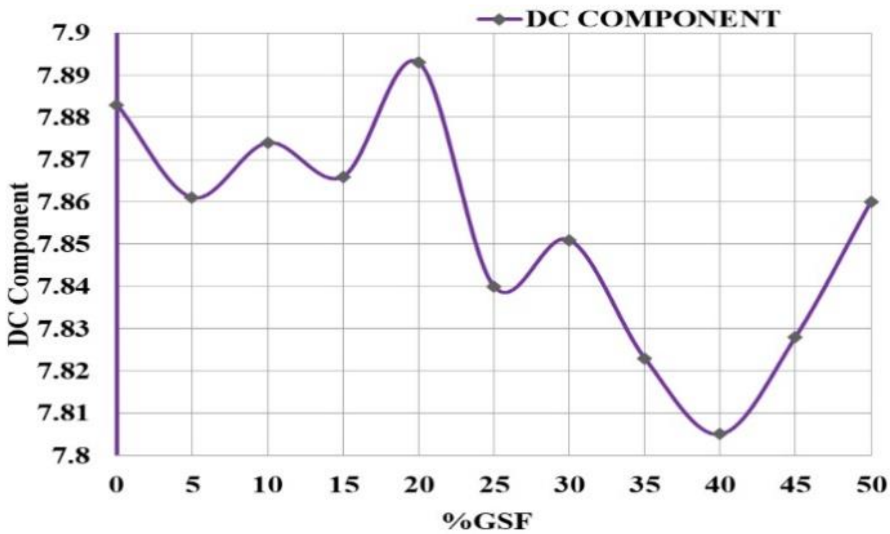

Fig. 7.5. DCC vs. %GSF

7.4.2.2 FCC Analysis

Using FFT, this analysis is performed to determine the FCC from the recorded output current. In this instance, the FFT findings have been utilized to retrieve the amplitude and phase data of the FCC. In Fig. 7.6, the FCC values that were computed for different %GSF values are shown.

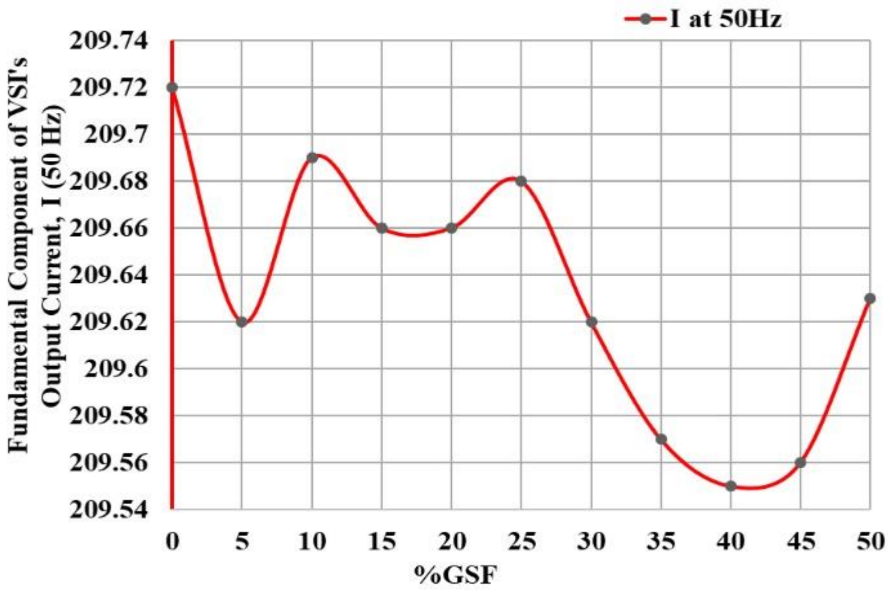

Fig. 7.6. FCC vs. %GSF

An analysis of Fig. 7.6 reveals that the FCC of the collected current and the various %GSF fails to sufficiently associate. Therefore, identifying GSF within the VSI using this attribute doesn't seem feasible.

7.4.2.3 THDC Analysis

THDC measures a signal's harmonic content [3], [8]. The current signal's THDC may be represented as follows [8]:

$$THDC(\%) = \frac{\sqrt{I_2^2+I_3^2+\cdots\cdots+I_n^2}}{I_1}\times 100 \qquad (7.1)$$

where,

I_1= root-mean-square (RMS) value for the fundamental frequency

$I_2, I_3, \cdots\cdots, I_n$= harmonic n's RMS value

As seen in Fig. 7.7, the THDC metrics during the GSF investigation derived for various %GSF in VSI are displayed. It demonstrates how variations in THDC(%) values are accompanied by variations in %GSF values. Moreover, the graphical analysis of Fig. 7.7 fails to sufficiently validate the GSF detection.

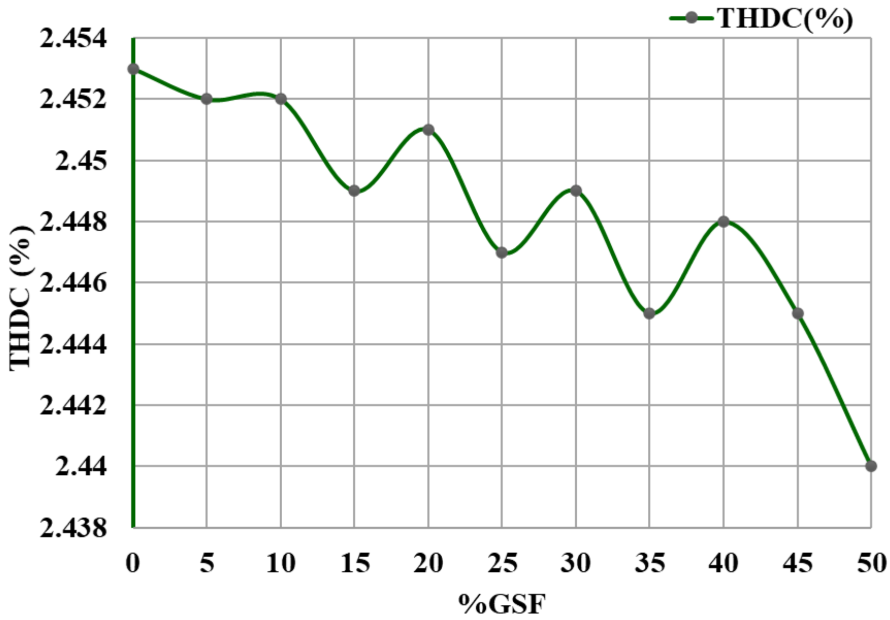

Fig. 7.7. THDC(%) vs. %GSF

7.4.2.4 SHC Analysis

The SHCs have also been computed from the VSI's output current. Every SHC in the acquired signal has been closely inspected for different %GSF values. Fig. 7.8 reveals how each of the SHCs' values alters while the %GSF rises. The SHC at 40 Hz, represented by I at 40 Hz, steadily declines unless the %GSF hits 20%, as can be seen by closely inspecting Fig. 7.8. Therefore, GSF within the VSI may be diagnosed using this statistical trait.

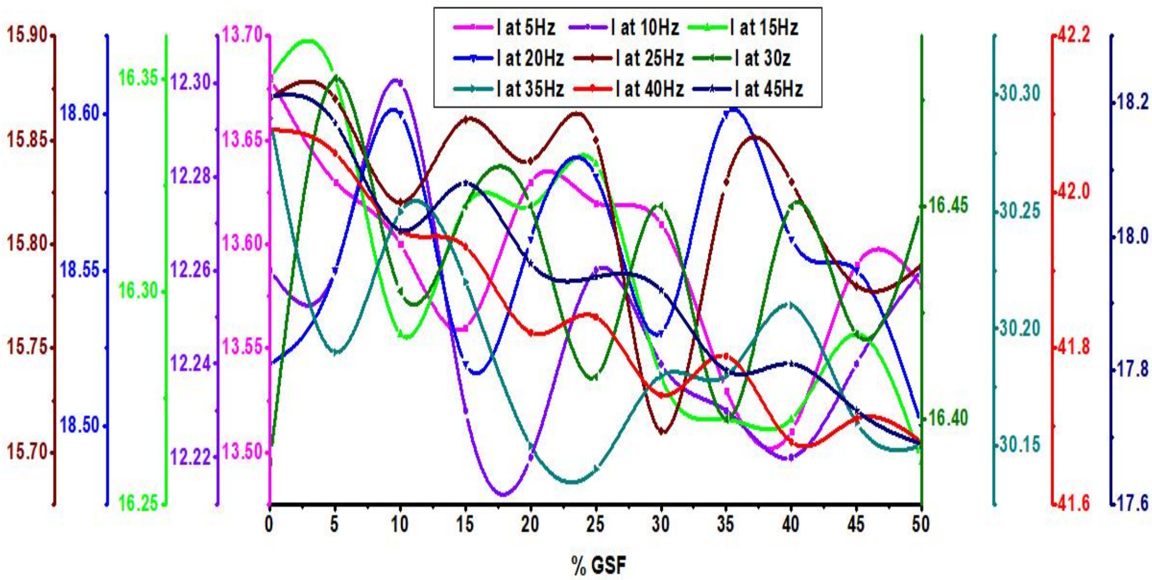

Fig. 7.8. SHCs vs. %GSF

7.5 Particular Outcomes and Discussion

The DCC, FCC, THDC, and SHCs of the collected current were among the several metrics that were carefully analyzed throughout the first phase of this investigation employing FFT. Meanwhile, the graphic analysis of Fig. 7.8 demonstrates, only the SHC at 40 Hz, represented as I at 40 Hz, progressively decreases unless the %GSF reaches 20%. Therefore, it is demonstrated that by continually monitoring the SHC at 40 Hz (I at 40 Hz), VSI's GSF up to 20% may be recognized. The suggested method may also be used for estimating the %GSF within the VSI.

7.6 Algorithm for GSF Detection

A GSF detection technique, as illustrated in Fig. 7.9 has been devised that resembles as follows:

(a) Record the current at the output of the VSI.
(b) Utilizing a sampling method, digitize the acquired current.
(c) Employing FFT on the digital data, assess SHC at 40 Hz (I at 40 Hz).
(d) Check for the GSF.

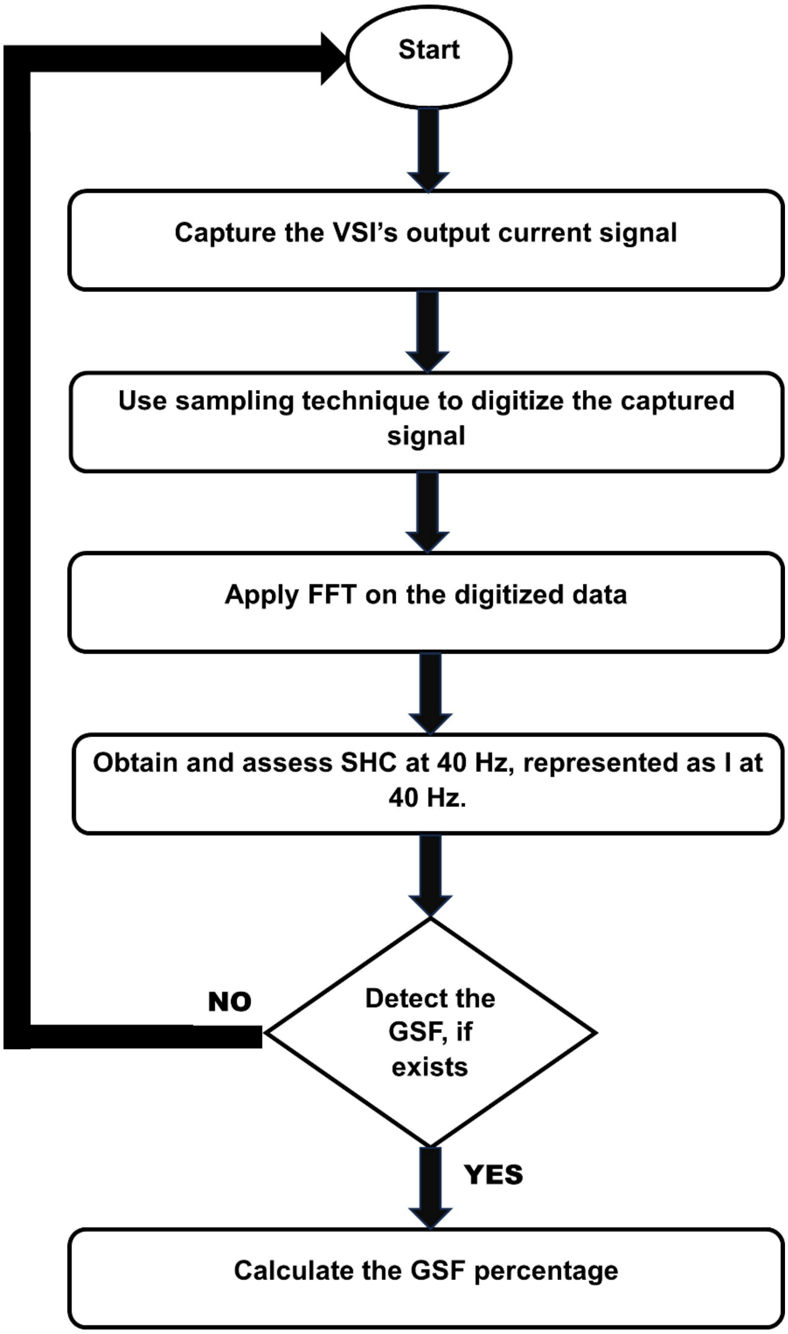

Fig. 7.9. Strategy for GSF detection

7.7 Comparative Analysis

Table 7.1 compares the suggested methodology with various types of inverter fault-detecting techniques.

Table 7.1. Comparison Analysis

Ref.	Detecting Faults	Capacity at Identifying Faults (%)
[6]	VSI's current sensors and IGBT fault	No
[9]	SCFs in CSIs	No
[10]	OCFs in CSIs	No
[11]	OCF in WPC’s IGBT modules	No
[12]	SCFs in inverter	No
Proposed method	VSI’s GSF	Yes

7.8 Conclusion

In this work, GSF in 3Ph VSI was identified by carrying out a statistical assessment utilizing FFT to evaluate the VSI’s output current under both optimal and defective situations. The values of the pertinent parameters have been observed to be fluctuating throughout the fault detection procedure.

The investigation additionally indicated that the %GSF in the VSI could be calculated using the approach suggested. Consequently, it has been found that this method successfully detects GSF (up to 20% GSF) in VSI by continually evaluating the SHC, I at 40 Hz. The particular results additionally demonstrate that the suggested method enables the determination of the %GSF.

References

[1] B. Keyvani-Boroujeni, B. Fani, G. Shahgholian, and H. H. Alhelou, “Virtual Impedance-Based Droop Control Scheme to Avoid Power Quality and Stability Problems in VSI-Dominated Microgrids,” *IEEE Access*, vol. 9, pp. 144999–145011, 2021, doi: 10.1109/ACCESS.2021.3122800.

[2] L. Xi *et al.*, "A Virtual Generation Ecosystem Control Strategy for Automatic Generation Control of Interconnected Microgrids," *IEEE Access*, vol. 8, pp. 94165–94175, 2020, doi: 10.1109/ACCESS.2020.2995614.

[3] S. S. Ghosh, S. Mukherjee, S. Chattopadhyay, and A. Das, "Premature Breakdown Identification in Photovoltaic Array Fed IGBT-based Voltage Source Converter," *Journal of Nano- and Electronic Physics*, vol. 15, no. 3, pp. 03016-1-03016–5, 2023, doi: 10.21272/jnep.15(3).03016.

[4] S. H. Latifi Majareh, F. Sedaghati, M. Hosseinpour, and S. R. Mousavi-Aghdam, "Design, analysis and implementation of a generalised topology for multilevel inverters with reduced circuit devices," *IET Power Electronics*, vol. 12, no. 14, pp. 3724–3731, Nov. 2019, doi: 10.1049/iet-pel.2019.0405.

[5] S. S. Ghosh, S. Chattopadhyay, S. Das, A. Das, G. R. K. Prasad, and A. Das, "Identification of GTO Switch Fault in Voltage Source Inverter in PV Integrated Microgrid," *Journal of Nano- and Electronic Physics*, vol. 16, no. 3, pp. 03022-1-03022–5, 2024, doi: 10.21272/jnep.16(3).03022.

[6] I. Jlassi, J. O. Estima, S. K. El Khil, N. M. Bellaaj, and A. J. M. Cardoso, "A Robust Observer-Based Method for IGBTs and Current Sensors Fault Diagnosis in Voltage-Source Inverters of PMSM Drives," *IEEE Trans Ind Appl*, vol. 53, no. 3, pp. 2894–2905, May 2017, doi: 10.1109/TIA.2016.2616398.

[7] S. S. Ghosh *et al.*, "Wavelet-based rapid identification of IGBT switch breakdown in voltage source converter," *Microelectronics Reliability*, vol. 152, p. 115283, Jan. 2024, doi: 10.1016/j.microrel.2023.115283.

[8] S. S. Ghosh, S. Chattopadhyay, S. H. Arigela, V. V. Kamesh, A. Das, and S. Das, "Expeditious Identification of IGBT Switch Fault in Bidirectional Microgrid Inverter Linked to Distributed Energy Resources," *Journal of Nano- and Electronic Physics*, vol. 16, no. 1, pp. 01019-1-01019–5, 2024, doi: 10.21272/jnep.16(1).01019.

[9] X. Guo, S. Sui, B. Wang, and W. Zhang, "A Current-Based Approach for Short-Circuit Fault Diagnosis in Closed-Loop Current Source Inverter," *IEEE Transactions on Industrial Electronics*, vol. 67, no. 9, pp. 7941–7950, Sep. 2020, doi: 10.1109/TIE.2019.2941143.

[10] M. T. Fard, J. He, and Z. Wang, "Fault Diagnosis and Fault-tolerant Operation of Current Source Inverter for Safety-Critical Applications," in *2020 IEEE Transportation Electrification Conference & Expo (ITEC)*, IEEE, Jun. 2020, pp. 925–929. doi: 10.1109/ITEC48692.2020.9161725.

[11] J. Zhang, H. Sun, Z. Sun, Y. Dong, and W. Dong, "Open-Circuit Fault Diagnosis of Wind Power Converter Using Variational Mode Decomposition, Trend Feature Analysis and Deep Belief Network," *Applied Sciences*, vol. 10, no. 6, p. 2146, Mar. 2020, doi: 10.3390/app10062146.

[12] S. F. Zarei, H. Mokhtari, and F. Blaabjerg, "Fault Detection and Protection Strategy for Islanded Inverter-Based Microgrids," *IEEE J Emerg Sel Top Power Electron*, vol. 9, no. 1, pp. 472–484, Feb. 2021, doi: 10.1109/JESTPE.2019.2962245.

[13] B. Keyvani-Boroujeni, G. Shahgholian, and B. Fani, "A Distributed Secondary Control Approach for Inverter-Dominated Microgrids With Application to Avoiding Bifurcation-Triggered Instabilities," *IEEE J Emerg Sel Top Power Electron*, vol. 8, no. 4, pp. 3361–3371, Dec. 2020, doi: 10.1109/JESTPE.2020.2974756.

[14] S. Subhra Ghosh, S. Chattopadhyay, and A. Das, "Harmonics Monitoring for Winding Fault Diagnosis of Brushless DC motor," *IET Conference Proceedings*, vol. 2020, no. 8, pp. 164–169, Jun. 2021, doi: 10.1049/icp.2021.1137.

[15] S. S. Ghosh, S. Chattopadhyay, and A. Das, "Fast Fourier transform and wavelet-based statistical computation during fault in snubber circuit connected with robotic brushless direct current motor," *Cognitive Computation and Systems*, vol. 4, no. 1, pp. 31–44, Mar. 2022, doi: 10.1049/ccs2.12041.

Chapter 8

FFT-based Monitoring of Snubber Quality Issue in Solid Oxide Fuel Cell-based Microgrid Inverters

Abstract- Deterioration of snubber functionality in the microgrid (MG) inverter is an acute concern. This chapter presents an innovative strategy for detecting nascent snubber-resistance faults (NSFs) in MG's 3-phase inverters (3PhIs) that is coupled to the solid-oxide fuel cell (SOFC). A study has been carried out to detect NSF by applying the fast Fourier transform (FFT) on the 3PhI's output current waveform. Investigations have been conducted on how NSF affects the inverter current's zero-frequency component (ZFC), fundamental component of current (FCC), total harmonic distortion factor (THDF), and components of sub-harmonic current (SCC). 3PhI's NSF has been effectively detected, according to the best-fit traits. In addition, an NSF identifying method has been recommended.

Keywords: Fast Fourier transform (FFT), fault recognition, microgrid inverter, snubber fault.

8.1 Introduction

Renewable energy systems predominantly employ grid-tied 3PhIs. These days, fuel cells can effectively address the major ecological issues [1]. By directly converting chemical energies, SOFC stacks generate electrical power [2]. The most crucial element of a grid-dependent integrated electrical system is the grid inverter [3]. Meanwhile, one of the parts that fails the most frequently is the inverter [1]. To increase the dependability of inverters, a method for identifying and diagnosing problems is necessary.

S.S. Moosavi et al. devised methods for identifying open circuit (OC) issues in the inverter of a battery-powered vehicle [4]. The dual-inverter drive's OC switch fault has been demonstrated by S. Yang et al. [5]. The authors in [6] suggested a method for detecting short circuit (SC) defects in islanded inverters. The authors [7], [8], [9] developed an OC defect detection method in the cascaded H-bridge multilevel inverters (CHMLIs) and voltage source inverters (VSIs) based on artificial neural networks (ANNs). The approach

[10] for identifying OC and SC flaws in multilevel inverters (MLIs) was introduced by S. Khomfoi et al. In [11], [12], [13], the random forest (RF) approach has been adopted to identify OC flaws in the three-phase H-bridge inverter (3PhHBI) and neutral-point-clamped (NPC) inverters. The authors suggested the OC problem identification techniques for H-bridge MLIs [14], 3-phase VSIs [15], and NPC MLIs [16]. Techniques for different MG inverters' OC fault detection were demonstrated in [17], [18], [19], [20], [21], [22] through the adoption of convolutional neural networks (CNNs), support vector machines (SVMs), clustering, continuous wavelet transform (CWT), and model reference adaptive system (MRAS).

Nonetheless, there hasn't been any substantial research on 3PhI NSF detection in MG. The MG 3PhI NSF identification approach is recommended in this chapter. The 3PhI's current signals have been utilized to diagnose NSF. Using the FFT on the current recorded at the 3PhI's output, the NSF has been identified by monitoring several parameters, such as the output current's zero frequency component (ZFC), fundamental component of current (FCC), total harmonic distortion factor (THDF), and components of sub-harmonic current (SCC).

8.2 3PhI Powered by a Grid-tied SOFC

In this section Fig. 8.1 depicts a schematic representation of the grid-linked SOFC stacks, voltage regulator (DC-DC), and 3PhI. A SOFC stack connected to a microgrid via an insulated gate bipolar transistor (IGBT)-based 3PhI makes up the system. Through a voltage regulator (DC-DC), the 3PhI's input voltage was altered with the primary goal of changing the voltage level.

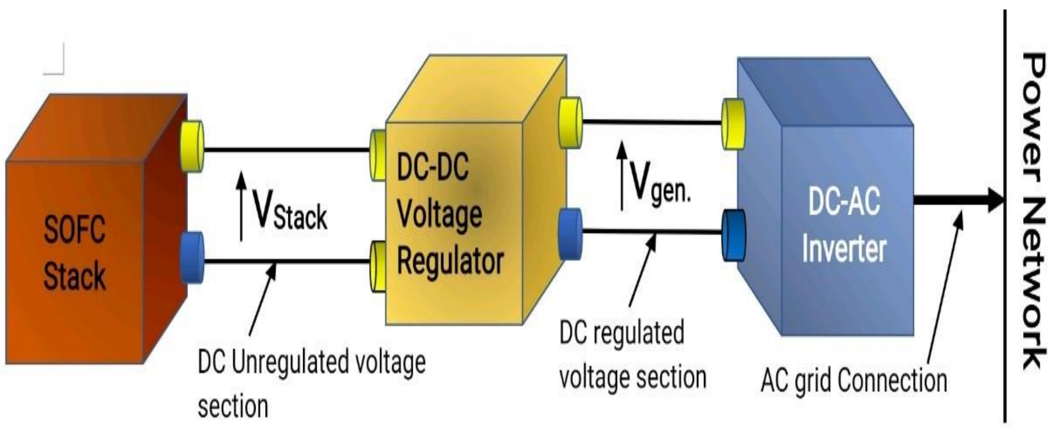

Fig. 8.1. Schematic of IGBT-based grid-tied 3PhI

To validate the presence of NSF at 3PhI, the acquired current was evaluated in the standard and various percentage of NSF (%NSF) instances.

8.3 Analysis of the Snubber Circuit Issue

The 3PhI NSF may be found using the method suggested in this chapter. Snubbers are important components of power electronics. A switching device may experience unexpected voltage spikes that cause sudden disruptions and perhaps damage the equipment [23], [24]. Snubbers enhance switching frequencies while improving the circuit's performance as well as efficacy and reliability.

Hence, an attempt was put forward in this work to identify the NSF of the 3PhI. In this work, the %NSF of the 3PhI has been altered by up to 40% for the NSF diagnosis.

8.4 FFT-Oriented NSF Identification

A great technique for comprehending periodic waveforms is the Fourier transform (FT) [24]. FT and FFT are used to convert a signal between the frequency and time domains [24]. Due to its efficiency optimization and substantial speed over the regular FT, the FFT is appropriate for real-time signal processing and analysis.

The obtained current was assessed here in both standard and different %NSF situations in order to confirm the existence of NSF at 3PhI. To identify the NSF problem, a number of variables related to the 3PhI's output current, including ZFC, FCC, THDF, and SCCs, have been tracked using the FFT.

8.4.1 FFT-Oriented Pattern Generation

The acquired current was evaluated through FFT analysis at various %NSF and under normal operating events. Fig. 8.2 displays the extracted output current. Fig. 8.3 exhibits the obtained output current's FFT window. Additionally, Fig. 8.4 illustrates the collected current's signal spectrum.

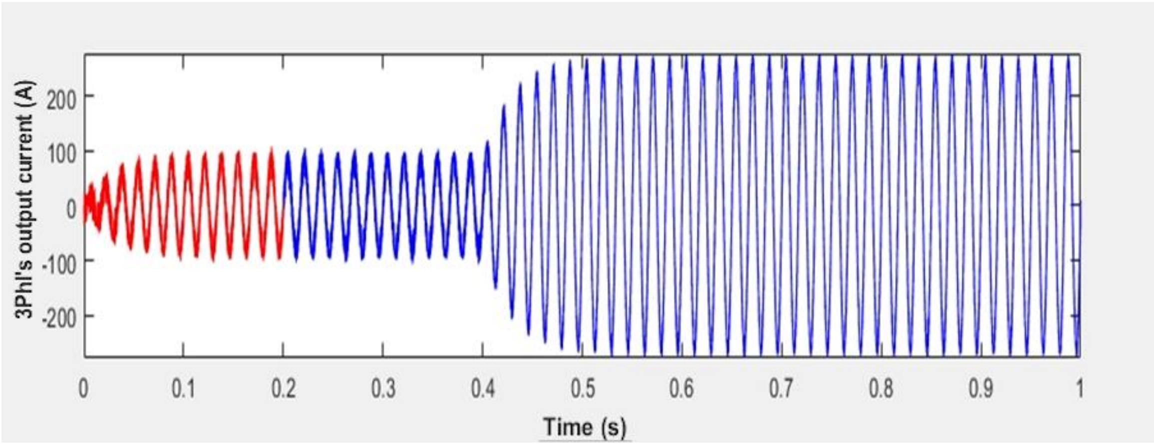

(a) at typical condition

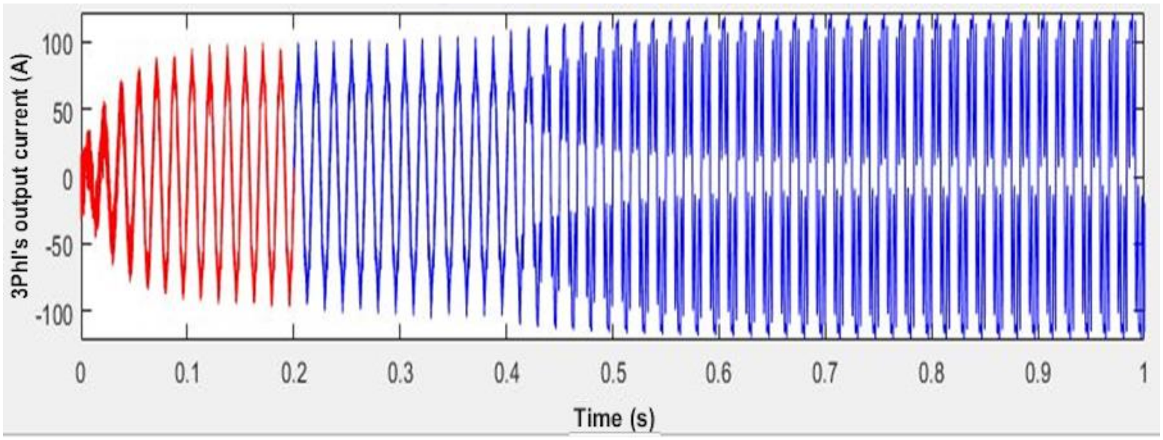

(b) at 25% of NSF

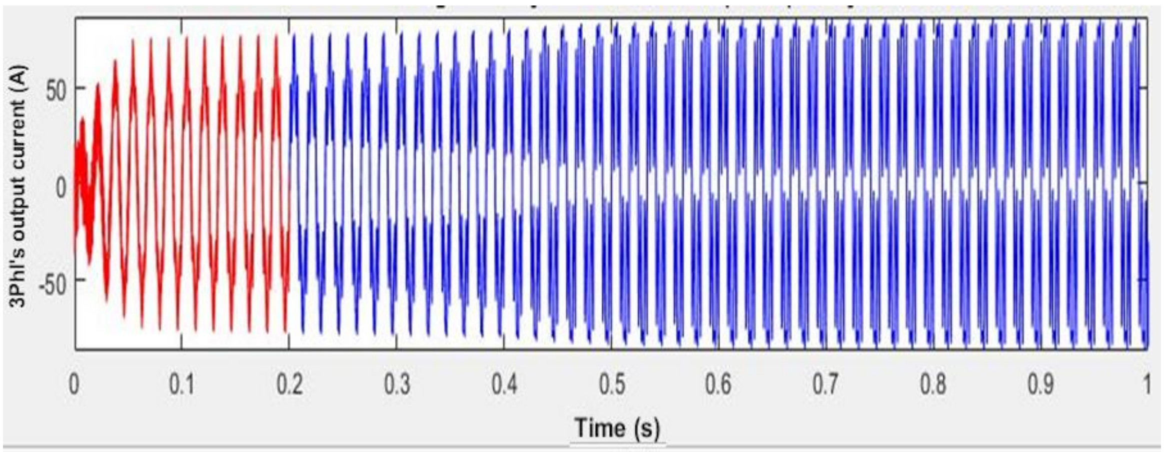

(c) at 35% of NSF

Fig. 8.2. Acquired output current from 3PhI at various conditions

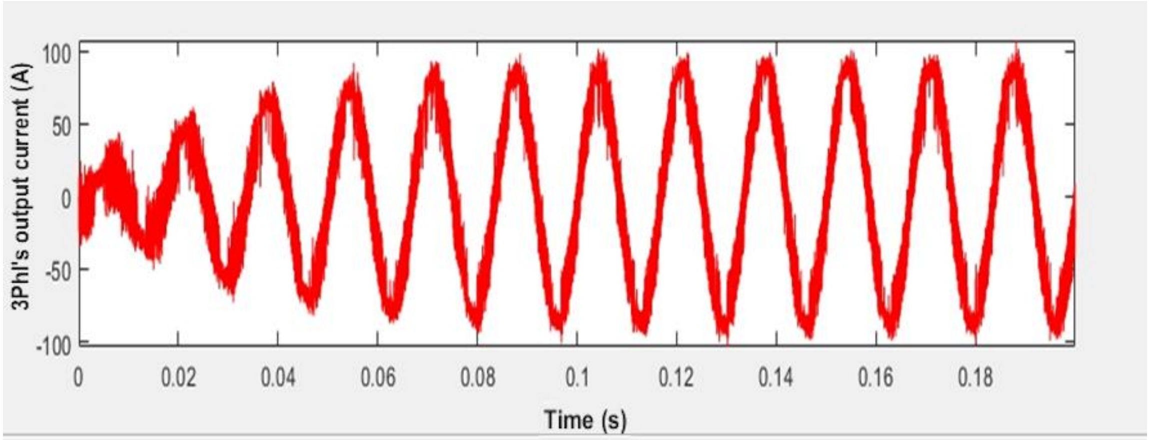

(a) at typical condition

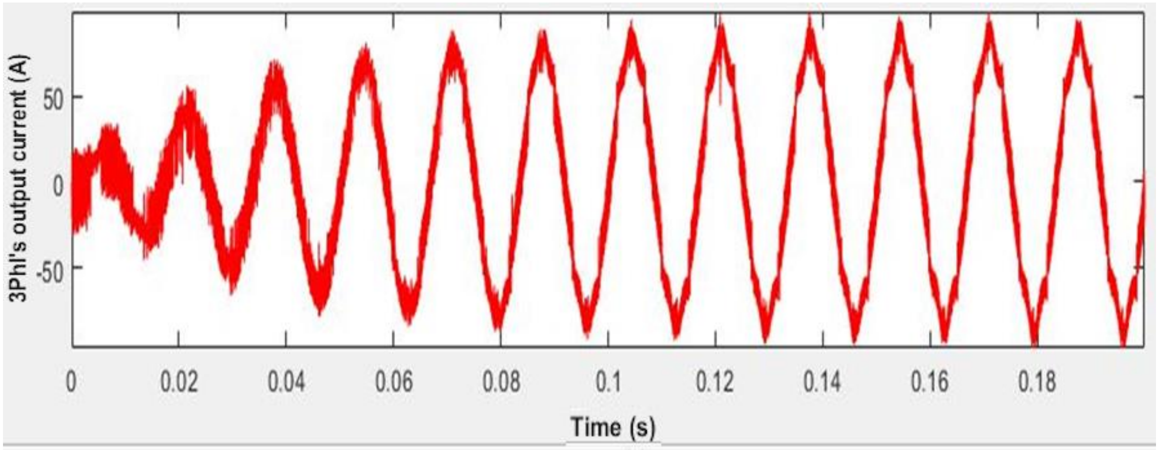

(b) at 25% of NSF

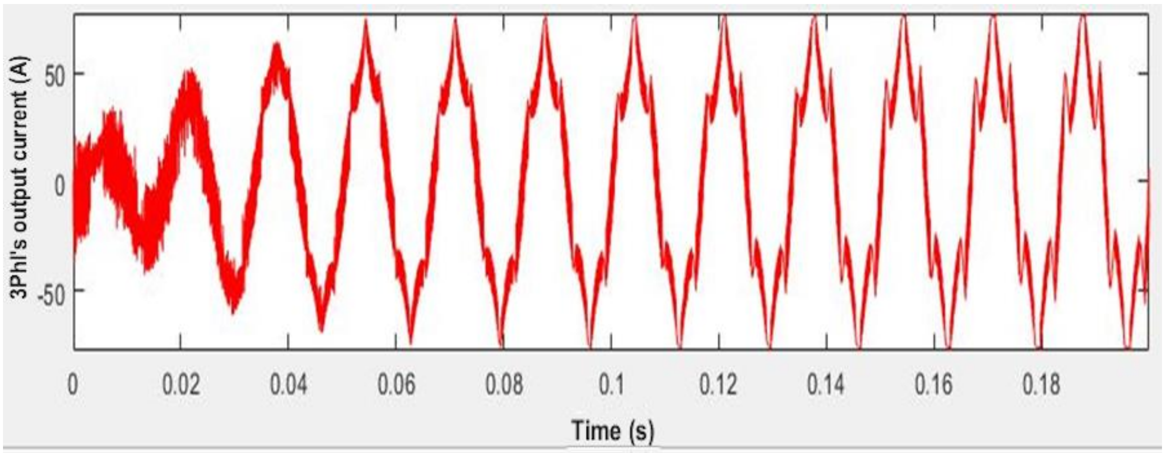

(c) at 35% of NSF

Fig. 8.3. FFT window of 3PhI's output current at various conditions

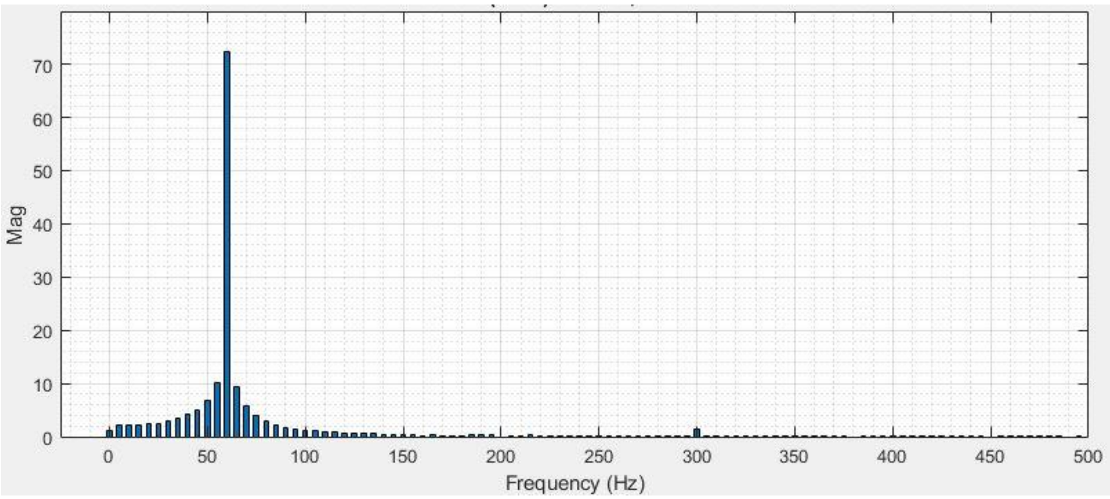

(a) at typical condition

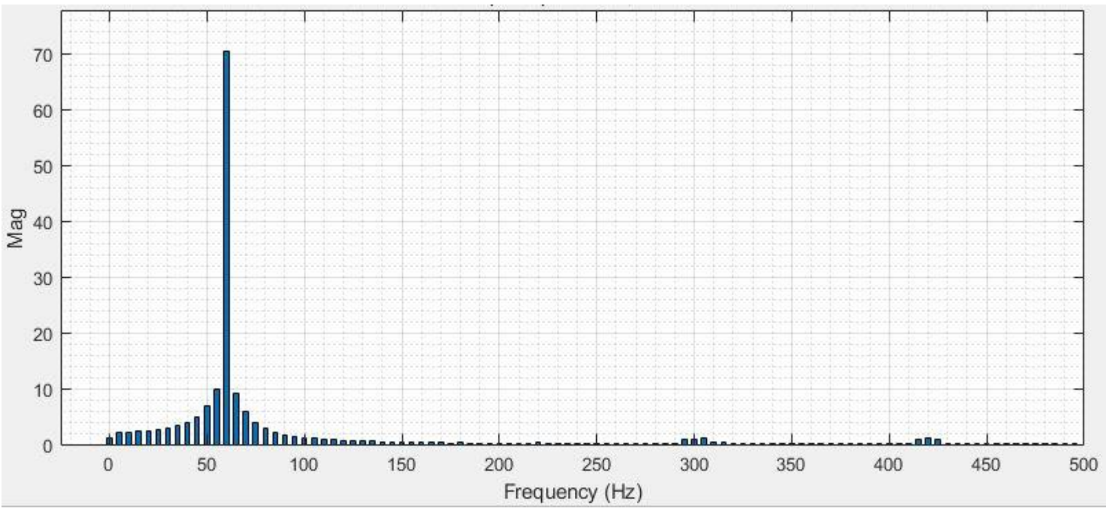

(b) at 25% of NSF

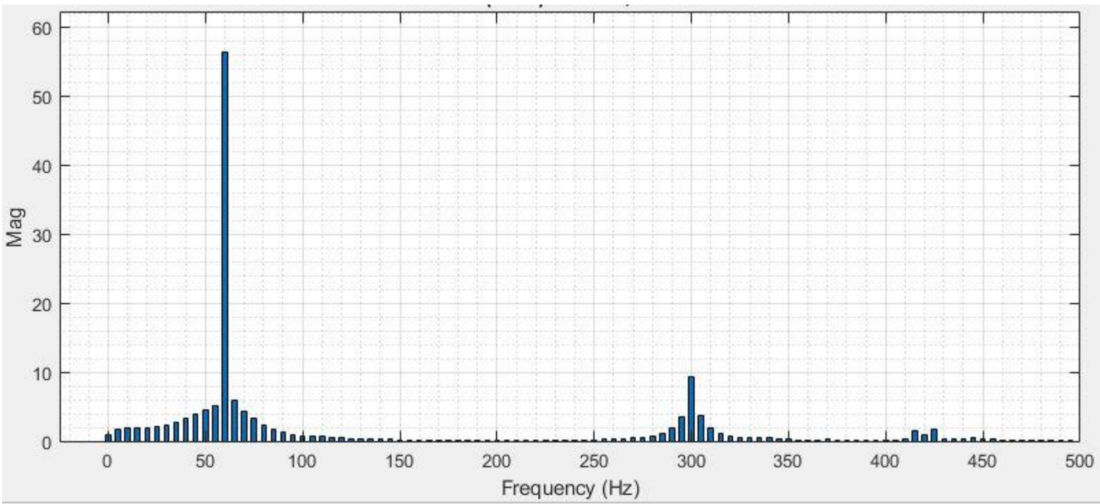

(c) at 35% of NSF

Fig. 8.4. 3PhI's collected currents signal spectra at various conditions

8.4.2 Retrieval of Zero Frequency and Different Fractional Harmonics

8.4.2.1 ZFC Analysis

The ZFC across various %NSF levels was derived by FFT-based computation of the recorded 3PhI's current signal. However, according to Fig. 7.5, there is no statistically significant correlation between the ZFC and %NSF. As an outcome, NSF within the 3PhI could not be revealed utilizing this feature.

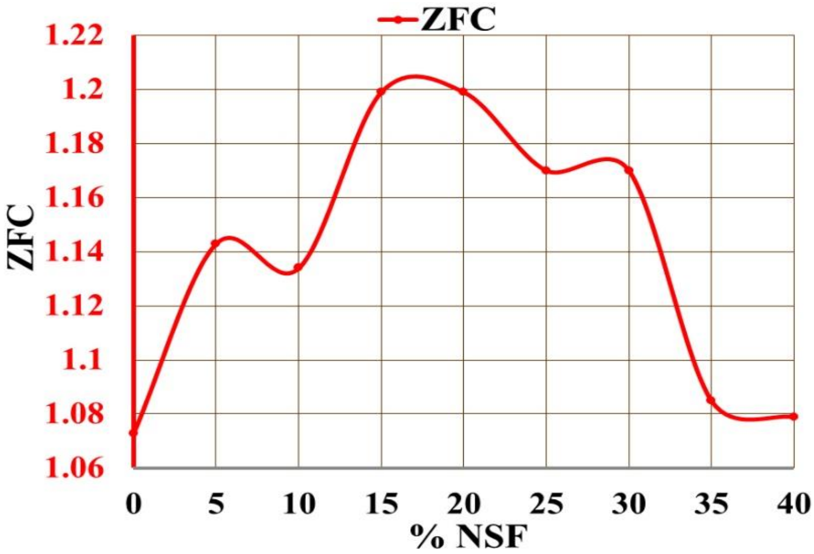

Fig. 8.5. ZFC vs. %NSF

8.4.2.2 FCC Analysis

Here, the FCC of the 3PhI's current is investigated through FFT. In Fig. 8.6, the FCC values that were computed for different %NSF values are shown.

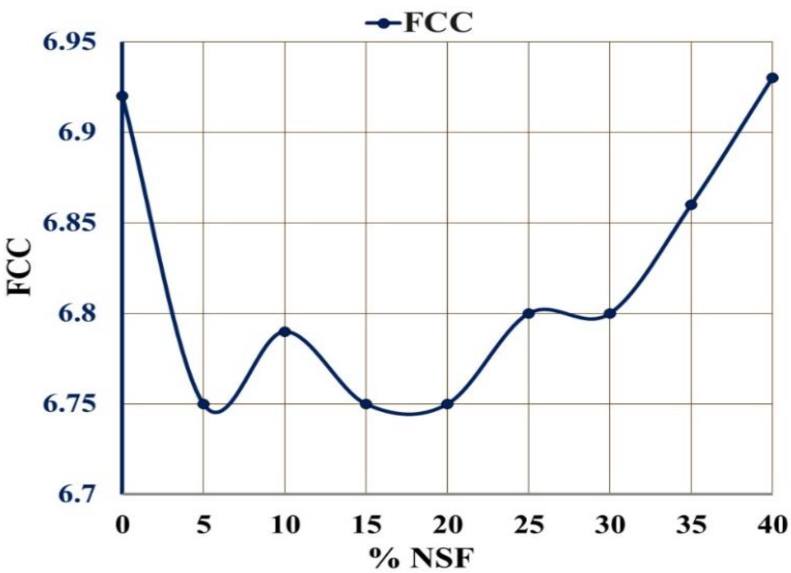

Fig. 8.6. FCC vs. %NSF

It is apparent that the FCC fluctuates along with the %NSF. It does not, however, provide a suitable pattern of association between the 3PhI's FCC and the %NSF values.

8.4.2.3 THDF Analysis

THDF measures a signal's harmonic content. The current signal's THDF may be represented as follows [24]:

$$THDF = \frac{\sqrt{\sum_{n=2}^{\infty} I_{n\_rms}^{2}}}{I_{f\_rms}} \qquad (8.1)$$

where,

I_{f_rms}= root-mean-square (RMS) value for the fundamental frequency

I_{n_rms}= harmonic n's RMS value

The Fig. 8.7 exhibits the retrieved THDF values for the determination of NSF at different % NSF in the 3PhI. As can be observed in Fig. 8.7, changes in the %NSF are accompanied by fluctuations in the THDF values. However, there did not exist an obvious relationship between shifts in the %NSF and alterations in the THDF.

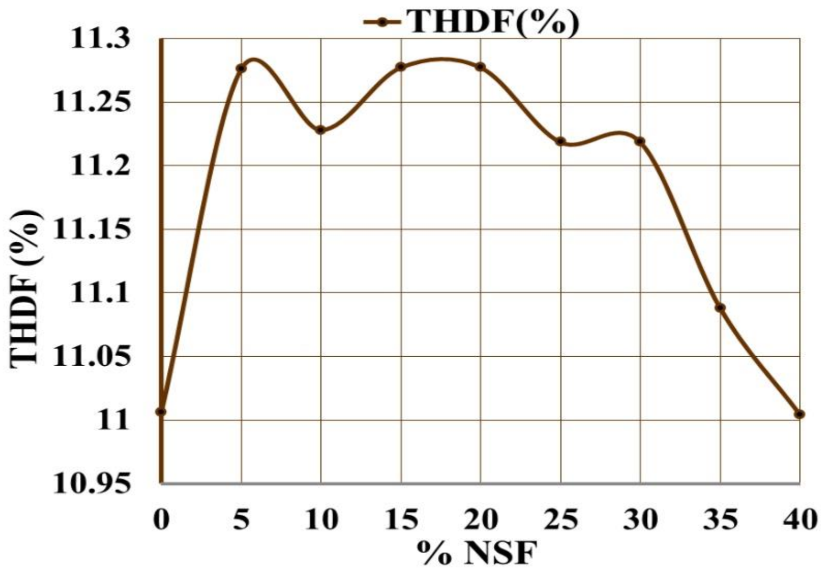

Fig. 8.7. THDF vs. %NSF

8.4.2.4 SCC Analysis

The SCCs have also been computed from the 3PhI's output current. Different SCCs in the acquired signal have been closely evaluated for different %NSF values. The values of each SCC change when the %NSF grows larger, as shown in Fig. 8.8.

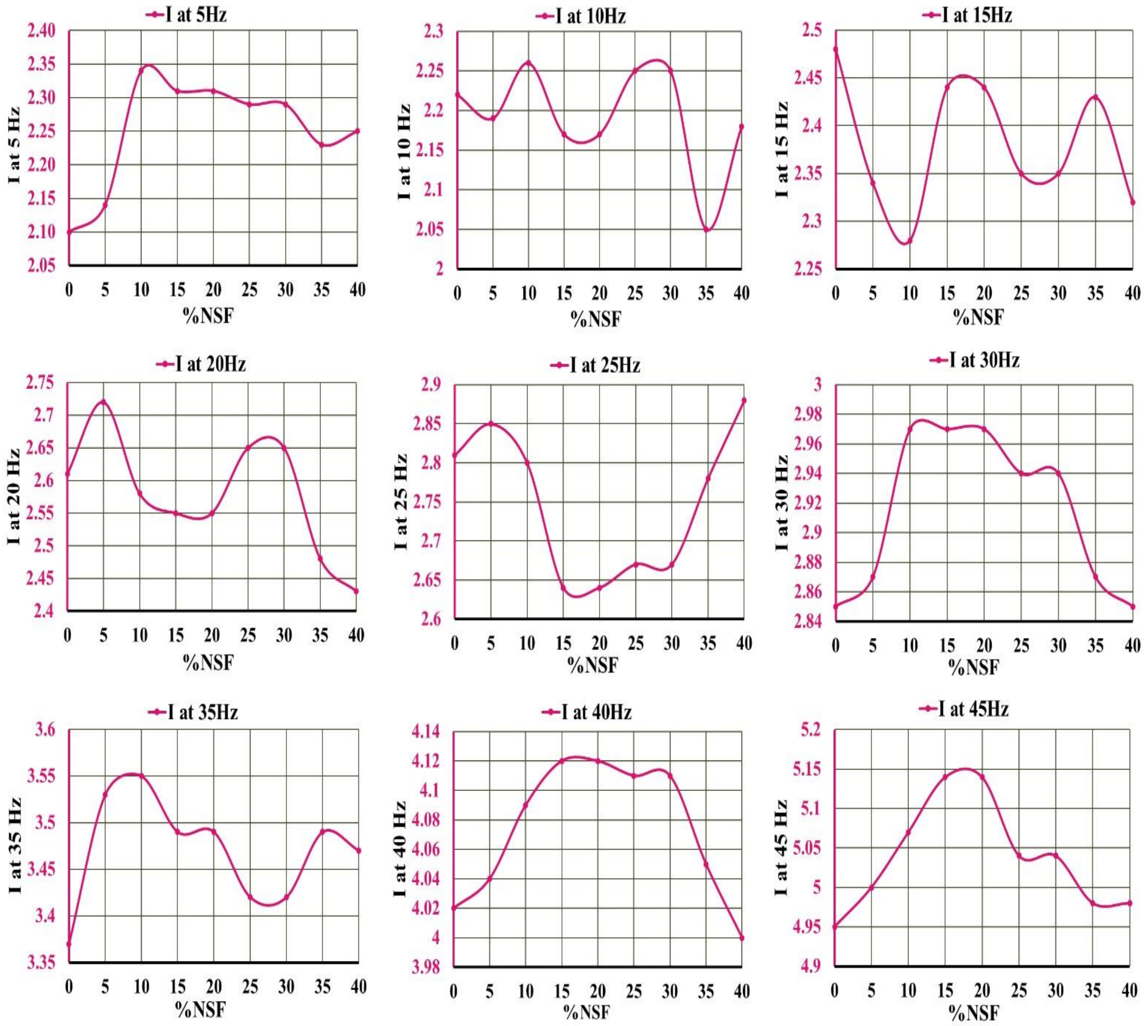

Fig. 8.8. SCC vs. %NSF

8.5 Analysis and Extraction of Features

The DCC, FCC, THDF, and SCCs of the collected current were among the several metrics that were carefully inspected throughout the first phase of this investigation.

Additionally, for all SCCs at different %NSF, the mean and standard deviation (MSD) values exhibited the highest degree of variation, as depicted in Fig. 8.9.

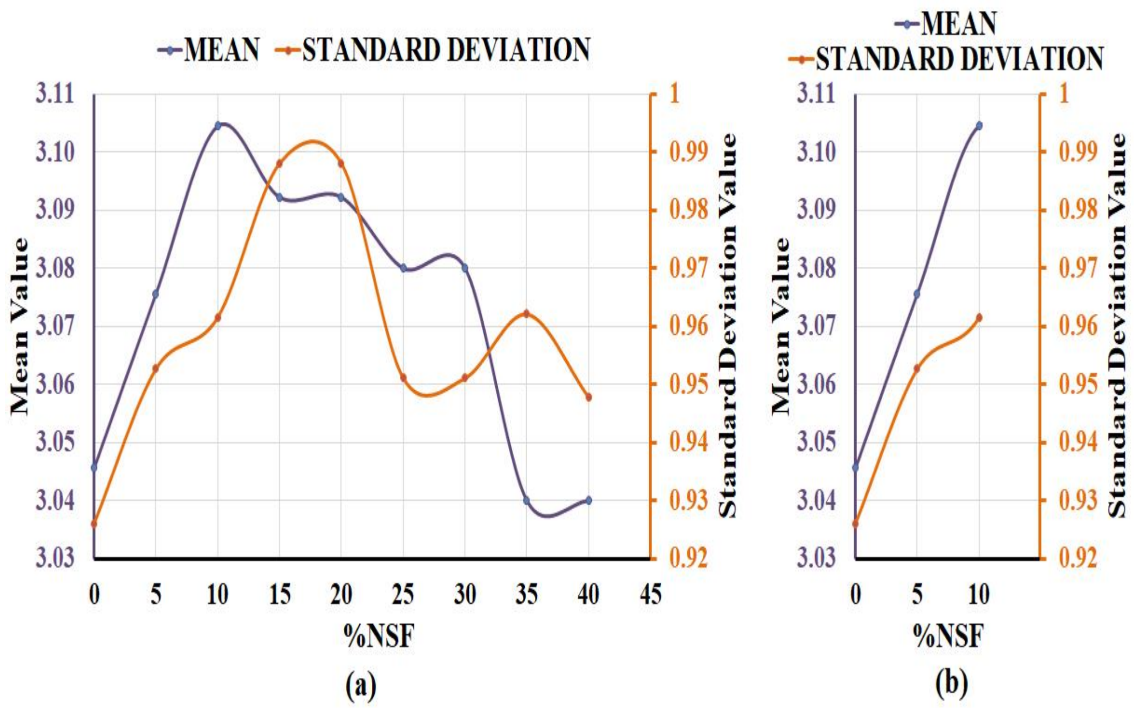

Fig. 8.9. SCC's MSD vs. %NSF - (a) till 40% NSF, and (b) till 10% NSF

Further Fig. 8.9 reveals that the suggested approach may also be implemented for estimating the NSF of only about 10% within the 3PhI.

8.6 Algorithm for NSF Detection

An NSF detection technique, as presented in Fig. 8.10 has been devised that resembles as follows:

(e) Record the current at the output of the 3PhI.

(f) Utilizing a sampling method, digitize the acquired current.

(g) Employing FFT on the digital data, obtain and assess the MSD of SCCs.

(h) Check for the NSF.

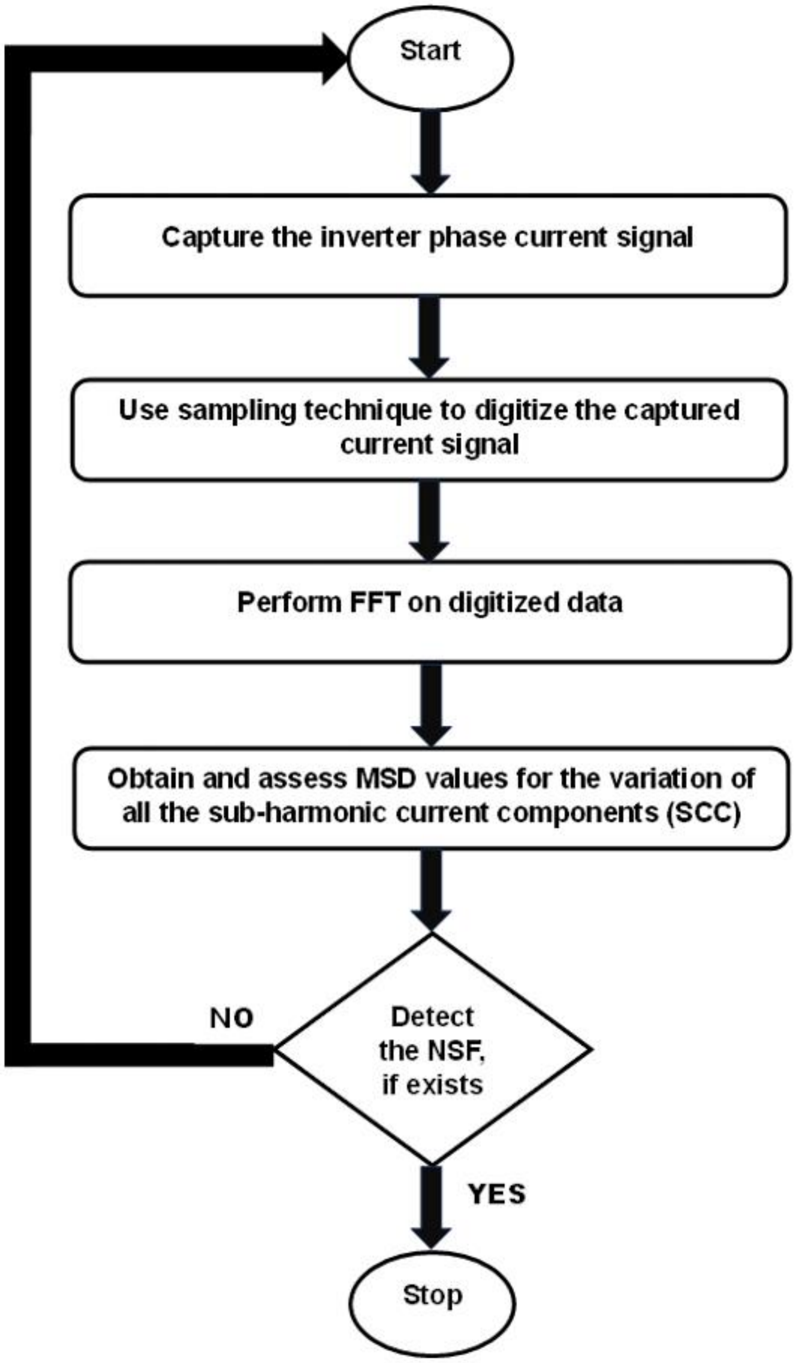

Fig. 8.10. Strategy for NSF detection

8.7 Validation on the Experimental Test Bench

The real-world cases executed on the testing facility have also been used to validate the proposed method, exhibited schematically in Fig. 8.11.

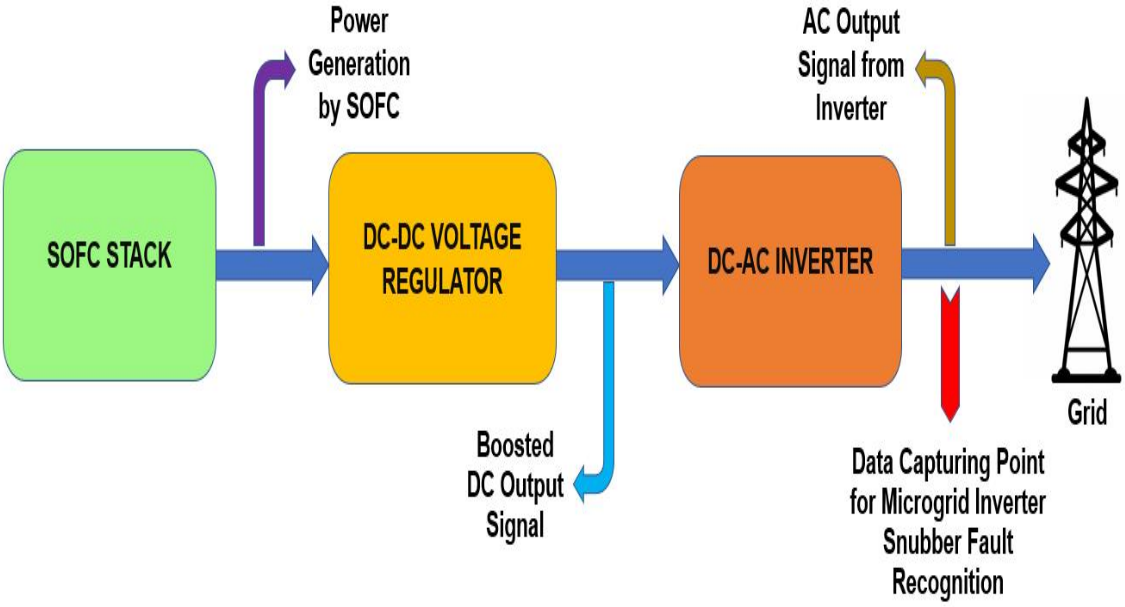

Fig. 8.11. Testing facility

The system's modelling specifications are listed in Table 8.1. Table 8.2 summarizes comparative statistics of the test outcomes of three distinct actual instances investigated with different NSF levels. The purpose of the study was to identify the best technique for detecting NSF.

Table 8.1. Modelling specifications

Parameters	Specifications
3PhI output voltage	440 V (phase-voltage)
Voltage regulator (DC-DC) capacitance	5000 μF
Voltage regulator (DC-DC) inductance	1 mH
Voltage regulator (DC-DC) reference voltage	660 V
Ohmic losses	0.126 ohm
SOFC stack's cell counts	384
Rated voltage of the SOFC stack	438 V
Rated power of the SOFC stack	50 kW
Molar gas constant	8.314 kJ/kmol K
Faraday's constant	96487 C/mol
Absolute temperature	1273 K
Load resistance's equivalent value	8.712 ohm

In this specific scenario, the error rate in percent was computed employing the formula [24] outlined below:

$$Error = \left(\frac{F_{NSF} - f_{NSF}}{f_{NSF}} \right) \times 100\% \qquad (8.2)$$

where,

F_{NSF} = %NSF value (known);

f_{NSF} = %NSF calculated using ZFC, FCC, THDF, or MSD values

Table 8.2. Comparative statistics of the test outcomes of three distinct actual instances

Parameters	**Case-1**	**Case-2**	**Case-3**
%NSF (known)	2%	7%	9%
%NSF calculated using ZFC	ZFC= 1.11	ZFC= 1.14	ZFC= 1.13
	%NSF= 2.15%	%NSF= 7.20%	%NSF= 8.70%
	Error= -7.5%	Error= -2.85%	Error= 3.33%
%NSF calculated using FCC	FCC= 6.825	FCC= 6.760	FCC= 6.777
	%NSF= 2.13%	%NSF= 6.85%	%NSF= 8.72%
	Error= -6.5%	Error= 2.14%	Error= 3.11%
%NSF calculated using THDF	THDF= 11.125	THDF= 11.275	THDF= 11.231
	%NSF= 1.85%	%NSF= 7.35%	%NSF= 9.30%
	Error= 7.5%	Error= -5%	Error= -3.33%
%NSF calculated using Mean (M) values	M= 3.06	M= 3.09	M= 3.12
	%NSF= 2.05%	%NSF= 7.10%	%NSF= 8.90%
	Error= -2.5%	Error= -1.43%	Error= 1.11%
%NSF obtained using Standard Deviation (SD) values	SD= 3.05	SD= 3.68	SD= 3.07
	%NSF= 2.06%	%NSF= 7.12%	%NSF= 8.88%
	Error= -2.5%	Error= -1.71%	Error= 1.33%

The statistical comparisons in Table 8.2 and the error rate comparisons in Fig. 8.12 make it evident that by utilizing the MSD data of SCCs is the only viable method of achieving the most optimal outcome in %NSF investigation.

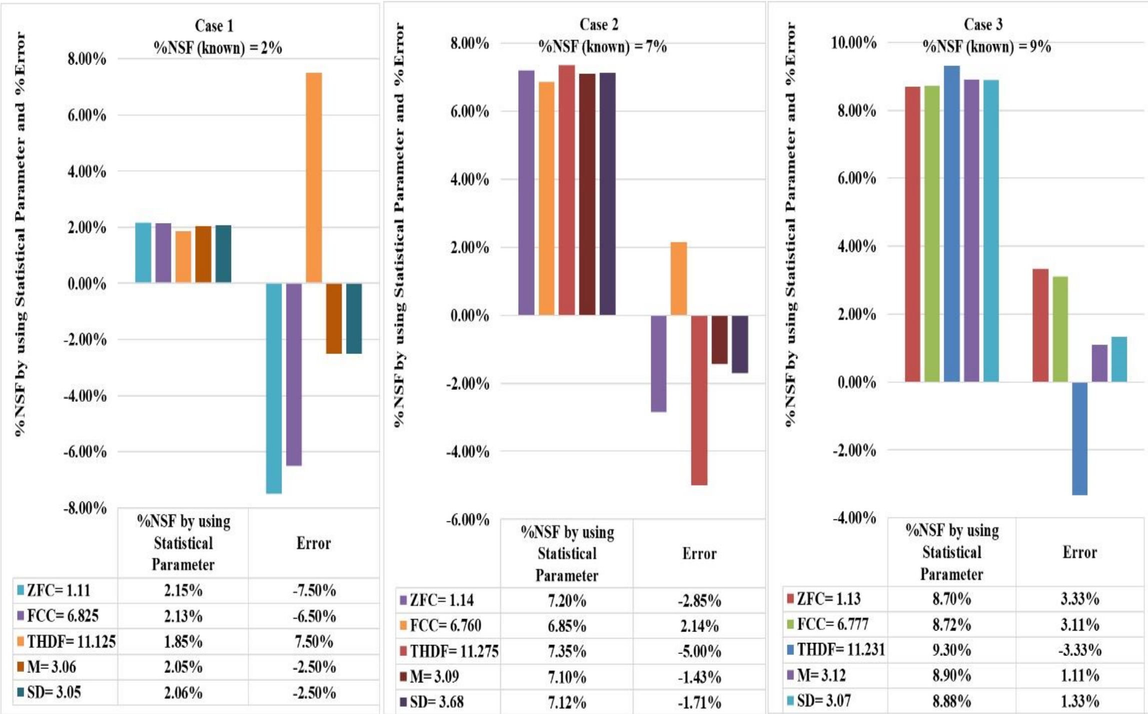

Fig. 8.12. Error rate comparisons

Consequently, after an exhaustive evaluation of the outcomes of the FFT-based investigation, it emerged that MSD data specifically seemed to be quite effective for identifying NSF. The suggested NSF recognition approach has additionally been implemented on gate turnoff (GTO) thyristors, thyristor-based inverters, and metal-oxide-semiconductor field-effect transistors (MOSFETs). The results show that the statistical characteristics of NSF are essentially unchanged. Hence, if an NSF occurs, regardless of the MG inverter, the proposed approach may be employed for NSF identification.

8.8 Comparative Analysis and Discussion

Table 8.3 summarizes the findings of comparisons among the suggested study alongside additional comparable approaches.

Table 8.3. Comparative Analysis

Reference	**Observed Parameters / Fault Detection Method**	**Identifying Faults in Inverters**	**Percent of fault detection capacity (%)**
[1]	Line and phase voltage deviation	3PhI' IGBT and current sensor defects	No
[5]	Current signal-oriented fault detection	OC faults in dual-inverter drive	No
[6]	Negative-sequence resistance	SC defects in islanded inverters	No
[7]	ANN	OC defects in CHMLI	No
[8]	ANN	OC in VSI	No
[9]	ANN	OC defect in CHMLI	No
[10]	ANN	OC and SC failures in CHMLI	No
[11]	RF	IGBT OC defects in NPC inverters	No
[12]	RF	OC failure in 3PhI	No
[13]	RF	OC failure in 3PhI	No
[14]	SVM	OC failure in MLI	No
[15]	Decision Tree	OC failures in VSI	No
[16]	Clustering	OC fault in NPC MLI	No
[17]	CNN	OC fault in 3PhI	No
[18]	CNN	OC fault in 3PhI	No
[19]	SVM	OC fault in 3PhI	No
[20]	Clustering	OC fault in 3PhI	No
[21]	CWT	OC fault in CHMLI	No
[22]	MRAS	OC defects in VSI	No
[25]	FFT	IGBT switch issue	No
[26]	DWT	IGBT switch issue	Yes
Proposed Method	FFT	NSF in 3PhI	Yes

8.8 Conclusion

In this work, an FFT-based analytical study of the inverter's output current has been performed in an attempt to diagnose NSF that manifests in 3PhI. For the purpose of identifying NSF, many statistical metrics have been observed. The values of the pertinent parameters have been observed to be fluctuating throughout the fault detection procedure. The variation in MSD levels for the different SCCs for different %NSF implies that earlier NSF detection in the inverter is definitely possible.

The investigation additionally indicated that the %NSF in the 3PhI could be obtained using the approach proposed. GTOs, MOSFETs, and thyristor-based inverters have also been made use of the NSF detection study. The results show that the statistical characteristics of NSF are essentially unchanged. Therefore, by using the recommended method, the NSF within any inverter may be found earlier by continual tracking of readings.

References

[1] Z. Li *et al.*, "A Fast Diagnosis Method for Both IGBT Faults and Current Sensor Faults in Grid-Tied Three-Phase Inverters With Two Current Sensors," *IEEE Trans Power Electron*, vol. 35, no. 5, pp. 5267–5278, May 2020, doi: 10.1109/TPEL.2019.2946692.

[2] M. S. Arshad *et al.*, "Advances and Perspectives on Solid Oxide Fuel Cells: From Nanotechnology to Power Electronics Devices," *Energy Technology*, vol. 11, no. 12, Dec. 2023, doi: 10.1002/ente.202300452.

[3] S. Chattopadhyay, *Nanogrids and Picogrids and their Integration with Electric Vehicles*. Institution of Engineering and Technology, 2022. doi: 10.1049/PBPO208E.

[4] S. S. Moosavi, A. Kazemi, and H. Akbari, "A comparison of various open-circuit fault detection methods in the IGBT-based DC/AC inverter used in electric vehicle," *Eng Fail Anal*, vol. 96, pp. 223–235, Feb. 2019, doi: 10.1016/j.engfailanal.2018.09.020.

[5] S. Yang, X. Sun, M. Ma, X. Zhang, and L. Chang, "Fault Detection and Identification Scheme for Dual-Inverter Fed OEWIM Drive," *IEEE Transactions on Industrial Electronics*, vol. 67, no. 7, pp. 6112–6123, Jul. 2020, doi: 10.1109/TIE.2019.2922924.

[6] S. F. Zarei, H. Mokhtari, and F. Blaabjerg, "Fault Detection and Protection Strategy for Islanded Inverter-Based Microgrids," *IEEE J Emerg Sel Top Power Electron*, vol. 9, no. 1, pp. 472–484, Feb. 2021, doi: 10.1109/JESTPE.2019.2962245.

[7] D. Chowdhury, M. Bhattacharya, D. Khan, S. Saha, and A. Dasgupta, "Wavelet decomposition based fault detection in cascaded H-bridge multilevel inverter using artificial neural network," in *2017 2nd IEEE International Conference on Recent Trends in Electronics, Information & Communication Technology (RTEICT)*, IEEE, May 2017, pp. 1931–1935. doi: 10.1109/RTEICT.2017.8256934.

[8] R. B. Dhumale and S. D. Lokhande, "Neural Network Fault Diagnosis of Voltage Source Inverter under variable load conditions at different frequencies," *Measurement*, vol. 91, pp. 565–575, Sep. 2016, doi: 10.1016/j.measurement.2016.04.051.

[9] G. Kiran Kumar, E. Parimalasundar, D. Elangovan, P. Sanjeevikumar, F. Lannuzzo, and J. B. Holm-Nielsen, "Fault Investigation in Cascaded H-Bridge Multilevel Inverter through Fast Fourier Transform and Artificial Neural Network Approach," *Energies (Basel)*, vol. 13, no. 6, p. 1299, Mar. 2020, doi: 10.3390/en13061299.

[10] S. Khomfoi and L. M. Tolbert, "Fault Diagnostic System for a Multilevel Inverter Using a Neural Network," *IEEE Trans Power Electron*, vol. 22, no. 3, pp. 1062–1069, May 2007, doi: 10.1109/TPEL.2007.897128.

[11] L. Kou, C. Liu, G. Cai, J. Zhou, Q. Yuan, and S. Pang, "Fault diagnosis for open-circuit faults in NPC inverter based on knowledge-driven and data-driven approaches," *IET Power Electronics*, vol. 13, no. 6, pp. 1236–1245, May 2020, doi: 10.1049/iet-pel.2019.0835.

[12] K. Dhibi *et al.*, "A Hybrid Fault Detection and Diagnosis of Grid-Tied PV Systems: Enhanced Random Forest Classifier Using Data Reduction and Interval-Valued Representation," *IEEE Access*, vol. 9, pp. 64267–64277, 2021, doi: 10.1109/ACCESS.2021.3074784.

[13] K. Dhibi *et al.*, "Reduced Kernel Random Forest Technique for Fault Detection and Classification in Grid-Tied PV Systems," *IEEE J Photovolt*, vol. 10, no. 6, pp. 1864–1871, Nov. 2020, doi: 10.1109/JPHOTOV.2020.3011068.

[14] W. Yuan, T. Wang, and D. Diallo, "A Secondary Classification Fault Diagnosis Strategy Based on PCA-SVM for Cascaded Photovoltaic Grid-connected Inverter," in *IECON 2019 - 45th Annual Conference of the IEEE Industrial Electronics Society*, IEEE, Oct. 2019, pp. 5986–5991. doi: 10.1109/IECON.2019.8927090.

[15] N.-T. Nguyen and H.-P. Nguyen, "Fault Diagnosis of Voltage Source Inverter for Induction Motor Drives Using Decision Tree," 2017, pp. 819–826. doi: 10.1007/978-981-10-1721-6_88.

[16] N. Torabi, F. Naghavi, and H. A. Toliyat, "Real-time fault isolation in multiphase multilevel NPC converters using active semi-supervised fuzzy clustering algorithm with pairwise constraints," in *2017 IEEE International Electric Machines and Drives Conference (IEMDC)*, IEEE, May 2017, pp. 1–7. doi: 10.1109/IEMDC.2017.8002409.

[17] W. Gong, H. Chen, Z. Zhang, M. Zhang, and H. Gao, "A Data-Driven-Based Fault Diagnosis Approach for Electrical Power DC-DC Inverter by Using Modified Convolutional Neural Network With Global Average Pooling and 2-D Feature Image," *IEEE Access*, vol. 8, pp. 73677–73697, 2020, doi: 10.1109/ACCESS.2020.2988323.

[18] Q. Sun, X. Yu, and H. Li, "Open-circuit Fault Diagnosis Based on 1D-CNN for Three-phase Full-bridge Inverter," in *2020 11th International Conference on Prognostics and System Health Management (PHM-2020 Jinan)*, IEEE, Oct. 2020, pp. 322–327. doi: 10.1109/PHM-Jinan48558.2020.00064.

[19] C. Bowen and T. Wei, "Switch open-circuit faults diagnosis of inverter based on wavelet and support vector machine," in *2019 14th IEEE International Conference on Electronic Measurement & Instruments (ICEMI)*, IEEE, Nov. 2019, pp. 1178–1184. doi: 10.1109/ICEMI46757.2019.9101567.

[20] T. H. Pham, S. Lefteriu, E. Duviella, and S. Lecoeuche, "Auto-adaptive and Dynamical Clustering for Double Open-Circuit Fault Diagnosis of Power Inverters," in *2019 4th Conference on Control and Fault Tolerant Systems (SysTol)*, IEEE, Sep. 2019, pp. 306–311. doi: 10.1109/SYSTOL.2019.8864777.

[21] W. Yang, W. Wang, X. Wang, J. Gu, and Z. Wang, "Fault diagnosis method of a cascaded H-bridge inverter based on a multisource adaptive fusion CNN-transformer," *IET Power Electronics*, Jan. 2024, doi: 10.1049/pel2.12664.

[22] S.-M. Jung, J.-S. Park, H.-W. Kim, K.-Y. Cho, and M.-J. Youn, "An MRAS-Based Diagnosis of Open-Circuit Fault in PWM Voltage-Source Inverters for PM Synchronous Motor Drive Systems," *IEEE Trans Power Electron*, vol. 28, no. 5, pp. 2514–2526, May 2013, doi: 10.1109/TPEL.2012.2212916.

[23] S. S. Ghosh, S. Chattopadhyay, and A. Das, "Fast Fourier transform and wavelet-based statistical computation during fault in snubber circuit connected with robotic brushless direct current motor," *Cognitive Computation and Systems*, vol. 4, no. 1, pp. 31–44, Mar. 2022, doi: 10.1049/ccs2.12041.

[24] S. S. Ghosh, S. Chattopadhyay, S. Banerjee, and A. Das, "Study of Budding Snubber Quality Deterioration in Solid Oxide Fuel Cell-Fed Inverter Used in Microgrid Energy Conversion," *Energy Technology*, Jul. 2024, doi: 10.1002/ente.202400568.

[25] S. S. Ghosh, S. Mukherjee, S. Chattopadhyay, and A. Das, "Premature Breakdown Identification in Photovoltaic Array Fed IGBT-based Voltage Source Converter," *Journal of Nano- and Electronic Physics*, vol. 15, no. 3, pp. 03016-1-03016–5, 2023, doi: 10.21272/jnep.15(3).03016.

[26] S. S. Ghosh *et al.*, "Wavelet-based rapid identification of IGBT switch breakdown in voltage source converter," *Microelectronics Reliability*, vol. 152, p. 115283, Jan. 2024, doi: 10.1016/j.microrel.2023.115283.

Chapter 9

DWT-based Monitoring of the Snubber Circuit Resistance Problem in Small Microgrid Inverter Connected with Robotic Brushless DC Motor

Abstract- In Chapter 3, a fast Fourier transform (FFT)-based investigation was attempted to identify the inverter switch's snubber circuit resistance failure (ISSCRF) in the small microgrid inverter (SMGI) connected with robotic brushless DC (BLDC) motors. However, it was eventually discovered that the FFT-based diagnosis utilized there for identifying ISSCRF has not produced any insightful findings that can be applied to ISSCRF evaluation.

This chapter discusses an effort to recognize the ISSCRF in robotic brushless DC (BLDC) motors through a discrete wavelet transform (DWT)-based approach. The presented study includes the wavelet coefficients of the stator current harmonic spectra's skewness, kurtosis, and root mean square (RMS) measurements to identify ISSCRF.

Keywords: BLDC motor, discrete wavelet transform (DWT), fault identification, ISSCRF.

9.1 Introduction

In this chapter wavelet-based statistical investigation was performed to get over the drawbacks of the FFT-based investigation that was discussed in Chapter 3 to detect ISSCRF. Skewness, kurtosis, and RMS measurements of the stator current harmonics spectra's wavelet coefficients are examined in this investigation to identify the ISSCRF in SMGI that is connected with robotic BLDC motor. To identify ISSCRF, the BLDC motor's stator current was monitored under normal conditions and at various ISSCRF percentages (%ISSCRFs) (up to 50%). To determine which selection parameters are the most appropriate for ISSCRF detection, comparative analysis is performed. Three case investigations have been used to validate a suggested fault detection technique for ISSCRF detection. Best-fit features are then utilized to modify the algorithm afterwards. Moreover, a comparative analysis of the work's innovative additions has been included.

9.2 DWT-Oriented ISSCRF Analysis

The wavelet transform constitutes a particularly useful technique for processing non-stationary data [1]. The discrete character of the signals' recording makes DWT appropriate for analysis [1], [2]. The amount of wavelet coefficients that DWT provides is defined according to the integers of discrete steps in scale and translation, indicated by m and n. For RMS, the scale and translation will be $a = a_0^m$ and $b = nb_0 a_0^m$. if the segmentation's step size of the scale and translation be a_0 and b_0, accordingly. The coefficients of the discrete wavelet are therefore expressed as follows [1]:

$$DWT(m,n) = \int_{-\infty}^{\infty} \frac{1}{\sqrt{a_0{}^m}} f(t) g(a_0{}^{-m}t - nb_0) d(t) \qquad (9.1)$$

where $g(a_0^{-m}t - nb_0)$ represents the translated and scaled discrete wavelet.

For investigation, the BLDC motor's phase-A stator current was recorded. The acquired current was decomposed till the DWT 9th level. The Daubechies wavelet's mother wavelet in this instance is identified as "db4". For both normal and defective circumstances (up to 50%) of ISSCRF, approximated and detail coefficients were calculated through DWT level 9. Some of the findings from the overall outcome are presented in Fig. 9.1. It is difficult to discern between varying ISSCRF percentages utilizing the graphical evaluation method demonstrated in Fig. 9.1 since all of the graphical findings seem to imply the same. Therefore, it is impossible to derive an exact finding from the data that may be utilized to identify the ISSCRF. Skewness, kurtosis, and RMS values of the stator current's harmonic spectra through DWT 9 levels were further calculated for the intent of detecting ISSCRF.

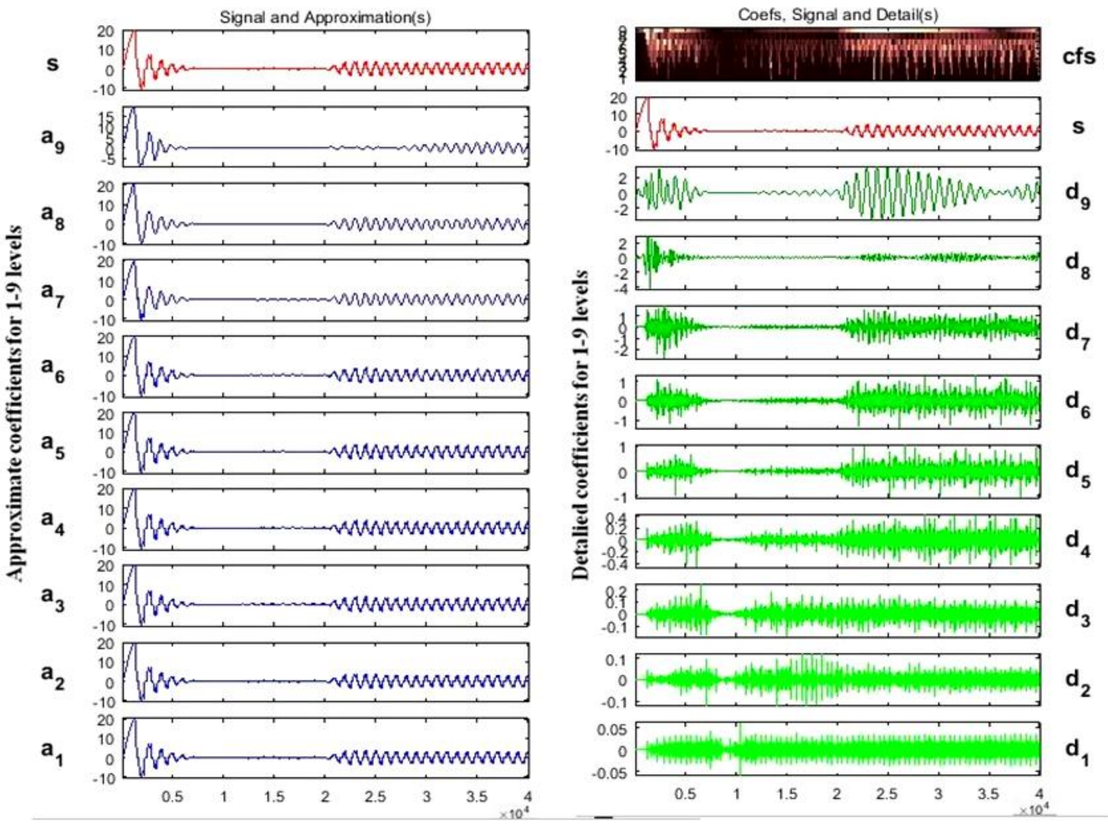

(a) during typical condition

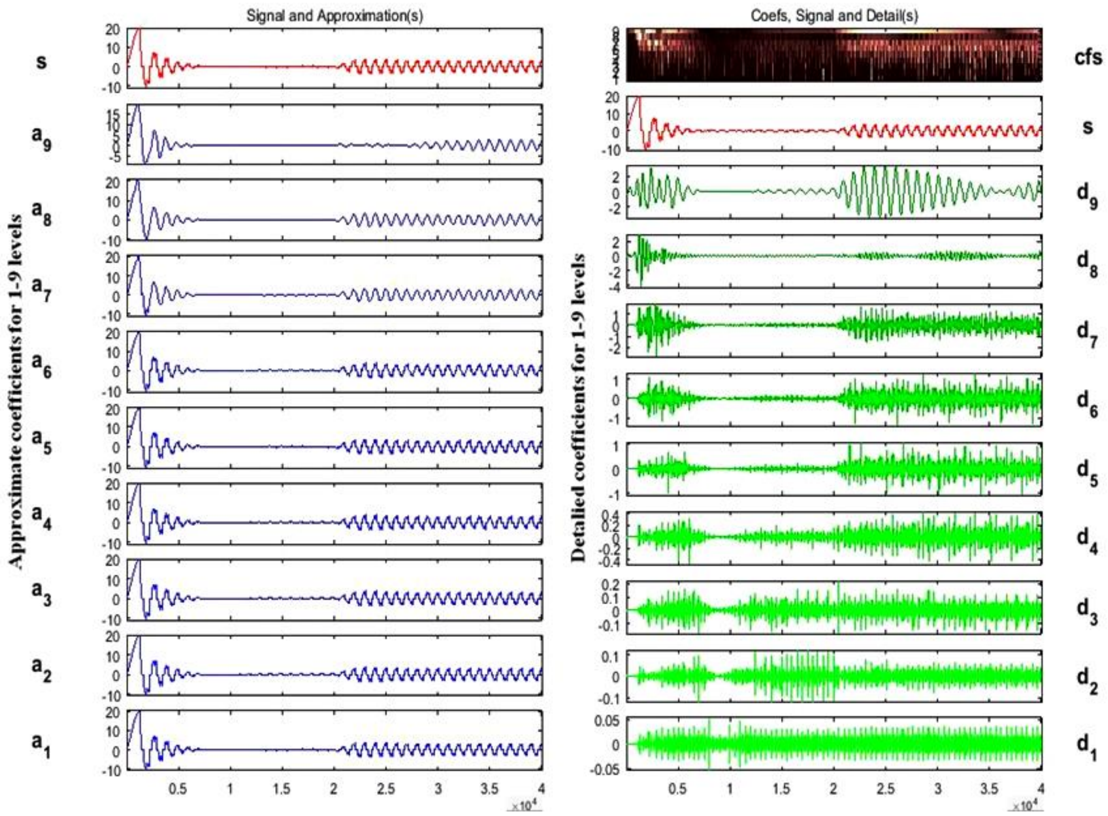

(b) during 5% fault

Fig. 9.1. Approximated and detail coefficients during various %ISSCRF

9.4.1 Considered Statistical Parameters

The coefficients of wavelet decomposition are represented as follows:

The approximated and detail coefficients' kurtosis, skewness, and RMS values are represented as A_K, D_K, A_S, D_S, A_R, and D_R, respectively. For both approximate and detail coefficients till the DWT level 9, the skewness, kurtosis, and RMS values may be written as follows [1]:

$$[s]=\begin{bmatrix}[A_S]\\ [D_S]\end{bmatrix}=\begin{bmatrix}A_{S1} & A_{S2} & A_{S3} & A_{S4} & A_{S5} & A_{S6} & A_{S7} & A_{S8} & A_{S9}\\ D_{S1} & D_{S2} & D_{S3} & D_{S4} & D_{S5} & D_{S6} & D_{S7} & D_{S8} & D_{S9}\end{bmatrix} \quad (9.2)$$

$$[k]=\begin{bmatrix}[A_K]\\ [D_K]\end{bmatrix}=\begin{bmatrix}A_{K1} & A_{K2} & A_{K3} & A_{K4} & A_{K5} & A_{K6} & A_{K7} & A_{K8} & A_{K9}\\ D_{K1} & D_{K2} & D_{K3} & D_{K4} & D_{K5} & D_{K6} & D_{K7} & D_{K8} & D_{K9}\end{bmatrix} \quad (9.3)$$

$$[R]=\begin{bmatrix}[A_R]\\ [D_R]\end{bmatrix}=\begin{bmatrix}A_{R1} & A_{R2} & A_{R3} & A_{R4} & A_{R5} & A_{R6} & A_{R7} & A_{R8} & A_{R9}\\ D_{R1} & D_{R2} & D_{R3} & D_{R4} & D_{R5} & D_{R6} & D_{R7} & D_{R8} & D_{R9}\end{bmatrix} \quad (9.4)$$

In acquired current signal examination and assessment of ISSCRF, which generate non-stationary signals, statistical factors are proven to be useful.

9.4.2 Evaluation of Statistical Factors for Approximation Coefficients

The A_K, A_S, and A_R were computed for standard and various %ISSCRF circumstances, and they are illustrated in Fig. 9.2, Fig. 9.3, and Fig. 9.4. It is noticeable in Fig. 9.2 that the A_K values for the 1st through 6th levels are quite similar, making it impossible to make any significant inferences. Also, the A_K readings for the 7th and 8th levels are highly erratic and do not yield any beneficial outcomes for problem identification. Fig. 9.3 and Fig. 9.4 show similar traits for the values for A_S and A_R, which are likewise ineffective for fault diagnosis.

However, when the %ISSCRF increases, it is evident from Fig. 9.2, Fig. 9.3, and Fig. 9.4 that only the value of A_{R9} is dropping, while the values of A_{K9} and A_{S9} are both rising. A_{K9}, A_{S9}, and A_{R9} can therefore be useful for ISSCRF evaluation.

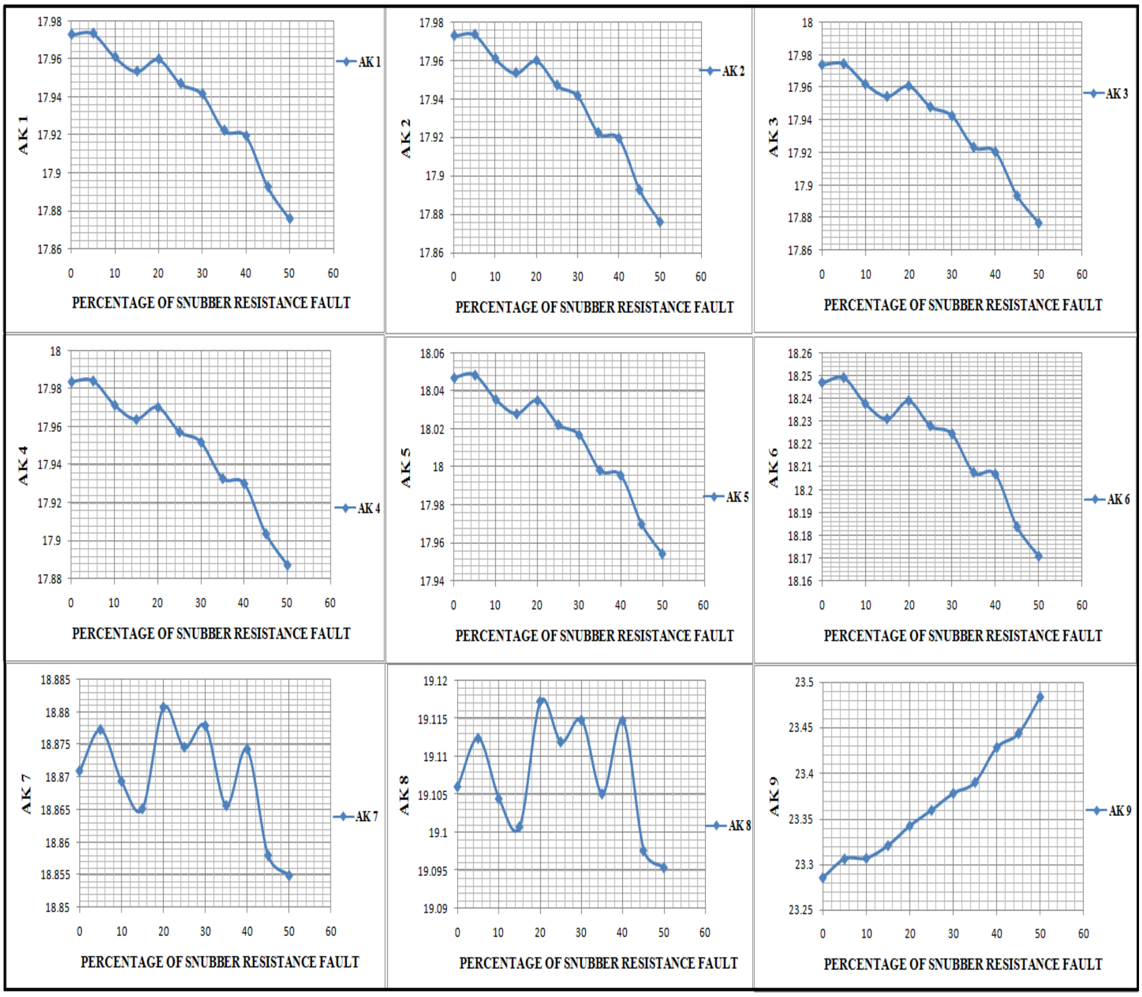

Fig. 9.2 A_K vs. %ISSCRF

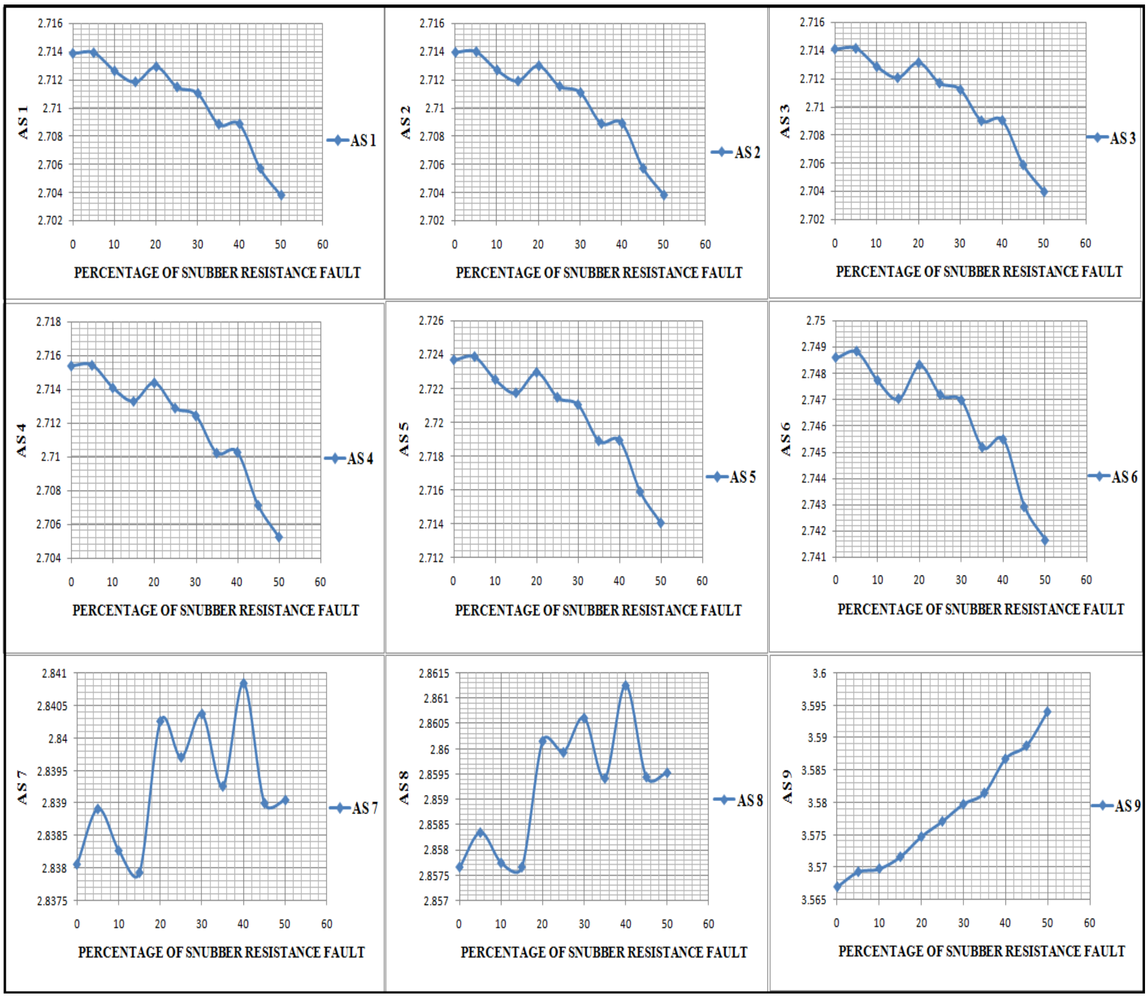

Fig. 9.3. As vs. %ISSCRF

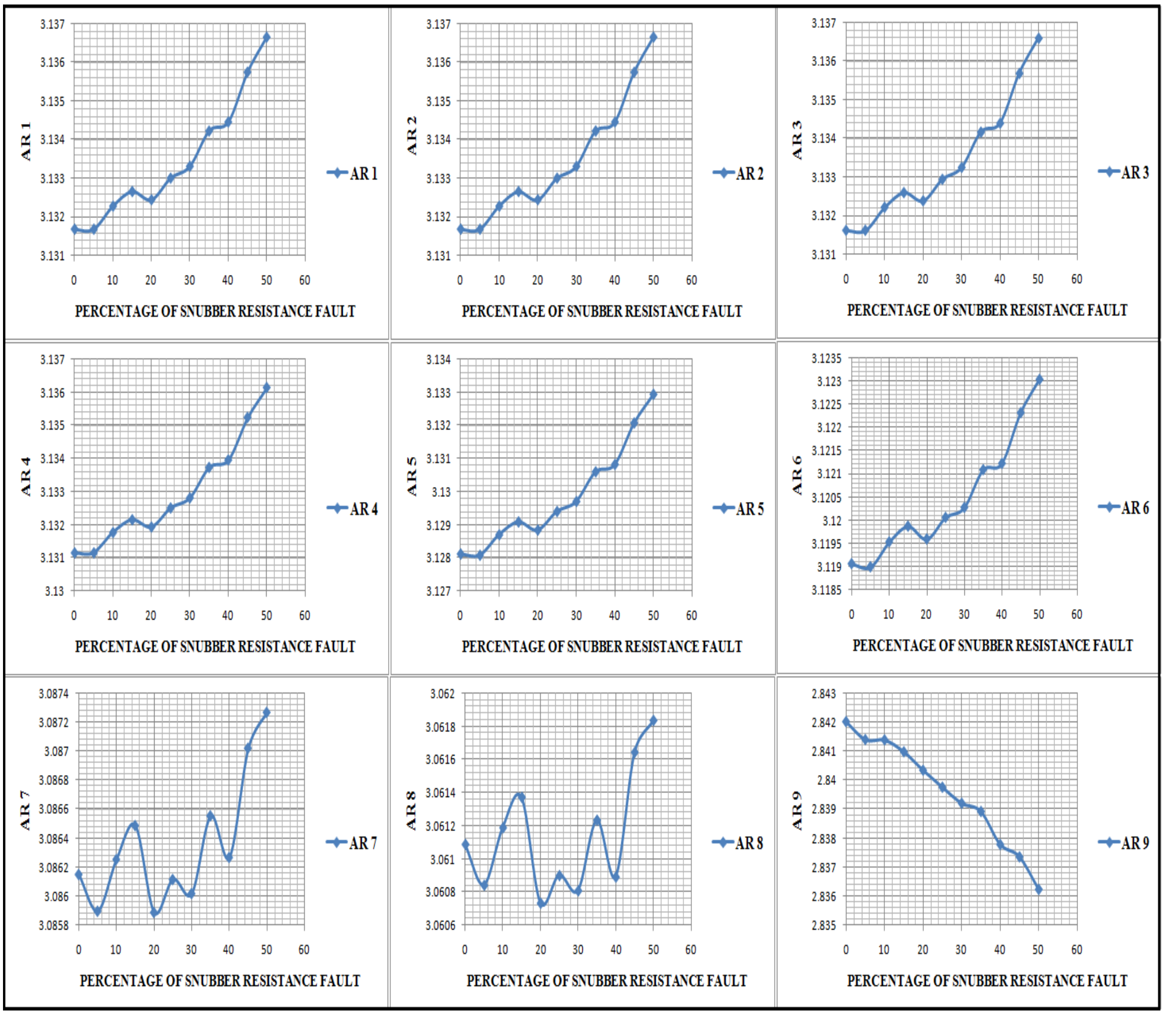

Fig. 9.4. A_R vs. %ISSCRF

9.4.3 Evaluation of Statistical Factors for Detail Coefficients

The D_K, D_S, and D_R were computed for standard and various %ISSCRF circumstances, and they are illustrated in Fig. 9.5, Fig. 9.6, and Fig. 9.7. Fig. 9.5 demonstrates that the majority of the outcomes are in a fairly erratic pattern, with the exception of the D_{K7} and D_{K9}, which decrease as the %ISSCRF increases. Following the observation of Fig. 9.6, it could be said that all the D_S level values are extremely irregular in character and that no useful inference can be drawn from them for the detection of ISSCRF. Further, only the D_{R6} and D_{R7} values are rising with the variations in the %ISSCRF, as evident in Fig. 9.7. The remaining values exhibit excessive irregular patterns, which hinder the ability to evaluate ISSCRF.

Therefore, for ISSCRF analysis, only the D_{K7}, D_{K9}, D_{R6}, and D_{R7} are likely to be helpful.

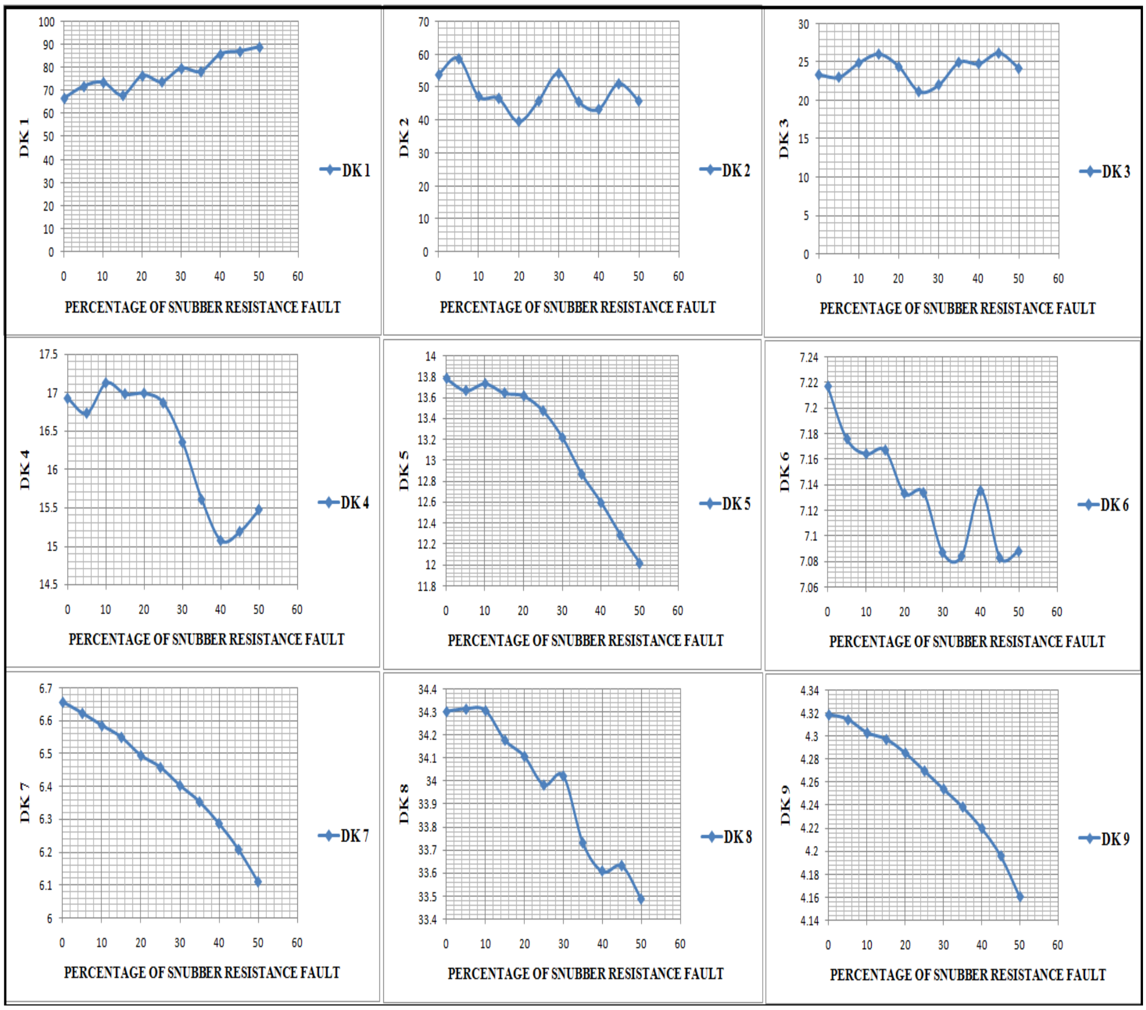

Fig. 9.5. D_K vs. %ISSCRF

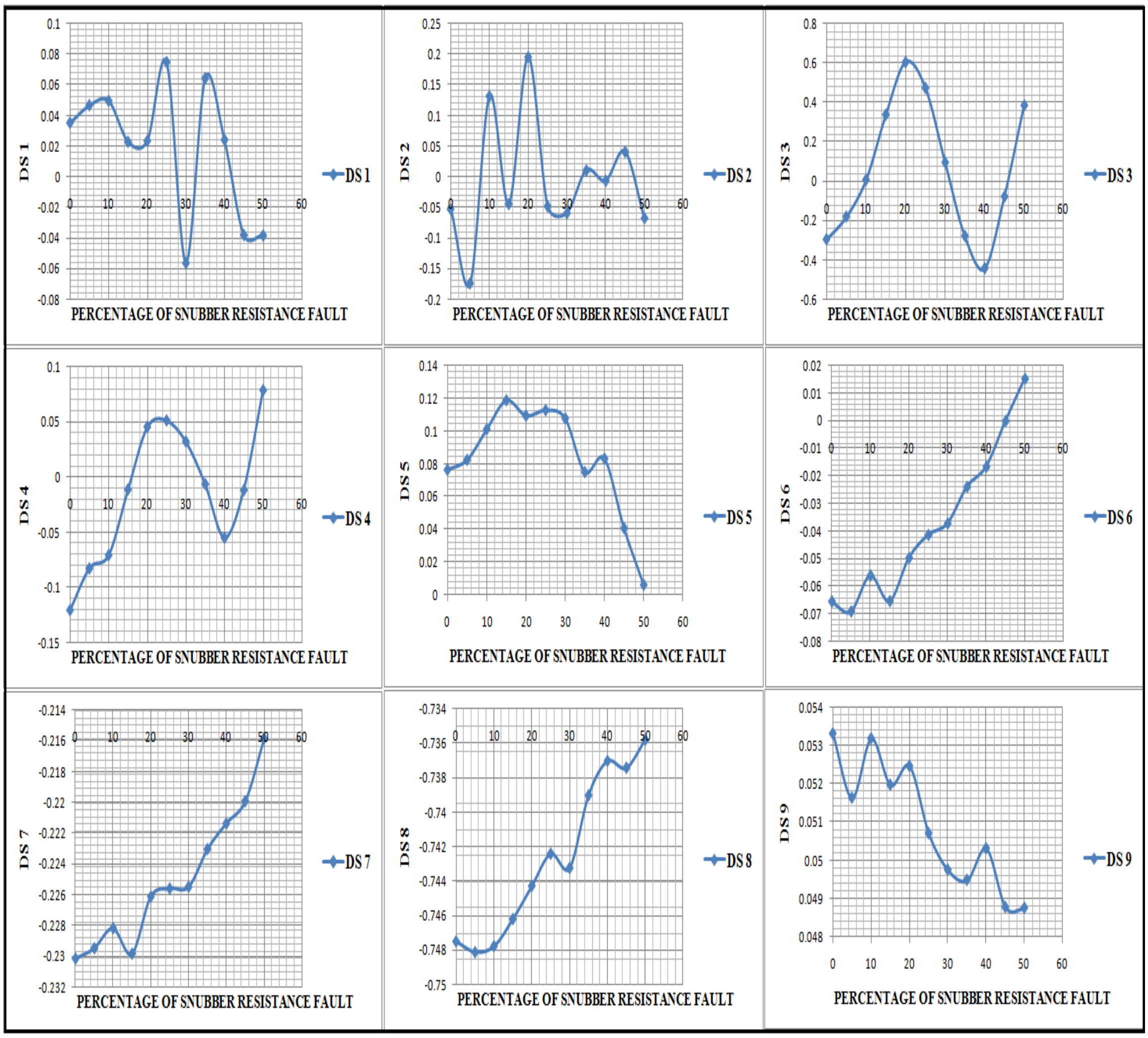

Fig. 9.6. D_S vs. %ISSCRF

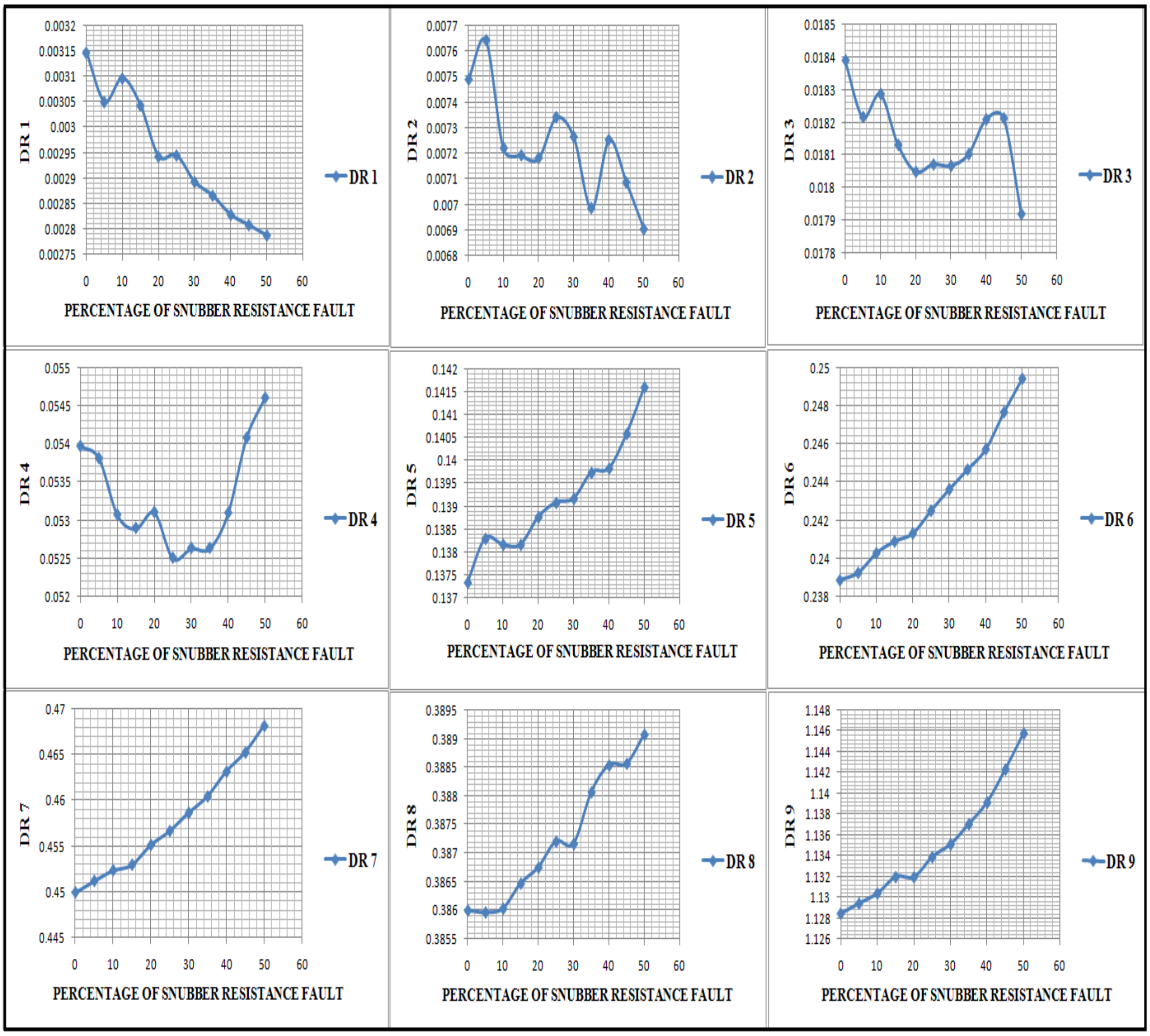

Fig. 9.7. D_R vs. %ISSCRF

9.4.4 Selection of Ideal Attribute

The likely effective curves for diagnosing ISSCRF were chosen from Fig. 9.2, Fig. 9.3, Fig. 9.4, Fig. 9.5, Fig. 9.6, and Fig. 9.7, as seen in Fig. 9.8.

Based on the analysis of Fig. 9.8, it is noted that while both the curves of A_{K9} and A_{S9} are increasingly pronounced, the curve of A_{R9} is decreasingly pronounced as the %ISSCRF develops further. Additionally, it was perceived that when the %ISSCRF rises, the curves of D_{R6} and D_{R7} are rising while those of D_{K7} and D_{K9} are falling. In addition, these curves' shapes have a smaller irregular characteristic than those of the remaining curves.

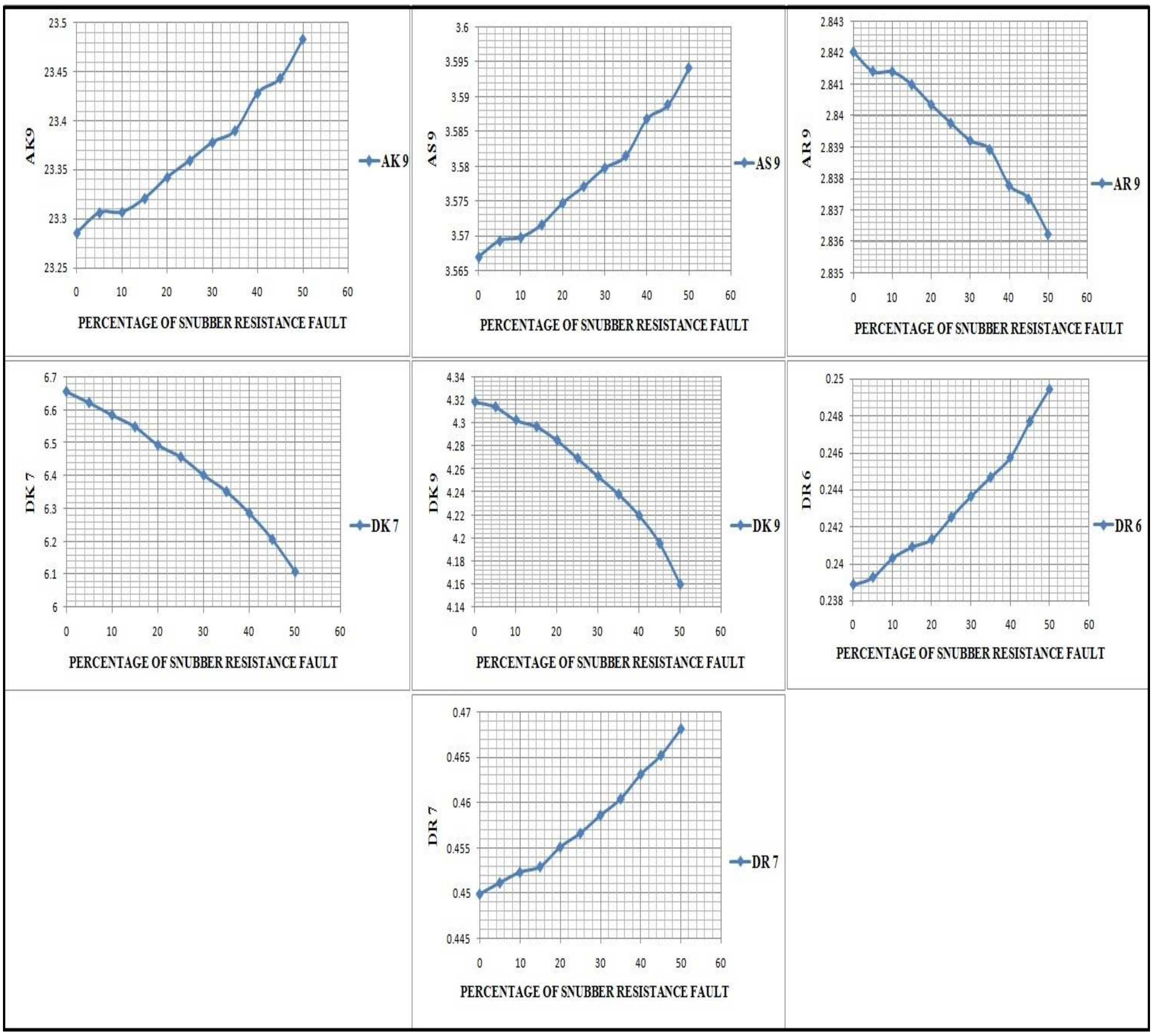

Fig. 9.8. Preferred curves for ISSCRF analysis

9.5 Algorithm, Real Case Studies, and Validation

The following algorithm was suggested for ISSCRF detection:

a) Acquire the stator current.

b) Apply DWT to the recorded data.

c) Identify A_{K9}, A_{S9}, A_{R9}, D_{K7}, D_{K9}, D_{R6}, and D_{R7}.

d) Check for ISSCRF.

This section presents the findings of investigations conducted on three BLDC motors with specified ratings and known %ISSCRF to validate the method. These studies' data were additionally utilized for the comparison analysis.

Table 9.1 provides the specifications of these BLDC motors utilized in the case studies.

Table 9.1. Technical specifications

Parameters	Case-1	Case-2	Case-3
Resistance	0.36 ohm	0.45 ohm	0.20 ohm
Inductance	1.05 mH	1.4 mH	0.48 mH
Rotor inertia	800 g.cm^2	173 g.cm^2	1600 g.cm^2
Peak-torque	2.1 N.m	1.00 N.m	4.2 N.m
Rated power	220 W	133 W	440 W
Number of poles	8	4	8
%ISSCRF known	29%	37%	46%

Table 9.2 summarizes the findings of the comparison study that was conducted. As indicated in Table 9.2, the computations were also conducted to determine the optimal method for detecting ISSCRF. Finally, a comparison of these data's percentage errors has been made, and the outcome is displayed in Fig. 10.

In this specific scenario, the error rate in percent was computed employing the formula [3] outlined below:

$$Error = \left(\frac{F_{ISSCRF} - f_{ISSCRF}}{f_{ISSCRF}} \right) \times 100\% \qquad (9.5)$$

where,

F_{ISSCRF} = %ISSCRF value (known);

f_{ISSCRF} = %ISSCRF calculated using A_{K9}, A_{S9}, A_{R9}, D_{K7}, D_{K9}, D_{R6}, or D_{R7} values

Table 9.2. Comparative analysis of experimental results from actual motors

Parameters	**1st Case**	**2nd Case**	**3rd Case**
%ISSCRF (known)	29 %	37 %	46 %
%ISSCRF using A_{K9}	A_{K9} = 23.377 %ISSCRF = 30% Error = -3.45%	A_{K9} = 23.385 %ISSCRF = 34% Error = 8.11%	A_{K9} = 23.465 %ISSCRF = 48% Error = -4.35%
%ISSCRF using A_{S9}	A_{S9} = 3.578 %ISSCRF = 27% Error = 6.90%	A_{S9} = 3.584 %ISSCRF = 38% Error = -2.70%	A_{S9} = 3.591 %ISSCRF = 47% Error = -2.17%
%ISSCRF using A_{R9}	A_{R9} = 2.8396 %ISSCRF = 26% Error = 10.34%	A_{R9} = 2.8389 %ISSCRF = 35% Error = 5.41%	A_{R9} = 2.8374 %ISSCRF = 45% Error = 2.17%
%ISSCRF using D_{K7}	D_{K7} = 6.43 %ISSCRF = 28% Erro r= 3.45%	D_{K7}= 6.34 %ISSCRF = 36% Error = 2.70%	D_{K7}= 6.21 %ISSCRF = 45% Error = 2.17%
%ISSCRF using D_{K9}	D_{K9}= 4.26 %ISSCRF = 28% Error = 3.45%	D_{K9}= 4.24 %ISSCRF = 35% Error = 5.41%	D_{K9}= 4.20 %ISSCRF = 45% Error = 2.17%
%ISSCRF using D_{R6}	D_{R6}= 0.244 %ISSCRF = 30% Error = -3.45%	D_{R6}= 0.245 %ISSCRF = 36% Error = 2.70%	D_{R6}= 0.249 %ISSCRF = 48% Error = -4.35%
%ISSCRF using D_{R7}	D_{R7}= 0.459 %ISSCRF = 31% Error = -6.90%	D_{R7}= 0.462 %ISSCRF = 38% Error = -2.70%	D_{R7}= 0.465 %ISSCRF = 44% Error = 4.35%

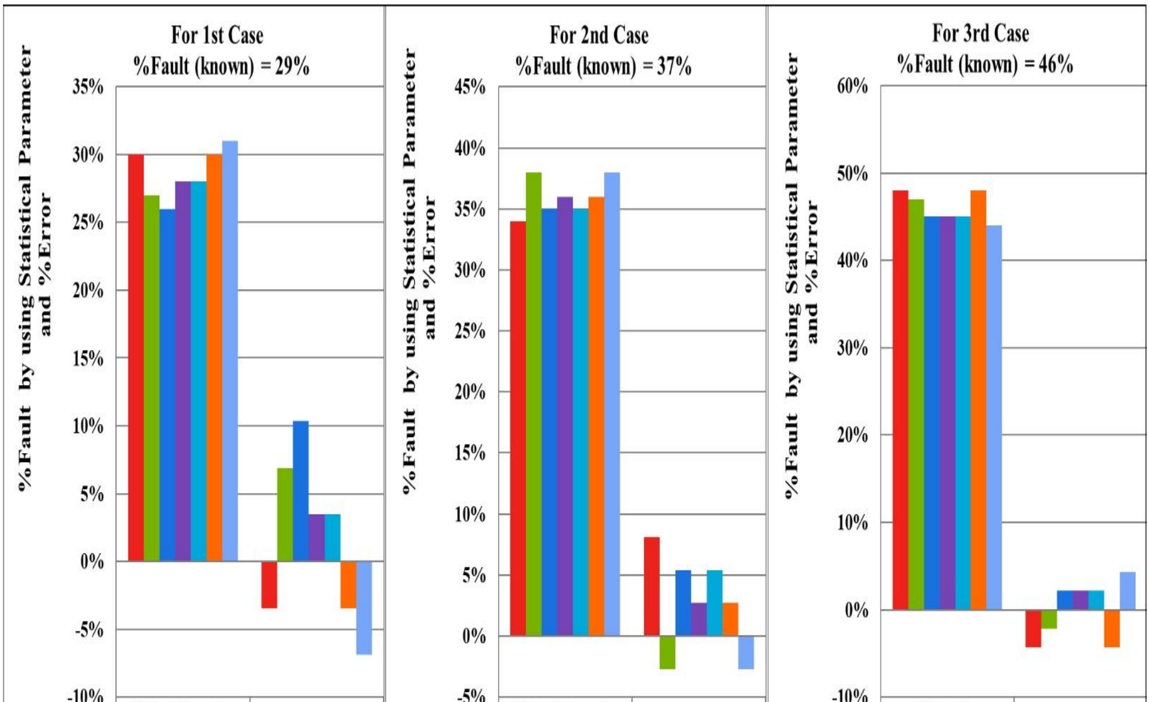

	%Fault by using Stastical Parameter	Error
AK9=23.377	30%	-3.45%
AS9=3.578	27%	6.90%
AR9=2.8396	26%	10.34%
DK7 = 6.43	28%	3.45%
DK9= 4.26	28%	3.45%
DR6= 0.244	30%	-3.45%
DR7= 0.459	31%	-6.90%

	%Fault by using Stastical Parameter	Error
AK9=23.385	34%	8.11%
AS9=3.584	38%	-2.70%
AR9=2.8389	35%	5.41%
DK7 = 6.34	36%	2.70%
DK9= 4.24	35%	5.41%
DR6= 0.245	36%	2.70%
DR7= 0.462	38%	-2.70%

	%Fault by using Stastical Parameter	Error
AK9=23.465	48%	-4.35%
AS9=3.591	47%	-2.17%
AR9=2.8374	45%	2.17%
DK7 = 6.21	45%	2.17%
DK9= 4.20	45%	2.17%
DR6= 0.249	48%	-4.35%
DR7= 0.465	44%	4.35%

Fig. 9.9. Comparison of percentage errors

To properly identify ISSCRF, a revised method has been presented here as follows:

a) Record the stator current.
b) Apply DWT to the acquired data.
c) Find D_{K7}.
d) Check for ISSCRF.

The Fig. 9.10 depicts this improved suggested method of ISSCRF detection.

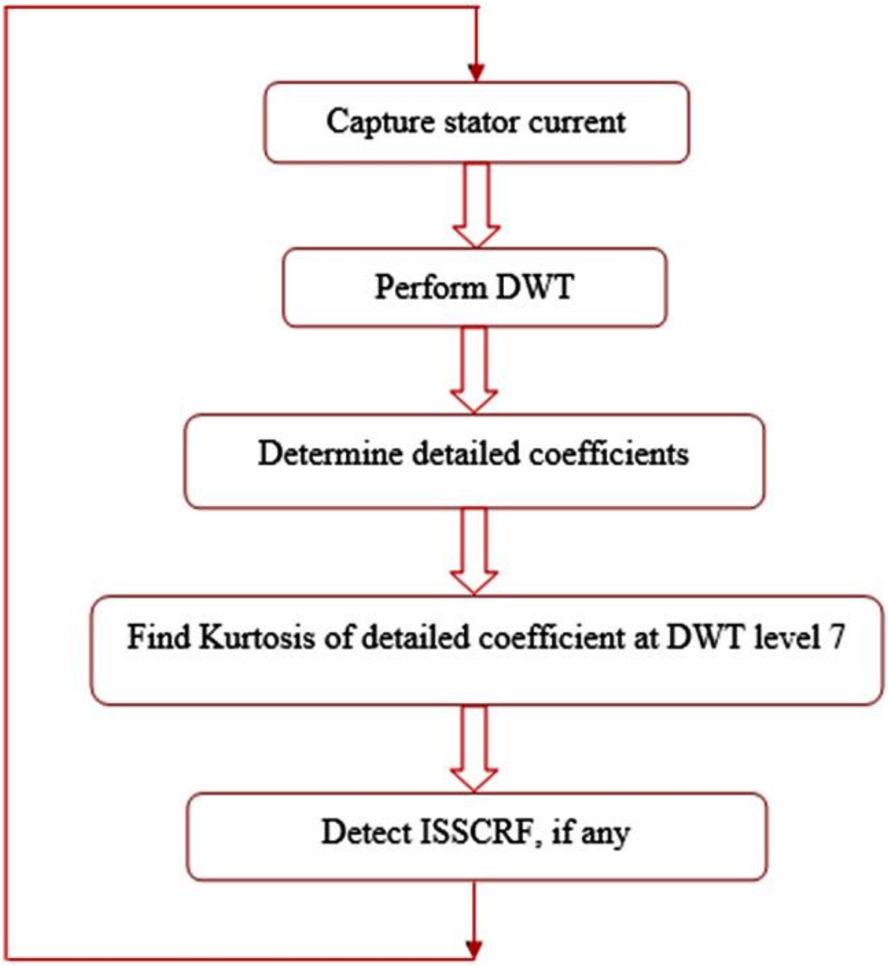

Fig. 9.10. Improved suggested method of ISSCRF detection

9.6 Comparative Assessment and Unique Contribution

In Chapter 3, the BLDC motor's stator current was diagnosed using FFT, and the chapter presents the results of studies on the different statistical characteristics of the motor's stator current under normal conditions and at various %ISSCRF. It was eventually discovered that the FFT-based diagnosis utilized here for identifying ISSCRF has not produced any insightful findings that can be applied to ISSCRF evaluation.

Furthermore, it was noted in this chapter that only the variables D_{K7}, D_{K9}, D_{R6}, and D_{R7} yield satisfactory findings that may be utilized for ISSCRF identification based on DWT-based statistical characteristics. In the end, however, it is evident from the comparative analysis conducted in Table 9.2 and the percentage error comparisons shown in Fig. 9.9 that the highest desirable outcome is only attained when D_{K7} is consulted.

Therefore, following a comprehensive comparison of the outcomes from the DWT-based analyses presented in this chapter and the FFT-based analyses in Chapter 3, it was discovered that D_{K7} has proven to be exceptionally efficient for ISSCRF detection based on the findings derived through both simulation and real-world scenarios. Thus, this detection method may be exploited to identify ISSCRF in a small microgrid inverter.

The literature review's fault diagnostics mostly address open-circuit (OC) and short-circuit (SC) problems in various inverter categories. In Table 9.3, a comparison between this study and other comparable research has been conducted.

Table 9.3. Comparative analysis

Reference	Observed Parameters / Fault Detection Method	Identifying Faults in Inverters	Percent of fault detection capacity (%)
[4]	Line and phase voltage deviation	3-phase inverters (3PhIs) IGBT, and current sensor defects	No
[5]	Current signal-oriented fault detection	OC faults in the dual-inverter drive	No
[6]	Negative-sequence resistance	SC defects in islanded inverters	No
[7], [8]	Artificial Neural Networks (ANN)	OC defects in cascaded H-bridge multilevel inverters (CHMLIs)	No
[9]	ANN	OC in voltage source inverters (VSIs)	No
[10]	ANN	OC and SC failures in CHMLI	No
[11], [12]	Random-Forest (RF)	OC failure in 3PhI	No
[13]	Support Vector Machines (SVMs)	OC failure in multilevel inverters (MLIs)	No
[14]	Decision Tree	OC failures in VSI	No
[15], [16]	CNN	OC fault in 3PhI	No
[17]	Clustering	OC fault in 3PhI	No
[18]	Continuous Wavelet Transform (CWT)	OC fault in CHMLI	No
[19]	FFT	IGBT switch issue	No
[20]	DWT	IGBT switch issue	Yes
Proposed Method	DWT	ISSCRF in SMGIs	Yes

Therefore, the unique accomplishment of this investigation involves the fact that it exploits the statistical character of D_{K7} to aid with ISSCRF identification extremely well.

The investigation additionally indicated that the %ISSCRF in the SMGI could be obtained using the approach proposed.

9.7 Conclusion

DWT-based statistical analysis was conducted in this chapter to overcome the limitations of the FFT-based analysis covered in Chapter 3 to detect ISSCRF in SMGI. The values of the pertinent parameters have been observed to be fluctuating throughout the fault detection procedure. The data gathered from DWT-based diagnostics has been compared and evaluated in an effort to determine the best reliable method for ISSCRF detection. Furthermore, it was discovered that D_{K7} has proven to be exceptionally efficient for ISSCRF detection. Consequently, the ISSCRF within any SMGI may be detected by applying the suggested approach by continual tracking of readings. Additionally, the analysis confirmed that the suggested approach may be used to derive the %ISSCRF in the SMGI.

References

[1] S. S. Ghosh, S. Chattopadhyay, and A. Das, "Fast Fourier transform and wavelet-based statistical computation during fault in snubber circuit connected with robotic brushless direct current motor," *Cognitive Computation and Systems*, vol. 4, no. 1, pp. 31–44, Mar. 2022, doi: 10.1049/ccs2.12041.

[2] S. Karmakar, S. Chattopadhyay, M. Mitra, and S. Sengupta, *Induction Motor Fault Diagnosis*. Singapore: Springer Singapore, 2016. doi: 10.1007/978-981-10-0624-1.

[3] S. S. Ghosh, S. Chattopadhyay, S. Banerjee, and A. Das, "Study of Budding Snubber Quality Deterioration in Solid Oxide Fuel Cell-Fed Inverter Used in Microgrid Energy Conversion," *Energy Technology*, Jul. 2024, doi: 10.1002/ente.202400568.

[4] Z. Li *et al.*, "A Fast Diagnosis Method for Both IGBT Faults and Current Sensor Faults in Grid-Tied Three-Phase Inverters With Two Current Sensors," *IEEE Trans Power Electron*, vol. 35, no. 5, pp. 5267–5278, May 2020, doi: 10.1109/TPEL.2019.2946692.

[5] S. Yang, X. Sun, M. Ma, X. Zhang, and L. Chang, "Fault Detection and Identification Scheme for Dual-Inverter Fed OEWIM Drive," *IEEE Transactions on Industrial Electronics*, vol. 67, no. 7, pp. 6112–6123, Jul. 2020, doi: 10.1109/TIE.2019.2922924.

[6] S. F. Zarei, H. Mokhtari, and F. Blaabjerg, "Fault Detection and Protection Strategy for Islanded Inverter-Based Microgrids," *IEEE J Emerg Sel Top Power Electron*, vol. 9, no. 1, pp. 472–484, Feb. 2021, doi: 10.1109/JESTPE.2019.2962245.

[7] D. Chowdhury, M. Bhattacharya, D. Khan, S. Saha, and A. Dasgupta, "Wavelet decomposition based fault detection in cascaded H-bridge multilevel inverter using artificial neural network," in *2017 2nd IEEE International Conference on Recent Trends in Electronics, Information & Communication Technology (RTEICT)*, IEEE, May 2017, pp. 1931–1935. doi: 10.1109/RTEICT.2017.8256934.

[8] G. Kiran Kumar, E. Parimalasundar, D. Elangovan, P. Sanjeevikumar, F. Lannuzzo, and J. B. Holm-Nielsen, "Fault Investigation in Cascaded H-Bridge Multilevel Inverter through Fast Fourier Transform and Artificial Neural Network Approach," *Energies (Basel)*, vol. 13, no. 6, p. 1299, Mar. 2020, doi: 10.3390/en13061299.

[9] R. B. Dhumale and S. D. Lokhande, "Neural Network Fault Diagnosis of Voltage Source Inverter under variable load conditions at different frequencies," *Measurement*, vol. 91, pp. 565–575, Sep. 2016, doi: 10.1016/j.measurement.2016.04.051.

[10] S. Khomfoi and L. M. Tolbert, "Fault Diagnostic System for a Multilevel Inverter Using a Neural Network," *IEEE Trans Power Electron*, vol. 22, no. 3, pp. 1062–1069, May 2007, doi: 10.1109/TPEL.2007.897128.

[11] K. Dhibi *et al.*, "A Hybrid Fault Detection and Diagnosis of Grid-Tied PV Systems: Enhanced Random Forest Classifier Using Data Reduction and Interval-Valued Representation," *IEEE Access*, vol. 9, pp. 64267–64277, 2021, doi: 10.1109/ACCESS.2021.3074784.

[12] K. Dhibi *et al.*, "Reduced Kernel Random Forest Technique for Fault Detection and Classification in Grid-Tied PV Systems," *IEEE J Photovolt*, vol. 10, no. 6, pp. 1864–1871, Nov. 2020, doi: 10.1109/JPHOTOV.2020.3011068.

[13] W. Yuan, T. Wang, and D. Diallo, "A Secondary Classification Fault Diagnosis Strategy Based on PCA-SVM for Cascaded Photovoltaic Grid-connected Inverter," in *IECON 2019 - 45th Annual Conference of the IEEE Industrial Electronics Society*, IEEE, Oct. 2019, pp. 5986–5991. doi: 10.1109/IECON.2019.8927090.

[14] N.-T. Nguyen and H.-P. Nguyen, "Fault Diagnosis of Voltage Source Inverter for Induction Motor Drives Using Decision Tree," 2017, pp. 819–826. doi: 10.1007/978-981-10-1721-6_88.

[15] Q. Sun, X. Yu, and H. Li, "Open-circuit Fault Diagnosis Based on 1D-CNN for Three-phase Full-bridge Inverter," in *2020 11th International Conference on Prognostics and System Health Management (PHM-2020 Jinan)*, IEEE, Oct. 2020, pp. 322–327. doi: 10.1109/PHM-Jinan48558.2020.00064.

[16] W. Gong, H. Chen, Z. Zhang, M. Zhang, and H. Gao, "A Data-Driven-Based Fault Diagnosis Approach for Electrical Power DC-DC Inverter by Using Modified Convolutional Neural Network With Global Average Pooling and 2-D Feature Image," *IEEE Access*, vol. 8, pp. 73677–73697, 2020, doi: 10.1109/ACCESS.2020.2988323.

[17] T. H. Pham, S. Lefteriu, E. Duviella, and S. Lecoeuche, "Auto-adaptive and Dynamical Clustering for Double Open-Circuit Fault Diagnosis of Power Inverters," in *2019 4th Conference on Control and Fault Tolerant Systems (SysTol)*, IEEE, Sep. 2019, pp. 306–311. doi: 10.1109/SYSTOL.2019.8864777.

[18] W. Yang, W. Wang, X. Wang, J. Gu, and Z. Wang, "Fault diagnosis method of a cascaded H-bridge inverter based on a multisource adaptive fusion CNN-transformer," *IET Power Electronics*, Jan. 2024, doi: 10.1049/pel2.12664.

[19] S. S. Ghosh, S. Mukherjee, S. Chattopadhyay, and A. Das, "Premature Breakdown Identification in Photovoltaic Array Fed IGBT-based Voltage Source Converter," *Journal of Nano- and Electronic Physics*, vol. 15, no. 3, pp. 03016-1-03016–5, 2023, doi: 10.21272/jnep.15(3).03016.

[20] S. S. Ghosh *et al.*, "Wavelet-based rapid identification of IGBT switch breakdown in voltage source converter," *Microelectronics Reliability*, vol. 152, p. 115283, Jan. 2024, doi: 10.1016/j.microrel.2023.115283.

Chapter 10

DWT-based Rapid Detection of IGBT Switch Failure of Voltage Source Converters in Microgrid

Abstract- In modern technology, the insulated gate bipolar transistor (IGBT) is a cornerstone component. By employing a microgrid (MG), conventional distribution networks may become more safe, stable, and dependable. Inverter-based MGs are a viable, alluring, and practical choice for energy distribution networks.

A technique for determining the IGBT switches breakdown failures (IBDFs) in three-phase voltage source converters (VSCs) connected to the photovoltaic (PV) system is presented in this chapter. The discrete wavelet transform (DWT) approach was used to analyze the VSC's phase voltage output. The presented study includes the wavelet coefficients of the VSC's phase voltage output harmonic spectra's skewness, kurtosis, and root mean square (RMS) measurements to detect IBDF. Comparative analysis was conducted for determining the most effective parameter for the identification of IBDF. Furthermore, the investigation's contrasting findings and distinctive contributions are presented.

Keywords: Discrete wavelet transform (DWT); microgrid, photovoltaic (PV); voltage source converter (VSC).

10.1 Introduction

As the world's power usage rises, it has become more imperative today to use renewable forms of energy, like photovoltaic (PV) [1]. Considering their widespread availability and minimal impact on the environment, PV energy systems are one of the most promising forms of renewable energy [2]. Since the adoption of green energy has risen decisively, power converters are extensively utilized [3], [4]. IGBTs facilitate electrical energy to be efficiently converted and regulated in power electronic systems. VSCs may conveniently connect to decentralized and variable sources of electricity. VSCs may handle electricity from such sources without requiring synchronization since they frequently provide power that is asynchronous in relation to the main grid. VSC technology makes it possible to connect autonomous grids [5]. VSCs have become prevalent in a growing range of power system uses to increase power controllability and efficient use of energy [6]. IGBTs are rated for high voltage and current. IGBTs can tolerate short-circuit situations for a substantial period of time, which is typically exceeding 10 microseconds, without experiencing catastrophic damage [7]. In VSCs, IGBTs are frequently used as power devices [7]. Semiconductor devices are among the most susceptible parts of power converters [8]. The primary reason for the shortened lifespans of power electronic devices is thermal stress in switching elements such as IGBTs and MOSFETs, especially when working at high switching frequencies [9]. It could lead to wear-out breakdowns that cause inconsistent system functioning or the failure of such components, like an open-circuit (OC) or short-circuit (SC) [9], [10].

The Fig. 10.1 illustrates that power equipment featuring IGBTs as well as MOSFETs is responsible for about 21% of converters' failures [9], [10], [11].

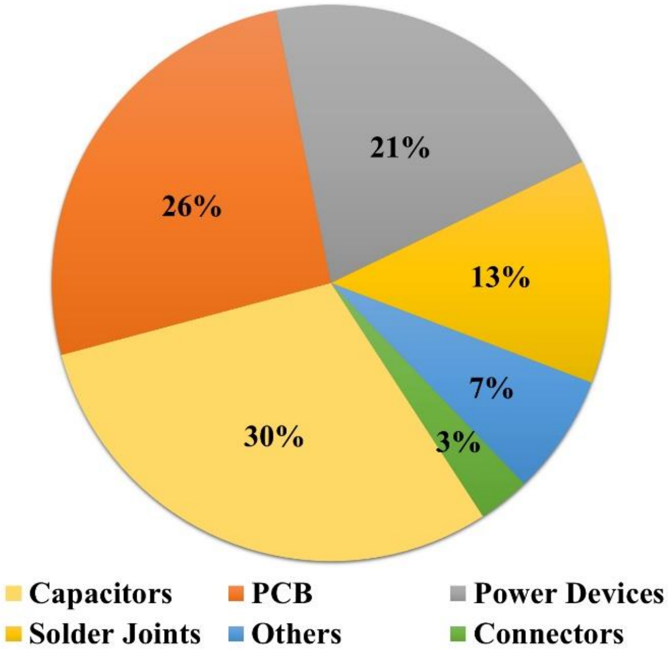

Fig. 10.1. Rates of failure of a conventional converter's major components

The authors propose [12] a rapid diagnostic method for nonsensical inverters OC fault. In [13], the authors introduced a method for detecting OC faults in the voltage source inverter (VSI) of drive systems. An intrinsic converter issue might lead to a rise in voltage harmonics, waveform deformation, and a decline in power quality [14], [15]. J. Zhang et al. proposed a novel method for determining OC defects in the IGBT modules of wind energy converters [16]. The identification of OC failures in three-phase VSI was proposed by the authors [17]. The IGBT OC issue with the modular multilevel converter (MMC) submodules was identified by Y. Shen et al. [18]. X. Sun et al. developed an error-identifying approach for systems based on VSC-HVDC converters [19]. The primary contributors to flaws in IGBT modules are OC or SC malfunctions [9]. M. Ma et al. devised a technique for detecting SC malfunctions in inverters [20]. C. Sui et al. suggested a strategy [21] to determine the OC issue in the VSC.

Additionally, there hasn't been much focus on the importance of developing a rapid and reliable IBDF detection technique for VSCs. A distinct technique for determining the IBDF of the VSCs has been outlined in this chapter.

A wavelet-based statistical investigation was performed here to detect IBDF. To identify IBDF, the VSC's phase voltage output was monitored under normal conditions and at various percentages of IBDF (%IBDF). While the voltage signal is unaffected by the loads, the current signal is significantly affected. Hence, the voltage signal was captured for the purpose of IBDF identification in this investigation.

10.2 Grid-Linked IGBT-Based VSC

The grid-tied PV array-powered VSC is depicted schematically in Fig. 10.2. In Fig. 10.3, the laboratory testing facility is illustrated.

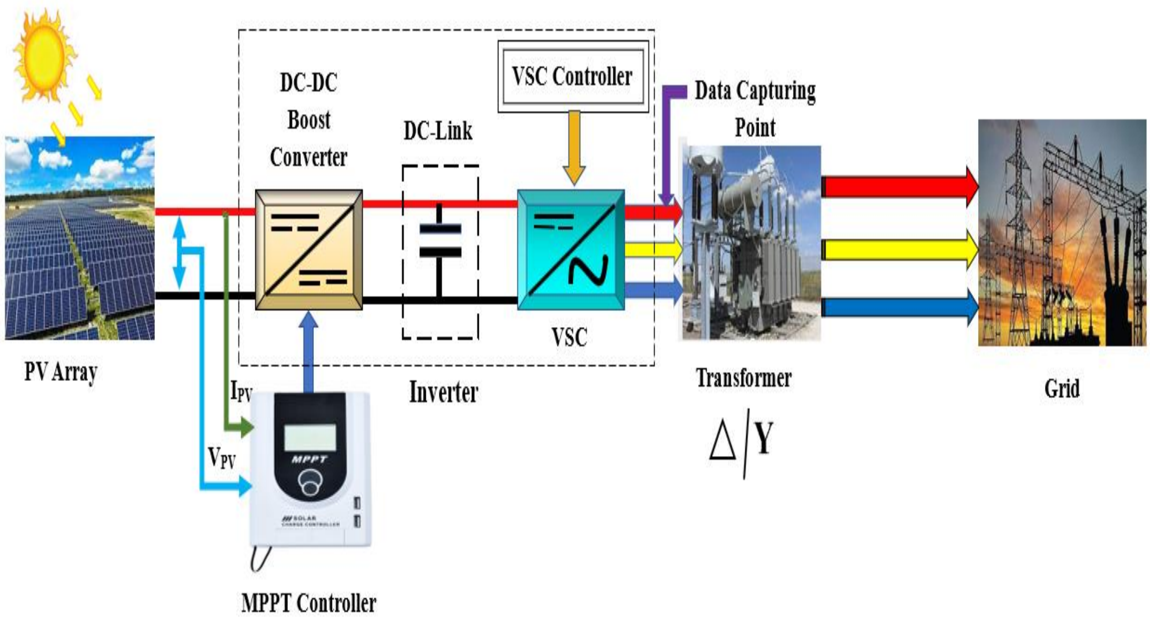

Fig. 10.2. Schematic of the PV array-powered VSC connected to the grid

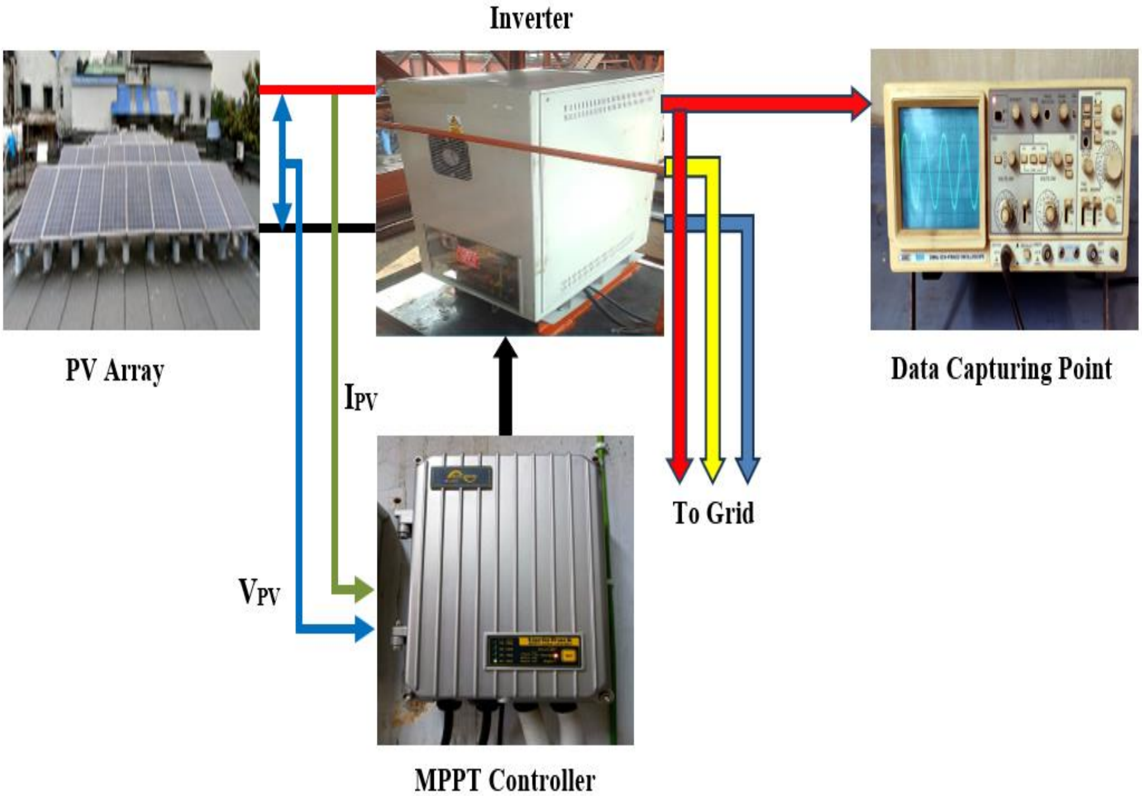

Fig. 10.3. Laboratory testing facility

10.2.1 PV System

A PNPN diode-based analogous PV module circuitry is used, as seen in Fig. 10.4.

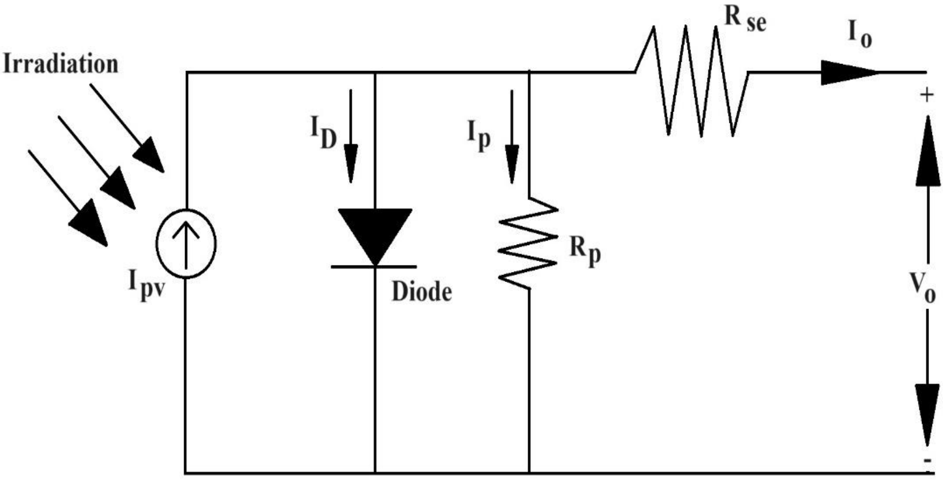

Fig. 10.4. PV module's equivalent circuit

The following formula [22] can be used to calculate the PV module's output current:

$$I_o = I_{pv} - I_D \left\{ \exp\left[\frac{q(V_o + I_o R_{se})}{AK_B T_{pv}} \right] - 1 \right\} - \frac{V_o + I_o R_{se}}{R_p} \qquad (10.1)$$

where,

I_o, V_o = PV cell's output current (A) and output voltage (V);

I_{pv}, I_D = PV cell's photocurrent and diode saturation current (A);

R_{se} = Solar cell series resistance (ohm);

R_p = Solar cell parallel resistance (ohm);

q = electron charge (1.602×10^{-19} coulomb);

A = P-N junction's ideality factor;

K_B = Boltzmann's constant ($1.3806452 \times 10^{-23}$ J/K);

T_{pv} = operational temperature of PV cell (Kelvin)

A 100 kW PV array is included in the model for this investigation. It generates the highest power when the module's temperature is 25°C and the irradiance is 1000 W/m^2. The technical details of the PV system are listed in Table 10.1.

Table 10.1. Technical details of the PV system

	Parameters	**Values**
Array Data	PV array count	1
	Quantity of PV modules linked in series with each string	5
	Parallel string count	66
	Maximum array power	100 kW
Module Data	Module type	SPR-305E-WHT-D
	Cells in every module (N_c)	96
	Maximum Power, P_{max} (W)	305.226
	SC current, I_{sc} (A)	5.96
	OC voltage, V_{oc} (V)	64.2
	Current during P_{max}, I_{pm} (A)	5.58
	Voltage during P_{max}, V_{pm} (V)	54.7
	Shunt resistance, R_{sh} (ohm)	269.60
	Series Resistance, R_{se} (ohm)	0.37

10.2.2 Maximum Power Point Tracking (MPPT)-equipped Boost Converter

The PV array is linked to a 25 kV grid. A 3-phase VSC featuring a boost converter was used to connect the PV array to the grid. The PV's intrinsic voltage of 272 V is boosted to 500 V by means of the MPPT-enabled boost converter. The schematic of the boost converter and the PV array is demonstrated in Fig. 10.5.

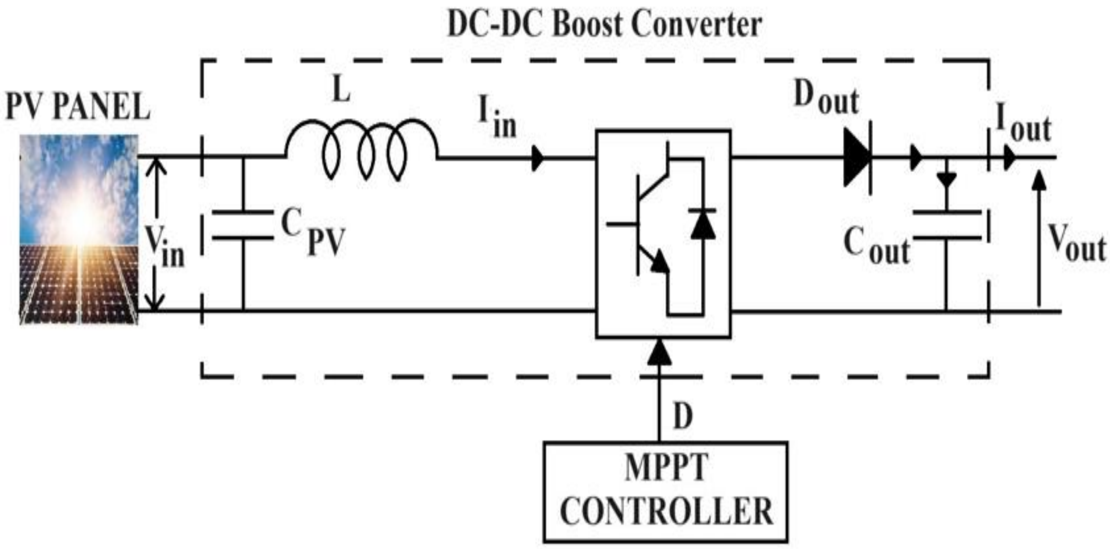

Fig. 10.5. MPPT boost converter's equivalent circuit

The following mathematical formulas illustrate the converter's topology according to the state-space model [9], [22], [23]

$$V_{in} = L\frac{dI_{in}}{dt} + V_{out}(1-D) \tag{10.2}$$

$$C_{out}\frac{dV_{out}}{dt} + I_{out} = (1-D)I_{in} \tag{10.3}$$

where,

V_{in} = Output of PV system and boost converter's input voltage;

V_{out} = intended output voltage of boost converter;

L, C_{out} = boost converter inductance and output capacitance;

D = boost converter's duty cycle;

I_{out} = boost converter's output current

I_{in} = boost converter's input current.

10.2.3 Overview of VSC

The equivalent circuit of the 3-phase inverter connected with an AC grid is illustrated in [9], [24].

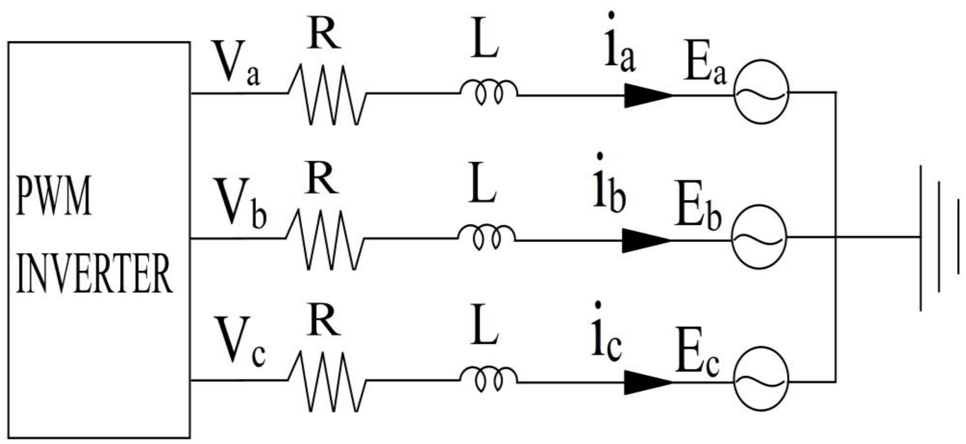

Fig. 10.6. AC grid-connected equivalent circuit of a 3-phase inverter

The representations for the grid's corresponding per-phase inductance and resistance are *R*, *L*. V_a, V_b, and V_c are the voltages at the inverter's output. 3-phase grid voltages are E_a, E_b, and E_c. Three-phase currents, i_a, i_b, and i_c, are injected into the grid. The following equations are produced after applying KVL to the inverter's output and converting the equations from *abc* to *dq* values using the Park and Clark transforms [9], [24]:

$$\frac{di_d}{dt} = -\frac{R}{L} i_d + \frac{1}{L} u_d \tag{10.4}$$

$$u_d = V_d - E_d - L\omega i_q \tag{10.5}$$

$$\frac{di_q}{dt} = -\frac{R}{L} i_q + \frac{1}{L} u_q \tag{10.6}$$

$$u_q = V_q - E_q + L\omega i_d \tag{10.7}$$

where,

i_d, i_q= d-q axis currents (A) at the inverter output;

V_d, V_q= d-q axis voltages (V) at the inverter output;

E_d, E_q= d-q axis grid voltages (V) of 3-phases;

ω= grid radial frequency in rad/s;

u_d, u_q= d-q axis steady-state control functions

The process of inverter triggering is carried out via pulse-width modulation (PWM). The modulation index (m), the DC link voltage (V_{dc}), and the inverter's voltage output are related in the manner illustrated below [9], [25]:

$$V_d = m_d \frac{V_{dc}}{2} \tag{10.8}$$

$$V_q = m_q \frac{V_{dc}}{2} \tag{10.9}$$

A consistent power factor is maintained since the VSC converts the DC link's voltage from 500 V to 440 V (phase to phase) AC. Two control loops are used by the VSC controls. One is an internal control loop that controls the grid's active and reactive currents, while the other is an external control loop that maintains the DC link's voltage to within +/- 250 V.

The suggested method for identifying IBDF was validated using MATLAB. Furthermore, the VSC's IBDF was also determined by the use of real-world case studies. To identify IBDF, the VSC's phase voltage output was monitored under normal conditions and at various %IBDF in the VSC.

10.3 Considered Fault and Problem Description

10.3.1 IGBT Failure

The grid-tied PV array-powered IGBT-oriented VSC's IGBT failure is considered for failure evaluation.

10.3.2 Causes of IGBT Failure

It may occur as a result of a disproportionate spike in current, that enhances the temperature and burns off the IGBT. An increase in voltage may also be the reason, leading to insulation breakdown. It causes the IGBT to malfunction in both cases by interfering with the circuitry related to path openings. Additionally, IGBTs may gradually deteriorate under conditions of sustained strain, leading to failure.

IGBT modules have complex assemblies composed of many material layers that come together to form chips and packages [9]. Numerous failure situations are possible with IGBT modules. Such forms of failure are primarily divided into two categories: chip failures and package failures [9], [26]. Each of the kinds of faults could be subsequently segmented as wear-out faults (WOFs) and overstressed faults (OSFs). Table 10.2 shows an array of IGBT failure types [9].

Table 10.2. IGBT failure types

Failure Types		**Causes**	**Diverse Impacts upon the System**
Chip related failure	OSF	Gate overvoltage	• Open circuit defects (OCD) • Short circuit defects (SCD) • Lift-off wire bonds • Secondary breakdowns
		Overvoltage in collector-emitter	
		Overcurrent	
		Burnouts due to cosmic rays	
	WOF	Time-varying dielectric's failures	• Switches and gate drivers' malfunctions • Leakage current increase • Decline in the chip's capacity to block voltage
		Injection of hot carriers	
		Electrochemical migrations (ECMs)	
Package related failure	OSF	Heat shocks	• Wear-outs • OCD or SCD • Package connectivity melting • Voltage breakdowns • Burnouts
		Mechanical pressures and shocks	
		Thermal runaway	
		Flashovers	
	WOF	Electromigration (EM) and ECM	• Bond-wire corrosion, Hot spots • Deterioration of the stiffness of different packaging layers • Crack in bond-wires, solder defect • Leakage current • Decline in the module's capacity to block voltage • Bond-wire's corrosions
		Thermal stresses (TSs)	
		Thermal fatigues (TFs)	
		Insulation deterioration	

10.3.3 Effects

Following the IBDF issue, it results in the circuitry path open. Table 10.2 shows the numerous negative impacts that different kinds of IGBT malfunctions can have on the system.

10.3.4 Problem Statement

IGBT shielding is quite difficult and complicated. When a defect appears, it will be destroyed by heat buildup during the desaturation stage, and the fault's increasing current rate during the early stages of an IGBT malfunction is nearly absurd [9], [27]. Therefore, speedy and accurate IBDF detection is indispensable. This analysis has attempted to identify the continuous rise in VSC's IBDF.

This chapter proposes a unique method for determining the IBDF of the VSCs. In this study, a 100% defect indicates the IGBT switch's total failure, while the modest defect percentage indicates the fault's onset affecting the IGBT's effective resistance

10.4 Approach for Fault Diagnosis

To identify IBDF, the VSC's phase voltage output was monitored under normal conditions and at various %IBDF. The discrete character of the voltage signals recorded makes DWT appropriate for analysis [28]. Through the extraction of a few characteristics deemed appropriate for defect diagnosis, statistical analysis was conducted.

10.4.1 Using DWT to Diagnose Faults

The computing unit is unable to instantly distinguish between the problems using the simple Fourier transform approach because the collected signal in this case is erratic. The wavelet transform constitutes a particularly useful technique for processing non-stationary data [9], [28]. Wavelet coefficients of the VSC's phase voltage output harmonic spectra's skewness, kurtosis, and root mean square (RMS) measurements were monitored to detect IBDF.

The amount of wavelet coefficients that DWT provides is defined according to the integers of discrete steps in scale and translation, indicated by m and n. For RMS, the scale and translation will be $a = a_0^m$ and $b = nb_0a_0^m$. if the segmentation's step size of the scale and translation be a_0 and b_0, accordingly. The coefficients of the discrete wavelet are therefore expressed as following [9], [28]:

$$DWT(m,n)=\int_{-\infty}^{\infty}\frac{1}{\sqrt{a_0{}^{m}}}f(t)g(a_0{}^{-m}t-nb_0)d(t) \qquad (10.1)$$

where $g(a_0^{-m}t-nb_0)$ represents the translated and scaled discrete wavelet.

For the IBDF investigation, the VSC's output phase voltage was recorded. The acquired voltage was decomposed till DWT 9th level. The Daubechies wavelet's mother wavelet in this instance is identified as "db4". For both normal and defective circumstances (up to 10%) of IBDF, approximated and detail coefficients were calculated through DWT level 9.

A few of the findings from the overall outcome are illustrated in Fig. 10.7. It is difficult to discern between varying IBDF percentages utilizing the graphical evaluation method demonstrated in Fig. 10.7, since all of the graphical findings seem to imply the same.

Therefore, it is impossible to derive an exact finding from the data that may be utilized to identify the IBDF. Skewness, kurtosis, and RMS values of the VSC's voltage harmonic spectra through DWT 9 levels were further calculated for the intent of detecting IBDF.

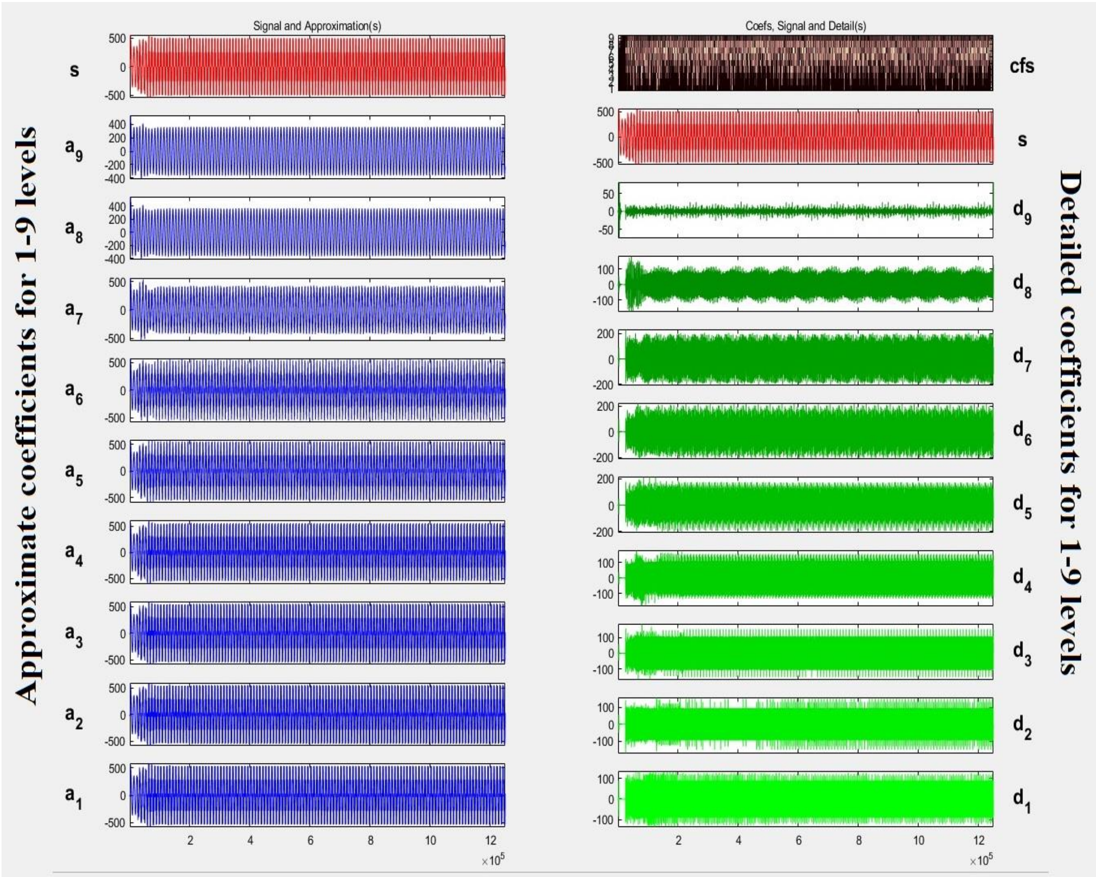

(a) during typical condition

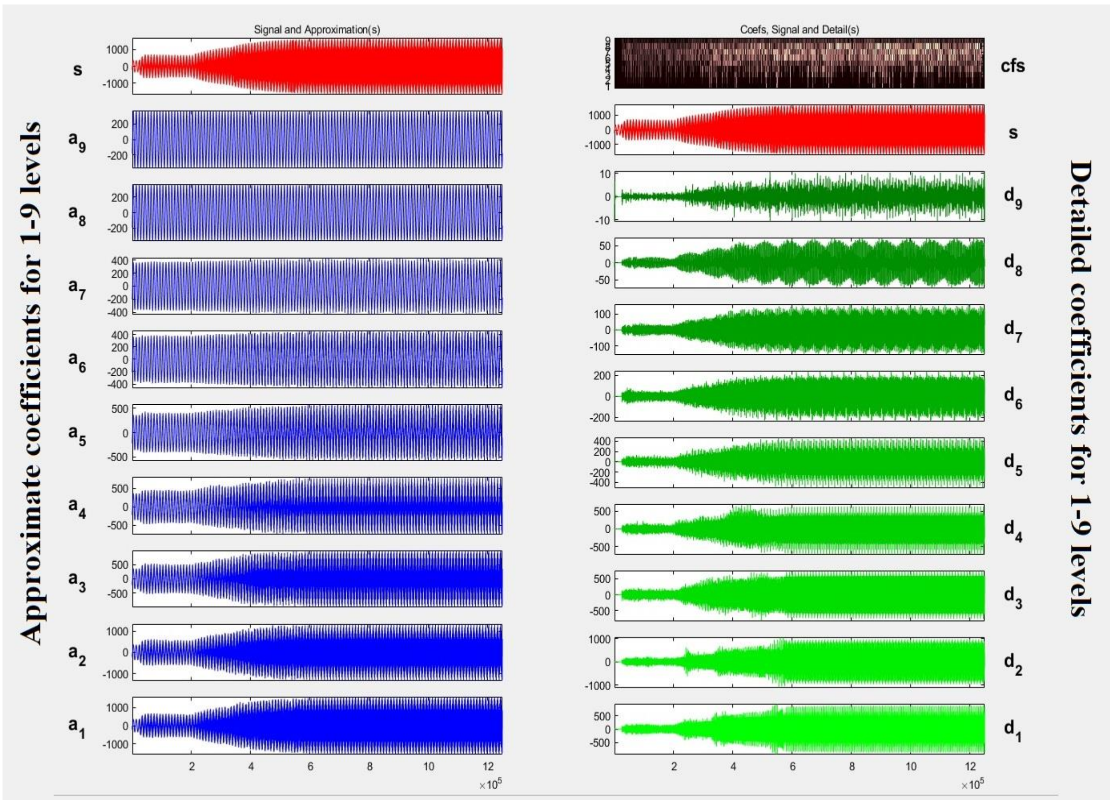

(b) during 5% fault

Fig. 10.7. Approximated and detail coefficients during various %IBDF

10.4.2 Considered Statistical Parameters

The coefficients of wavelet decomposition are represented as follows:

The approximated and detail coefficients' kurtosis, skewness, and RMS values are represented as K_A, K_D, S_A, S_D, R_A, and R_D, respectively. For both approximate and detail coefficients till the DWT level 9, the skewness, kurtosis, and RMS values may be written as follows [9]:

$$[s] = \begin{bmatrix} [S_A] \\ [S_D] \end{bmatrix} = \begin{bmatrix} S_{A1} & S_{A2} & S_{A3} & S_{A4} & S_{A5} & S_{A6} & S_{A7} & S_{A8} & S_{A9} \\ S_{D1} & S_{D2} & S_{D3} & S_{D4} & S_{D5} & S_{D6} & S_{D7} & S_{D8} & S_{D9} \end{bmatrix} \quad (10.2)$$

$$[k] = \begin{bmatrix} [K_A] \\ [K_D] \end{bmatrix} = \begin{bmatrix} K_{A1} & K_{A2} & K_{A3} & K_{A4} & K_{A5} & K_{A6} & K_{A7} & K_{A8} & K_{A9} \\ K_{D1} & K_{D2} & K_{D3} & K_{D4} & K_{D5} & K_{D6} & K_{D7} & K_{D8} & K_{D9} \end{bmatrix} \quad (10.3)$$

$$[R] = \begin{bmatrix} [R_A] \\ [R_D] \end{bmatrix} = \begin{bmatrix} R_{A1} & R_{A2} & R_{A3} & R_{A4} & R_{A5} & R_{A6} & R_{A7} & R_{A8} & R_{A9} \\ R_{D1} & R_{D2} & R_{D3} & R_{D4} & R_{D5} & R_{D6} & R_{D7} & R_{D8} & R_{D9} \end{bmatrix} \quad (10.4)$$

In acquired voltage signal examination and assessment of IBDF, which generate non-stationary signals, statistical factors are proven to be useful.

10.4.3 Evaluation of Statistical Factors for Approximation Coefficients

The K_A, R_A, and S_A were computed for standard and various %IBDF circumstances, and they are illustrated in Fig. 10.8, Fig. 10.9, Fig. 10.10. It is noticeable in Fig. 10.8 that till 3% of IBDF, the K_A values for the 1st to 3rd levels are quite similar, following then, these numbers grew till IBDF became 5%. From the 4th to 6th decomposition levels, K_A readings rose until the IBDF reached 4%. At the 7th DWT level, K_A readings rose until the IBDF reached 3%. Also, the K_A readings for the 8th and 9th levels are highly erratic and do not yield any beneficial outcomes for problem identification.

As the %IBDF climbs to 4%, the graphical representation in Fig. 10.8 illustrates how the R_A readings from the 1st through 4th and 6th stages of DWT display an exponentially expanding aspect. The visual examination of Fig. 10.9 additionally demonstrates that the RA readings for the 5th, and 7th to 9th DWT levels do not effectively rise or fall exponentially as the %IBDF increases and that hinders the ability to identify IBDF.

K_{A4} to K_{A7}, R_{A1} to R_{A4}, and R_{A6} values will therefore be useful for IBDF evaluation.

Furthermore, as the S_A values in Fig. 10.10 are meandering in form, a graphic evaluation of these data likewise does not offer compelling evidence for problem identification.

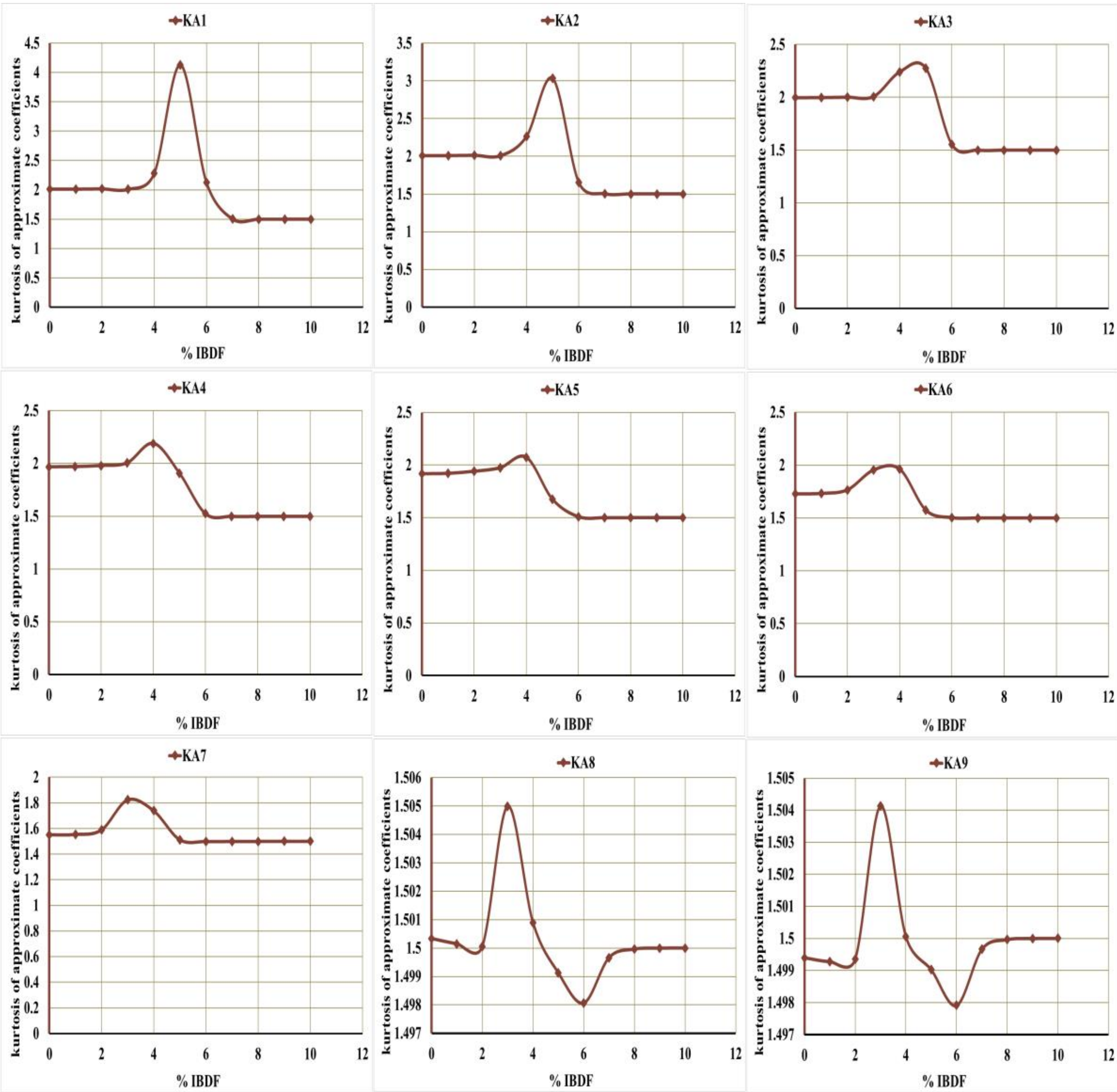

Fig. 10.8. K_A vs. %IBDF

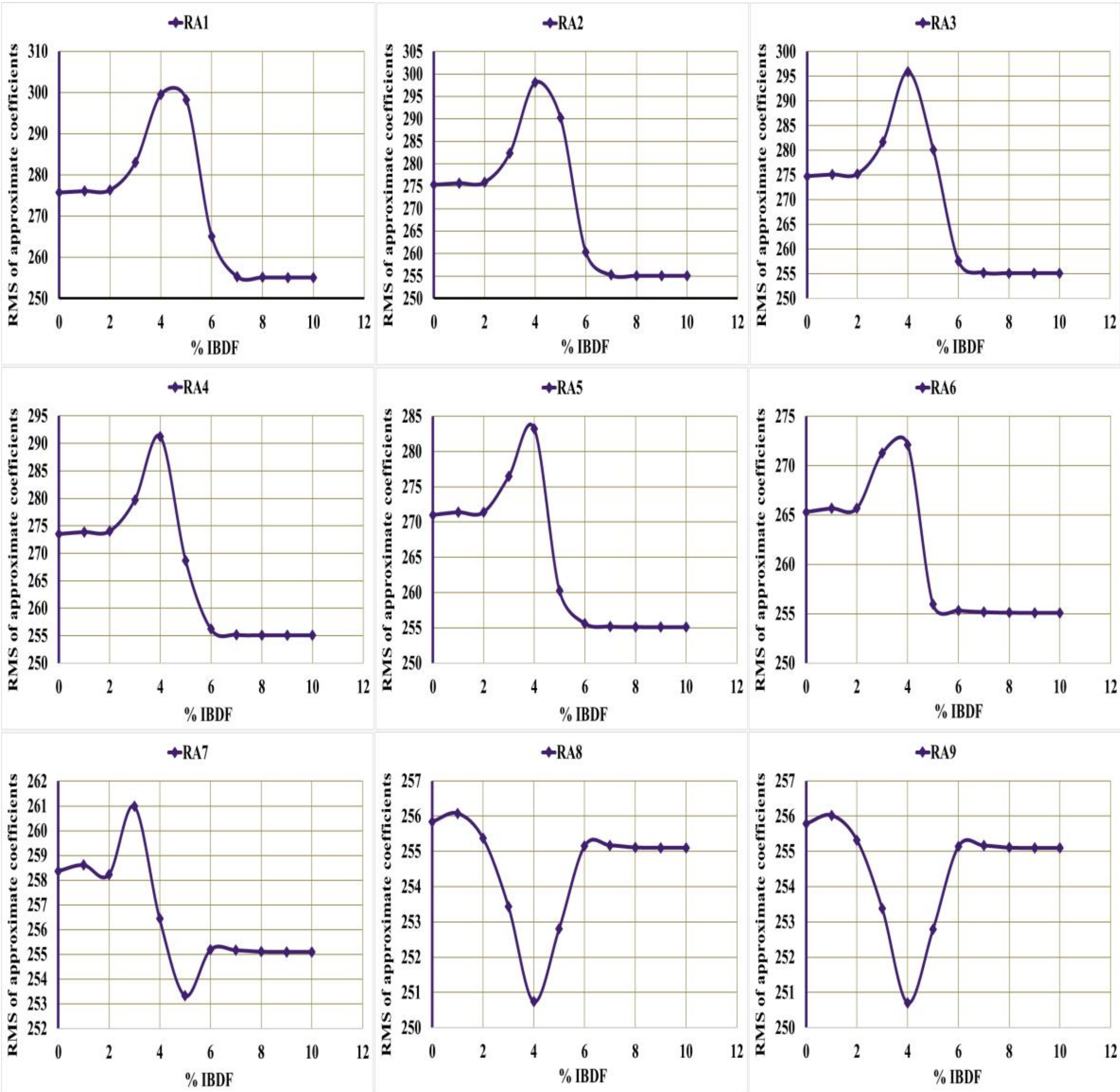

Fig. 10.9. R_A vs. %IBDF

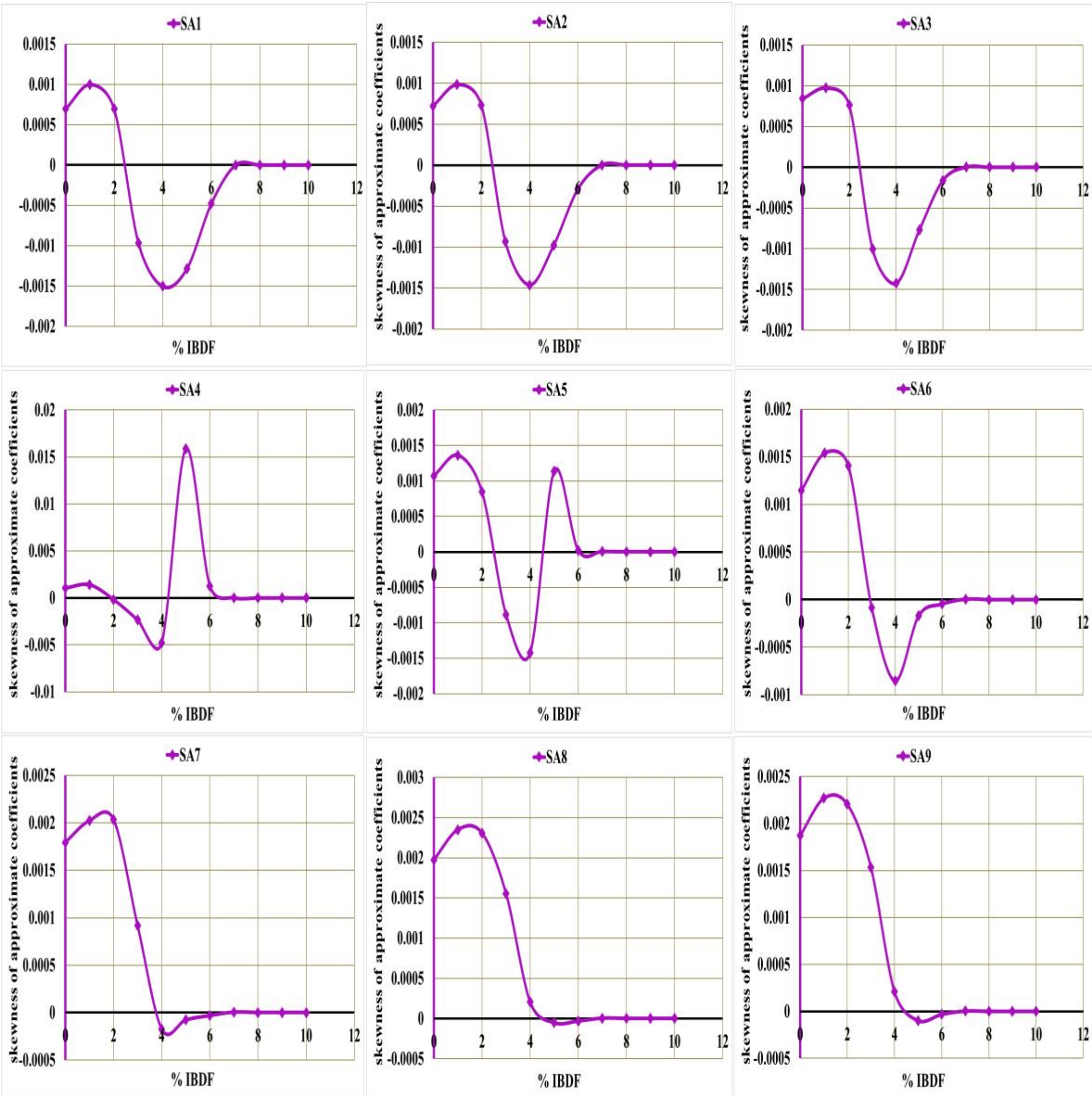

Fig. 10.10. S_A vs. %IBDF

10.4.4 Evaluation of Statistical Factors for Detail Coefficients

The K_D, R_D, and S_D were computed for standard and various %IBDF circumstances, and they are illustrated in Fig. 10.11, Fig. 10.12, and Fig. 10.13. The K_D readings are displayed in Fig. 10.11, which indicates that no specific hypotheses could be made using this information for defect detection.

According to a graphical study of Fig. 10.12, R_{D1}, R_{D2}, R_{D4} to R_{D6}, and R_{D9} readings lack a proper pattern of gradual growth or decline. So, that could not be helpful for the IBDF detection study. It is noticeable that till 5% of IBDF, the R_{D3} values rise exponentially, following then, these readings decrease as the %IBDF grows. Furthermore, the R_{D7} value rises exponentially till 4% and then these readings decrease as %IBDF evolves. Whereas, the R_{D8} value grows exponentially till 3%, following which these readings also decrease as %IBDF increases.

S_{D1} to S_{D4}, and S_{D9} in Fig. 10.13 demonstrates that the majority of the outcomes are in a fairly erratic pattern and that no useful inference can be drawn from them for the detection of IBDF. The remaining, S_{D5} to S_{D8} values, also hinder the ability to evaluate IBDF.

Therefore, for IBDF analysis, only the R_{D3}, R_{D7}, and R_{D8} are likely to be helpful.

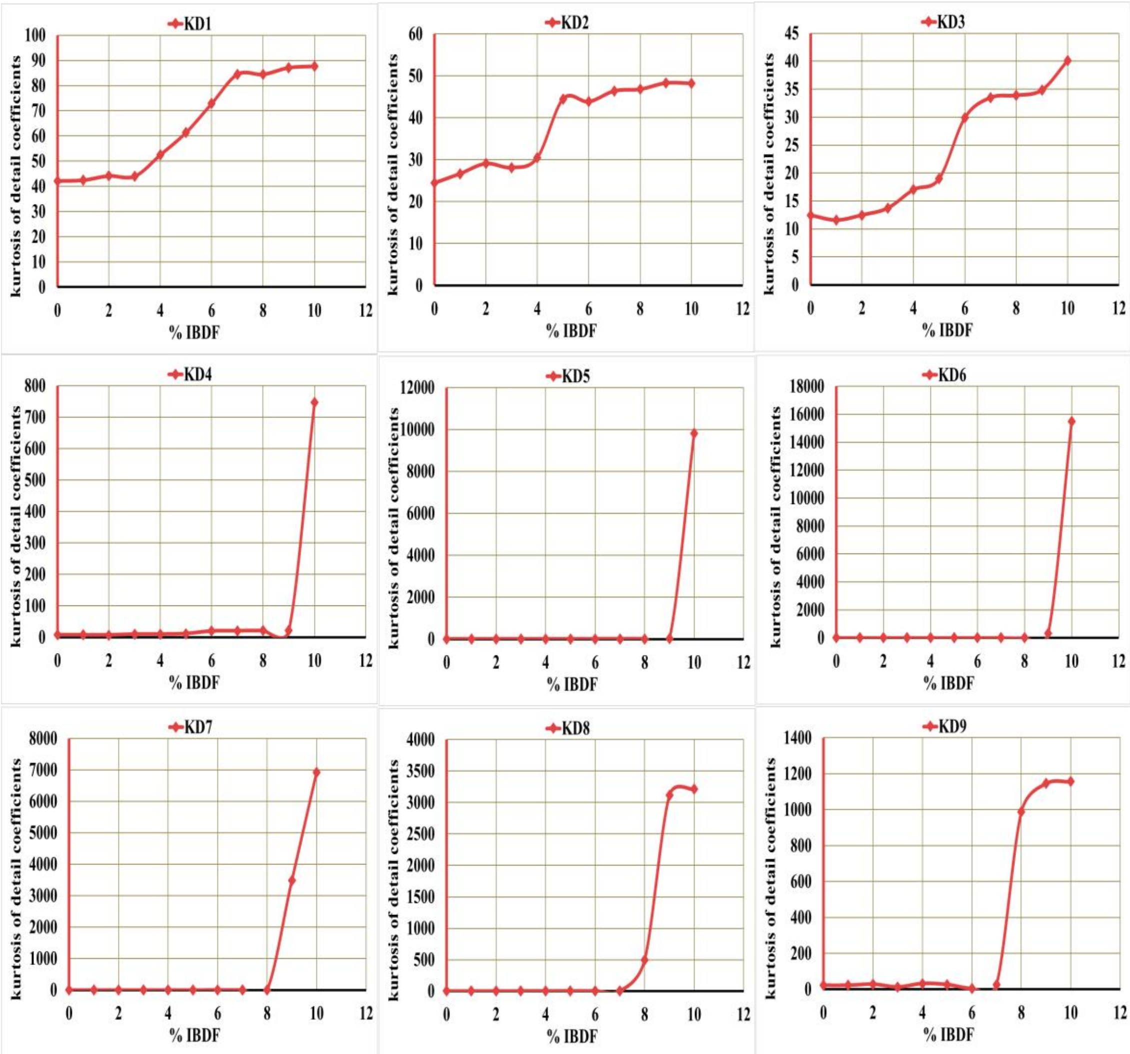

Fig. 10.11. K_D vs. %IBDF

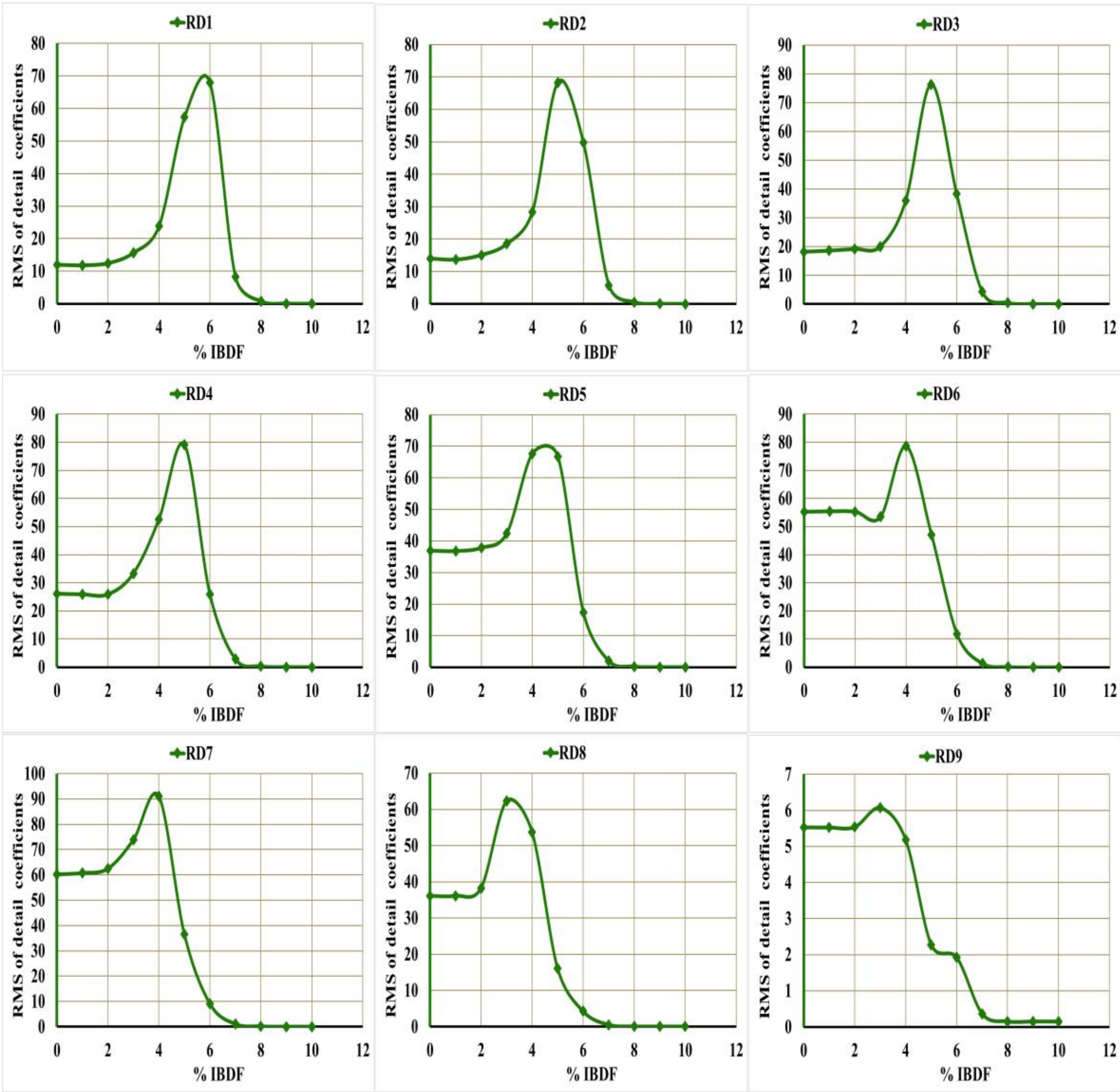

Fig. 10.12. R_D vs. %IBDF

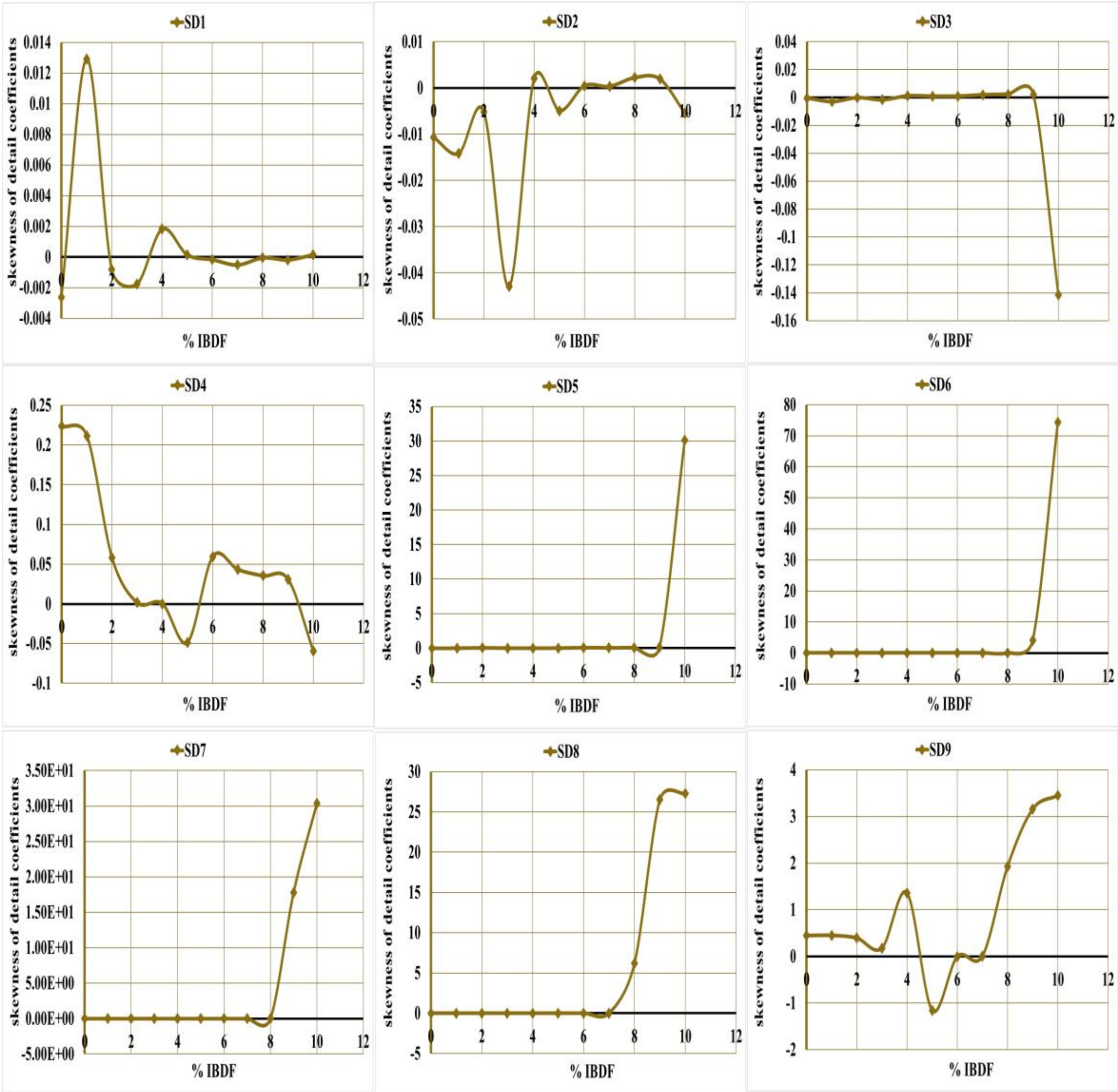

Fig. 10.13. S_D vs. %IBDF

10.5 Discussing Preferable Optimal Parameter and Precise Outcome

The likely effective curves for diagnosing IBDF were chosen from Fig. 10.8, Fig. 10.9, Fig. 10.10, Fig. 10.11, Fig. 10.12, Fig. 10.13, as seen in Fig. 10.14.

Based on the analysis of Fig. 10.14, it is noted that the curves of K_{A4}, K_{A5}, K_{A6} are increasingly pronounced until the IBDF reached 4%, and K_{A7} readings rose until the IBDF reached 3%.

Additionally, it appears that the characteristics of the curves of R_{A1} to R_{A4}, R_{A6}, and R_{D7} continue to rise exponentially until 4% of IBDF, and then these readings decrease as %IBDF evolves. Whereas the R_{D8} value grows exponentially till 3% of IBDF. Besides, till 5% of IBDF, the R_{D3} value rises exponentially, following then, these readings decrease as %IBDF grows.

Here, Fig. 10.14 illustrates the exponential changes of R_{D3}, with less non-linear variations until 3% than between 3% and 5% IBDF. To optimize the calculation within a linear scale, two fault ranges- 0% to 3% along with 3% to 5%, have been examined using logarithmic readings of R_{D3}. Table 10.3 makes it evident that the logarithmic scale curves, especially for the 3% to 5% range, have a greater linearity. This implies that IBDF fault diagnosis may be accomplished efficiently with the R_{D3} logarithmic scale.

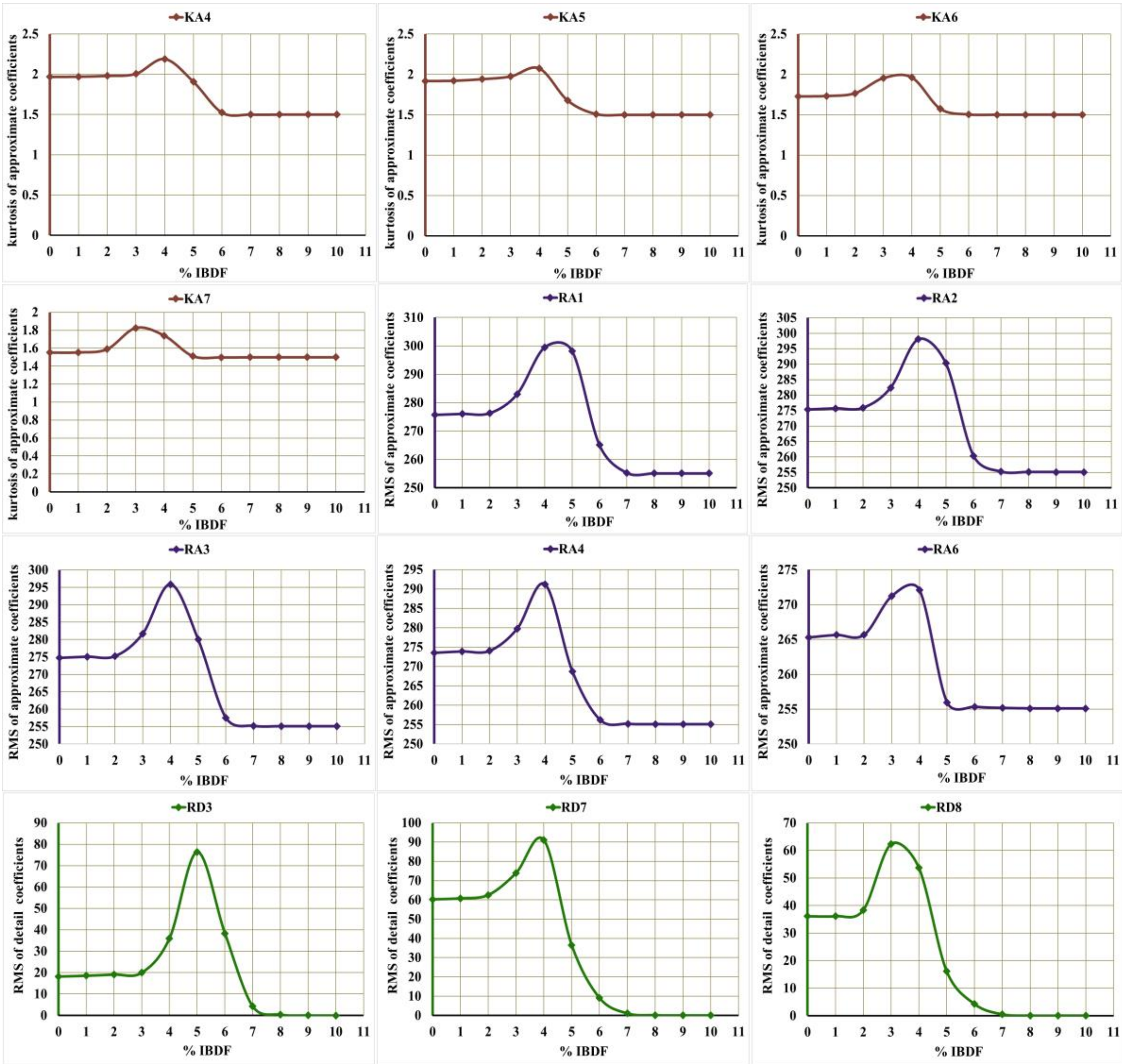

Fig. 10.14. Preferred curves for IBDF analysis

Table 10.3. The characteristics of R_{D3}, log (R_{D3})

<table>
<tr><th>Fault Ranges</th><th>R_{D3}</th><th>$\log(R_{D3})$</th></tr>
<tr><td>0%-3%</td><td>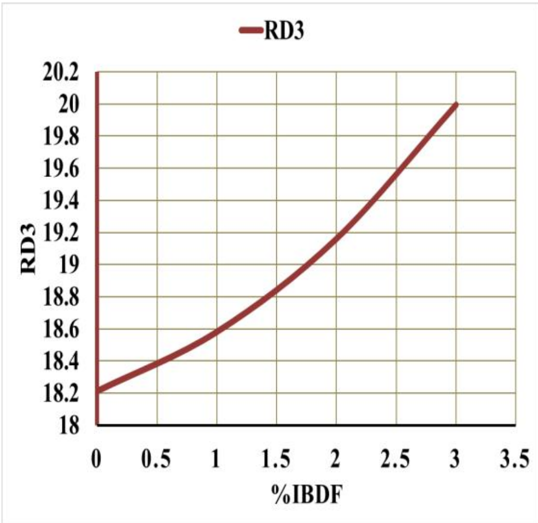
</td><td>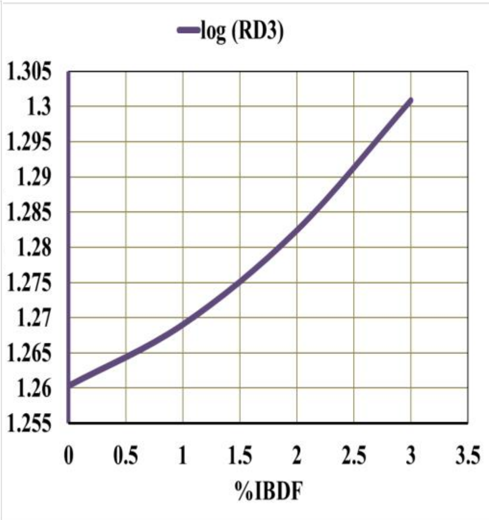
</td></tr>
<tr><td>3%-5%</td><td>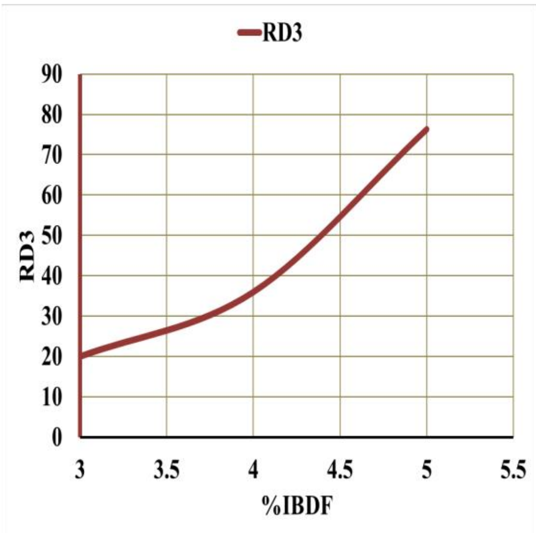
</td><td>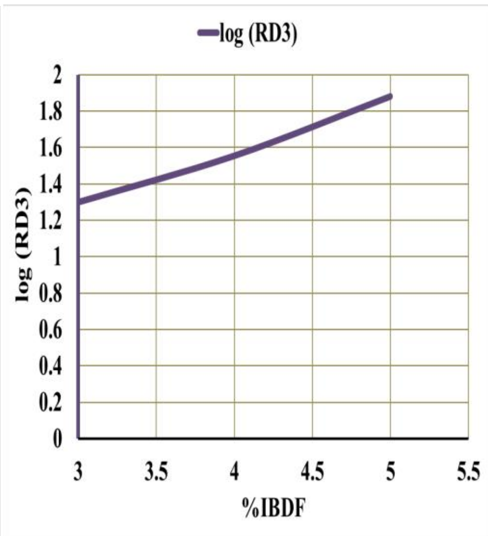
</td></tr>
</table>

10.6 Algorithm for Detecting IBDF

The Fig. 10.15 depicts the suggested method of IBDF detection.

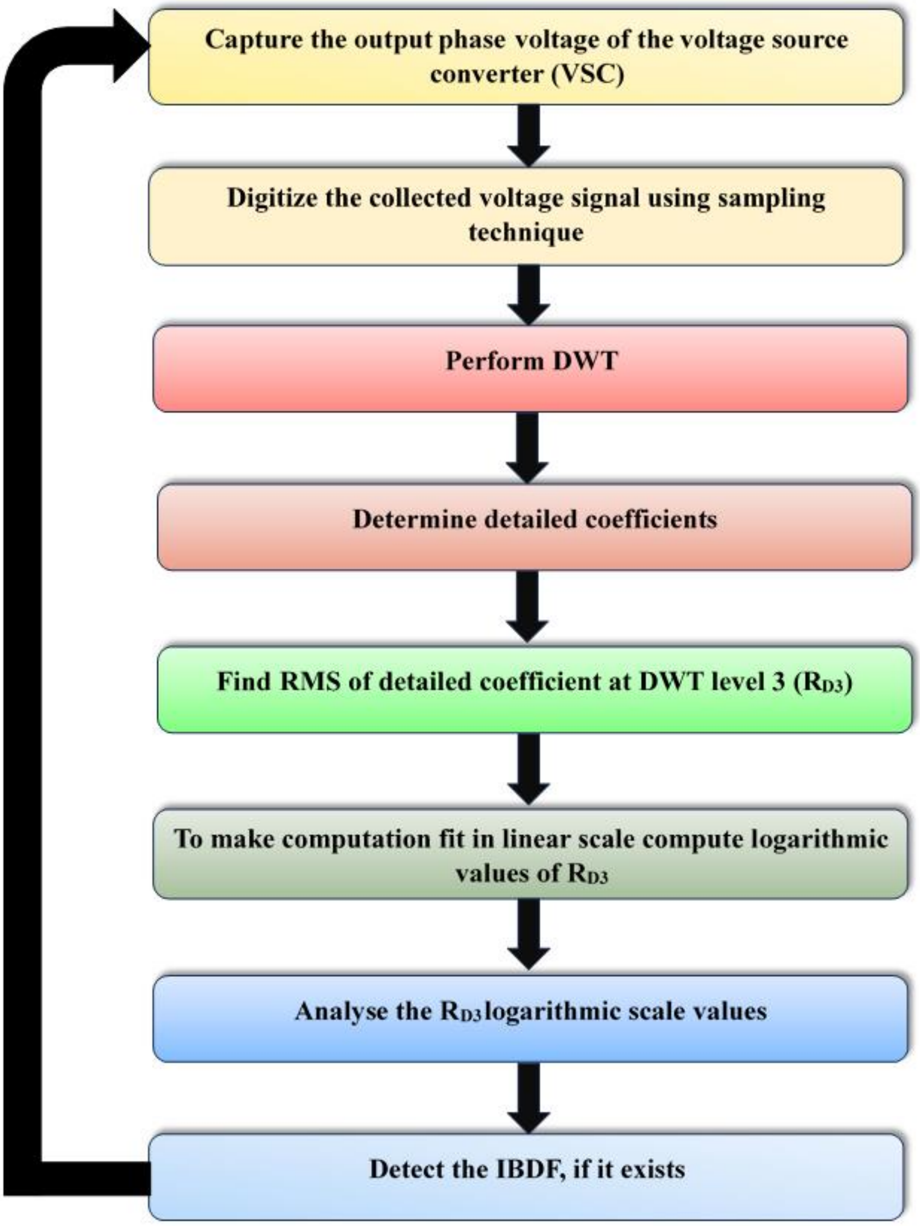

Fig. 10.15. IBDF identification algorithm

The following algorithm was suggested for IBDF detection:

a) Acquire the VSC's phase voltage output.
b) Digitize the recorded voltage signal using the sampling procedure.
c) Apply DWT to the recorded data.
d) Compute R_{D3}.
e) Analyse logarithmic readings of R_{D3}.
f) Check for IBDF.

10.7 Comparative Assessment and Unique Contribution

Table 10.4 summarizes the findings of comparisons among the suggested study alongside additional comparable IGBT problem identification research approaches. For failure recognition [29], [30], [31], [32], the current signal had been exploited. A voltage signal analysis-oriented failure identification technique was introduced by Y. Shen et al. [18]. In [33], [34], [35], a few additional IGBT failure detection techniques using various parameters were proposed.

Table 10.4. Comparative analysis

Ref.	Variable(s) Assessed	Predictive Method?	%IBDF Computing Possibility
[7], [14], [29], [30], [31], [32]	Current	Yes	No
[18]	Voltage	Yes	No
[33]	Each submodule's capacitor voltages	Yes	No
[34]	DC current signal	Yes	No
[35]	Capacitor voltage and circulatory current	Yes	No
Proposed Method	Voltage	Yes	Yes

10.8 Conclusion

In this work, a DWT-based analytical study of the VSC's output phase voltage has been performed in an attempt to diagnose IBDF. For the purpose of identifying IBDF, many statistical metrics have been observed. The values of the pertinent parameters have been observed to be fluctuating throughout the fault detection procedure. Furthermore, it was discovered that R_{D3} has proven to be exceptionally efficient for IBDF detection. The data gathered from DWT-based diagnostics has been compared and evaluated in an effort to determine the best reliable method for IBDF detection. Therefore, by using the recommended method, the VSC's IBDF may be found by continual tracking of readings. The investigation additionally indicated that the %IBDF in the VSC could be obtained using the approach suggested.

References

[1] B. Dhouib, M. A. Zdiri, Z. Alaas, and H. Hadj Abdallah, “Fault Analysis of a Small PV/Wind Farm Hybrid System Connected to the Grid,” *Applied Sciences*, vol. 13, no. 3, p. 1743, Jan. 2023, doi: 10.3390/app13031743.

[2] W. Yuan, T. Wang, D. Diallo, and C. Delpha, “A Fault Diagnosis Strategy Based on Multilevel Classification for a Cascaded Photovoltaic Grid-Connected Inverter,” *Electronics (Basel)*, vol. 9, no. 3, p. 429, Mar. 2020, doi: 10.3390/electronics9030429.

[3] D. Luo *et al.*, “A Fault Detection Method of IGBT Bond Wire Fatigue Based on the Reduction of Measured Heatsink Thermal Resistance,” *Electronics (Basel)*, vol. 11, no. 7, p. 1021, Mar. 2022, doi: 10.3390/electronics11071021.

[4] B. Li *et al.*, “Modeling the impact of EVs in the Chinese power system: Pathways for implementing emissions reduction commitments in the power and transportation sectors,” *Energy Policy*, vol. 149, p. 111962, Feb. 2021, doi: 10.1016/j.enpol.2020.111962.

[5] D. Li, A. Ukil, K. Satpathi, and Y. M. Yeap, “Improved S Transform-Based Fault Detection Method in Voltage Source Converter Interfaced DC System,” *IEEE Transactions on Industrial Electronics*, vol. 68, no. 6, pp. 5024–5035, Jun. 2021, doi: 10.1109/TIE.2020.2988193.

[6] J. Rocabert, A. Luna, F. Blaabjerg, and P. Rodríguez, “Control of Power Converters in AC Microgrids,” *IEEE Trans Power Electron*, vol. 27, no. 11, pp. 4734–4749, Nov. 2012, doi: 10.1109/TPEL.2012.2199334.

[7] H. O. A. Ahmed, Y. Yu, Q. Wang, M. Darwish, and A. K. Nandi, “Intelligent Fault Diagnosis Framework for Modular Multilevel Converters in HVDC Transmission,” *Sensors*, vol. 22, no. 1, p. 362, Jan. 2022, doi: 10.3390/s22010362.

[8] G. Qiu, F. Wu, K. Chen, and L. Wang, “A Robust Accuracy Weighted Random Forests Algorithm for IGBTs Fault Diagnosis in PWM Converters without Additional Sensors,” *Applied Sciences*, vol. 12, no. 4, p. 2121, Feb. 2022, doi: 10.3390/app12042121.

[9] S. S. Ghosh *et al.*, “Wavelet-based rapid identification of IGBT switch breakdown in voltage source converter,” *Microelectronics Reliability*, vol. 152, p. 115283, Jan. 2024, doi: 10.1016/j.microrel.2023.115283.

[10] S. Rahimpour, H. Tarzamni, N. V. Kurdkandi, O. Husev, D. Vinnikov, and F. Tahami, "An Overview of Lifetime Management of Power Electronic Converters," *IEEE Access*, vol. 10, pp. 109688–109711, 2022, doi: 10.1109/ACCESS.2022.3214320.

[11] S. S. Ghosh, S. Chattopadhyay, and A. Das, "Identification of an Incipient Snubber Failure in Inverter Employed in Solid Oxide Fuel Cell (SOFC) Fed Microgrid," *IEEE Trans Instrum Meas*, vol. 74, pp. 1–10, 2025, doi: 10.1109/TIM.2025.3544391.

[12] K. M. Reddy and B. Singh, "Multi-Objective Control Algorithm for Small Hydro and SPV Generation-Based Dual Mode Reconfigurable System," *IEEE Trans Smart Grid*, vol. 9, no. 5, pp. 4942–4952, Sep. 2018, doi: 10.1109/TSG.2017.2676013.

[13] Q.-T. An, L. Sun, and L.-Z. Sun, "Current Residual Vector-Based Open-Switch Fault Diagnosis of Inverters in PMSM Drive Systems," *IEEE Trans Power Electron*, vol. 30, no. 5, pp. 2814–2827, May 2015, doi: 10.1109/TPEL.2014.2360834.

[14] B. Li, S. Shi, B. Wang, G. Wang, W. Wang, and D. Xu, "Fault Diagnosis and Tolerant Control of Single IGBT Open-Circuit Failure in Modular Multilevel Converters," *IEEE Trans Power Electron*, vol. 31, no. 4, pp. 3165–3176, Apr. 2016, doi: 10.1109/TPEL.2015.2454534.

[15] B. Song, G. Qi, and L. Xu, "A new approach to open-circuit fault diagnosis of MMC sub-module," *Systems Science & Control Engineering*, vol. 8, no. 1, pp. 119–127, Jan. 2020, doi: 10.1080/21642583.2020.1731005.

[16] J. Zhang, H. Sun, Z. Sun, Y. Dong, and W. Dong, "Open-Circuit Fault Diagnosis of Wind Power Converter Using Variational Mode Decomposition, Trend Feature Analysis and Deep Belief Network," *Applied Sciences*, vol. 10, no. 6, p. 2146, Mar. 2020, doi: 10.3390/app10062146.

[17] Z. Li, H. Ma, Z. Bai, Y. Wang, and B. Wang, "Fast Transistor Open-Circuit Faults Diagnosis in Grid-Tied Three-Phase VSIs Based on Average Bridge Arm Pole-to-Pole Voltages and Error-Adaptive Thresholds," *IEEE Trans Power Electron*, vol. 33, no. 9, pp. 8040–8051, Sep. 2018, doi: 10.1109/TPEL.2017.2773130.

[18] Y. Shen, T. Wang, Y. Amirat, and G. Chen, "IGBT Open-Circuit Fault Diagnosis for MMC Submodules Based on Weighted-Amplitude Permutation Entropy and DS Evidence Fusion Theory," *Machines*, vol. 9, no. 12, p. 317, Nov. 2021, doi: 10.3390/machines9120317.

[19] X. Sun, X. Gao, and S. Ji, "Serious fault identification for VSC-HVDC converters," in *2020 4th International Conference on HVDC (HVDC)*, IEEE, Nov. 2020, pp. 762–767. doi: 10.1109/HVDC50696.2020.9292759.

[20] M. Ma, X. Meng, N. Xiang, H. Wang, and X. Zhang, "Fault location method of IGBT short-circuit for a grid-tied Neutral-Point-Clamped inverter system," *Microelectronics Reliability*, vol. 126, p. 114225, Nov. 2021, doi: 10.1016/j.microrel.2021.114225.

[21] C. Sui, Y. He, Z. Li, and M. Chen, "The Post-Fault Current Model of Voltage Source Converter and Its Application in Fault Diagnosis," *IEEE Trans Power Electron*, vol. 36, no. 2, pp. 1209–1214, Feb. 2021, doi: 10.1109/TPEL.2020.3007586.

[22] S. A. Mohamed, M. A. Tolba, A. A. Eisa, and A. M. El-Rifaie, "Comprehensive Modeling and Control of Grid-Connected Hybrid Energy Sources Using MPPT Controller," *Energies (Basel)*, vol. 14, no. 16, p. 5142, Aug. 2021, doi: 10.3390/en14165142.

[23] J. Hossain, N. Sakib, E. Hossain, and R. Bayindir, "Modelling and Simulation of Solar Plant and Storage System: A Step to Microgrid Technology," *International Journal of Renewable Energy Research*, no. v7i2, 2017, doi: 10.20508/ijrer.v7i2.5620.g7053.

[24] D. Haribabu, A. Vangari, and J. N. Sakamuri, "Dynamics of voltage source converter in a grid connected solar photovoltaic system," in *2015 International Conference on Industrial Instrumentation and Control (ICIC)*, IEEE, May 2015, pp. 360–365. doi: 10.1109/IIC.2015.7150768.

[25] N. Mohan, T. M. Undeland, and W. P. Robbins, *Power Electronics*, 2nd ed. John Wiley and Sons, Inc, 2003.

[26] A. Abuelnaga, M. Narimani, and A. S. Bahman, "A Review on IGBT Module Failure Modes and Lifetime Testing," *IEEE Access*, vol. 9, pp. 9643–9663, 2021, doi: 10.1109/ACCESS.2021.3049738.

[27] C. Xu, B. Zhao, Z. Chen, J. Liu, Q. Song, and Z. Yu, "A Novel Converter-Breaker Integrated Voltage Source Converter Based on High-Surge IGCT and Fault Self-Clearing Strategy for DC Grid," *IEEE Trans Power Electron*, vol. 35, no. 12, pp. 12668–12672, Dec. 2020, doi: 10.1109/TPEL.2020.2996504.

[28] S. S. Ghosh, S. Chattopadhyay, and A. Das, "Fast Fourier transform and wavelet-based statistical computation during fault in snubber circuit connected with robotic brushless direct current motor," *Cognitive Computation and Systems*, vol. 4, no. 1, pp. 31–44, Mar. 2022, doi: 10.1049/ccs2.12041.

[29] Q. Wang, Y. Yu, H. O. A. Ahmed, M. Darwish, and A. K. Nandi, "Fault Detection and Classification in MMC-HVDC Systems Using Learning Methods," *Sensors*, vol. 20, no. 16, p. 4438, Aug. 2020, doi: 10.3390/s20164438.

[30] Q. Wang, Y. Yu, H. O. A. Ahmed, M. Darwish, and A. K. Nandi, "Open-Circuit Fault Detection and Classification of Modular Multilevel Converters in High Voltage Direct Current Systems (MMC-HVDC) with Long Short-Term Memory (LSTM) Method," *Sensors*, vol. 21, no. 12, p. 4159, Jun. 2021, doi: 10.3390/s21124159.

[31] Q. Guo, X. Zhang, J. Li, and G. Li, "Fault diagnosis of modular multilevel converter based on adaptive chirp mode decomposition and temporal convolutional network," *Eng Appl Artif Intell*, vol. 107, p. 104544, Jan. 2022, doi: 10.1016/j.engappai.2021.104544.

[32] F. Deng, Z. Chen, M. R. Khan, and R. Zhu, "Fault Detection and Localization Method for Modular Multilevel Converters," *IEEE Trans Power Electron*, vol. 30, no. 5, pp. 2721–2732, May 2015, doi: 10.1109/TPEL.2014.2348194.

[33] X. Qu, B. Duan, Q. Yin, M. Shen, and Y. Yan, "Deep Convolution Neural Network Based Fault Detection and Identification for Modular Multilevel Converters," in *2018 IEEE Power & Energy Society General Meeting (PESGM)*, IEEE, Aug. 2018, pp. 1–5. doi: 10.1109/PESGM.2018.8586661.

[34] J. Wang, X. Zheng, and N. Tai, "DC Fault Detection and Classification Approach of MMC-HVDC Based on Convolutional Neural Network," in *2018 2nd IEEE Conference on Energy Internet and Energy System Integration (EI2)*, IEEE, Oct. 2018, pp. 1–6. doi: 10.1109/EI2.2018.8582391.

[35] W. Jiao, Z. Liu, and Y. Zhang, "Fault Diagnosis of Modular Multilevel Converter with FA-SVM Algorithm," in *2019 Chinese Control Conference (CCC)*, IEEE, Jul. 2019, pp. 5093–5098. doi: 10.23919/ChiCC.2019.8866021.

Chapter 11

DWT-based Investigation of an Incipient Snubber Fault in Solid Oxide Fuel Cell (SOFC)-Powered Microgrid Inverter

Abstract- This chapter presents an innovative strategy for detecting initial snubber circuitry failure (ISCF) detection method in microgrid's (MG's) insulated gate bipolar transistor (IGBT)- based 3-phase inverters (3PhIs) that is linked to the solid-oxide fuel cell (SOFC). A study has been carried out to detect ISCF by applying the discrete wavelet transform (DWT) on the 3PhI's output current waveform. The presented study includes the wavelet coefficients of the 3PhI's output current harmonic spectra's kurtosis and skewness measurements to detect ISCF. Comparative analysis was conducted for determining the most effective parameter for the identification of ISCF. An ISCF identifying algorithm has been recommended. Moreover, the study's contrasting findings and distinctive contributions are presented.

Keywords: Discrete wavelet transform (DWT), fault detection, microgrid inverter, snubber fault.

11.1 Introduction

The majority of renewable energy facilities use grid-tied 3PhIs. MGs are replacing distant power plants with distributed, local power generation [1]. MGs exhibit high durability and can operate in islanded, autonomous, or grid-connected modes [2]. Ecosystems are suffering as a result of the growing need for power [3]. A worldwide agreement and concerted effort to embrace alternative forms of energy in response to environmental issues has emerged in recent years [4]. One of the newest innovations in sustainable energy production is SOFCs [3], [5]. SOFCs provide numerous benefits such as quiet operation, reduced carbon emissions, substantial cogeneration capability, absence of mechanical motion, and elevated power density [6], [7]. By directly converting chemical energies, SOFC stacks generate electrical power [8].

Grid-tied inverters are an integral component of dispersed power-generating systems used by MGs [9] along with being the most important component of a grid-linked system [10]. Meanwhile, one of the parts that fails the most frequently is the inverter [11]. IGBT is a widely employed switch in a microgrid inverter (MGI) [12]. IGBTs facilitate electrical energy to be efficiently converted and regulated in power electronic systems. IGBTs are rated for high current and voltage. In MGs, inverters typically incorporate IGBTs [7]. Because of quick fluctuations in current and voltage, IGBT turn-off procedures may result in voltage surges that harm the IGBT along with other circuitry parts. Switches' voltage surges are mitigated by means of snubber circuits [13].

Power equipment featuring IGBTs as well as MOSFETs is responsible for about 21% of converters' failures [14], [15]. The primary reason for the shortened lifespans of power electronic devices is thermal stress in switching elements such as IGBTs and MOSFETs, especially when working at high switching frequencies. It could lead to wear-out breakdowns that cause inconsistent system functioning or the failure of such components, like an open-circuit (OC) or short-circuit (SC) [7], [14], [15]. To increase the dependability of inverters, a method for identifying and diagnosing problems is necessary.

S. F. Zarei et al. proposed a malfunction identification method for islanded inverters [16]. Authors [17] identified the MGI switch's OC issue. S.S. Moosavi et al. devised methods for identifying open circuit (OC) issues in the inverter of a battery-powered vehicle [18]. The authors provided an evaluation approach for inverters' IGBT/Diode failures [19]. For modular multilevel converter (MMC), the researchers [20] proposed a way to identify OC problems.

Numerous methods have been proposed for identifying defects in the MMC submodule, including the Filippov methodology [21], neural networks [22], Park transform [23], machine learning (ML) [24], and Fourier and wavelet transforms [25], [26]. For cascaded H-bridge multi-level inverters (CHMLIs), a means for identifying open circuit malfunctions [27] was presented by M. Ali et al. The artificial neural network (ANN)-based methods for identifying OC and SC breakdowns for CHMLIs [28], [29], [30], [31] were demonstrated. Additionally, using convolutional neural networks (CNNs), researchers illustrated OC detection methods [32], [33] for 3-phase H-bridge inverter (TPHBI). The researchers have presented an additional ISCF identification technique for a 3PhI [34]. The method tracks ISCF to a level of 10%. Nevertheless, neither article [13] nor [34] can give details on the accuracy rates (ARs) or defect detection duration (DD). J. Fan et al. proposed a CNN-based ISCF detection technique [35]. The AR of the proposed method for detecting ISCF is 95%. However, the DD is not disclosed by this study either.

Nonetheless, there hasn't been any substantial research on 3PhI ISCF detection in microgrid. A distinct technique for determining the ISCF has been outlined in this chapter. A wavelet-based statistical investigation was performed here to detect ISCF. To identify ISCF, the 3PhI's output current harmonic spectra were monitored under normal conditions and at various percentages of ISCF (%ISCF) (0 to 85%).

11.2 Grid-Linked IGBT-Based Inverter

The grid-tied SOFC-powered IGBT-based inverter is depicted schematically in Fig. 11.1. It illustrates a schematic representation of the grid-linked SOFC stacks, voltage regulator (DC-DC), and 3PhI.

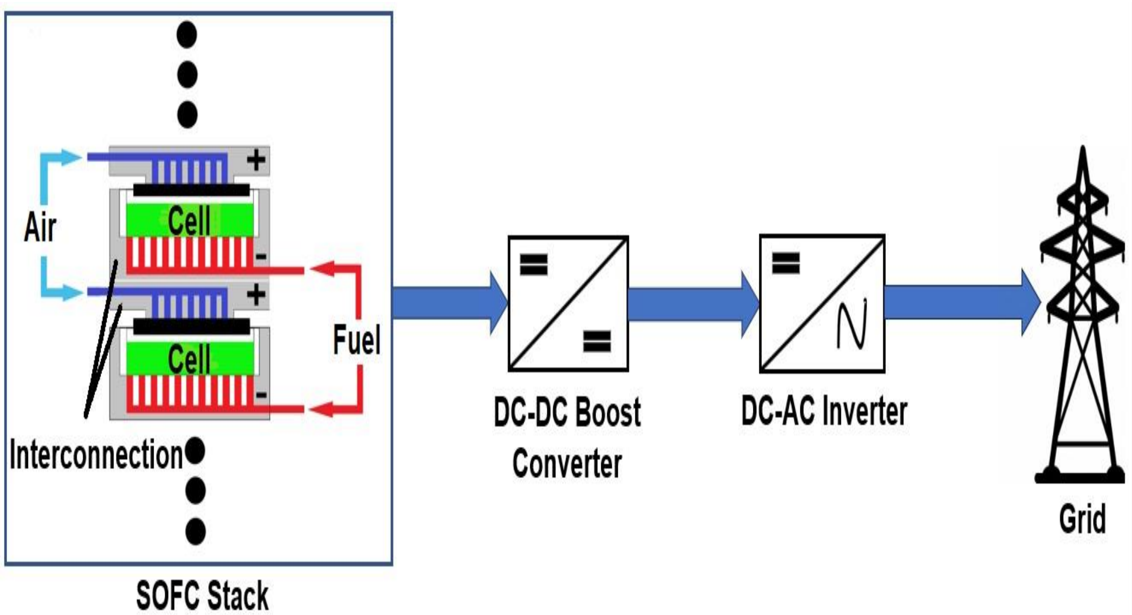

Fig. 11.1. Schematic of the SOFC-powered IGBT-based inverter linked to the grid

11.2.1 SOFC Stack

In this section, SOFCs are undoubtedly serving as a clean, efficient power source in the microgrid. It generates energy via an electrochemical process. It uses chemical processes inside the cell to produce dc electricity. The three forms of losses occurring in SOFC are ohmic, concentration, and activation losses. Nernst equation [36] may be used to calculate the voltage output of the SOFC while accounting for all of the fuel cells' losses as below:

$$E_{ro} = N\left[E_t + \frac{R_g T_s}{2F_c}\ln\left(\frac{p_{H_2}\sqrt{p_{O_2}}}{p_{H_2O}}\right)\right] \quad (11.1)$$

$$V_{sofco} = E_{ro} - V_{act} - V_{conc} - V_{ohm} \quad (11.2)$$

Although if the fuel cell's ohmic loss is the sole factor considered, the SOFC's output voltage could be computed as below:

$$V_{sofco} = E_{ro} - r_{sofc}I_{sofco} \quad (11.3)$$

where, E_{ro}= OC reversible voltage (V);

V_{sofco}= SOFC voltage output (V);

E_t= reversible cell potential (V) at standard conditions;

T_s= temperature of the fuel stack (K);

R_g= ideal gas constant, (8.314 kJ/kmol K);

F_c= Faraday's constant, (96487 C/mol);

N= stack's cell count;

p_{O_2}= partial Oxygen pressure (Pa);

p_{H_2}= partial Hydrogen pressure (Pa);

p_{H_2O}= partial water pressure (Pa);

$V_{ohm}, V_{act}, V_{conc}$ = voltage drops in (V) due to ohmic loss, activation loss, and concentration loss;

I_{sofco}= SOFC's current output (A)

r_{sofc}= SOFC internal resistance (ohms);

11.2.2 Boost Converter

The boost converter is implemented to enhance the SOFC's lower-voltage output to an elevated voltage suitable to feed the inverter. Fig. 11.2 demonstrates their connectivity. It makes sure that the inverter's dc input is consistent and properly controlled. This ensures the inverter operates in the optimum efficiency range and minimizes energy loss while converting.

The following mathematical formulas [7], [37] illustrate the converter's topology according to the state-space model:

$$V_{bin} = L_b\frac{dI_{bin}}{dt} + V_{bout}(1 - D_b) \quad (11.4)$$

$$C_{bout}\frac{dV_{bout}}{dt} + I_{bout} = (1 - D_b)I_{bin} \tag{11.5}$$

where, V_{bin}, I_{bin}= input voltage and current to the boost converter;

V_{bout}, I_{bout}= voltage and current at boost converter output terminal;

L_b, C_{bout}= boost converter inductance and output capacitance;

D_b= boost converter's duty cycle;

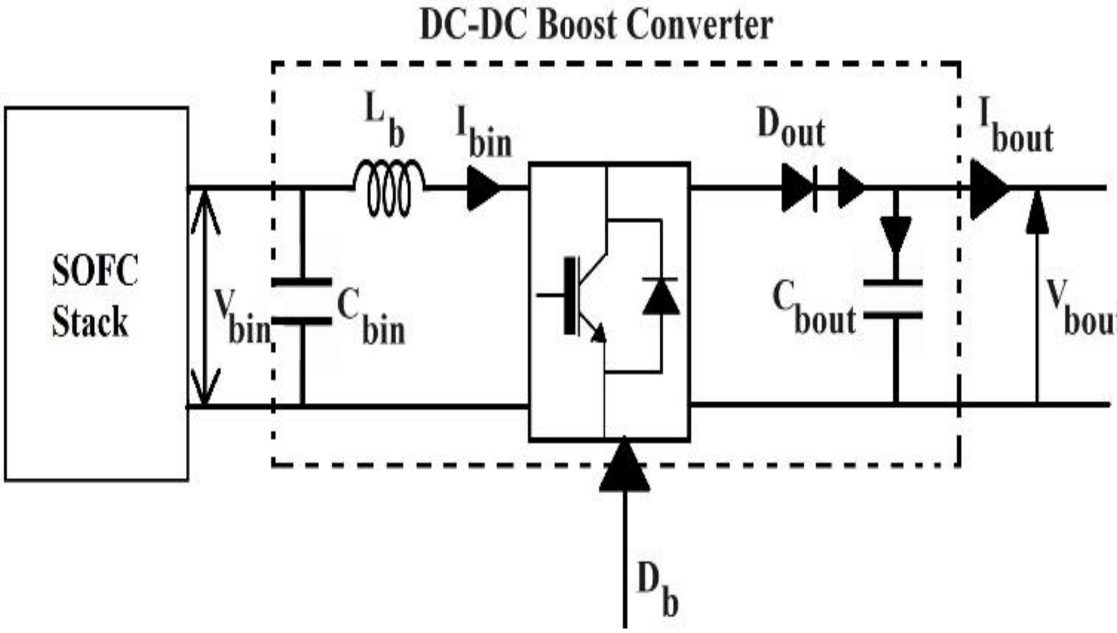

Fig. 11.2. Boost converter's equivalent circuit

11.2.3 Overview of DC-AC Inverter

The equivalent circuit of the 3PhI connected with an AC grid is illustrated in Fig. 11.3.

The representations for the grid's corresponding per-phase inductance and resistance are R, L. V_a, V_b, and V_c are the voltages at the inverter's output side. The 3-phase grid voltages are E_a, E_b, E_c respectively. Three-phase currents, i_a, i_b, i_c, are injected into the grid. The following equations are produced after applying KVL to the inverter's output and converting the equations from *abc to dq* values using the Park and Clark transforms [14], [38]:

$$V_d = E_d + L\frac{di_d}{dt} - \omega L i_q + R i_d \tag{11.6}$$

$$V_q = E_q + L\frac{di_q}{dt} + \omega L i_d + R i_q \tag{11.7}$$

$$V_d - E_d + \omega L i_q = L\frac{di_d}{dt} + Ri_d = u_d \quad (11.8)$$

$$V_q - E_q - \omega L i_d = L\frac{di_q}{dt} + Ri_q = u_q \quad (11.9)$$

where, i_d, i_q= d-q axis currents (A) at the inverter output;

V_d, V_q= d-q axis voltages (V) at the inverter output;

E_d, E_q= d-q axis grid voltages (V) of 3-phases;

ω= grid radial frequency (rad/s);

u_d, u_q= d-q axis steady-state control functions

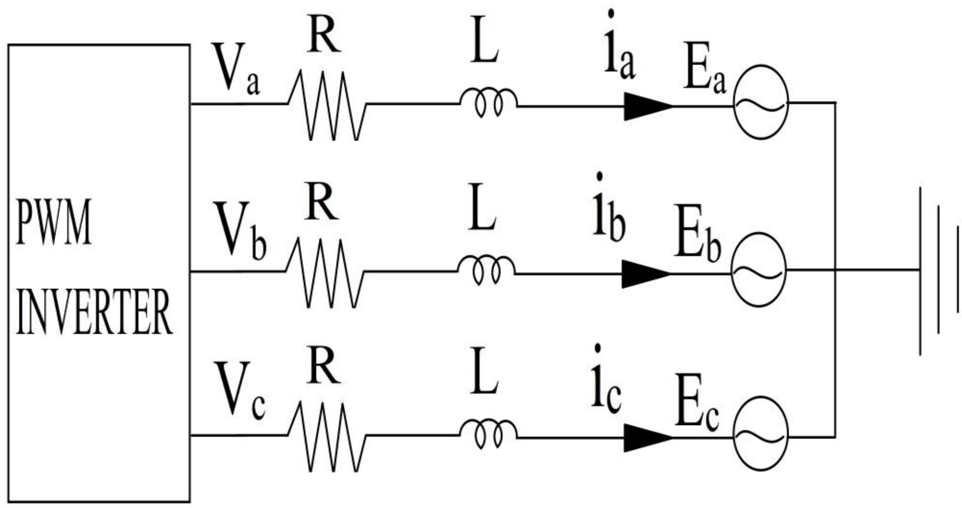

Fig. 11.3. AC grid-connected equivalent circuit of a 3-phase inverter

The process of inverter triggering is carried out via pulse-width modulation (PWM). To identify ISCF, the 3PhI's output current harmonic spectra were monitored under normal conditions and at various %ISCF.

11.3 Fault in Snubber Circuitry

This chapter addresses fault diagnosis of resistance-capacitance (RC) snubber circuits. A small resistor and capacitor in series are frequently employed as RC snubber circuits for inductive loads. Snubbers restrict the rate of voltage increase (dV/dt), also limit di/dt, ripples, when employed with devices such as thyristors, IGBTs, MOSFETs, and other switching components.

The snubber resistance defect, referred to here as ISCF, can be caused by aging, temperature, and different variables. ISCF arises when the snubber resistor's effective resistance's value gradually drops. In severe circumstances, it drops to zero, short-circuiting the snubber path. Here, an effort was made to identify a little and steady drop in the snubber resistance's value.

Simple snubber circuits consist of a resistor linked in series with a capacitor attached in parallel to the semiconductor switches. In Fig. 11.4, the RC snubber circuitry utilized in the 3PhI circuit is displayed.

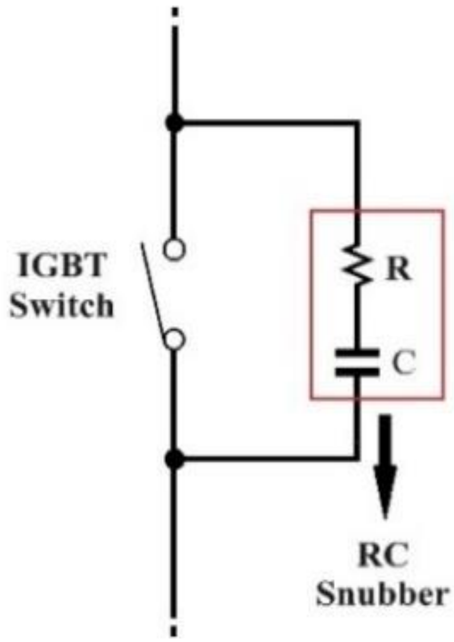

Fig. 11.4. Inverter's RC snubber circuit

These formulae [13] outlined below can be used to calculate the values of the snubber resistance and snubber capacitance:

$$R_{SN} = 2.\delta_d \sqrt{\frac{L_c}{C_c}} \tag{11.10}$$

$$C_{SN} = L_c \left(\frac{I_{rs}}{K_i.V_s}\right)^2 \tag{11.11}$$

where, R_{SN}, C_{SN}= snubber's resistance and capacitance value;

K_i, δ_d = optimum current and optimum damping factor;

V_s= source voltage;

I_{rs}= recovery current of semiconductor switch;

C_c, L_c= circuit capacitance and inductance, respectively

11.4 Approach for Fault Diagnosis

To identify ISCF, the 3PhI's output current harmonic spectra were monitored under normal conditions and at various %ISCF. The discrete character of the current signals recorded makes DWT appropriate for analysis [13]. Through the extraction of a few characteristics deemed appropriate for defect diagnosis, statistical analysis was conducted. The investigation's time frame is 1 second, and the sample frequency is 25 kHz.

11.4.1 Using DWT to Diagnose Faults

The computing unit is unable to instantly distinguish between the problems using the simple Fourier transform approach because the collected signal in this case is erratic. The wavelet transform constitutes a particularly useful technique for processing non-stationary data [13], [14]. Wavelet coefficients of the acquired current's harmonic spectra's kurtosis and skewness measurements were monitored to detect ISCF.

The amount of wavelet coefficients that DWT provides is defined according to the integers of discrete steps in scale and translation, indicated by m and n. For RMS, the scale and translation will be $a = a_0^m$ and $b = nb_0 a_0^m$. if the segmentation's step size of the scale and translation be a_0 and b_0, accordingly. The coefficients of the discrete wavelet are therefore expressed as following [13], [14]:

$$DWT(m,n) = \int_{-\infty}^{\infty} \frac{1}{\sqrt{{a_0}^m}} f(t) g({a_0}^{-m} t - nb_0) d(t) \qquad (11.12)$$

where $g(a_0^{-m} t - nb_0)$ represents the translated and scaled discrete wavelet.

For ISCF investigation, the inverter's output current was recorded. The acquired current was decomposed till DWT 9th level. The Daubechies wavelet's mother wavelet in this instance is identified as "db4". For both normal and defective circumstances (up to 85%) of ISCF, approximated and detail coefficients were calculated through DWT level 9.

Kurtosis and skewness values of the 3PhI's output current harmonic spectra through DWT 9 levels were further calculated for the intent of detecting ISCF.

11.4.2 Considered Statistical Parameters

The coefficients of wavelet decomposition are represented as follows:

The approximated and detail coefficients' kurtosis and skewness values are represented as K_A, K_D, S_A, and S_D, respectively. For both approximate and detail coefficients till the DWT level 9, the kurtosis, skewness values may be written as follows [7]:

$$[k] = \begin{bmatrix} [K_A] \\ [K_D] \end{bmatrix} = \begin{bmatrix} K_{A1} & K_{A2} & K_{A3} & K_{A4} & K_{A5} & K_{A6} & K_{A7} & K_{A8} & K_{A9} \\ K_{D1} & K_{D2} & K_{D3} & K_{D4} & K_{D5} & K_{D6} & K_{D7} & K_{D8} & K_{D9} \end{bmatrix} \quad (11.13)$$

$$[s] = \begin{bmatrix} [S_A] \\ [S_D] \end{bmatrix} = \begin{bmatrix} S_{A1} & S_{A2} & S_{A3} & S_{A4} & S_{A5} & S_{A6} & S_{A7} & S_{A8} & S_{A9} \\ S_{D1} & S_{D2} & S_{D3} & S_{D4} & S_{D5} & S_{D6} & S_{D7} & S_{D8} & S_{D9} \end{bmatrix} \quad (11.14)$$

In acquired current signal examination and assessment of ISCF, which generate non-stationary signals, statistical factors are proven to be useful.

11.4.3 Evaluation of Statistical Factors for Approximation Coefficients

The K_A and S_A were computed for standard and various %ISCF circumstances, and they are illustrated in Fig. 11.5, and Fig. 11.6.

The K_A readings are displayed in Fig. 11.5, which indicates that no specific hypotheses could be made using this information for defect detection. The graphical representation in Fig. 11.6 illustrates how the S_A readings at all stages of DWT display an exponentially expanding aspect until the ISCF reaches 5% and following then, these readings decrease as the %ISCF grows. Furthermore, the graphic evaluation of S_A data does not offer compelling evidence for problem identification.

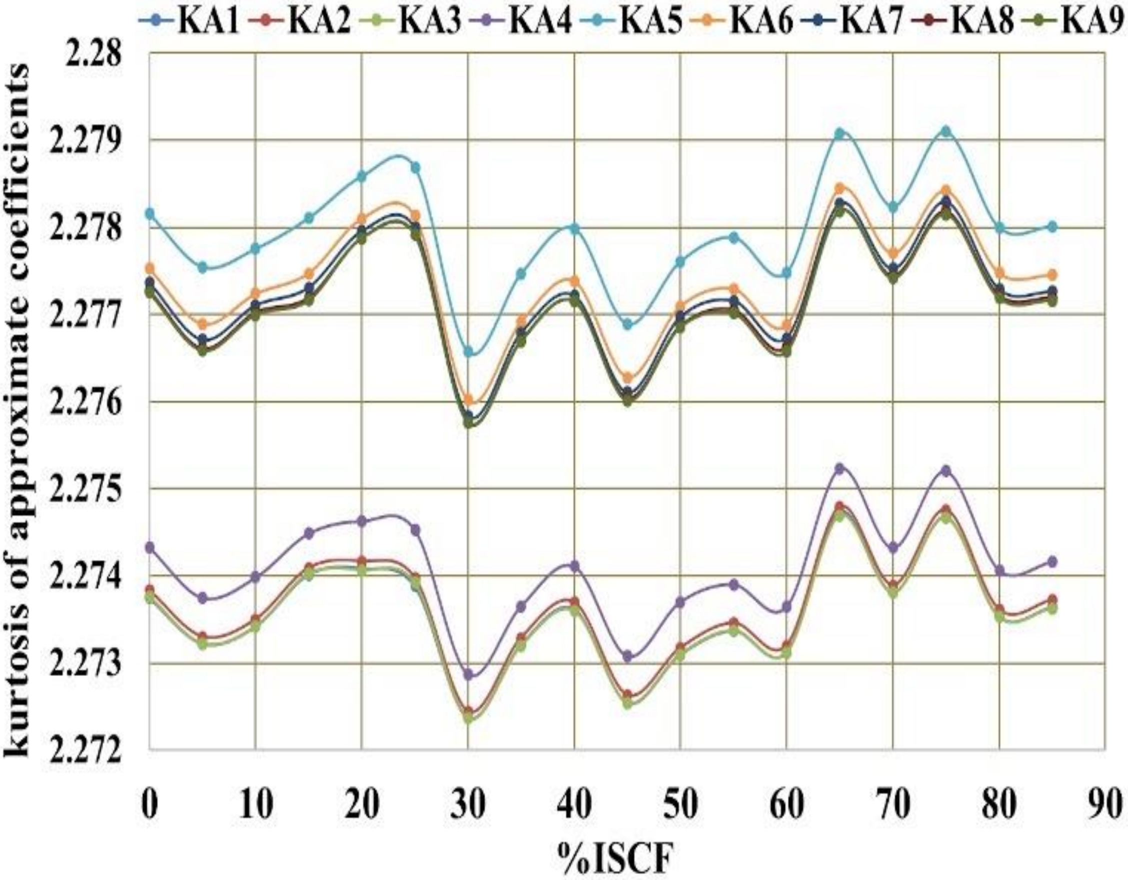

Fig. 11.5. K_A vs. %ISCF

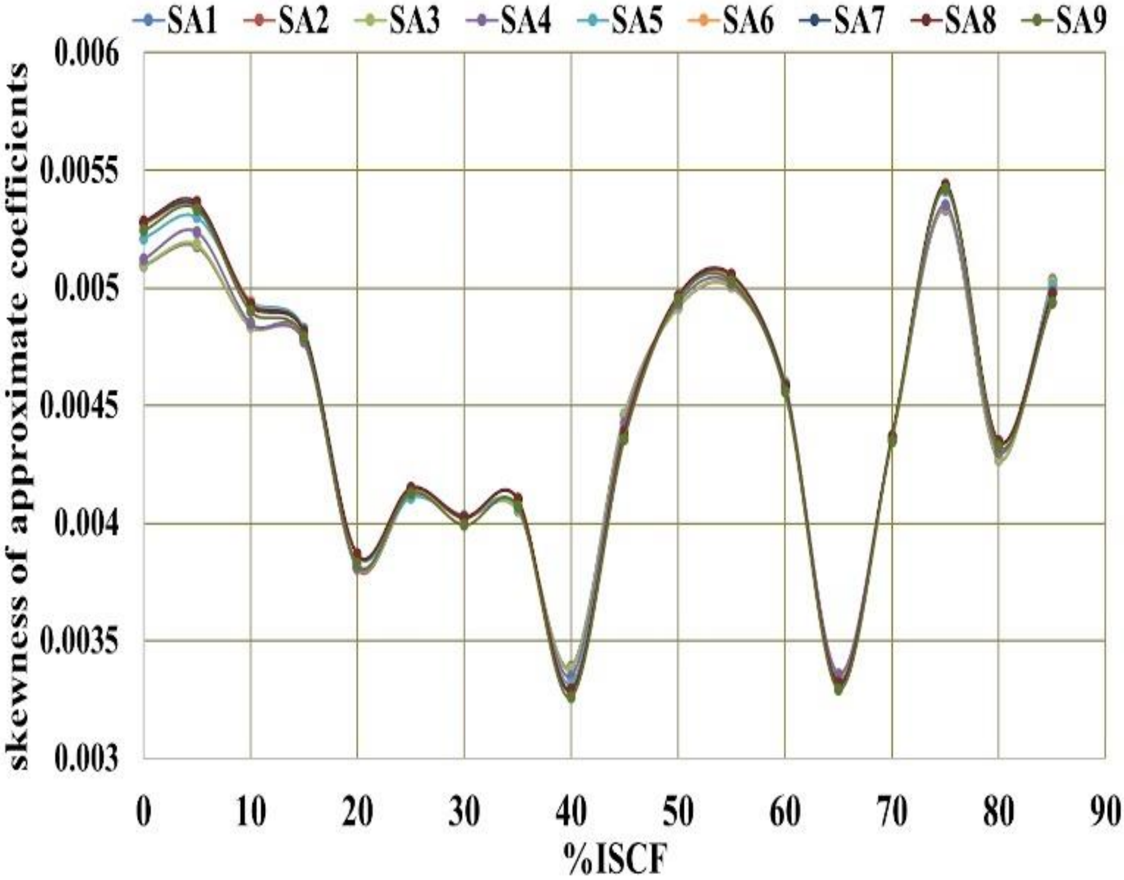

Fig. 11.6. S_A vs. %ISCF

11.4.4 Evaluation of Statistical Factors for Detail Coefficients

The K_D and S_D were computed for standard and various %ISCF circumstances, and they are illustrated in Fig. 11.7, and Fig. 11.8.

The K_D readings are displayed in Fig. 11.7, which indicates that no specific hypotheses could be made using this information for defect detection.

According to a graphical study of Fig. 11.7, K_{D1} to K_{D9} readings lack a proper pattern of gradual growth or decline. So, that could not be helpful for the ISCF detection study.

Furthermore, S_{D1}, S_{D4}, S_{D5}, S_{D6}, S_{D8}, and S_{D9} in Fig. 11.8 demonstrates that the majority of the outcomes are in a fairly erratic pattern and that no useful inference can be drawn from them for the detection of ISCF. It is noticeable that till 25% of ISCF, the S_{D2} value rises. Whereas, at the 3rd and 7th decomposition levels, S_D readings rose until the ISCF reached 15%.

Therefore, only the S_{D2}, S_{D3}, and S_{D7} values only hinder the ability to evaluate ISCF.

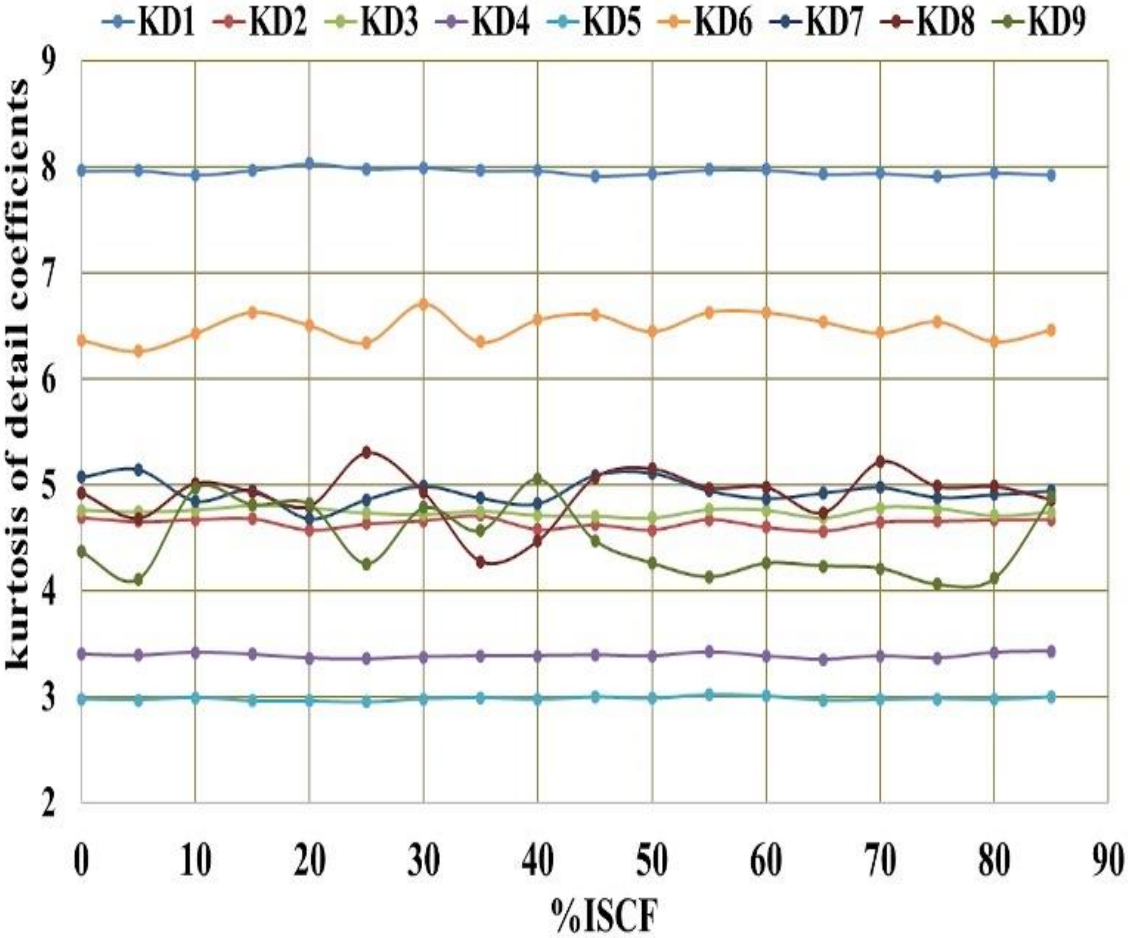

Fig. 11.7. K_D vs. %ISCF

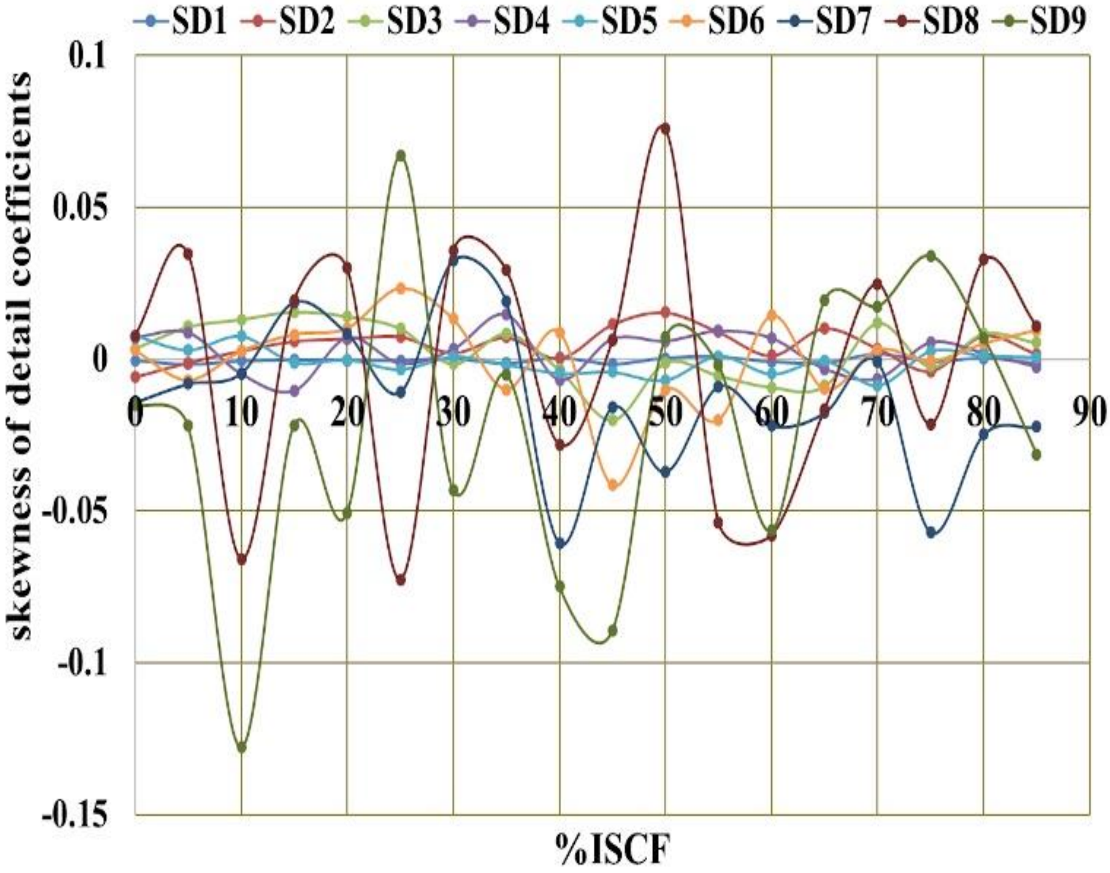

Fig. 11.8. S_D vs. %ISCF

11.4.5 Discussing Preferable Optimal Parameter and Precise Outcome

The likely effective curves for diagnosing ISCF are chosen from Fig. 11.5, Fig. 11.6, Fig. 11.7, and Fig. 11.8, as seen in Fig. 11.9, Fig. 11.10, and Fig. 11.11.

Based on the analyses of Fig. 11.9, Fig. 11.10, and Fig. 11.11, it is noted that the curve of S_{D2} values grows exponentially till 25% of ISCF. Following then, these readings decrease as %ISCF grows more. Whereas, S_{D3} and S_{D7} both values grow exponentially till 15% of ISCF, and following then, both these readings decrease as %ISCF grows further.

Finally, Fig. 11.9 makes it clear that using S_{D2} values is the only way to adequately conduct ISCF detection.

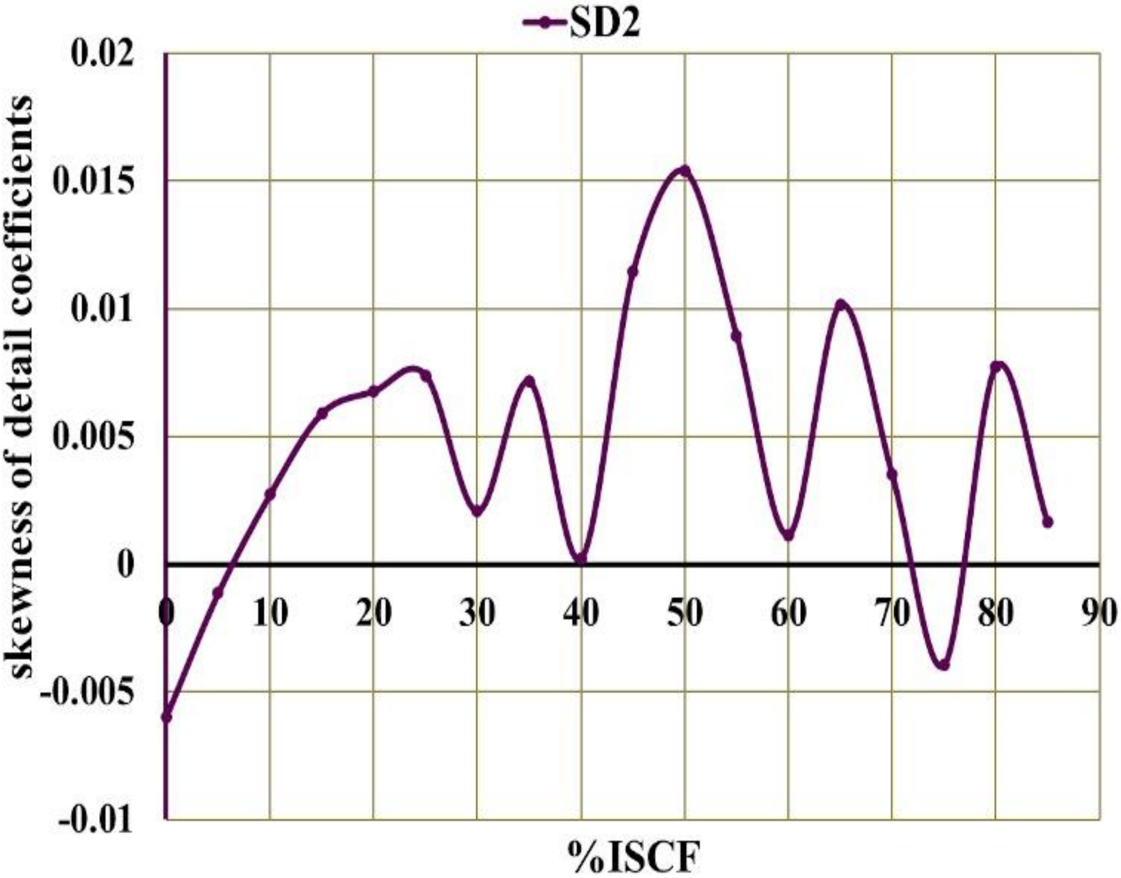

Fig. 11.9. S_{D2} vs. %ISCF

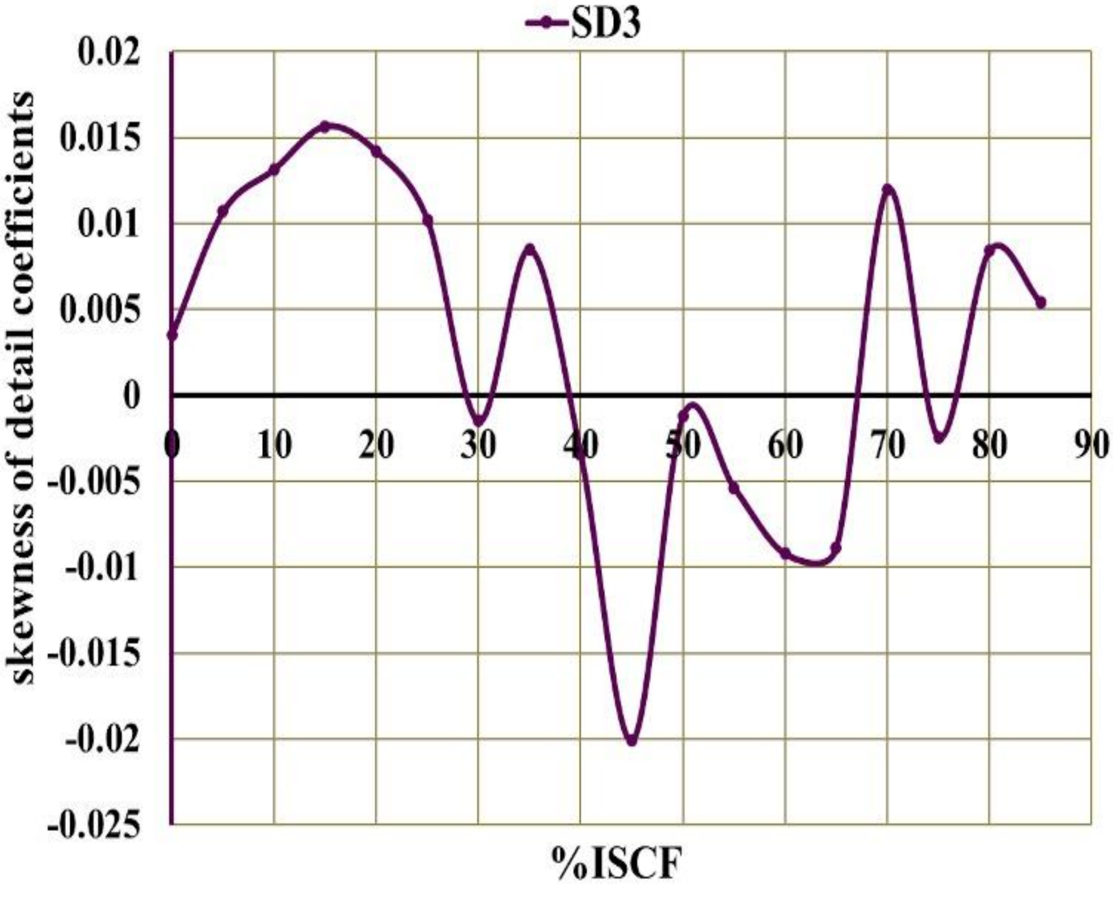

Fig. 11.10. S_{D3} vs. %ISCF

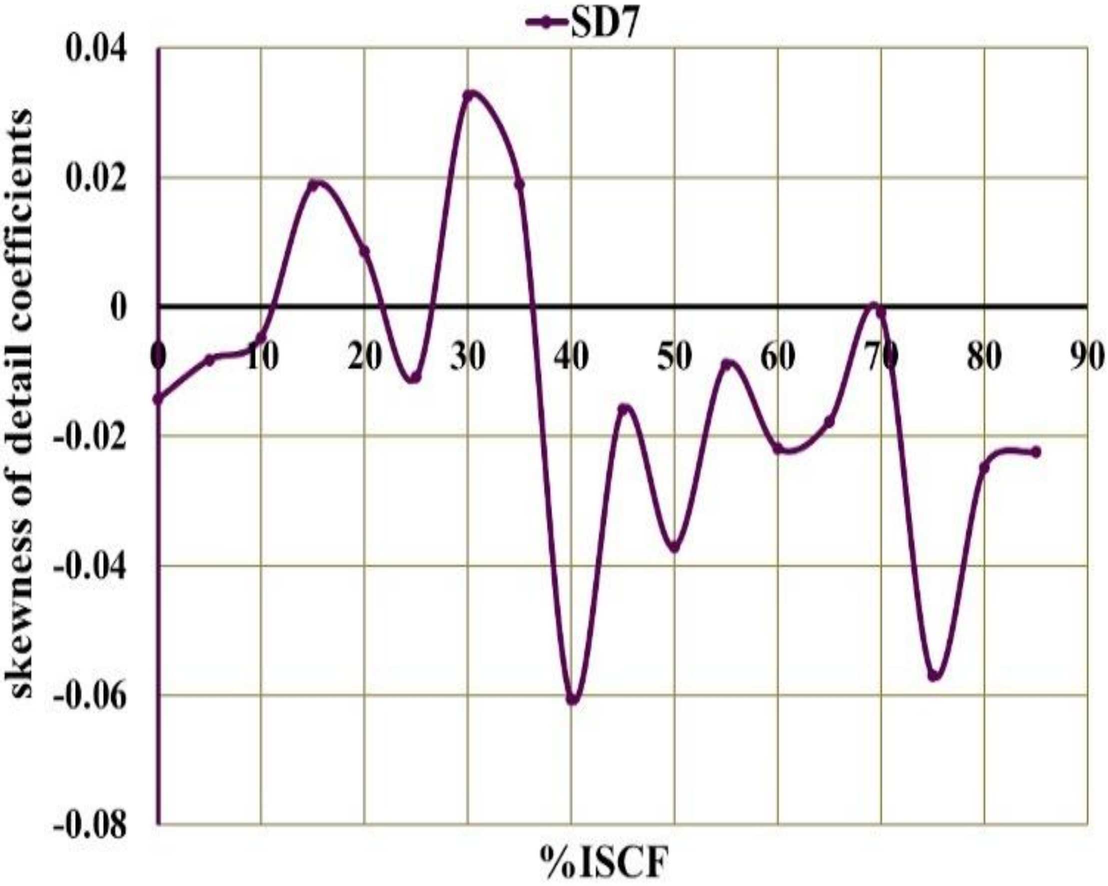

Fig. 11.11. S_{D7} vs. %ISCF

11.5 Algorithm for Detecting ISCF

The Fig. 11.12 depicts the suggested method of ISCF detection.

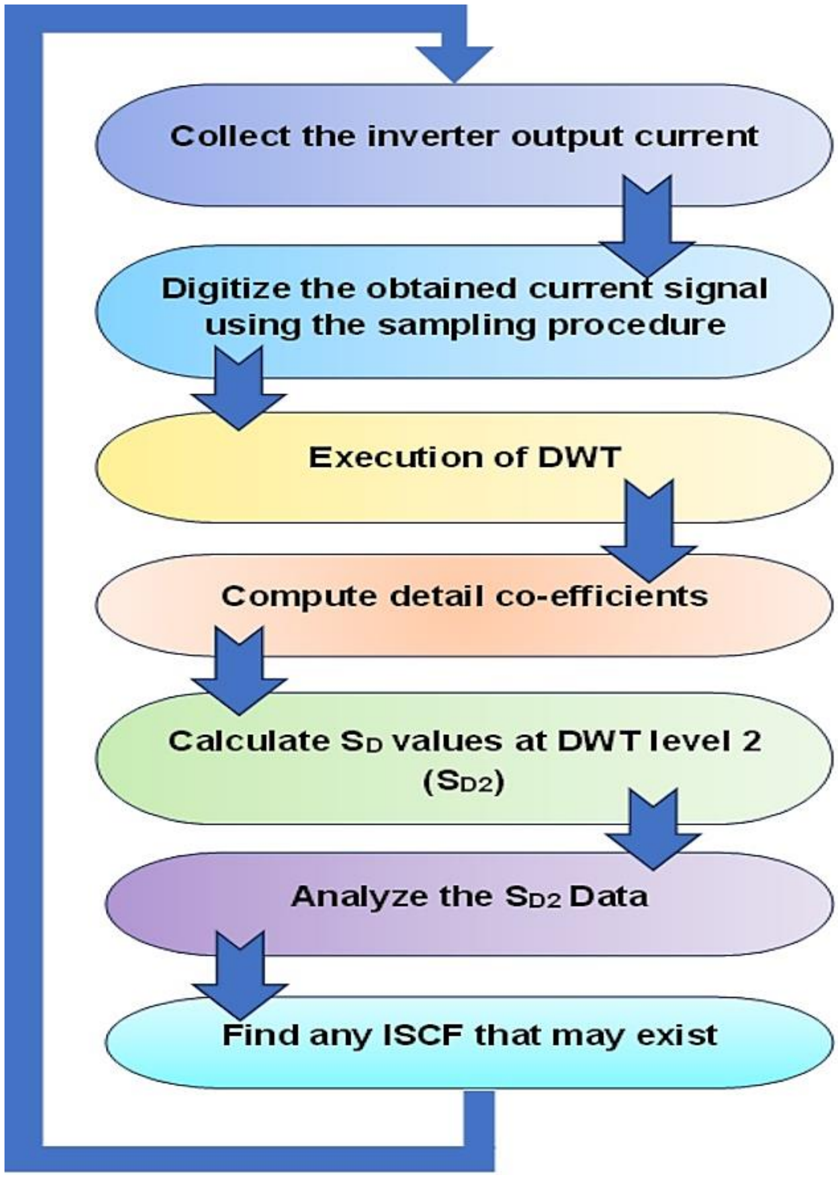

Fig. 11.12. ISCF identification algorithm

The following algorithm was suggested for ISCF detection:

g) Acquire the current at the inverter output.

h) Digitize the recorded current signal using the sampling procedure.

i) Apply DWT to the recorded data.

j) Calculate detail coefficients after DWT.

k) Compute S_{D2}.

l) Analyse the readings of S_{D2} and check for ISCF.

11.6 Validation at Laboratory Testing Facility

The technical details of the system are listed in Table 11.1. Case studies carried out at the testing facility system, as seen in Fig. 11.13, have been used to validate the suggested approach.

Table 11.1. Modelling specification

Parameter	Value
Ideal gas constant	8.314 kJ/kmol K
Absolutely temperature	1273 K
Faraday's constant	96487 C/mol
Stack's cell count	384
SOFC stack voltage	438 V
SOFC stack power	50 kW
Ohmic loss	0.126 ohm
Boost converter's inductance	1 mH
Boost converter's capacitance	5000 µF
Equivalent value of load resistance	8.712 ohm
Reference voltage for the boost converter	660 V
3PhI's output voltage	440 V (phase to phase) AC

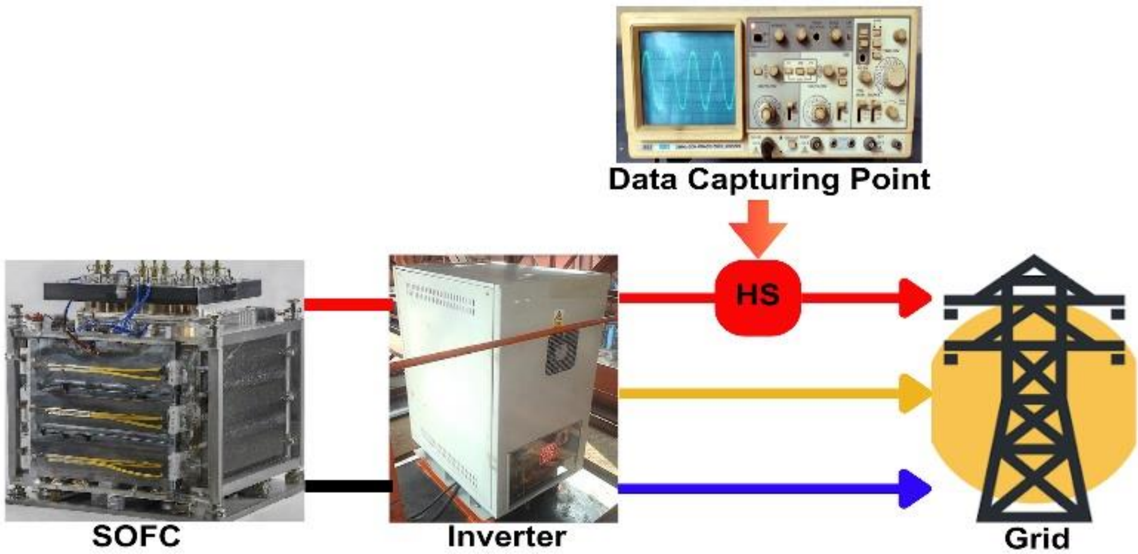

Fig. 11.13. Lab testing workbench

Three numbers of hall sensors (HSs) were installed at the three output terminals of 3PhI to record current. The Fig. 11.13 illustrates just one of these HSs. The current has been recorded through the DAS utilizing these hall probes. The technical details of the DAS and probes are listed in Table 11.2.

Table 11.2. Specification of the Hall probe and DAS

Devices	Specifications
Hall Probe	LEM PR30 ACV 600V CAT III, 30A, 100 kHz
DAS	OROS OR35, Speed- 100 kS/s per channel, Channels- 8

Comparative analyses of the lab results from three separate instances that were examined with varying %ISCF are shown in Table 11.3. In this specific scenario, the error rate in percent was computed employing the formula [34] outlined below:

$$Error = \left|\left(\frac{F_{ISCF} - f_{ISCF}}{f_{ISCF}}\right) \times 100\%\right| \qquad (11.15)$$

where,

F_{ISCF} = %ISCF value (known);

f_{ISCF} = %ISCF calculated using values of either S_{D2}, S_{D3} or S_{D7}

Table 11.3. Comparative analysis of experimental results

Types of Data	Case 1	Case 2	Case 3
%ISCF (known)	7%	10%	14%
S_{D2}	0.0019	0.0027	0.0051
%ISCF acquired by S_{D2}	6.91%	9.92%	13.78%
Error	1.30%	0.81%	1.60%
S_{D3}	0.0122	0.0129	0.0152
%ISCF acquired by S_{D3}	7.18%	9.73%	13.76%
Error	2.51%	2.77%	1.74%
S_{D7}	-0.0073	-0.0038	0.0179
%ISCF acquired by S_{D7}	6.89%	10.11%	13.75%
Error	1.60%	1.09%	1.82%

The comparative study in Table 11.3 exhibits that analyzing the S_{D2} values may yield the most substantially feasible outcomes for the %ISCF evaluation, with up to a 99.19% accuracy. Thus, this detection method may be exploited to identify ISCF in MG's 3PhIs.

The confusion matrix presented in Table 11.4 illustrates the effectiveness of the proposed ISCF detection method. It predicts the presence of ISCF with great accuracy. Lower rates of false positives and false negatives, however, indicate fewer false detections and false alarms; higher true positive and negative percentages are indicative of more accurate defect detection. In conclusion, the findings confirm that the recommended method can correctly detect ISCF.

Table 11.4. Confusion matrix

		Actual Fault	
		Positive	Negative
Predicted Fault	Positive	True Positive (94%)	False Positive (6%)
	Negative	False Negative (6%)	True Negative (94%)

11.7 Comparative Assessment and Unique Contribution

In this section, Table 11.5 summarizes the findings of comparisons among the suggested study alongside additional comparable approaches. The literature review's fault diagnostics mostly address OC, SC, and other problems in 3PhIs; however, very few attempts are made to identify ISCF.

The following are the unique contributions established by the investigation:

a) This investigation involves the fact that it exploits the statistical character of S_{D2} to aid with ISCF identification extremely well.
b) It additionally indicated that the %ISCF in the 3PhI could be obtained using the approach proposed.
c) It has been demonstrated that the recommended ISCF detection method has a defect DD of 0.04s and that the maximum AR of 99.19% may be achieved when the optimal parameter is chosen for detecting faults.
d) The method reduces the number of pertinent factors that may be used to determine ISCF.

e) Implementing the recommended ISCF detection approach requires a DAS and the soft computing device.

As a result, the proposed technique may be applied in practical situations with ease and at a reasonable cost.

Table 11.5. Comparative analysis

Ref.	Failure types	Fault recognition (in %)	DT and AR
[13]	ISCF in converter circuit of brushless DC motor's drive (BLDCMD)	Yes	DT= Not available, AR= Not available
[19]	Switch faults in inverter	No	DT= 0.02 s, AR= 97.4%
[27]	OC defect in CHMLI	No	DT= 3.80 ms, AR= 98.88%
[28]	CHMLI OC defect	No	DT= Not available, AR= 99.9%
[29]	CHMLI OC defect	No	DT= 10 ms, AR= 100%
[30]	Voltage source inverter's OC defect	No	DT= 15.47ms, AR= Not available
[31]	OC and SC in CHMLI	No	DT= Not available, AR= 97.5%
[32]	TPHBI's OC defect	No	DT= 0.25 ms, AR= 100%
[33]	TPHBI's OC defect	No	DT= Not available, AR= 99.95%
[34]	ISCF in 3PhI	Yes	DT= Not available, AR= Not available
[35]	ISCF in BLDCMD	No	DT= Not available, AR= 95%
Proposed method	MG inverter's ISCF	Yes	DT= 0.04 s, AR= 99.19%

11.8 Conclusion

In this work, a DWT-based analytical study of the 3PhI's output current has been performed in an attempt to diagnose ISCF. For the purpose of identifying ISCF, many statistical metrics have been observed. The values of the pertinent parameters have been observed to be fluctuating throughout the fault detection procedure. The data gathered from DWT-based diagnostics has been compared and evaluated in an effort to determine the best reliable method for ISCF detection.

Furthermore, it was discovered that S_{D2} has proven to be exceptionally efficient for ISCF detection. Consequently, the ISCF within any 3PhI may be detected by applying the suggested approach by continual tracking of readings. Additionally, the analysis confirmed that the suggested approach may be used to derive the %ISCF in the 3PhI.

References

[1] A. Kumar, A. Mohapatra, and S. N. Singh, "Sequence Measurement-Based Islanding Detection of DGs in Microgrid With Enhanced Power Quality," *IEEE Trans Instrum Meas*, vol. 70, pp. 1–11, 2021, doi: 10.1109/TIM.2021.3102688.

[2] Q. Liu, T. Caldognetto, and S. Buso, "Review and Comparison of Grid-Tied Inverter Controllers in Microgrids," *IEEE Trans Power Electron*, vol. 35, no. 7, pp. 7624–7639, Jul. 2020, doi: 10.1109/TPEL.2019.2957975.

[3] A. Essaghouri *et al.*, "Effects of Radial and Circumferential Flows on Power Density Improvements of Tubular Solid Oxide Fuel Cells," *Energies (Basel)*, vol. 15, no. 19, p. 7048, Sep. 2022, doi: 10.3390/en15197048.

[4] G. Zhang, Y. Shi, A. Maleki, and M. A. Rosen, "Optimal location and size of a grid-independent solar/hydrogen system for rural areas using an efficient heuristic approach," *Renew Energy*, vol. 156, pp. 1203–1214, Aug. 2020, doi: 10.1016/j.renene.2020.04.010.

[5] A. Fernandes, T. Woudstra, A. van Wijk, L. Verhoef, and P. V. Aravind, "Fuel cell electric vehicle as a power plant and SOFC as a natural gas reformer: An exergy analysis of different system designs," *Appl Energy*, vol. 173, pp. 13–28, Jul. 2016, doi: 10.1016/j.apenergy.2016.03.107.

[6] U. M. Damo, M. L. Ferrari, A. Turan, and A. F. Massardo, "Solid oxide fuel cell hybrid system: A detailed review of an environmentally clean and efficient source of

energy," *Energy*, vol. 168, pp. 235–246, Feb. 2019, doi: 10.1016/j.energy.2018.11.091.

[7] S. S. Ghosh, S. Chattopadhyay, and A. Das, "Identification of an Incipient Snubber Failure in Inverter Employed in Solid Oxide Fuel Cell (SOFC) Fed Microgrid," *IEEE Trans Instrum Meas*, vol. 74, pp. 1–10, 2025, doi: 10.1109/TIM.2025.3544391.

[8] M. S. Arshad *et al.*, "Advances and Perspectives on Solid Oxide Fuel Cells: From Nanotechnology to Power Electronics Devices," *Energy Technology*, vol. 11, no. 12, Dec. 2023, doi: 10.1002/ente.202300452.

[9] S. S. Ghosh, S. Mukherjee, S. Chattopadhyay, and A. Das, "Premature Breakdown Identification in Photovoltaic Array Fed IGBT-based Voltage Source Converter," *Journal of Nano- and Electronic Physics*, vol. 15, no. 3, pp. 03016-1-03016–5, 2023, doi: 10.21272/jnep.15(3).03016.

[10] S. Chattopadhyay, *Nanogrids and Picogrids and their Integration with Electric Vehicles*. Institution of Engineering and Technology, 2022. doi: 10.1049/PBPO208E.

[11] Z. Li *et al.*, "A Fast Diagnosis Method for Both IGBT Faults and Current Sensor Faults in Grid-Tied Three-Phase Inverters With Two Current Sensors," *IEEE Trans Power Electron*, vol. 35, no. 5, pp. 5267–5278, May 2020, doi: 10.1109/TPEL.2019.2946692.

[12] Z. Huang, Z. Wang, and H. Zhang, "A Diagnosis Algorithm for Multiple Open-Circuited Faults of Microgrid Inverters Based on Main Fault Component Analysis," *IEEE Transactions on Energy Conversion*, vol. 33, no. 3, pp. 925–937, Sep. 2018, doi: 10.1109/TEC.2018.2822481.

[13] S. S. Ghosh, S. Chattopadhyay, and A. Das, "Fast Fourier transform and wavelet-based statistical computation during fault in snubber circuit connected with robotic brushless direct current motor," *Cognitive Computation and Systems*, vol. 4, no. 1, pp. 31–44, Mar. 2022, doi: 10.1049/ccs2.12041.

[14] S. S. Ghosh *et al.*, "Wavelet-based rapid identification of IGBT switch breakdown in voltage source converter," *Microelectronics Reliability*, vol. 152, p. 115283, Jan. 2024, doi: 10.1016/j.microrel.2023.115283.

[15] S. Rahimpour, H. Tarzamni, N. V. Kurdkandi, O. Husev, D. Vinnikov, and F. Tahami, "An Overview of Lifetime Management of Power Electronic Converters," *IEEE Access*, vol. 10, pp. 109688–109711, 2022, doi: 10.1109/ACCESS.2022.3214320.

[16] S. F. Zarei, H. Mokhtari, and F. Blaabjerg, "Fault Detection and Protection Strategy for Islanded Inverter-Based Microgrids," *IEEE J Emerg Sel Top Power Electron*, vol. 9, no. 1, pp. 472–484, Feb. 2021, doi: 10.1109/JESTPE.2019.2962245.

[17] L. M. A. Caseiro and A. M. S. Mendes, "Real-Time IGBT Open-Circuit Fault Diagnosis in Three-Level Neutral-Point-Clamped Voltage-Source Rectifiers Based on Instant Voltage Error," *IEEE Transactions on Industrial Electronics*, vol. 62, no. 3, pp. 1669–1678, Mar. 2015, doi: 10.1109/TIE.2014.2341558.

[18] S. S. Moosavi, A. Kazemi, and H. Akbari, "A comparison of various open-circuit fault detection methods in the IGBT-based DC/AC inverter used in electric vehicle," *Eng Fail Anal*, vol. 96, pp. 223–235, Feb. 2019, doi: 10.1016/j.engfailanal.2018.09.020.

[19] H. Renaudineau, P. Paradell-Solà, L. Trilla, A. Filba-Martinez, D. Cardoner, and J. L. Domínguez-García, "Reliability Assessment of a Fault-Tolerant PV Multistring Inverter," *Energies (Basel)*, vol. 13, no. 24, p. 6525, Dec. 2020, doi: 10.3390/en13246525.

[20] B. Song, G. Qi, and L. Xu, "A new approach to open-circuit fault diagnosis of MMC sub-module," *Systems Science & Control Engineering*, vol. 8, no. 1, pp. 119–127, Jan. 2020, doi: 10.1080/21642583.2020.1731005.

[21] C. Morel, A. Akrad, R. Sehab, T. Azib, and C. Larouci, "Open-Circuit Fault-Tolerant Strategy for Interleaved Boost Converters via Filippov Method," *Energies (Basel)*, vol. 15, no. 1, p. 352, Jan. 2022, doi: 10.3390/en15010352.

[22] Q. Wang, Y. Yu, H. O. A. Ahmed, M. Darwish, and A. K. Nandi, "Fault Detection and Classification in MMC-HVDC Systems Using Learning Methods," *Sensors*, vol. 20, no. 16, p. 4438, Aug. 2020, doi: 10.3390/s20164438.

[23] J. O. Estima, N. M. A. Freire, and A. J. M. Cardoso, "Recent advances in fault diagnosis by Park's vector approach," in *2013 IEEE Workshop on Electrical Machines Design, Control and Diagnosis (WEMDCD)*, IEEE, Mar. 2013, pp. 279–288. doi: 10.1109/WEMDCD.2013.6525187.

[24] W. Xing *et al.*, "An Open-circuit Fault Detection and Location Strategy for MMC with Feature Extraction and Random Forest," in *2021 IEEE Applied Power Electronics Conference and Exposition (APEC)*, IEEE, Jun. 2021, pp. 1111–1116. doi: 10.1109/APEC42165.2021.9487126.

[25] C. Voloşencu, *Fault Detection and Diagnosis*. London, UK: InTech, 2018. doi: 10.5772/intechopen.76272.

[26] C. Wang, F. R. Lizana, Z. Li, A. V. Peterchev, and S. M. Goetz, "Submodule short-circuit fault diagnosis based on wavelet transform and support vector machines for modular multilevel converter with series and parallel connectivity," in *IECON 2017 - 43rd Annual Conference of the IEEE Industrial Electronics Society*, IEEE, Oct. 2017, pp. 3239–3244. doi: 10.1109/IECON.2017.8216547.

[27] M. Ali, Z. Din, E. Solomin, K. M. Cheema, A. H. Milyani, and Z. Che, "Open switch fault diagnosis of cascade H-bridge multi-level inverter in distributed power generators by machine learning algorithms," *Energy Reports*, vol. 7, pp. 8929–8942, Nov. 2021, doi: 10.1016/j.egyr.2021.11.058.

[28] D. Chowdhury, M. Bhattacharya, D. Khan, S. Saha, and A. Dasgupta, "Wavelet decomposition based fault detection in cascaded H-bridge multilevel inverter using artificial neural network," in *2017 2nd IEEE International Conference on Recent Trends in Electronics, Information & Communication Technology (RTEICT)*, IEEE, May 2017, pp. 1931–1935. doi: 10.1109/RTEICT.2017.8256934.

[29] G. Kiran Kumar, E. Parimalasundar, D. Elangovan, P. Sanjeevikumar, F. Lannuzzo, and J. B. Holm-Nielsen, "Fault Investigation in Cascaded H-Bridge Multilevel Inverter through Fast Fourier Transform and Artificial Neural Network Approach," *Energies (Basel)*, vol. 13, no. 6, p. 1299, Mar. 2020, doi: 10.3390/en13061299.

[30] R. B. Dhumale and S. D. Lokhande, "Neural Network Fault Diagnosis of Voltage Source Inverter under variable load conditions at different frequencies," *Measurement*, vol. 91, pp. 565–575, Sep. 2016, doi: 10.1016/j.measurement.2016.04.051.

[31] S. Khomfoi and L. M. Tolbert, "Fault Diagnostic System for a Multilevel Inverter Using a Neural Network," *IEEE Trans Power Electron*, vol. 22, no. 3, pp. 1062–1069, May 2007, doi: 10.1109/TPEL.2007.897128.

[32] W. Yuan, Z. Li, Y. He, R. Cheng, L. Lu, and Y. Ruan, "Open-Circuit Fault Diagnosis of NPC Inverter Based on Improved 1-D CNN Network," *IEEE Trans Instrum Meas*, vol. 71, pp. 1–11, 2022, doi: 10.1109/TIM.2022.3166166.

[33] W. Gong, H. Chen, Z. Zhang, M. Zhang, and H. Gao, "A Data-Driven-Based Fault Diagnosis Approach for Electrical Power DC-DC Inverter by Using Modified Convolutional Neural Network With Global Average Pooling and 2-D Feature Image," *IEEE Access*, vol. 8, pp. 73677–73697, 2020, doi: 10.1109/ACCESS.2020.2988323.

[34] S. S. Ghosh, S. Chattopadhyay, S. Banerjee, and A. Das, "Study of Budding Snubber Quality Deterioration in Solid Oxide Fuel Cell-Fed Inverter Used in Microgrid Energy Conversion," *Energy Technology*, Jul. 2024, doi: 10.1002/ente.202400568.

[35] J. Fan, J. Lee, I. Jung, and Y. Lee, "Online Monitoring of Power Converter Degradation Using Deep Neural Network," *Applied Sciences*, vol. 11, no. 24, p. 11796, Dec. 2021, doi: 10.3390/app112411796.

[36] S. S. Kumar, C. M. N. Mukundan, P. Jayaprakash, and M. V. M. Kumar, "Grid Tied Solid Oxide Fuel Cell Power Generation System for Peak Load Management," in *2019 IEEE International Conference on Electrical, Computer and Communication Technologies (ICECCT)*, IEEE, Feb. 2019, pp. 1–6. doi: 10.1109/ICECCT.2019.8869475.

[37] J. Hossain, N. Sakib, E. Hossain, and R. Bayindir, "Modelling and Simulation of Solar Plant and Storage System: A Step to Microgrid Technology," *International Journal of Renewable Energy Research*, no. v7i2, 2017, doi: 10.20508/ijrer.v7i2.5620.g7053.

[38] D. Haribabu, A. Vangari, and J. N. Sakamuri, "Dynamics of voltage source converter in a grid connected solar photovoltaic system," in *2015 International Conference on Industrial Instrumentation and Control (ICIC)*, IEEE, May 2015, pp. 360–365. doi: 10.1109/IIC.2015.7150768.

Chapter 12

Conclusion and Future Scope

This thesis provides and validates new approaches for the early and precise identification of impending faults, addressing the crucial problem of switching device fault analysis in low-voltage inverters (LVIs) used in microgrid (MG) applications.

12.1 Work Summary

A comprehensive overview of the literature on defect detection techniques for AC microgrid power converters (MPCs) has been presented in Chapter 2. This study established the stage for the next research contributions by demonstrating the several ways that MPCs might fail and stressing the need for reliable monitoring systems to facilitate quick fault identification.

An attempt has been made to examine the identification of inverter switch's snubber circuit resistance failure (ISSCRF) in brushless DC (BLDC) motors, an increasingly prevalent robotics application, in Chapter 3.

Chapter 4 discussed the crucial problem of prematurely IGBT breakdown failure (PIBDF) in voltage source converters (VSCs) coupled to photovoltaic (PV) grids. The investigation was conducted utilizing the fast Fourier transform (FFT) approach performed to the VSC's output phase voltage. The impacts on the DC, and fundamental components, as well as harmonic distortions of the acquired signal, have then been examined for varying faulty percentage amounts. This study offered substantial new details about trustworthy PIBDF indicators.

Chapter 5 focused on identifying quick IGBT switch fault (ISF) in MG bidirectional inverters (BDIs) connected to distributed sources of energy. To determine ISF, a statistical analysis using FFT on the BDI's output current has been carried out. It was noted that the parameter readings varied under both ideal and substandard conditions. Using the most favourable characteristics, an attempt has been performed to effectively identify the ISF. Additionally, a process enabling ISF detection is suggested. It has been shown that the FFT-based flaw detection approach is an effective way to find ISF in advance in BDI.

In Chapter 6, an FFT-based methodology for measuring minute changes in the effective resistance of MOSFET (ERM) in single-phase H-bridge inverters (1phHBIs) was proposed. This chapter made a substantial addition to the quick fault identification technique for MOSFET switch fault (MSF) by applying statistical evaluation of the FFT spectra of the inverter's output current. A successful recognition of the MSF has been accomplished relying on the best-fit features. Furthermore, ERM measurement during MSF is made possible by the approach. A method for identifying MSF has also been suggested.

In Chapter 7, the detection of GTO switch failures (GSF) in PV integrated microgrids' three-phase (3Ph) voltage source inverters (VSIs) has been investigated. An investigation on the 3-Phase VSI's current at the output terminal using the FFT was carried out in order to identify GSF. The effects of GSF on different parameters of the acquired current have been investigated at different GSF levels. Here, an attempt has been made to successfully detect the GSF using the most suitable attribute. Furthermore, a method for recognizing GSF has been suggested.

Chapter 8 focused on detecting emerging snubber quality issues, notably nascent snubber-resistance failures (NSFs), in MG's 3-phase inverters (3PhIs) powered by SOFCs. The study examined the impact of snubber resistance failures on different current components using FFT analysis of the inverter output current, leading to a suggested NSF detection technique.

Chapter 9 presents an attempt to use a DWT-based method to identify the ISSCRF in robotic BLDC motors. By using DWT on the stator current, the study successfully illustrated how statistical calculations, such as the values of wavelet coefficients' kurtosis, skewness, and root mean square (RMS), can accurately detect ISSCRF. The effectiveness of the suggested fault identification algorithm for precise diagnosis was demonstrated by validation. This method provides a sensitive diagnostic tool to supplement the earlier FFT-based techniques discussed in Chapter 3.

Chapter 10 demonstrates a method for identifying the breakdown failures of IGBT switches in PV-coupled 3-phase VSCs. The DWT approach was used to analyze the VSC's phase voltage output. In order to determine the ideal parameters for quick defect identification, this study carefully examined the wavelet coefficients' kurtosis, skewness, and RMS values.

Lastly, employing DWT on the inverter's output current, Chapter 11 concentrated on identifying initial snubber circuitry failure (ISCF) in IGBT-based MG inverters connected to SOFCs. The study developed a comprehensive flaw identification system by comparing the wavelet coefficients' kurtosis and skewness values.

12.2 Outcomes

An in-depth overview of the several ways that the AC MPC modules might malfunction is presented in Chapter 2. A variety of failure detection methods (FDMs) are covered here. It describes several kinds of MPC faults, their causes, and effects. A review of existing methods for various MPC switching element fault diagnosis is conducted. The power electronic switches (PESs) and capacitor issues with MPCs are reviewed in this chapter. The findings showed that every contemporary techniques offer reliable defect diagnosis and converter protection. But because of their very short reaction times, some of the techniques are incapable of preventing the system from failing soon after the problem arises. By outlining the various ways that MPCs may malfunction and emphasizing the necessity of dependable monitoring systems to enable prompt fault diagnosis, this study set up the foundation for future research contributions.

Chapter 3 examines the fast Fourier transform (FFT)-based identification of ISSCRF in a small MG inverter linked to robotic BLDC motors. The investigation examines how various ISSCRF percentages (%ISSCRF) affect the DC component (DCC), the fundamental component of current (FCC), and the total harmonic distortion (THD) of the BLDC motor's stator current. It presents the results of studies on the DCC, THD, and FCC of the motor's stator current under normal conditions and at various %ISSCRF. However, no distinct association between the DCC, FCC, and THD of the stator's current and various ISSCRF percentages could be identified. But this FFT-based diagnostic employed for diagnosing ISSCRF ultimately yielded no significant findings applicable to ISSCRF assessment. Since stator current is transitory in nature, it has been discovered that FFT-based fault detection is an inappropriate approach for detecting ISSCRF in a BLDC motor. To overcome the limitations of this FFT-based diagnosis, Chapter 9 explores wavelet transform-based fault evaluation.

The critical issue of PIBDF in VSCs connected to PV grids was covered in Chapter 4. The FFT method applied to the output phase voltage of the VSC was used to carry out the research. The effects on the obtained signal's DC, fundamental components, and harmonic distortions have then been analyzed for various percentage values of the PIBDF (%PIBDF). Certain subharmonic component characteristics have been examined in both the IGBT's normal and malfunctioning states. FFT has been performed on the recorded VSC's output voltage to extract the DCC, fundamental component of voltage (FCV), THD, and sub-harmonic components of voltage (SCV) for various %PIBDF in VSC. Although there is no discernible result that can be implemented to the identification of VSC's PIBDF. Further, for PIBDF identification, the standard deviation and mean values (SDMVs) for the change in the value of all the SCVs for different %PIBDFs have been computed, and it has been discovered that these values change under normal and defective conditions. Therefore, this approach may be used to identify VSC's PIBDF up to 5%. We can also determine the VSC's %PIBDF with the help of the proposed work, according to further investigation.

Chapter 5 illustrated a rapid detection method for identifying the ISF in MG's BDI that is coupled to distributed sources of energy. The FFT has been used to analyze the output current of the BDI in order to determine ISF. The impacts on the collected BDI's output current quality characteristics, such as fundamental current component (FCC), THD, and subharmonics (SHCs) at various ISF percentage levels (%ISFs) have been investigated. Yet, these tests are unable to yield any insightful results that might be exploited to identify ISF in BDI. Furthermore, the SDMVs for the variance in all SHC values for different %ISF have been measured. It shows that the standard deviation value (SDV) of the SHCs continues to increase until it reaches 3% of ISF. It then declines as long as the ISF reaches 10%. Thus, it can be concluded that regularly monitoring the SDV of the SHCs is the most efficient method of rapidly detecting ISF (up to an ISF of 3% in BDI). The following analysis shows that the suggested work also makes it easier for us to determine the BDI's %ISF. An ISF detection technique has also been suggested. A comparison study comparing the approach suggested and several different inverter failure diagnostic methods has also been provided. It was additionally determined through comparison assessment that the technique proposed makes it feasible for calculating the %ISF of the BDI.

In Chapter 6, a methodology based on FFT was presented to measure minute variations in ERM in 1phHBIs. The rapid fault diagnosis method for MOSFET switch fault (MSF) was investigated in this chapter by using statistical analysis of the FFT spectra of the inverter's output current. The effects of MSF on the FCC, DCC, total harmonic distortion of current (THDC), and SHCs have been investigated at different MSF percentage (%MSF) levels. The DCC, FCC, THDC, and SHCs of the captured current that was evaluated through FFT-based assessment for different %MSF. However, these assessments have failed to yield any crucial details that might be applicable towards the identification of MSF in 1phHBI. Additionally, each SHC values associated with various %MSFs have had their variance's SDMVs assessed. According to the analysis, only the SDVs for the SHCs steadily increase as MSF climbs to 15%. Therefore, it is clear that by continuously examining the SDVs of the SHCs, MSF (up to 15%) in 1phHBI may be detected. An MSF detection technique has been devised. Following a comparison of the suggested methodology with other kinds of inverter fault identification systems have been presented. Additionally, the technique makes ERM computation possible during MSF.

The identification of GSF in the 3Ph VSIs of PV integrated MGs has been addressed in Chapter 7. An investigation on the 3Ph VSI's current at the output terminal using the FFT was carried out in order to identify GSF. The FCC, DCC, THDC, and SHCs of VSI output currents over various percents of GSF (%GSFs) have been retrieved and have been investigated using the FFT. Finally, the study showed that only the SHC at 40 Hz, which is expressed as I at 40 Hz, gradually drops until the %GSF hits 20%. By continuously monitoring the SHC at 40 Hz (I at 40 Hz), it is thus shown that VSI's GSF up to 20% may be identified. A method for detecting GSF has been suggested. A comparison of the proposed approach in relation to existing types of inverter fault detecting systems has been provided. The proposed technique may also be used to the estimation of the %GSF in the VSI.

Chapter 8 focused on identifying emergent snubber quality problems in 3-phase MG inverters driven by SOFCs, particularly nascent snubber-resistance failures (NSFs). An investigation has been conducted to identify NSF by using the FFT on the output current waveform of the 3PhI. Investigations have been conducted on how NSF affects the inverter current's zero-frequency component (ZFC), FCC, THDC, and sub-harmonic current (SCC). The study demonstrated that there are no statistically significant correlations between the ZFC, FCC, THDC, and SCCs with %NSF. As an outcome, NSF within the 3PhI could not be revealed utilizing this feature. Furthermore, the mean and standard deviation (MSD) values were computed for each SCC at varying %NSF. Furthermore, by continuously monitoring MSD values, it was discovered that the proposed method could also be used to estimate the NSF up to 10% inside the 3PhI. A method for detecting GSF has been suggested. The real-world cases executed on the testing facility have also been used to validate the proposed method. The purpose of the study was to identify the best technique for detecting NSF. The statistical comparisons and the error rate comparisons make it evident that by utilizing the MSD data of SCCs is the only viable method of achieving the most optimal outcome in %NSF investigation. The proposed NSF identification method has also been used to identify NSF in GTOs, MOSFETs, and thyristor-based inverters. The findings demonstrate that NSF's statistical properties have remained relatively constant. Therefore, the suggested method may be used for NSF identification in the event of an NSF, irrespective of the MG inverter.

An effort to find the ISSCRF in robotic BLDC motors using a DWT-based technique is presented in Chapter 9. The presented study includes the wavelet coefficients of the stator current harmonic spectra's skewness, kurtosis, and root mean square (RMS) measurements to identify ISSCRF. In order to detect ISSCRF, the stator current of the BLDC motor was tracked both under normal operating circumstances and at different %ISSCRFs, up to 50%. The A_K, A_S, and A_R were computed for standard and various %ISSCRF circumstances. Based on the evaluation of statistical factors for approximation coefficients, A_{K9}, A_{S9}, and A_{R9} are possibly helpful in evaluating ISSCRF. The D_K, D_S, and D_R were also computed for standard and various %ISSCRF circumstances. Based on the evaluation of statistical factors for detailed coefficients, only the D_{K7}, D_{K9}, D_{R6}, and D_{R7} are likely to be helpful. Based on the further analysis, it is noted that while both the curves of A_{K9} and A_{S9} are increasingly pronounced, the curve of A_{R9} is decreasingly pronounced as the %ISSCRF develops further. Additionally, it was perceived that when the %ISSCRF rises, the curves of D_{R6} and D_{R7} are rising while those of D_{K7} and D_{K9} are falling. In addition, these curves' shapes have a smaller irregular characteristic than those of the remaining curves. Three case studies and a percentage error comparison analysis between the findings were carried out to obtain the best-fit parameter for ISSCRF detection. Lastly, the highest desirable outcome is only attained when D_{K7} is consulted. The investigation additionally indicated that the %ISSCRF in the inverter could be obtained using the approach proposed.

A technique for determining the IGBT switches' breakdown failures (IBDFs) in three-phase VSCs connected to the PV system is presented in Chapter 10. The DWT approach was used to analyze the VSC's phase voltage output. This study carefully examined the wavelet coefficients' kurtosis, skewness, and RMS values to detect IBDF. The acquired voltage was decomposed till the DWT 9th level. The Daubechies wavelet's mother wavelet in this instance is identified as "db4". For both normal and defective circumstances (up to 10%) of IBDF, approximated and detail coefficients were calculated through DWT level 9. It is difficult to discern between varying percentages of IBDF (%IBDF) utilizing the graphical evaluation method demonstrated, since all of the graphical findings seem to imply the same. Skewness, kurtosis, and RMS values of the VSC's voltage harmonic spectra through DWT 9 levels were further calculated for the intent of detecting IBDF. The K_A, R_A, and S_A were computed for standard and various %IBDF circumstances. Further analyses revealed that the K_{A4} to K_{A7}, R_{A1} to R_{A4}, and R_{A6} values may be useful for IBDF evaluation. Similarly, the K_D, R_D, and S_D were also computed for standard and various %IBDF circumstances and it was discovered that only the R_{D3}, R_{D7}, and R_{D8} are likely to be helpful. The likely effective curves for diagnosing IBDF were chosen for further evaluation. The evaluation illustrates that the exponential changes of R_{D3}, with less non-linear variations from 0% to 3% than between 3% and 5% IBDF. To optimize the calculation within a linear scale, two fault ranges- 0% to 3% along with 3% to 5%, have been examined using logarithmic readings of R_{D3}. It shows clearly that the curves in the logarithmic scale are more linear, particularly for 3% to 5%. This suggests that fault diagnosis of IBDF can be effectively done using the logarithmic scale of R_{D3}. Further, based on the analyses IBDF detection algorithm is suggested. Furthermore, the investigation's contrasting findings and distinctive contributions are also presented.

Chapter 11 demonstrated a 3-phase inverter's (3PhI) initial snubber circuitry failure (ISCF) recognition approach for IGBT inverters coupled to SOFCs employed in microgrid systems. Investigative work has been carried out on the inverter's current output using DWT to identify snubber defects. During the analysis, wavelet coefficients of the output current of the inverter are taken into account together with their kurtosis and skewness values. This study examined the DWT decomposition at 9 levels. The "Daubechies" wavelet's mother wavelet in this instance is identified as "db4". Several parameters have been computed to evaluate the typical and atypical circumstances (for 0% to 85% ISCF) after detail and approximation coefficients were determined. The K_A and S_A were computed for standard and various percentages of ISCF (%ISCF). Furthermore, the graphic evaluations of K_A and S_A data do not offer compelling evidence for problem identification. Moreover, the K_D and S_D were also computed for standard and various %ISCF circumstances. The graphic evaluations of these data illustrate that only the S_{D2}, S_{D3}, and S_{D7} values hinder the ability to evaluate ISCF. The likely effective curves for diagnosing ISCF are chosen for further analysis. Finally, it was demonstrated that using S_{D2} values is the only way to adequately conduct ISCF detection. The algorithmic proposal for detecting ISCF is presented and has been validated using case studies conducted on the lab testing platform. The comparative study is done, and it exhibits that analyzing the S_{D2} values may yield the most substantially feasible outcomes for the %ISCF evaluation, with up to a 99.19% accuracy. The efficacy of the suggested ISCF detection technique is shown by the confusion matrix, and it shows high accuracy in predicting the existence of ISCF. In summary, the findings indicate that the suggested approach can accurately identify ISCF in 3PhI.

12.3 General Conclusion

This thesis proposes and validates an array of effective fault analysis methodologies for switching devices used in LVIs, which significantly advances the fields of power electronics and microgrid dependability. These include a set of sophisticated signal processing and statistical techniques for the fault analysis of different switching devices (IGBTs, MOSFETs, and GTOs) and related components (snubber circuits) across a range of LVI applications in microgrids. These parts are essential to the functioning of MPCs, and their failure might result in decreased efficiency, worse power quality, or possibly the system shutting down entirely. As a result, prompt and precise defect detection is crucial. These suggested FDMs are very appropriate for real-time applications in real-world settings since they were created with a focus on simplicity, quick reaction times, and low computing burden. The suggested techniques may be readily integrated into existing systems without requiring significant hardware modifications, in contrast to intricate or resource-intensive alternatives.

The results of this work provide a viable and effective solution to increase the resilience, operational lifespan, and dependability of microgrid systems by improving the fault detection capabilities of LV MPCs. The suggested methods provide early identification, reducing maintenance expenses and preventing significant equipment failures. In light of rising energy needs and system complexity, the thesis lays the groundwork for future studies in intelligent and adaptive diagnostic systems, opening the door to more intelligent and sustainable MG operations.

12.3 Future Scope

The study described in this thesis provides a number of exciting directions for further research that might enhance the fields of microgrid reliability and switching device failure analysis:

12.3.1 Artificial Intelligence and Advanced Machine Learning Integration

Using the existing signal processing techniques in conjunction with cutting-edge machine learning (ML) and artificial intelligence (AI) approaches like deep learning neural networks or reinforcement learning might result in defect diagnostic systems that are more intelligent and adaptable. This may improve fault detection's precision, speed, and predictive power, particularly in complicated or multi-fault situations.

12.3.2 Forecasting and Estimating Remaining Usable Life (RUL)

It would be a major improvement to extend the present fault identification abilities to prognostics, which entails forecasting the RUL of switching devices. This might provide genuine predictive maintenance, reducing microgrid interruptions and operating costs by enabling component replacements prior to catastrophic failures.

12.3.3 Considering Fault-Tolerant Control Methods

Future studies might concentrate on creating and putting into practice fault-tolerant control techniques for LVIs, relying on failure detection systems. To improve overall system resiliency and power supply continuity, this would enable the microgrid system to continue functioning even after a malfunction has been identified, although with reduced performance.

12.3.4 Diagnosing and Isolating Multiple Faults

Future research might investigate thorough techniques for identifying, differentiating, and isolating several concurrent failures in the same inverter or across several microgrid components. In order to do this, more advanced algorithms that can handle intricate fault signatures would be needed.

12.3.5 Effects of Cyber-Physical Security on the Identification of Faults

It is essential to look at how cyber-physical assaults affect the dependability and integrity of fault diagnostic systems as microgrids become more digitally integrated. Future studies could concentrate on creating robust and safe fault detection systems that can withstand cyberattacks.

The insights and techniques established in this thesis can be improved and extended by following these research possibilities, which will help create microgrid systems that are incredibly dependable, effective, and resilient for a sustainable energy future.

Sankha Subhra Ghosh
23/09/2025